BABCOCK-LEIGHTON SOLAR DYNAMO MODEL: THE ROLE OF ACTIVE REGION INFLOWS FOR THE SATURATION OF THE SOLAR DYNAMO

By

Kinfe Teweldebirhan Gebreegzabihar

SUBMITTED IN PARTIAL FULFILLMENT OF THE
REQUIREMENTS FOR THE DEGREE OF
DOCTOR OF PHILOSOPHY IN PHYSICS
AT
ADDIS ABABA UNIVERSITY
ADDIS ABABA, ETHIOPIA
JUNE 2018

ADDIS ABABA UNIVERSITY
DEPARTMENT OF
PHYSICS

Supervisor: _____
Prof. Mark S. Miesch

Examiners: _____
Dr. Ramudin Reshid

_____
Prof. Bidya Binay Karak

ADDIS ABABA UNIVERSITY

Date: **June 2018**

Author: **Kinfe Teweldebirhan Gebreegzabihar**

Title: **Babcock-Leighton Solar Dynamo Model: The Role Of Active Region Inflows For The Saturation Of The Solar Dynamo**

Department: **Physics**

Degree: **Ph.D.** Convocation: **June** Year: **2018**

Permission is herewith granted to Addis Ababa University to circulate and to have copied for non-commercial purposes, at its discretion, the above title upon the request of individuals or institutions.

Signature of Author

To my parents,

To my wife Lemlem

and

To my Daughters Tewobstia and Ruwana.

Table of Contents

List of Figures

Abstract

Helioseismology has detected that solar photospheric active regions are surrounded by spatially extended, converging flow with typical flow velocities of 20-30 m/s. They extend up to 30 degrees from the center of the active region. It has been proposed that this converging flow may act as a saturation mechanism for the solar dynamo, and as such, may determine the strength of solar cycles. In this work we explore questions such as: Are the converging flows towards active regions an effective saturation mechanism for Babcock-Leighton solar dynamo models?

These inflows can potentially play an important role in flux-transport models of the solar cycle. The model of inflow towards the active regions is developed within the framework of the Surface flux Transport And Babcock-LEighton (STABLE) solar dynamo model. STABLE is designed to capture both the 11-year solar cycle and the evolution of photospheric magnetic flux with high fidelity. The STABLE model solves the kinematic magnetohydrodynamic (MHD) induction equations in a 3D, rotating, spherical shell. The induction equation is solved by means of the Anelastic Spherical Harmonic (ASH) code, which currently serves as the dynamical core for the STABLE model. STABLE uses the SpotMaker spot deposition algorithm to place bipolar magnetic regions (BMRs) on the solar surface in response to the dynamo-generated toroidal magnetic field. In this way, the model can be regarded as a unification of BL dynamo models (2.5D in radius/latitude) and surface flux transport models (2.5D in latitude/longitude) into a more self-consistent framework that builds on the successes of each while capturing the full 3D structure of the evolving magnetic field. The subsequent evolution of these BMRs due to differential rotation, meridional circulation, inflow and turbulent diffusion naturally generates a mean poloidal field as originally described by Babcock (1961) and Leighton (1964).

We verified the STABLE model by reproducing a 2D mean-field benchmark and this model, and reproduces some basic features of the solar cycle including an 11 yr periodicity,

equatorward migration of toroidal flux in the deep convection zone, and poleward propagation of poloidal flux at the surface. The poleward-propagating surface flux originates as trailing flux in BMRs, migrates poleward in multiple non-axisymmetric streams, and eventually reverses the polar field, thus sustaining the dynamo. We also present some representative dynamo simulations, focusing on the special case of kinematic magnetic induction and axisymmetric flow fields. Not all solutions are supercritical; it can be a challenge for the BL mechanism to sustain the dynamo when the turbulent diffusion near the surface is $\geq 10^{12}$ cm^2 s^{-1}. However, if BMRs are sufficiently large, deep, and numerous, then sustained, cyclic, dynamo solutions can be found that exhibit solar-like features. Furthermore, we find that the shearing of radial magnetic flux by the surface differential rotation can account for most of the net toroidal flux generation in each hemisphere, as has been recently argued for the Sun by [Cameron and Schüssler(2015)].

We find that inflows into active regions can indeed enhance flux cancellation and regulate the strength of magnetic cycles. We find that inflows decrease the amplitude of the polar field, relative to a no-inflows scenario (that is the tilt angle saturation [Karak and Miesch(2017)]). Stronger (weaker) inflows lead to larger (smaller) reductions of the polar field. Our STABLE simulations show that converging flows toward the BMRs significantly inhibits the build-up of the polar field and provide a non-linear feedback mechanism capable of saturating the global dynamo of the solar cycle within the Babcock-Leighton paradigm. To our knowledge this is the first 3D Babcock-Leighton model with explicit BMRs to demonstrate that converging flows can serve as a viable saturation mechanism for the solar dynamo. We also discuss how the converging flows play a key role in determining the strength of magnetic cycles.

Acknowledgements

First and above all, I praise God, the almighty for providing me this opportunity and granting me the capability to proceed successfully.

This journey has only been possible with the assistance of a few friends. First and foremost, my most heartfelt gratitude goes to my advisor Mark S. Miesch for his support, friendship, generosity, commitment and incredibly wise advice to shape my professional career. Mark gave me the opportunity to work in advanced solar physics research and computer programming at a time when I knew nothing abut the programming. I am so grateful that he decided to take me on as a PhD student in 2014, which I was in the middle of no where and I am privileged to have been his PhD student thus far. Mark has become a trusted mentor and a valued friend and has provided me with opportunities beyond compare. Over the years, he have acted to kindle my scientific enthusiasm, to provide perspective on life, and to help me find my way. It was an honor and pleasure to have him as my supervisor. I will never forget his words of encouragement I have learned so much from his positive outlook, work ethic, dedication and deep insights have contributed greatly to my own growth and I hope to carry with me throughout my career. Mark! I immensely thankful for the wonderful opportunity you gave me.

I am grateful to Dr. Abrham Amaha, my home University supervisor and for his wonderful friendship and support. I would like to thank Physics Department of Addis Ababa University. I wish to thank Dr. Belayneh Mesfin for his friendly approach and support when he was head of physics department, Addis Ababa University. I wish to thank Dr. Teshome, head of the Physics department, Addis Ababa University.I wish to thank wezero Tsilat, secretary in Physics department for her kindly approach and facilitate in the department. I am deeply indebted Prof. V. N. Mal'nev, my late advisor, for his constructive suggestions and he was teaching me the Plasma Physics course in Addis Ababa University. Thanks to my M.Sc. late advisor Dr. Legesse Wetro.

I would like to thank all my friends. I would also like to thank Lisa Upton, for her many enlightening conversations about this dissertation and I would like to thank Kyle Augustson and Bidya Karak. My strongest thank is addressed to my parents and my intimate relatives. They are the hero of my success with out their push and support, this stage is unthinkable. Thanks to my loving wife Lemlem for her support, as well as her

patience in taking care of our kids. Thanks to my daughters Tewebstia and Ruwana. I thank Dr. Teshome Senbeta, Dr. Ramudin Reshid and Prof. Bidya Binay Karak for serving on my thesis committee or examiner.

Finally, this dissertation would not have been possible without the support of several institutions. I wish to thank the High Altitude Observatory of National Center for Atmospheric Research (NCAR/HAO), Advanced Study Program of National Center for Atmospheric Research (NCAR/ASP) for funding my visit to NCAR/HAO in support of this research. The simulations in this dissertation were performed using resources provided by NCAR High-performance computing (HPC) maneged by Computational and Information Systems Laboratory (CISL), supper computer NCAR Cheyenne. The National Center for Atmospheric Research is sponsored by the National Science Foundation. None of this analysis would have been possible without the resources; many research journals and books, and I am indebted to the authors of those publications and books.

Chapter 1

Introduction

1.1 The Solar Magnetic Field

The Sun, like the Earth, generates a magnetic field that extends out into space. However, the Sun's magnetic field changes both its shape and intensity over the surface, and over time, much more rapidly. The Sun is an active star whose magnetism has a direct impact on the Earth and our technological society. Being able to understand and anticipate this magnetic activity is crucial and has thus been the subject of intense research. It is currently believed that the Sun operates an internal dynamo to generate, sustain and organize magnetic fields on both small and large scales. Given the complexity of the problem, i.e. the self-generation of magnetic fields by a turbulent rotating plasma and the non-linear interactions which yield this wide range of dynamical phenomena, numerical models of the magnetohydrodynamics of the Sun have been developed.

Our Sun is a typical main sequence G-type star with well-measured radius ($R_\odot = 6.96 \times 10^8$ m), mass ($m_\odot = 1.99 \times 10^{30}$ kg), and luminosity ($L_\odot = 3.85 \times 10^{26}$ W). Its $\sim$ 5,800 K surface temperature provides roughly 1.4 kW m^{-2} energy near the Earth, ideal for the existence of liquid water and hence the sustainment of life. The solar interior can be divided into three layers (see Figure 1.1): the core, the radiation zone, and the convection zone. The core extends to about $0.2R_\odot$, is extremely hot ($\sim$15 MK = $\sim 15 \times 10^6$ K), and hosts the Sun's energy source: the proton-proton chain fusion process. Outside the core,

the radiation zone extends to about $0.7R_{\odot}$ where the photons carry the fusion energy upward and encounter continuous scattering along the way. The convection zone resides between $0.7R_{\odot}$ to $1.0R_{\odot}$, where the plasma is convectively unstable and thus forms convection cells. Motions of plasma become the major means of transferring the energy. Shear at the base of the convection zone, coupling with the large-scale motions of the convection zone, including the differential rotation and the meridional flow, are believed to give rise to the solar magnetic field and its cyclic behaviors through the dynamo effect. Between the solar interior and atmosphere lies the photosphere at which the plasma turns optically thin. The convective flows below forms cell-like structures known as granules and supergranules.

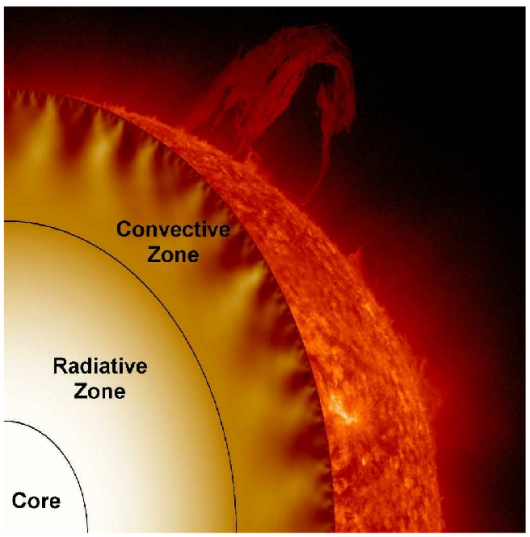

Figure 1.1: Solar interior:
Core, radiative zone, convection zone. Credit: L. Upton, D. Hathaway NASA/MSFC.

Solar granulation is driven by radiative cooling in a thin layer within about 100 km of the photosphere. As radiation streams away from a location on the photosphere the plasma cools, compresses, and sinks, pulled down by gravity. Surrounding fluid rushes in to fill the void, driven by horizontal pressure gradients. Upflows are thus a passive response to the negative buoyancy of downflows and are relatively isentropic in comparison to the

distribution of low entropy in downflows. The nature of the induced circulation is such that the maximum upflow velocity occurs adjacent to the downflow region. With a little effort, one can discern other characteristic spatial and temporal scales in photospheric measurements over and above that of granulation. The most apparent of these is known as supergranulation (L $\sim$ 30 Mm, $\tau \sim$ 20 h). Although supergranulation is detectable in photospheric Dopplergrams in local helioseismic inversions and in the correlation tracking of granular features, it is most readily observed as the dynamical substrate underlying the quiet magnetic network, both figuratively and literally [Schrijver and Siscoe(2010)], [Miesch(2005)].

Magnetic field concentrations emerge from the convection zone, the largest manifest themselves as sunspots (Figure 1.4*b*) where the field ($\mathbf{B}$) can be as strong as a few thousand kG (kilo Gauss, or 0.1 T). Many absorption lines form in this cool, thin layer; the ones sensitive to magnetic field can be used to probe the solar surface magnetism. It is now generally accepted among astrophysicists that the origin of the Sun's magnetic field, which is highly variable both in space and in time, must be sought in inductive motions; these are localised in its outer convective zone, which extends from the visible surface of the Sun (r = $R_\odot$) down to about $r = 0.69R_\odot$. The natural decay time for the fundamental dipole mode is of order 4×10^9 years, which is of the same order as the age of the solar system [Moffatt(1978)].

As stated above understanding the activity and magnetic cycle of the Sun is crucial since its variability has a direct impact on our technological society by disturbing high frequency signals, impairing satellites and damaging power grids. For several decades the scientific community has developed observational, theoretical and numerical tools in order to be able to understand the inner workings of the Sun, while at the same time aiming to be able to predict its activity. The current accepted scenario states that this surface magnetism is linked to an internal dynamo. several studies of solar dynamo models have been developed to test and validate ideas and distinguish among scenarios of the solar

dynamo.

The surface of the Sun is covered in magnetism on all scales, with global-scale structures including prominences that reach high into the solar atmosphere (Figure 1.2*a*) as well as smaller concentrated magnetic structures like sunspots, where the magnetism becomes strong enough to largely halt the turbulent convection leaving dark regions at the surface (Fig. 1.2*b*). On the smallest scales visible at the surface, magnetic fields are swept aside by vigorous granulation which are convective cells that overturn every 10-15 minutes and have flows that are near the speed of sound ($\sim$ 2 km/s). The magnetism collects in the surrounding network of downflow lanes, where it is swept out by the slower flows of supergranulation, whose characteristic timescales are closer to a day. There the magnetism traces out the supergranular network, and expands outwards into the solar chromosphere and corona. Solar magnetism is far from being static, and it evolves on many timescales, with a prominent and regular eleven-year cycle of sunspots and global-scale polarity reversals.

Observations of magnetic activity on the Sun reveal extremely complex behavior but systematic patterns also exist, at least some of which may be traced back to field generation in the convection zone and tachocline. Thus, a wide variety of magnetic activity is of relevance to solar interior dynamics; here we will only scratch the surface. The most familiar and compelling magnetic activity pattern in the Sun is the sunspot cycle and the corresponding butterfly diagram. Sunspots and other manifestations of magnetic activity emerge in well-defined latitudinal bands which migrate toward the equator on a timescale of about 11 years. As these activity bands converge on the equator, the polarity of the global field reverses and the emergence pattern repeats, returning to its previous magnetic configuration after two reversals, yielding a net 22-year periodicity [Miesch(2005)].

There are number of phenomena on the solar surface which have direct relation with solar activity. One of the most known ones are sunspots, which are magnetic structures that appear dark on the solar surface. Each sunspot is characterized by a dark core, the

umbra, and a less dark halo, the penumbra (see Figure 1.2*b*). The presence of a penumbra distinguishes sunspots from the usually smaller pores. Concentrations of magnetic field cause dark areas on the solar surface which have radii between 2 to 20 Mm and life times between one day to a few months. Their temperature is about 3000 to 4000 K, which is cooler than their surrounding temperature, so they look darker (Figure 1.4*a*).

The Sun goes through a natural solar cycle approximately every 11 years. The cycle is marked by the increase and decrease of sunspots which are visible dark regions on the Sun's surface and cooler than surroundings. The greatest number of sunspots in any given solar cycle is designated as the "solar maximum" and the lowest number is referred to as the "solar minimum" phase. We stand at the very end of cycle 24; solar cycle 24 is the 24^{th} solar cycle since 1755 (see Figure 1.5), when extensive recording of solar sunspot activity began. It is the current solar cycle, and began in December, 2008. There was only minimal activity until early 2010 and it reached its maximum in April 2014. Solar cycle 24 has the lowest sunspot number in over a century (see Figure 1.5). The current solar cycle 24, is the weakest solar cycle in more than a century and it is now we are at the solar minimum phase which would be the beginning of solar cycle 25 in the late 2020 (extended minimum for the Cycle 24/25 minimum in 2020) [Hathaway and Upton(2016), Jiang and Cao(2017)].

1.1.1 Sunspots and the Butterfly Diagram

The sunspot areas are thought to be more physical measures of solar activity and they are a phonomenen at the surface regions where there is a strong magnetic field. The sunspots have been known to humanity for about 2000 years. Their rising and waning every 11 years is the best known manifestation of the solar cycle. The cyclic evolution of sunspots is generally represented in the butterfly diagram (see Figure 1.5; upper penel). The positional information, both latitude and longitude distribution of sunspots and active regions are restricted to heliographic latitudes $\sim 30^{\circ}$ wide, symmetric about the equator

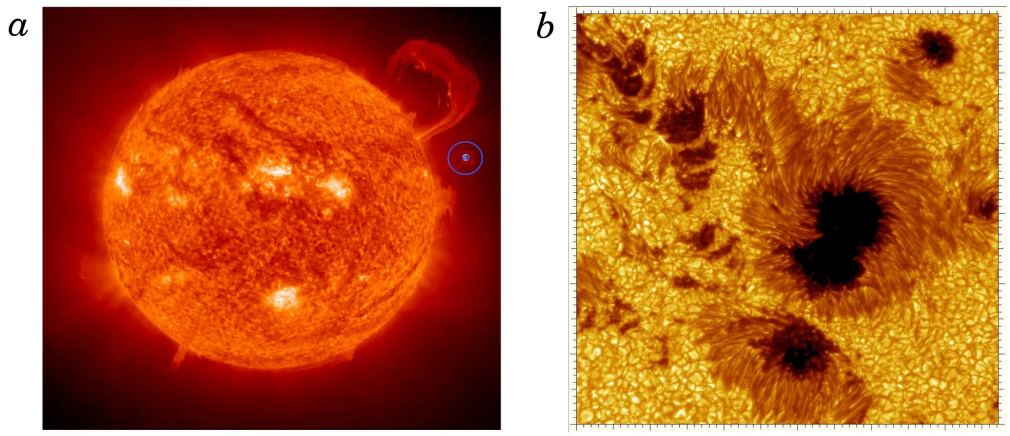

Figure 1.2: Solar magnetism:
Solar magnetism at many scales. (a) On global-scales, a large prominence lifting off the limb of the Sun is revealed in this SOHO EIT image. A scaled-image of the Earth (inside blue circle) is provided for comparison. (b) On finer scales, as seen in this image from the SSVT, sunspots at the surface are regions of strong magnetism. Tick marks indicate 1Mm spacings. Individual sunspots are roughly the size of the Earth.

The magnetic butterfly diagram illustrates how the distribution of magnetic flux changes over time. Sunspots appear in bands on either side of the equator. Cycles typically overlap by 2-3 years. At the beginning of each cycle, the active regions emerge at latitudes of about 30 degrees. As the cycle progresses, the active regions emerge closer and closer to the equator. Near the end of the cycle, they appear almost at the solar equator, an effect known as Spörer's Law. Cancellation of polarity across the equator leaves behind an excess of following polarity that is transported to the poles. The north and south poles have opposite polarities that reverse from cycle to cycle. The timing of this polar field reversal is near the time of the solar cycle maximum. The maximum coverage of solar magnetic activity occurs when the active region bands reach at about latitude of $\simeq 15°$. The magnetic polarity sense (direction of the magnetic field in to or out of the solar surface) of active regions are of opposite sign in each hemisphere. With the start of a new sunspot cycle, the leading polarities of active regions in both hemispheres switch sign; this is known as Hale's Law. Therefore, it takes $\sim$22 years for each hemisphere to complete a

full magnetic cycle, although the progression of the toroidal, active region belts from mid-latitudes to the equator takes ∼11 years. This ∼11 year cycle is typically referred to as the solar cycle and ∼ 22 years cycle [Ossendrijver(2003), Hathaway(2010), Weber.(2014)].

The solar photospheric magnetic field is commonly measured using the Zeeman effect. The interaction between the electron magnetic moment and the field splits the atomic energy levels. For a transition between two split energy levels, the spectral line will split correspondingly, and each component will have a distinctive polarization state. The relative wavelength of these polarized components can be used to probe the magnetic field at where the line is formed in the photosphere. The Sun shows magnetic field on all observable scales with a significant range in field strength, from individual sunspots with magnetic field strengths of 2500 to 3000 gauss to the average field strength of the global field of only a few gauss [Schrijver and Siscoe(2009)].

The connection between sunspots and magnetism was made in 1908 by George Ellery Hale through the use of a device called the spectroheliograph, and the knowledge that certain spectral lines split into multiple components in the presence of a static magnetic field, known as the Zeeman Effect. Measuring the Zeeman splitting in magnetically sensitive lines in the spectra of sunspots and detecting the polarization of the split spectral components (Figure 1.3), Hale provided the first unambiguous and quantitative demonstration that sunspots are the seat of strong magnetic fields. Not only was this the first detection of a magnetic field outside the Earth, but the inferred magnetic field strength, 0.3 T, turned out a few thousand times greater than the Earths own magnetic field. It was subsequently realized that the Lorentz force associated with such strong magnetic fields would also impede convective energy transport from below, and therefore lead naturally to the lower temperatures observed within the sunspots, as compared to the surrounding photosphere [Charbonneau(2013)].

The large scale magnetic activity pattern on the solar photosphere is in the form of bipolar magnetic regions, with the leading magnetic polarity area (leading in the direction

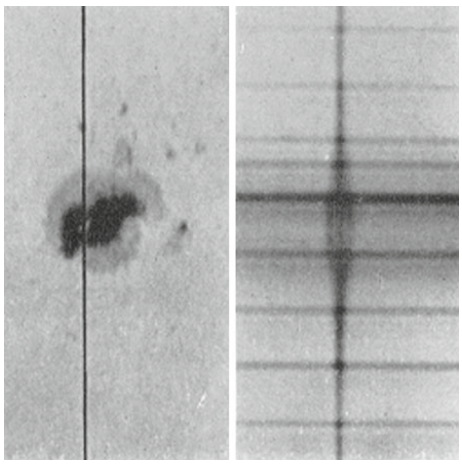

Figure 1.3: Zeeman splitting:
The magnetically induced Zeeman splitting in the spectrum of a sunspot. The vertical dark line on the left image is the slit having produced the vertical stack of spectra on the right image (with wavelength running horizontally). Reproduced from the 1919 paper by Hale et al. [Charbonneau(2013)].

of solar rotation) of opposite polarity sign of the following region (see Figure 1.4; right panel). A line drawn between these two polarity areas is approximately the East-West oriented, but typically tilted (Joys law). The strongest of these regions appear as sunspots when observed in white light (see Figure 1.4; left). More is revealed when the Sun is observed in extreme ultraviolet wavelengths (see Figure 1.2). The bipolar magnetic regions, or active regions, are the source regions of strong solar activity, such as solar flares, and serve as footprints for coronal loops.

Sunspot number

Sunspots are the most striking manifestations of solar activity and appear when deep-seated toroidal flux ropes rise through the convective envelope and emerge at the photosphere. Their incidence, as measured by area occupied or the traditional sunspot number R (Equation 1.1.1), follows the irregular 11-year activity cycle that is best demonstrated by the butterfly diagram in (see Figure 1.5).

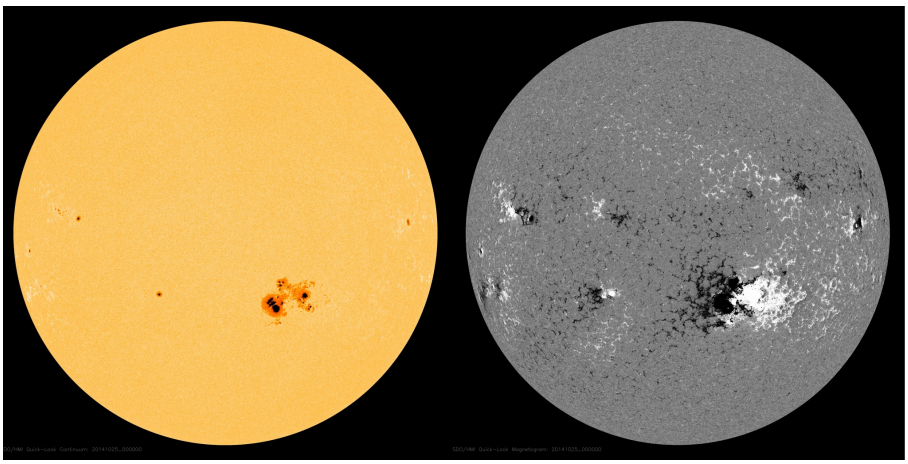

Figure 1.4: Sunspots:
A full-disk line-of-sight magnetogram (right), the Black (white) indicates magnetic regions of negative (positive) opposite polarity of magnetic field in active regions and sunspots and continuum intensity image (left) of the solar photosphere, both taken on, Oct, 25, 2014 by the HMI instrument onboard the SDO satellite. The sun's rotation axis is vertical on both images. Leading spots in one hemisphere have opposite magnetic polarity to those in the other hemisphere and the polarities flip from one cycle to the next. Public domain images downloaded from the SDO mission website: https://sdo.gsfc.nasa.gov.

$$R = k(10g + n) \tag{1.1.1}$$

where k is a correction factor for the observer, g is the number of identified sunspot groups, and n is the number of individual sunspots. In (Equation 1.1.1) R is Wolf's relative sunspot number where as traditionally, sunspot numbers are given as daily numbers, monthly averages, yearly averages, and smoothed numbers.

The true nature of solar activity was only revealed when Hale discovered that dark spots are the sites of strong magnetic fields. Sunspots typically occur as a pair, aligned approximately with a parallel of latitude but with the leading spot (in the sense of the solar rotation) usually somewhat closer to the equator. The leading and following spots have opposite magnetic polarities, and the appearance of sunspot pairs at the photosphere is best understood as caused by the emergence of a toroidal flux tube from deep in the

underlying convection zone. Hale found that the polarities of the spots are consistent in each hemisphere but antisymmetric about the equator. Moreover, these polarities reverse at the end of each 11-year activity cycle, so that there is a magnetic cycle with a period of 22 years (see §1.1.2). The sunspots are associated with active regions, and there are smaller scale fields on a wide range of scales all over the solar surface. Near the poles there are weaker unipolar fields that are most prominent at sunspot minimum, and reverse at sunspot maximum [Hathaway(2010)].

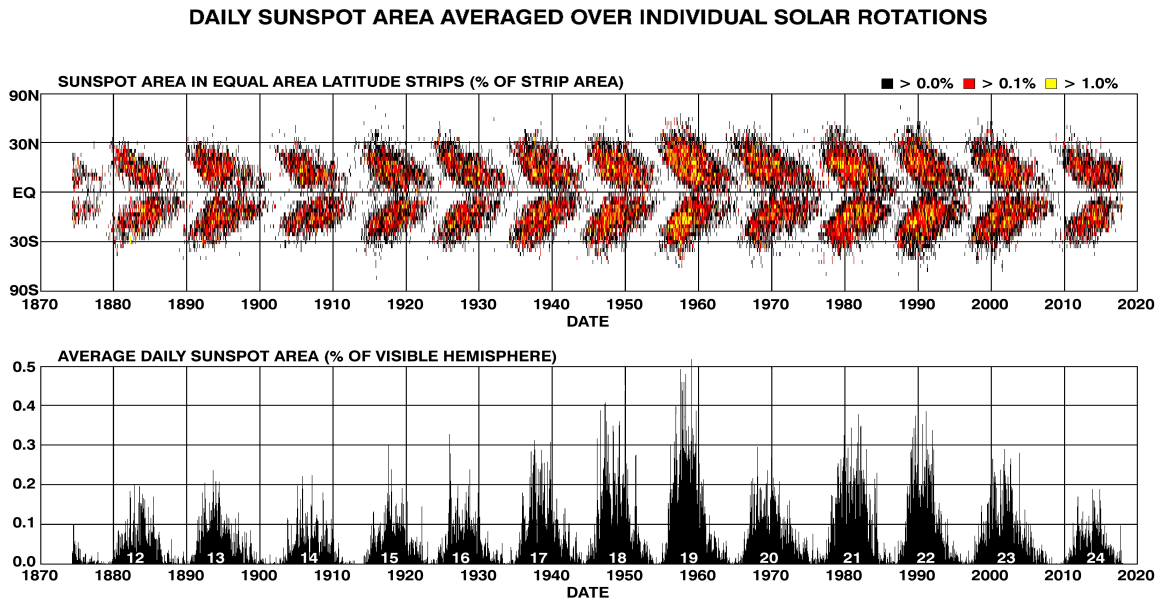

Figure 1.5: Butterfly diagram:
Cyclic activity on the Sun since 1874. The lower panel shows the daily sunspot area as a function of latitude and time, as a percentage of the visible hemisphere that is covered by sunspots and averaged over individual solar rotations, which varies quasiperiodically with an 11-year period, showing emergence of sunspots at the surface. The butterfly diagram illustrated with a color code in the upper panel shows the corresponding incidence of sunspots as a function of latitude and time. Sunspots form in two bands, at the beginning of a new cycle, spots appear at high latitudes, around latitudes of $\pm$ 30° from the equator and migrate toward the equator as the cycle progresses. When their number is near maximum, the global-scale polarities reverse. The activity zones spread until they extend to the equator, and then gradually die away, disappearing at the equator as the first spots of the next cycle appear at higher latitudes. (courtesy of D. Hathaway, NASA/MSFC; see http://solarscience.msfc.nasa.gov/images/bfly.gif)

Within the sunspots, the magnetism can evolve on very short timescales. In some active regions the strong magnetic fields reconnect, leading to explosive releases of energy in the form of high-energy photon flares and eruptive plasma coronal mass ejections. As these photons and magnetized plasma storms strike the Earths magnetosphere, they can profoundly affect our modern society, imperiling astronauts and satellites in space and scrambling communications and navigation systems on the ground. The largest solar storms can threaten the very infrastructure of national power grids and can disrupt or destroy computational systems.

As the cycle progresses, the sunspots will become more numerous, peaking in number roughly midway through (see Figure 1.5; lower panel). Generally, the number of sunspots present on the solar disk increases rapidly at the start of a new solar cycle and then declines more gradually. It is during the later half of the cycle that the largest storms and eruptive events tend to occur, though major flares and eruptions can occur at any time. Near the middle of the roughly eleven-year solar cycle, when the number of sunspots is near maximum, the magnetic poles of the Sun flip in polarity. As the number of sunspots declines and the active latitudes approach the equator, a cycle begins anew with sunspots of opposite polarity emerging at high latitudes. Though the timing of the solar cycle is fairly regular, the magnetic activity shows modulation on longer timescales as well. Some cycles are strong, with many spots, while some cycles are weak. At times, as during the Maunder Minimum (see Figure 1.6), the surface of the Sun has remained barren of sunspots for decades [Brown(2009)].

1.1.2 Hale's Polarity Laws

The radial magnetic field averaged over longitude for each solar rotation is shown in Figure 1.7. This Magnetic Butterfly Diagram exhibits Hale's Polarity Laws and the polar field reversals as well as Joy's Law [Hale et al.,(1919)]: The following spot of the pair tends to appear farther from the equator than the preceding spot, and the higher the latitude, the

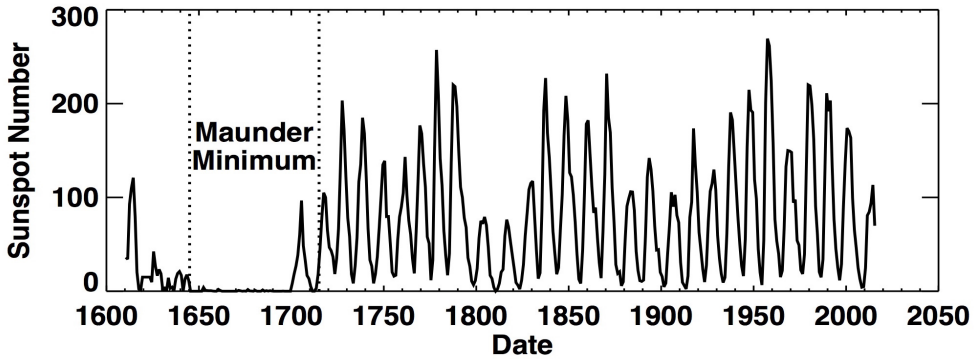

Figure 1.6: Maunder minimum

Sunspot Cycles. The amplitude of the sunspot cycles from 1600 to present varies substantially. This includes theMaunderMinimum, a period from 1645 to 1715 when the magnetic fields were too weak to produce sunspots. (Courtesy of L, Upton and D.H. Hathaway; http://solarcyclescience.com/solarcycle.html).

greater is the inclination of the axis to the equator. Joy's Law and Hale's Polarity Laws are apparent in the butterfly wings. The equatorial sides of these wings are dominated by the lower latitude, preceding spot polarities while the poleward sides are dominated by the higher latitude (due to Joy's Law), following spot polarities. These polarities are opposite in opposite hemispheres and from one cycle to the next (Hale's Law). This figure also shows that the higher latitude fields are transported toward the poles where they eventually reverse the polar field at about the time of sunspot cycle maximum.

Hale and his collaborators did much more than just measure magnetic fields in sunspots. Through painstaking observations and analyses spanning nearly two decades, they went on to demonstrate the existence of a number of regularities in the magnetic fields of sunspots, now known as Hale's polarity laws. Having noted early on that large sunspots often appear grouped in pairs of opposite magnetic polarities, they could show that:

At any given time, the polarity of the leading spots (with respect to the direction of solar rotation) of sunspot pairs is the same in a given solar hemisphere;

At any given time, the polarity of the leading spots of sunspot pairs is opposite in the North and South hemispheres;

Sunspot polarities reverse in each hemisphere from one 11-yr sunspot cycle to the next.

This polarity ordering is fairly easy to discern on the magnetogram of Figure 1.4 The most straightforward interpretation of this common opposite polarity grouping is that we are seeing the surface manifestation of a large-scale toroidal field residing somewhere below the photosphere, having risen upwards and pierced the photosphere in the form of a so-called "Ω-loop" (see Figure 1.8 frame, *c*), its intersection with the photosphere producing sunspot pairs of opposite polarities. If this is the case, and if the magnetic flux ropes have not suffered too much twisting about the axis defined by the trajectory of their apex, then the sign of the deep-seated toroidal component $\mathbf{B}_\phi$ is then given by the magnetic polarity of the trailing sunspots. This picture of sunspot pairs, taken in conjunction with Hale's polarity laws, therefore indicate that the sun's internal toroidal field is antisymmetric about the equator and reverses polarity from one sunspot cycle to the next [Charbonneau(2013)].

1.1.3 The Magnetic Cycle

The butterfly diagram is an important diagnostic of the solar dynamo, but a naive comparison with magnetic field intensities obtained from dynamo calculations can be misleading. Since sunspots are the product of flux tubes rising from the magnetic layer at the bottom of the convection zone, the solar butterfly diagram reflects dynamo action in that location. Secondly, the distribution of the deep-seated magnetic field is masked by the process of flux emergence. The stability of the flux tubes depends on the magnetic field intensity, latitude and other parameters. Hence the latitudinal distribution of sunspots does not necessarily reflect that of the magnetic field. Paradoxically, it appears that the differential rotation and the α-effect (BL α-effect) provide more favorable conditions for dynamo action at high latitudes than at the latitudes of sunspot emergence [Ossendrijver(2003)].

Figure 1.7 is a synoptic (time-latitude) diagram of the longitudinally-averaged photospheric radial magnetic field component, covering the last four sunspot cycles. Such a

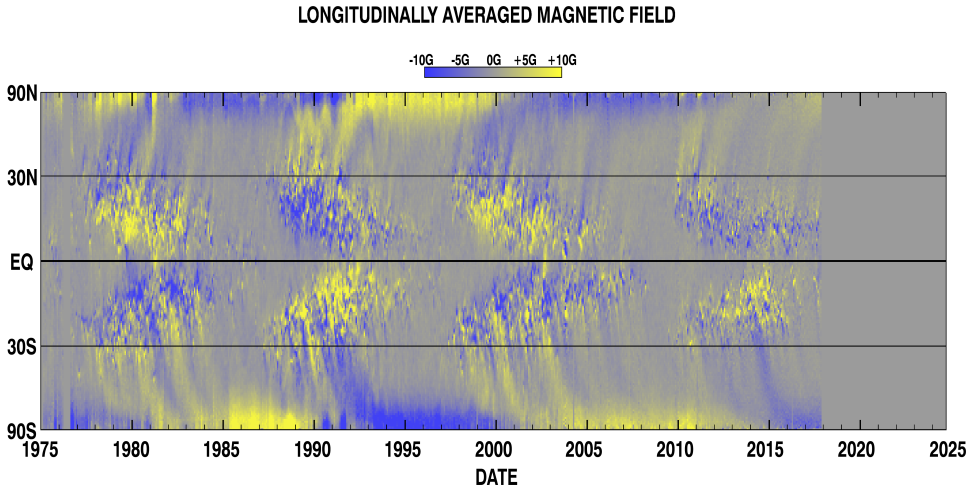

Figure 1.7: A magnetic butterfly diagram;
this shows the distribution of the surface magnetic field (longitudinally averaged) over the last four solar cycles. The poles have opposite polarities that switch from one cycle to the next near the time of solar maximum. This illustrates Hale's Polarity Law, Joy's Law, polar field reversals, and the transport of higher latitude magnetic field elements toward the poles. (Courtesy of L, Upton and D.H. Hathaway; see http://solarcyclescience.com/solarcycle.html).

diagram is constructed by averaging magnetograms (like the one on 1.4) in longitude over each successive solar rotation, and stacking side-by-side the resulting latitudinal distribution of ϕ-averaged magnetic field to form a temporal sequence. The most immediately striking global patterns apparent on Fig. 1.7 are certainly the cyclic variations on a $\sim$ 22 yr period, accompanying polarity reversals, and the (anti)symmetry about the solar equator [Charbonneau(2013)].

1.2 Solar Dynamo Operation

While regular observations of sunspots go back to the early seventeenth century, and discovery of the sunspot cycle to 1843, it is the landmark work of George Ellery Hale and collaborators that, in the opening decades of the twentieth century, demonstrated the

magnetic nature of sunspots and of the solar activity cycle. In particular, Hale's celebrated polarity laws established the existence of a well-organized toroidal magnetic flux system, residing somewhere in the solar interior, as the source of sunspots. In 1919, Larmor suggested the inductive action of fluid motions as one of a few possible explanations for the origin of this magnetic field, thus opening the path to contemporary solar cycle modelling. Larmor's suggestion fitted nicely with Hale's polarity laws, in that the inferred equatorial antisymmetry of the solar internal toroidal fields is precisely what one would expect from the shearing of a large-scale poloidal magnetic field by an axisymmetric and equatorially symmetric differential rotation pervading the solar interior. However, two decades later T.S. Cowling placed a major hurdle in Larmor's path, so to speak, by demonstrating that even the most general purely axisymmetric flows could not, in themselves, sustain an axisymmetric magnetic field against Ohmic dissipation. This result became known as Cowling's antidynamo theorem [Charbonneau(2010)].

Solar magnetism and the cycles of magnetic activity must arise from organized dynamo action in the Sun's interior. This dynamo action is achieved by turbulent plasma motions in the solar convection zone, which spans the outer 30% of the Sun in radius (see Figure 1.1). Here vigorous convective motions and rotation couple to drive the differential rotation and meridional circulation. These flows are important ingredients in stellar dynamo theory, and in many theories the differential rotation plays an important role in building and organizing the global-scale fields. The meridional circulations may be important for returning flux to the base of the convection zone and advecting it equatorward, enabling cycles of magnetic activity [Brown(2009)].

In any dynamo model, the toroidal magnetic field is generated from the poloidal field by the differential rotation, which has now been mapped by helioseismology. The distinctive features of the flux transport dynamo model are that the meridional circulation plays a crucial role in this model and the poloidal magnetic field is generated by the BabcockLeighton (BL) process involving the decay of tilted bipolar sunspots. Bipolar

sunspots are assumed to form due to the buoyant rise of the toroidal magnetic flux through the convection zone and their tilts result from the action of the Coriolis force on the rising flux tubes leading to Joy's law [Hale et al.,(1919)]. When a tilted pair of bipolar sunspots decays, turbulent diffusion spreads the magnetic flux to produce a poloidal magnetic component (see chapter 3 [Babcock(1961)]. An over-all poloidal field develops from the contributions due to many bipolar sunspots and is advected poleward by the meridional circulation, which is poleward in the upper layers of the convection zone. The polar magnetic field of the Sun is built up in this process [Hathaway(2010), Hazra et al.(2017), Miesch and Teweldebirhan(2016)].

Magnetographic mapping of the Sun's surface magnetic field Figure 1.7 have also revealed that the Sun's poloidal magnetic component undergoes cyclic variations, changing polarities at times of sunspot maximum. Note in Figure 1.7 the poleward drift of the surface fields, away from sunspot latitudes. This pattern is believed to originate from the transport of magnetic flux released by the decay of sunspots at low latitudes. The surface polar cap flux amounts to about 10^{22} Mx, while the total unsigned flux emerging in active regions in the course of a typical cycle adds up to a few 10^{25} Mx; this is usually taken to indicate that the solar internal magnetic field is dominated by its toroidal component [Charbonneau(2010)].

Computer simulation studies, over the past few decades, have significantly improved our understanding of these phenomena. Some studies, like those for the atmospheres of the Earth and Sun, have provided physical explanations and predictions of the observations. Others, like those for the deep interiors of the Earth and Sun, have provided detailed theories and predictions of the dynamics that cannot be directly observed. As computers continue to improve in speed and memory, computer programs are able to run at greater spatial and temporal resolutions, which improves the quality of and confidence in the simulations. Numerical and programming methods have also improved and need to continue to improve to take full advantage of the improvements in computer hardware.

Now it is generally believed that the magnetic field of the Sun is produced by a mechanism called Solar Dynamo. A magnetohydrodynamic dynamo operating in the Sun is most likely responsible for producing the solar magnetic activity cycle. While the first solar dynamo models were built half a century ago, recent views differ significantly from those models. According to present concepts, the large-scale solar dynamo is of flux-transport type, which involves three basic processes: (i) generation of toroidal fields by shearing the pre-existing poloidal fields by differential rotation (the Ω-effect); (ii) regeneration of poloidal fields by lifting and twisting the toroidal fluxtubes (the α-effect); (iii) flux transport by meridional circulation and convection. This class of dynamos has been successful in explaining many large-scale solar cycle features, including a particularly difficult one - the correct phase relationship between the equatorward-migrating sunspot belt and the poleward drifting large-scale, diffuse fields. The dynamo cycle period in such models is primarily governed by the meridional flow speed near the bottom of the convection zone.

1.3 Organization of the Dissertation

We begin this Chapter 1, with a review some of the observed features of solar magnetism, solar activity. These types of observations which can potentially give us insight into what is occurring inside the Sun from a dynamical perspective and will provide us some background for the theoretical studies to be described, particularly those of Chapters 3, 4, 5 and 6. The remainder of this thesis is organized in six Chapters. In Chapter 2 general aspects of magnetohydrodynamics most pertinent to magnetic field amplification in electrically conducting fluid such as the the Sun are in some detail reviewed. In Chapter 3 the mathematical formulation of the solar dynamo problem is laid out in some detail, together with the various simplifications that are commonly used in modelling. In this thesis we describe STABLE (Surface flux Transport And BabcockLEighton) solar dynamo

model in somewhat more detail than the papers produced on STABLE before this thesis and consider the operation of the dynamo for the special case when the imposed flow fields are kinematic and non-axisymmetric. In this case the mean (axisymmetric) induction equation decouples from the non-axisymmetric components and behaves essentially as a 2D FTD model. This serves to verify the model and to provide a baseline for future simulations that will include non-axisymmetric flows and Lorentz-force feedbacks. After describing the formulation of the STABLE dynamo model in Chapter 3, we test it against a 2D FTD benchmark in Chapter 4. Then we include the Converging flows towards the active regions to examine the global solar activity cycle and mathematical formulation of the inflow into active regions in Chapter 5. We then give an illustrative example of a solar dynamo simulation in Chapter 6.We close by summarizing our main results of this Dissertation in Chapter 7.

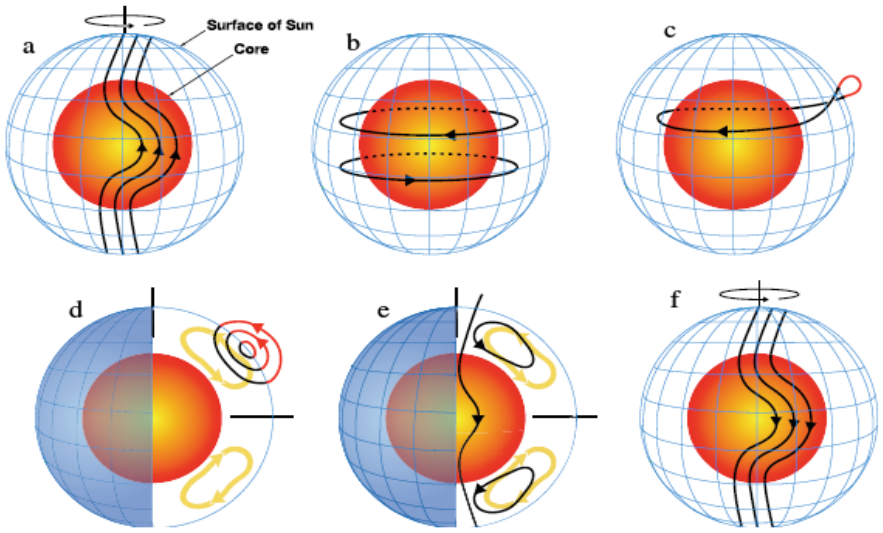

Figure 1.8: Schematic presentation of a solar Flux-Transport dynamo process. The red inner sphere represents the Sun's radiative interior and core, while the blue mesh indicates the solar surface. (a) The Sun's differential rotation, which is prograde fastest at the equator, shears the poloidal field near the base of the convection zone. (b) A toroidal field is produced due to shearing by differential rotation, referred to as the Ω-effect in mean-field dynamo theory. (c) When the toroidal magnetic field is amplified to a threshold field strength, buoyant magnetic flux loops rise toward the surface, eventually emerging through the photosphere to form active regions, twisting and tilting toward the equator due to rotational influences. A poloidal component of the magnetic field is thus achieved from helical action in the convection zone, akin to the α-effect from mean-field theory interface dynamos. (d) Meridional flows in the (r, θ) plane (yellow circulation with arrows) carry surface magnetic flux poleward, eventually inducing a polar field reversal. (e) Some of the flux is transported downward to the bottom of the convection zone and toward the equator by meridional circulation. These poloidal fields have sign opposite to those at the beginning of the sequence in (a). This action can also account for the equatorial migration of active region bands during the course of the solar cycle. (f) The reversed poloidal field is then again sheared near the bottom of the convection zone by differential rotation, producing a toroidal field opposite of that shown in (b), and the solar cycle marches on. [Dikpati and Gilman(2007)].

Chapter 2

Essentials Of Magnetohydrodynamics

2.1 The Magnetohydrodynamic Equations

The magnetic field of the Sun is generated by dynamo action in its conducting interior. Dynamo action turns out to be a rather common phenomenon in the cosmos, and has been invoked to explain magnetic fields in widely different objects ranging from planets to interstellar clouds and galaxies. Before discussing the specifics of the solar dynamo, it is necessary to provide a more general theoretical framework. The dynamo problem can be formulated mathematically as a quest for solutions with a non-decaying total magnetic energy of an appropriate set of equations.

First and foremost, a plasma is an ionized gas. When a solid is heated sufficiently that the thermal motion of the atoms break the crystal lattice structure apart, usually a liquid is formed. When a liquid is heated enough that atoms vaporize off the surface faster than they recondense, a gas is formed. When a gas is heated enough that the atoms collide with each other and knock their electrons off in the process, a plasma is formed: the so-called 'fourth state of matter'. Exactly when the transition between a 'very weakly ionized gas' and a 'plasma' occurs is largely a matter of nomenclature. The important point is that an ionized gas has unique properties. In most materials the dynamics of motion are

determined by forces between near-neighbor regions of the material. In a plasma, charge separation between ions and electrons gives rise to electric fields, and chargedparticle flows give rise to currents and magnetic fields. These fields result in 'action at a distance', and a range of phenomena of startling complexity, of considerable practical utility and sometimes of great beauty [Goldston and Rutherford(1995)].

The plasma state is often referred to as the fourth state of matter, an identification that resonates with the element of fire, which along with earth, water and air made up the elements of Greek cosmology according to Empedocles. Fire may indeed result in a transition from the gaseous to the plasma state, in which a gas may be fully or, more likely, partially ionized. For the present we identify as plasma any state of matter that contains enough free charged particles for its dynamics to be dominated by electromagnetic forces. The inner and outer layers of the Sun and stars in general are made up of matter in an ionized state and from these regions winds blow through interstellar space contributing, along with stellar radiation, to the ionized state of the interstellar gas. Thus, much of the matter in the Universe exists in the plasma state. The Earth and its lower atmosphere is an exception, forming a plasma-free oasis in a plasma universe. The upper atmosphere on the other hand, stretching into the ionosphere and beyond to the magnetosphere, is rich in plasma effects [Boyd and Sanderson(2003)].

Physical conditions in the solar interior up to the photosphere are such that the interaction of fluid flow and magnetic field is well-described by the magnetohydrodynamical approximation (hereafter MHD). Magnetohydrodynamics (hereafter MHD) is concerned with the behavior of electrically conducting but globally neutral fluids flowing at non-relativistic speeds and obeying Ohms law. Remarkably, most astrophysical fluids meet these apparently stringent requirements, the most glaring exception being the relativistic inflows and outflows powered by compact objects such as black holes or neutron stars [Charbonneau(2013)]. MHD is a mathematical basis for dynamo theory, the general

assumptions underlying the MHD approach are (i) the validity of the continuum approximation and non-relativistic dynamics, and (ii) the quasineutrality of the plasma. It is further assumed that the collisional coupling between different ions constituting the plasma is sufficiently strong to treat the plasma as a single fluid (e.g. the temperature is the same for all ions).

These chapters establishes the physical and mathematical bases of MHD, the theory describing the dynamical interactions of the flow of an electrically conducting fluid with a magnetic field. After an overview of classical hydrodynamics, the magnetohydrodynamic induction equation is derived from Maxwell's equations, together with the volumetric form of the magnetic Lorentz force applicable to a fluid. Various useful concepts such as magnetic energy, helicity, vector potential, flux-freezing and force- free magnetic fields are also introduced and discussed. The fluid dynamics and thermal dynamics of these processes are governed by the classical conservation laws for mass, momentum, and energy. However, since we are considering a continuous fluid, these laws are written in terms of the densities of mass, momentum, energy, and force.

2.2 Fluid Description of a Plasma

2.2.1 The Continuity Equation

Before embarking on the actual derivation of the MHD equations it is helpful to discuss briefly some general concepts of fluid dynamics. First, as already mentioned, the fluid is treated as a continuous medium so that all macroscopic quantities are continuous functions of position r and time t. This assumption of continuity presupposes that one is interested in phenomena which vary on a hydrodynamic length scale L_H which, at the very least, is much greater than the average interparticle distance.

To derive the expression of conservation of fluid mass, we consider an arbitrarily shaped fictitious surface, S fixed in space and enclosing a volume, V embedded in a fluid

of density $\rho(\mathbf{r}, t)$, at position $\mathbf{r}$ and time, t, and moving with velocity, $\mathbf{v}(\mathbf{r})$ The mass flux associated with the flow across the (closed) surface is

$$\Phi_m = \oint_S \rho V \cdot \hat{n} dS \tag{2.2.1}$$

where $\hat{n}$ is a unit vector everywhere perpendicular to the surface, and by convention oriented towards the exterior. A fixed shape closed surface S lying entirely within the fluid and enclosing a volume V . If $\rho(\mathbf{r}$, t) is the mass density of the fluid at position $\mathbf{r}$ and time t then the total mass of fluid enclosed by S (mass of fluid contained within V) at time t is is given by

$$M = \int_V \rho dV \tag{2.2.2}$$

The rate at which mass is flowing (mass flux) outwards associated with the flow across the (closed) surface is

$$\frac{\partial M}{\partial t} = -\Phi_m \tag{2.2.3}$$

This quantity will evidently vary if the mass flux given by Equation (2.2.1) is non-zero and the minus sign is a direct consequence of the exterior orientation of n. Inserting Equations (2.2.2) and (2.2.1) into Equation (2.2.3) the resulting expression yields:

$$\frac{\partial}{\partial t} \int_V \rho dV = -\int_S \rho \mathbf{v} \cdot \hat{n} dS \tag{2.2.4}$$

Applying the divergence theorem to the right hand side of Equation (2.2.4) once more, this becomes

$$\frac{\partial}{\partial t} \int_V \rho dV = -\int_V \nabla \cdot (\rho \mathbf{v}) dV, \tag{2.2.5}$$

$$\int_V \left[\frac{\partial \rho}{\partial t} + \int_V \nabla \cdot (\rho \mathbf{v}) \right] dV = 0. \tag{2.2.6}$$

This is valid for any volume V lying entirely within the fluid from which we conclude that the integrand must be identically zero at every point in the fluid. Hence, mass conservation is expressed by the equation of continuity

$$\frac{\partial \rho}{\partial t} + \nabla \cdot (\rho \mathbf{v}) = 0 \tag{2.2.7}$$

This Equation can be interpreted as the local (Eulerian) time rate of change of mass density, ρ is determined by the convergence (i.e., negative divergence) of mass flux, $\rho\mathbf{v}$ at that location and time, t. Note that the Lagrangian time derivative of density (dρ/dt), which is the rate at which the density of a fluid parcel changes as it moves with the flow, is the sum of the Eulerian time derivative ($\partial\rho/\partial t$) and the advection of density ($\mathbf{v} \cdot \nabla$) ρ. Note that the he Lagrangian derivative is also known as the material derivative. Therefore, Equation (2.2.7) can also be written as

$$\frac{d\rho}{dt} = -\rho \boldsymbol{\nabla} \cdot \mathbf{v} \tag{2.2.8}$$

Incompressible fluids have constant densities, so that in this limiting case the continuity equation reduces to

$$\boldsymbol{\nabla} \cdot \mathbf{v} = 0. \tag{2.2.9}$$

Water is perhaps the most common example of an effectively incompressible fluid (under the vast majority of naturally occurring conditions anyway. The gaseous nature of most astrophysical fluids may lead you to think that incompressibility is likely to be a pretty lousy approximation in cases of interest in this course. It turns out that the incompressibility can lead to a pretty good approximation of the behavior of compressible fluids provided that the flows Mach number (ratio of flow speed to sound speed) is much smaller than unity [Charbonneau(2013)].

The density of a fluid can vary by means other than mechanical forcing; in many astrophysical circumstances, thermal dilation effects are in fact the primary driver of density variations. Most fluids will dilate when heated, a property measured by the coefficient of thermal dilation:

$$\alpha = -\frac{1}{\rho}\frac{\partial \rho}{\partial T}. \tag{2.2.10}$$

In an environment stratified by gravity, such as the atmospheres and interiors of the Sun and stars, a localized heat input can then, via thermal dilation, lead to the appearance of a buoyancy force through a decrease in density of the heated volume element. If not equilibrated sufficiently quickly by thermal diffusion, this will generate a flow known as thermal convection, which will play an important role in all solar dynamo models considered in later chapters roughout the whole thesis [Charbonneau(2013)].

2.2.2 The Magnetohydrodynamic Induction Equation

The magnetic induction equation describes how new magnetic field is continually generated by convection of electrically conducting fluid, which on average balances the removal of the field by diffusion. This equation is derived from the Maxwell equations, Maxwell's set of electromagnetic equations modified by the MHD approximation . That is, when fluid velocities ($\mathbf{v}$) are small relative to the speed of light (c) the displacement current in Maxwell's equations can be neglected. This approximation is certainly valid for the problems suggested in this thesis, since we already assume these velocities are small relative to the speed of sound. Even supersonic flows usually have velocities much less than the speed of light [Glatzmaier(2012)]. Physical conditions in the solar interior up to the photosphere are such that the interaction of fluid flow and magnetic field is well-described by the MHD approximation. So far we have applied the arguments of classical fluid dynamics to obtain a closed set of equations for the plasma fluid variables, we have taken almost no account of the fact that a plasma is a conducting fluid. This we do now by specifying the force per unit mass $\mathbf{F}$. Except in astrophysical contexts, where gravity is an important influence on the motion of the plasma, electromagnetic forces are dominant. For a fluid element with charge density q and current density $\mathbf{J}$ we then have

$$\rho\mathbf{F} = q\mathbf{E} + \mathbf{J}\times\mathbf{B} \tag{2.2.11}$$

where the fields $\mathbf{E}$ and $\mathbf{B}$ are determined by Maxwells equations.

$$\boldsymbol{\nabla}\cdot\mathbf{E} = \frac{\varrho_e}{\epsilon_o} \qquad [Gauss'\ law], \tag{2.2.12}$$

$$\boldsymbol{\nabla}\cdot\mathbf{B} = 0 \qquad [Anonymous], \tag{2.2.13}$$

$$\boldsymbol{\nabla}\times\mathbf{E} = -\frac{\partial\mathbf{B}}{\partial t} \qquad [Faraday's\ law], \tag{2.2.14}$$

$$\boldsymbol{\nabla}\times\mathbf{B} = \mu_o\mathbf{J} - \mu_o\epsilon_o\frac{\partial\mathbf{E}}{\partial t} \qquad [Ampere's/Maxwell's\ law]. \tag{2.2.15}$$

where, the quantity ϱ_e is the electrical charge density, $\mathbf{J}$ is the electrical current density, ϵ_o is the permittivity in vacuum and μ_o is magnetic permeability.The main objective is to obtain a macroscopic description of the plasma in which the fields are those induced by the plasma motion. Thus, we now introduce the basic assumption of MHD that the fields vary on the same time and length scales as the plasma variables.

The fluid motions are non-relativistic, the electrostatic force can be neglected as compared to the magnetic force and Maxwells displacement current can be neglected. Consequently, Equation (2.2.11) becomes

$$\rho\mathbf{F} = \mathbf{j}\times\mathbf{B} \tag{2.2.16}$$

and (2.2.15) is replaced by original form of Amperes law:

$$\boldsymbol{\nabla}\times\mathbf{B} = \mu_o\mathbf{J} \quad . \tag{2.2.17}$$

In general, the application of an electric field $\mathbf{E}$ across an electrically conducting substance will generate an electrical current density $\mathbf{J}$. Ohm's law postulates that the relationship between $\mathbf{J}$ and $\mathbf{E}$ is linear:

$$\mathbf{J}' = \sigma\mathbf{E}' \quad . \tag{2.2.18}$$

where σ is the electrical conductivity and the Equation (2.2.18) Ohms law is expected to hold in a conducting substance at rest. Our task is now to generalize the governing equations of hydrodynamics to include the effects of the electric and magnetic fields, and to obtain evolution equations for these two physical quantities. Keep in mind that electrical charge neutrality, as required by MHD.

In the context of a fluid that moves with velocity $\mathbf{v}$, MHD describes the behavior of an electrically neutral mixture of electrically charged microscopic constituents in which the collision frequency largely exceeds any relevant plasma frequencies. In such a (moving) collisionally dominated plasma, Ohms law holds in a reference frame comoving with the fluid at the macroscopic scale. The non-relativistic limit the usual Lorentz transformation for the electrical current density simplifies to $\mathbf{J}' = \mathbf{J}$, and that for the electric field to $\mathbf{E}' = \mathbf{E} + \mathbf{v} \times \mathbf{B}$, so that Ohms law takes on the generalized form

$$\mathbf{j} = \sigma(\mathbf{E} + \mathbf{v} \times \mathbf{B}) \tag{2.2.19}$$

use Equation (2.2.17) then electric field is given by:

$$\mathbf{E} = \frac{1}{\sigma}\mathbf{J} - \mathbf{v} \times \mathbf{B} \tag{2.2.20}$$

then

$$\mathbf{E} = \frac{1}{\mu_o \sigma}\nabla \times \mathbf{B} - \mathbf{v} \times \mathbf{B} \tag{2.2.21}$$

We now insert this expression for the electric field into Faradays law to obtain the justly famous MHD induction equation:

$$\frac{\partial \mathbf{B}}{\partial t} = \nabla \times (\mathbf{v} \times \mathbf{B} - \eta \nabla \times \mathbf{B}) \tag{2.2.22}$$

where η, is the magnetic diffusivity given by:

$$\eta = \frac{1}{\mu_o \sigma} \quad . \tag{2.2.23}$$

The above Equation (2.2.22) describes how the magnetic field in a perfectly conducting fluid changes with time under the influence of a velocity field **v**and the time rate of change of the magnetic field is controlled by two terms. The first term on the right-hand side, which involves the fluid velocity, is called the convection term (the inductive action of fluid flowing across a magnetic field), while the second term, which involves the conductivity, is called the diffusion term (the Ohmic dissipation of the electrical currents sustaining the field). Usually for a time dependent magnetic field, one or other of these two terms dominates. To determine which term dominates, it is useful to introduce a dimensionless parameter R_m , called the magnetic Reynolds number, which is defined as the ratio of the typical magnitude of the convection term to the typical magnitude of the diffusion term. The solution of induction equation must also satisfy the $\nabla \cdot \mathbf{B} = 0$ at all times

2.2.3 Scaling Analysis

The evolution of a magnetic field under the action of a prescribed flow **v**, will depend greatly on whether or not the inductive term on the RHS of Equation (2.2.22) dominates the diffusive term. This is takes place by replacing the temporal derivative by $1/\tau$ and the spatial derivatives by $1/\ell$, where τ and ℓ are time and length scales that suitably characterizes the variations of both **v** and **B**:

$$\frac{B}{\tau} = \frac{1}{\ell} v_0 B + \eta \frac{B}{\ell^2} \tag{2.2.24}$$

where B and v_0 are a typical values for the flow velocity and magnetic field strength over the domain of interest. The ratio of the first to second term on the RHS of Equation (2.2.22) is a dimensionless quantity known as the magnetic Reynolds number

$$R_m = \frac{v_0 \ell}{\eta} \tag{2.2.25}$$

The magnetic Reynolds number not depend on the magnetic field strength. which

measures the relative importance of induction versus dissipation over length scales of order ℓ. In Equation (2.2.25) the v_0 and ℓ are characteristic values for the flow speed and length scale, respectively, the latter assumed here to adequately characterize the spatial variations of both the flow and magnetic field.

The scaling analysis simply says that in the limit $R_m \gg 1$, induction by the flow dominates the evolution of $\mathbf{B}$, while in the opposite limit of $R_m \ll 1$, induction makes a negligible contribution and $\mathbf{B}$, simply decays away under the influence of Ohmic dissipation. One may anticipate great simplifications of magnetohydrodynamics if we operate in either of these limits. If $R_m \ll 1$, only the second term is retained on the RHS of Equation (2.2.24), which leads immediately to

$$\tau_d = \frac{\ell^2}{\eta} \tag{2.2.26}$$

Where the τ_d the quantity known as the magnetic diffusion time. It measures the time taken for a magnetic field contained in a volume of typical linear dimension ℓ to dissipate and/or diffusively leak out of the volume.

The opposite limit $R_m \gg 1$, infinite conductivity, defined the ideal MHD limit case ($\eta = 0$). Then it is the first term that is retained on the RHS of Equation (2.2.22) becomes identical to the evolution Equation, (2.2.27) for a line element advected by a flow $\mathbf{v}$. This imply that the magnetic field lines move with the fluid, a result known as Alfvén's theorem and dubbed flux freezing.

$$\frac{\partial \mathbf{B}}{\partial t} = \nabla \times (\mathbf{v} \times \mathbf{B}), \tag{2.2.27}$$

In Equation 2.2.24 scaling analysis, limit $R_m \gg 1$, gives:

$$\tau_A = \frac{\ell}{v_0} \tag{2.2.28}$$

Where τ_A is time scale associated with the flow velocity.

2.2.4 Momentum Equation

Another important dimensionless quantity that is calculated from the celebrated Navier-Stokes equation;

$$\frac{D\mathbf{v}}{Dt} = -\frac{1}{\rho}\boldsymbol{\nabla} p + \frac{1}{\rho}\boldsymbol{\nabla}\cdot\tau \tag{2.2.29}$$

Where τ is the viscous stress tensor, with components

$$\tau_{ij} = -2\rho\nu(e_{ij} - \frac{1}{3}(\boldsymbol{\nabla}\cdot v)\delta_{ij}) \tag{2.2.30}$$

Where the physical coefficient, ν, is define as kinemathic viscosity.

In Equation 2.2.29 any additional volumetric body forces (gravity, Lorentz force, etc.) are simply added to the RHS. Incompressible or not, the behavior of viscous flows will often hinge on the relative importance of the advective and dissipative terms in the Navier-Stokes equation:

$$\rho(\mathbf{v}\cdot\boldsymbol{\nabla})\mathbf{v} \leftrightarrow \boldsymbol{\nabla}\cdot\tau \tag{2.2.31}$$

Introducing characteristic length scales v_0, ℓ, ρ_0 and ν_0, dimensional analysis and the ratio of these two terms is a dimensionless quantity called the Reynolds Number:

$$R_e = \frac{v_0\ell}{\nu_0} \tag{2.2.32}$$

This measures the importance of viscous forces versus fluid inertia. It is a key dimensionless parameter in hydrodynamics, as it effectively controls fundamental processes such as the transition to turbulence, as well as more mundane matters such as boundary layer thicknesses.

Another important dimensionless quantity to be encountered in subsequent solar dynamo models is the magnetic Prandtl number, equal to the ratio of the magnetic Reynolds number to the viscous Reynolds number, or, equivalently, of viscosity over magnetic diffusivity:

$$P_m = \frac{\nu}{\eta} \tag{2.2.33}$$

For physical conditions characteristic of non-degenerate stellar interiors, the use of microscopic values for ν and η yields Pm in the range 0.1-0.01.

An other important parameters that must be cosidered is convecive Rossby Number

$$R_{oc} \equiv \sqrt{\frac{R_a}{T_a P_r}} \tag{2.2.34}$$

where R_a,T_a and P_r are are Rayleigh number, the Taylor number, the Prandtl number the Taylor number respectively. R_{oc} is a measure of the strength of buoyancy relative to Coriolis forces. Variations in R_{oc} of even a factor of two could lead to drastic changes in the convection patterns, and especially in the resulting mean flow profles.

2.2.5 Conservation of Energy

The energy budget in solar dynamo is entropy, the energy dissipated in heat by viscous friction. The usual accounting of energy flow into and out of a volume element V fixed in space leads to the following differential equation expressing the conservation of the plasma's internal energy per unit mass (e, in units J/kg):

$$\frac{De}{Dt} + (\gamma - 1)e\nabla\cdot\mathbf{u} = \frac{1}{\rho}\,\nabla\cdot\left[(\chi + \chi_r)\nabla T\right] \tag{2.2.35}$$

Where $(\chi + \chi_r)\nabla T$ the heat flux in or out of the fluid element, with physical coefficients χ and χ_r the coefficients of thermal and radiative conductivity, respectively.

Joule Heating

In the presence of finite electrical conductivity, the volumetric heating associated with the dissipation of electric currents must be included on the RHS of the energy equation, in the form of the so-called Joule heating function:

$$\phi_B = \frac{\mathbf{J}^2}{\sigma} = \frac{\eta}{\mu_0}(\nabla \times \mathbf{B})^2 \tag{2.2.36}$$

Joule heating makes an insignificant contribution to the energy budget in the solar dynamo model. When it occurs, heating by magnetic energy dissipation, such as in

flares, involves dynamical mechanisms that lead to effective dissipation far more rapid and efficient than Joule heating.

This and the viscous dissipation function, must be added to the right-hand side of the equation of energy per unit volume, is then

$$\frac{De}{Dt} + (\gamma - 1)e\nabla\cdot\mathbf{u} = \frac{1}{\rho}\left[\nabla\cdot\left[(\chi + \chi_r)\nabla T\right] + \phi_\nu + \phi_B\right] \tag{2.2.37}$$

ϕ_ν is the viscous heating, and is given at Equation, with deformation tensor.

$$\phi_\nu = \frac{1}{2}\left(\frac{\partial v_i}{\partial x_k} + \frac{\partial v_k}{\partial x_i}\right) \tag{2.2.38}$$

and the resistive (Ohmic) dissipation, ϕ_B is given by Equation (2.2.36).

The Full Set of MHD Equations

Now collect the set of partial differential equations are governing the behavior of magnetized fluids in the MHD limit. These equations are fully nonlinear in velocity and magnetic field variables, we write these equations in a frame of reference rotating with angular velocity, Ω, with the centrifugal force absorbed within the pressure gradient term [Miesch(1998)] [Charbonneau(2013)], [Schrijver and Siscoe(2009)], [Brun et al.(2004)], [Charbonneau(2010)], [Clune et al.(1999)].

The full set of MHD equations combines the induction equation with a version of the NavierStokes equations that includes the Lorentz force $\mathbf{J}\times\mathbf{B}$. This results in equations for continuity, force balance, energy conservation, and magnetic field, respectively:

$$\frac{\partial\rho}{\partial t} + \nabla\cdot(\rho\mathbf{v}) = 0, \tag{2.2.39}$$

The momentum equation

$$\frac{D\mathbf{v}}{Dt} = -\frac{1}{\rho}\nabla p - 2\Omega\times\mathbf{v} + \mathbf{g} + \frac{1}{\rho}\nabla\cdot\tau + \frac{1}{\mu_0\rho}(\nabla\times\mathbf{B})\times\mathbf{B} \quad , \tag{2.2.40}$$

The energy equation,

$$\frac{De}{Dt} + (\gamma - 1)e\nabla\cdot\mathbf{v} = \frac{1}{\rho}\left[\nabla\cdot\left[(\chi + \chi_r)\nabla T\right] + \phi_\nu + \phi_B\right] \quad , \tag{2.2.41}$$

And the MHD

$$\frac{\partial \mathbf{B}}{\partial t} = \nabla \times (\mathbf{v} \times \mathbf{B} - \eta \nabla \times \mathbf{B}) \quad . \tag{2.2.42}$$

Equations (2.2.39 - 2.2.42) must be complemented by suitable equations expressing an equation of state. Note that gravity g is explicitly included on the RHS of momentum equation. We must choose an equation of state in order to close the system of equations. The equation of state specifies the plasma pressure, (2.2.43) as a function of the temperature and density, and its form depends on various assumptions that must be made concerning the effect of collisions. Appropriate initial and boundary conditions for all physical quantities involved then complete the specification of the problem. The resulting set of equations defines full set of magnetohydrodynamics equations, quite literally the dynamics of magnetized fluids.

$$P = f(\rho, T) \tag{2.2.43}$$

More complicated equations of state are of course possible and easily incorporated into the model, but the ideal gas approximation simplifes the physics and provides a good first approximation.

These equations (2.2.39 - 2.2.42) are further complemented by the constraint equation:

$$\nabla \cdot \mathbf{B} = 0 \tag{2.2.44}$$

2.3 MHD Waves

As an aside here, we point out one property of the magnetic field that guides our thinking about its effects in the force balance of Equation (2.2.40): using a vector formula we see that

$$\mathbf{F} = \frac{1}{\mu_0}(\nabla \times \mathbf{B}) \times \mathbf{B} = \frac{1}{\mu_0}\left[(\mathbf{B}.\nabla)\mathbf{B} - \frac{1}{2}\nabla(\mathbf{B}^2)\right] \tag{2.3.1}$$

which shows that the Lorentz force is the sum of an isotropic pressure-like force and a tension force related to the curvature of the field. The ratio of the magnetic and gas pressure terms in Equation (2.2.40) is commonly referred to as the plasma β-value:

$$\beta = \frac{2\mu_0 p}{\mathbf{B}^2} \tag{2.3.2}$$

The natural approach to the dynamo problem would be to solve the MHD equations for a given setup that includes a magnetic field in order to see whether the magnetic field can be maintained by the velocity field.

The first term on the RHS of Equation (2.3.1) is the magnetic tension, and the second the magnetic pressure. Fluctuations in magnetic pressure can propagate as a longitudinal wave, much as a sound wave. In fact, two such magnetosonic waves modes actually exist, according to whether the magnetic pressure fluctuation is in phase with the gas pressure fluctuation (the so-called fast mode), or in antiphase (the slow mode). In addition, magnetic tension can produce a restoring force that allows the propagation of wave-on-a-string-like transverse waves, known as Alfvén waves.

Small-amplitude Alfvén waves travel with a speed v_a given by

$$v_a = \frac{B_0}{\sqrt{\mu_0 \rho}} \tag{2.3.3}$$

where B_0 is the magnitude of the (uniform) magnetic field along which the wave is propagating, and ρ is the (constant) fluid density. Mechanical forcing of a magnetic field permeating a compressible fluid will in general excite all three wave modes. This is an essential aspect of the development and propagation of perturbations in the solar corona and wind, but plays a minor role in solar interior dynamics, unless one happens to be interested in subsurface magnetohelioseismology [Schrijver and Siscoe(2009)], [Charbonneau(2013)].

2.4 Magnetic Energy

Consider the expression resulting from dotting $\mathbf{B}$, into the induction equation, integrating over the spatial domain (V) under consideration, and making judicious use of various well-known vector identities and of Gauss theorem:

$$\frac{d}{dt}\int_V \frac{\mathbf{B}^2}{2\mu_0}dV = \oint(\mathbf{S}.\hat{n})dS - \int_V(\mathbf{v}\cdot\mathbf{F})dV - \int_V \sigma^{-1}\mathbf{J}^2 dV \tag{2.4.1}$$

where $\hat{n}$ is a outward-directed unit vector normal to the boundary surface, and the vector quantity S is the Poynting flux:

$$\mathbf{S} = \frac{1}{2\mu_0}\mathbf{E}\times\mathbf{B} \tag{2.4.2}$$

Examine now the three terms on the RHS of Equation 2.4.1; the first is the Poynting flux component into the domain, integrated over the domain boundaries, i.e., the flux of electromagnetic energy in (integrand < 0) or out (integrand > 0) of the domain. This term evidently vanishes in the absence of applied magnetic or electric fields on the boundaries. The second is the work done by the Lorentz force ($\mathbf{F}$) on the flow. In general this term can be either positive or negative; in the dynamo context we are interested in the $\mathbf{v}\cdot\mathbf{F} > 0$ situation, where the flow transfers energy to the magnetic field. The third term is evidently always negative, and represents the rate of energy loss due to Ohmic dissipation. Equation 2.4.1 then naturally leads to interpret the quantity $\frac{\mathbf{B}^2}{2\mu_0}$ as the magnetic energy density, and the total magnetic energy (ε_B) within the domain is:

$$\varepsilon_B = \frac{1}{2\mu_0}\int_V \mathbf{B}^2 dV \tag{2.4.3}$$

The MHD dynamos that will be the focus of much of what follows are fluid systems that convert mechanical energy into magnetic energy, through the agency of the $\mathbf{v}\cdot\mathbf{F}$ term on the RHS of Equation (2.4.1) [Charbonneau(2013)].

Chapter 3

The STABLE Solar Dynamo Model Formulation

3.1 The Solar Dynamo Model

In the experiements we are doing in our simulations, we use three different saturation mecanisms. These are; first, the quenching on mangetic flux Equation 3.5.10: we use this quenching mechanism in Chapters 3 and 4 and much of these Chapters was published [Miesch and Teweldebirhan(2016)]. The second and third saturation mechanisms are the tilt angle saturation, Equation 6.2.9 and inflow towards active regions (see Chapter 5 for details; Equations 5.2.51 - 5.2.53) respectively.

The magnetic field of the Sun is generated by dynamo action in its conducting interior and the cyclic evolution of solar magnetic features is believed to be due to a dynamo operating in the Sun. A dynamo is a process by which the magnetic field in an electrically conducting fluid is maintained against Ohmic dissipation. In astrophysical objects, which are made of highly conducting plasma, there can always be a dynamo whenever the plasma consists of seed magnetic fields and flow field. The Sun is a middle-aged star, a massive plasma ball held together by its own gravitational attraction. In the solar plasma there can also be various kinds of dynamo actions such as small-scale as well as global dynamos, growing, decaying or oscillatory dynamos, depending on the flow field pattern [Ossendrijver(2003)]. In this study we focus on large-scale solar dynamo mechanism,

due to the challenge posed by the solar activity cycle. The solar dynamo models have evolved significantly since the first solar dynamo models developed (Parker, 1955), then in order to accommodate observational constraints early solar dynamo models involved two basic processes: (i) generation of toroidal fields by shearing pre-existing poloidal fields by differential rotation (the Ω-effect), (ii) re-generation of poloidal fields by lifting and twisting of toroidal flux tubes by helical motion (the so-called α-effect). These are called the $\alpha\Omega$ dynamos. According to recent concepts, it also involves an essential third process - flux transport by meridional circulation and tilt angle is another important ingredient for the solar dynamo. Flux-transport type solar dynamos have been very successful in explaining many large-scale solar cycle features, including the phase relationship between the equatorward migrating sunspot belt and the poleward drifting large-scale, which is the polar field, and diffuse fields. The dynamo cycle period in such models is primarily governed by the meridional flow speed. After giving a historical background on classical dynamo models, we review the successes of various recent flux-transport dynamos. We then demonstrate how the meridional circulation plays a key role in governing the Sun's memory about its own magnetic field [Dikpati and Gilman(2007)].

Many models were built on the $\alpha\Omega$ dynamos, particularly focussing on reproducing the butterfly diagram. But in contrast to the equatorward-migrating sunspot belts, the weak, diffuse fields outside the sunspot zones are observed to drift poleward and to cause the reversal of the Sun's polar fields, while maintaining a certain phase relationship with the sunspots, namely the polar field changing sign from positive to negative when the sunspots magnetic fields (the follower spots field) are already negative. This particular feature was not reproduced by any large-scale dynamo model of pure $\alpha\Omega$ type, no matter whether it is an early type convection-zone dynamo (with the α-effect and Ω-effect working in the bulk of convection zone), a thin-layer dynamo (with both the α-effect and Ω-effect working in the tachocline), an interface dynamo (with both the α-effect and Ω-effect working at the base of the convection zone with a slight separation between them) or a

pure Babcock-Leighton dynamo (with α-effect working at the surface and the Ω-effect in the tachocline) [Charbonneau(2010)].

The basic concept for the large-scale solar dynamo involves a cycle during which the poloidal field and the toroidal field are mutually generated by one another. The winding of the poloidal field by differential rotation creates a toroidal field. A reversed poloidal field results from the formation of magnetic loops in the toroidal field, which become twisted by the Coriolis force due to solar rotation. In turn, the reversed poloidal field then becomes the source of a reversed toroidal field. In this way, the 11-year cycle of solar activity is connected to a 22-yr cycle of magnetic polarity [Cameron and Schüssler(2015)].

Over the last two decades, Babcock-Leighton (BL) dynamo models have emerged as a leading paradigm for explaining the origin of the solar activity cycle [Dikpati and Gilman(2009), Charbonneau(2010), Karak et al.(2014)]. The defining characteristic of BL models is the critical role of magnetic flux emergence and dispersal in the operation of the dynamo. Emerging flux structures appear in the solar photosphere as bipolar magnetic regions (BMRs) with systematic orientations such that the trailing flux (in the sense of rotational motion) is displaced poleward relative to the leading flux [Stenflo and Kosovichev(2012), McClintock and Norton(2013)]. The subsequent evolution of this flux in response to differential rotation, meridional circulation, and convection, generates a mean poloidal field that can ultimately reverse the Sun's dipole moment, at least at the surface (see §4.2). The preferential tilt of BMRs is known as Joy's law and this process of poloidal field generation is known as the Babcock-Leighton mechanism.

Most current BL dynamo models may also be classified as Flux Transport dynamo (FTD) models in which the meridional circulation (MC) regulates the cycle period [Dikpati and Gilman(2009), Charbonneau(2010), Karak et al.(2014)]. The equatorward migration of toroidal flux inferred from the solar butterfly diagram (§4.2) is attributed to an equatorward flow of 2-3 m s^{-1} near the base of the convection zone (CZ) where the progenitor flux for BMRs is thought to originate. Though this presumed equatorward

flow at the base of the CZ has not yet been detected, it has long been inferred based on the observed poleward circulation in the upper CZ and the constraint of mass conservation. Recent photospheric observations and helioseismic inversions have called into question this simple single-celled picture of the MC [Hathaway(2012), Zhao et al.(2013)]. However, FTD models are still viable as long as the circulation at the base of the CZ is equatorward and convection contributes to the transport of poloidal flux across the CZ [Hazra et al.(2014)]. Both conditions are supported by theory and global convection simulations, even when the overall MC profile is multi-cellular [Miesch(2005), Miesch et al.(2012), Passos et al.(2015)].

The BL mechanism has a solid empirical grounding; we observe it operating in the solar photosphere as BMRs continually emerge and disperse. The amount of flux emerging is more than enough to reverse the polar fields, at least at the surface, and there is evidence that the strength of the following cycle is correlated with the BL poloidal source term and with the strength of the Sun's polar fields during cycle minimum, as predicted [Schatten et al.(1978),Svalgaard et al.(2005),Dasi-Espuig et al.(2010),Muñoz-Jaramillo et al.(2012)]. Other observed solar cycle features that are well reproduced by BL/FTD models include the equatorward migration of toroidal flux (solar butterfly diagram), the phase relationship between toroidal and poloidal fields, the phase coherence across grand minima, and the flux budget in active regions [Dikpati and Gilman(2009), Charbonneau(2010), Karak et al.(2014), Cameron and Schüssler(2015)].

Though global MHD simulations of convective dynamos have made great strides in recent years [Charbonneau(2014)], they still cannot capture the full multi-scale complexity of flux emergence and the BL mechanism. Until they do, hybrid approaches are necessary to model the solar cycle with maximum fidelity.

We describe one such hybrid approach here. We call it the STABLE (Surface flux Transport And Babcock-LEighton) solar dynamo model. STABLE is an FTD model

but unlike most previous FTD models that only address the axisymmetric (2D) magnetic field components, STABLE is fully 3D. So, it can capture the 11-year solar cycle as well as the explicit distortion and dispersal of photospheric BMRs that underlies the BL mechanism. The latter capability in effect makes STABLE a 3D generalization of 2D (latitude/longitude) surface flux transport (SFT) models, which have had notable success in capturing the observed evolution of photospheric fields [DeVore et al.(1984), Wang et al.(1991), Schrijver and DeRosa(2003), Baumann et al.(2004), Cameron et al.(2010), Upton and Hathaway(2014), Jiang et al.(2014a), Jiang et al.(2014b), Hickmann et al.(2015)].

A 3D, kinematic FTD/SFT model similar to STABLE was recently described by [Yeates and Munoz-Jaramillo(2013)]. Meanwhile, [Lemerle et al.(2015)] describe a somewhat different approach to unifying SFT models and FTD models based on retaining the 2D nature of each class of model and coupling them, so that each model provides the source term that sustains the other. There have also been a few 3D mean-field dynamo models based on a turbulent α-effect as opposed to the BL mechanism (e.g. [Chan et al.(2004)]). One of the main advantages of the 3D approach over 2D FTD models is the potential for a more realistic depiction of flux emergence. Though we acknowledge that this potential has not yet been fully realized, substantial progress in this direction has been made by [Yeates and Munoz-Jaramillo(2013)] who employ a kinematic flow that lifts and twists toroidal magnetic fields, mimicking the effects of magnetic buoyancy. In the future we will implement this and other flux emergence algorithms into STABLE.

Another promising reason to develop a 3D FTD model is the potential for data assimilation (DA). If solar dynamo models are to be used for the prediction of future solar activity, they must assimilate observational data. If the model is axisymmetric, this data assimilation typically makes use of the mean radial magnetic field at the surface of the Sun as a function of latitude and time (e.g. [Dikpati and Gilman(2007)]; [Jiang et al.(2013)]). This is effectively 1D DA. However, SFT models can exploit the observations more fully, assimilating the full observed radial magnetic field as a function of latitude, longitude

and time (2D DA; see references listed above). Thus, SFT models are able to model the time-evolving surface magnetic field of the Sun with more fidelity. However, since they are not dynamo models, their predictive potential is relatively short-term, spanning less than a decade. STABLE will be capable of assimilating complete 2D magnetograms (2D DA) for use with both short-term and long-term solar activity forecasting. The 2D surface fields will also provide boundary conditions for corona and heliosphere models.

There are many other reasons for developing a 3D, nonlinear, MHD FTD model. Another is turbulent transport. The 3D formulation will allow us to replace turbulent diffusion and magnetic pumping with 3D convective flow fields either computed self-consistently or derived from observations. It will also allow us to capture magnetoshear instabilities in the solar tachocline which may induce non-axisymmetric patterns in flux emergence and may contribute to poloidal field generation via an α-effect Other sources of non-axisymmetric activity include converging flows into active regions ([Cameron and Schüssler,(2012)]) and longitudinal variations in the meridional circulation.

In the 2D flux transport dynamo model and the surface flux transport (SFT) model, we average over the azimuthal direction ϕ and solve the axisymmetric dynamo equation in the $r - \theta$ plane. On the other hand, in the SFT model, we focus our attention only on the B_r component of the magnetic field at the solar surface spanned by the $\phi - \theta$ coordinates and study its evolution on this surface under the joint action of diffusion, meridional circulation and differential rotation. Neither of these approaches provides a fully satisfactory depiction of the BL process and each approach has its own limitations [Hazra et al.(2017)].

To study the coupling between rotation, magnetism and the large-scale flows achieved in solar and stellar convection zones, we must employ a global model which simultaneously captures the spherical shell geometry and admits the possibility of zonal jets and large eddy vortices, and of convective plumes that may span the depth of the convectio zone. The solar convection zone is intensely turbulent and microscopic values of viscosity and

magnetic and thermal diffusivities in the Sun are estimated to be very small. Numerical simulations cannot hope to resolve all scales of motion present in real solar and stellar convection and must instead strike a compromise between resolving dynamics on small scales and capturing the connectivity and geometry of the global scales.

In the interiors of the Sun and most stars, the collisional mean-free path of microscopic constituents is much shorter than competing plasma length scales, fluid motions are non-relativistic, and the plasma is electrically neutral and non-degenerate. Under these physical conditions, Ohms law holds, and so does Ampères law in its pre-Maxwellian form. Maxwells equations can then be combined into a single evolution equation for the magnetic field **B**, known as the magnetohydrodynamical (MHD) induction equation.

$$\frac{\partial \mathbf{B}}{\partial t} = \nabla \times (\mathbf{v} \times \mathbf{B} - \eta \nabla \times \mathbf{B}) \tag{3.1.1}$$

where

$$\eta = \frac{1}{\mu_o \sigma} \quad [m^2 s^{-1}] \tag{3.1.2}$$

In Equation 3.1.2, η is the microscopic magnetic diffusivity, (σ being the electrical conductivity), μ_o is the permeability of free space, in general only a function of depth for spherically symmetric solar/stellar structural models. Of course, the magnetic field is still subject to the divergence-free condition $\boldsymbol{\nabla \cdot}\ \mathbf{B} = 0$. The first term on right hand side of Equation 3.1.1 represents the inductive action of the flow field, and it can act as a source term for **B**; the second term, on the other hand, describes the resistive dissipation of the current systems supporting the magnetic field, and is thus always a global sink for **B**. The relative importance of these two terms is measured by a dimensionless quantity knownas the magnetic Reynolds number R_m, obtained by dimensional analysis of Equation 3.1.1, given by

$$R_m = \frac{v_0 L}{\eta} \tag{3.1.3}$$

Here η, v_0, and L are typical numerical values for the magnetic diffusivity, flow speed, and length scale over which, **B**, varies significantly. The latter, in particular, is not easy

to estimate a priori, as even laminar MHD flows have a nasty habit of generating their own magnetic length scales (usually $\propto Rm^{-1/2}$ at high R_m). Nonetheless, on length scales comparable to the Sun itself, R_m is immense, and so is the usual viscous Reynolds number. This implies that energy dissipation will occur on length scales very much smaller than the solar radius.

To solve Equation 3.1.1 an evolution equation for the flow field $\mathbf{v}$, must also be provided. Where as the evolution of the velocity field $\mathbf{v}$, in the presence of the magnetic field, $\mathbf{B}$, is given by the magnetic Navier-Stokes equation:

$$\frac{D\mathbf{v}}{Dt} = \frac{\partial \mathbf{v}}{\partial t} + (\mathbf{v}\cdot\boldsymbol{\nabla})\mathbf{v} = -\frac{1}{\rho}\nabla p - 2\Omega \times \mathbf{v} + \mathbf{g} + \frac{1}{\rho}\boldsymbol{\nabla}\cdot\tau + \frac{1}{\mu_0\rho}(\boldsymbol{\nabla}\times\mathbf{B}) \times \mathbf{B} \qquad (3.1.4)$$

Here ρ is density, p is pressure, $\mathbf{g}$ is gravitational field, τ is the viscous stress tensor, and η is magnetic diffusivity. Since one needs the values of ρ and p under dynamical conditions in order to solve (3.1.4), in the most general circumstances, Equations 3.1.1 and 3.1.4 must be complemented combined with suitable equations expressing conservation of mass and energy, and an appropriate equation of state to close the set of equations describing the evolution of the system. Appropriate initial and boundary conditions for all physical quantities involved then complete the specification of the problem. The resulting set of equations defines MHD, quite literally the dynamics of magnetized fluids. While the basic equations of the problem are well established, it is extremely difficult to solve this set of equations in an astrophysically realistic dynamo situation. That is why solar dynamo theory is still only a partially understood theory. There are two possible approaches to the solar dynamo problem. The first is direct numerical simulation, or DNS, in which one discretizes all the MHD equations and solves them numerically. Then the second is the kinematic approach, in which the velocity field is given and one solves only the induction equation, 3.1.1 for the magnetic field. Since the outer layers of the Sun are unstable to convection, the main challenge of the DNS is to model the convection properly. It is the turbulent stresses in the convection zone which drive such large-scale flows as the

differential rotation and the meridional circulation, which are crucial for dynamo action. Doing a DNS of the solar dynamo is extremely challenging for the following reasons.

1. The solar convection zone is highly stratified, with quantities like density and pressure varying by several orders of magnitude from the bottom to the top.

2. The largest relevant scales (10^6 km) differ from the smallest scales of fibril flux tubes (10^2 km) by 4 orders of magnitude

3. The fluid and magnetic Reynolds numbers are huge, $\sim 10^8$ - 10^{10}.

Since the kinematic approach is easier than the DNS approach, it is no wonder that historically the field of solar dynamo first developed by following the kinematic approach. During the initial years of dynamo research, not much was known about the large-scale flow fields such as the differential rotation in the interior of the Sun. Still reasonable (or what seemed reasonable at that time) assumptions about differential rotation led to solutions showing periodic behavior with equatorward propagation-to account for the observed fact that sunspots appear at increasingly lower latitudes with the progress of the solar cycle. There was a renaissance in the kinematic mean-field modeling in the 1990s when helioseismology succeeded in mapping the differential rotation in the interior of the Sun.

Additionally, a kinematic model has one important practical advantage, namely that the information provided by helioseismology about the large-scale flow fields like the differential rotation and the meridional circulation can be directly inserted in the kinematic Equations 3.1.1.

3.2 Kinematic Induction

It is now generally accepted that the Sun's magnetic cycle is produced by a dynamo process, which is based on the nonlinear interaction between the velocity field and the

magnetic field of the solar plasma. This nonlinear interaction is mathematically described by the well-known magnetohydrodynamical (MHD) equations. The evolution of the magnetic field, $\mathbf{B}$, in response to the velocity field, $\mathbf{v}$, which is given in consistent with observations is given by the induction equation:

$$\frac{\partial \mathbf{B}}{\partial t} = \boldsymbol{\nabla} \times (\mathbf{v} \times \mathbf{B} - \eta \boldsymbol{\nabla} \times \mathbf{B}) \tag{3.2.1}$$

Where $\mathbf{B} = \mathbf{B}(r, \theta, \phi, t)$ is fully 3D magnetic field and is reprented in terms of toroidal and poloidal magnetic potentials, A and C respectivelly defined as:

$$\mathbf{B} = \boldsymbol{\nabla} \times (A\hat{\boldsymbol{r}}) + \boldsymbol{\nabla} \times \boldsymbol{\nabla} \times (C\hat{\boldsymbol{r}}) \tag{3.2.2}$$

Though we will consider self-consistent fully 3D and time dependent flows in the future, this time, we explain the basic formulation of the STABLE dynamo model solves the kinematic magnetohydrodynamic (MHD) induction equation, the second alternative approaches to solve the solar dynamo problem. The STABLE model solves the kinematic magnetohydrodynamic (MHD) induction equation is first reported in [Miesch and Dikpati(2014)] (MD14) and later more detail by [Miesch and Teweldebirhan(2016)] (MT16) [Hazra et al.(2017)] (HM17) [Karak and Miesch(2017)](KM17). This model is a 3D generalization of the pre-existing axisymmetric 2D flux transport dynamo models and it solves the induction equation in a full 3D rotating spherical shell. STABLE is a 3D Babcock-Leighton/Flux Transport dynamo model in which the source of poloidal field is the explicit emergence, distortion, and dispersal of bipolar magnetic regions (BMRs).

In this section, we explain the fundamental formulation of the STABLE model solves the kinematic magnetohydrodynamic (MHD) induction equation in a 3D, rotating, spherical shell, which geneartes the mean flows (the Differential roration and the meridioral circulation) and turbulent diffusivity. In the next chapter we will introduce the converging flow towards the active region in the frame work of STABLE model. The dynamo problem consists in finding/producing a (dynamically consistent) flow field $\mathbf{v}$, that has inductive properties capable of sustaining $\mathbf{B}$, against Ohmic dissipation. Ultimately, the

amplification of $\mathbf{B}$, occurs by stretching of the pre-existing magnetic field. This is readily seen upon rewriting the inductive term in the MHD induction equation to make the contributions of shear, advection and compressible effects more explicit as

$$\boldsymbol{\nabla}\times(\mathbf{v}\times\mathbf{B}) = (\mathbf{B}\cdot\nabla)\mathbf{v} - (\mathbf{v}\cdot\nabla)\mathbf{B} - \mathbf{B}(\boldsymbol{\nabla}\cdot\mathbf{v}) + \mathbf{v}(\boldsymbol{\nabla}\cdot\mathbf{B}) \tag{3.2.3}$$

In Equation 3.2.3 the last tem on the right hand side is zero, and the first term on the right hand side of this expression lead to exponential amplification of the magnetic field, at a rate proportional to the local velocity gradient. Under the anelastic approximation the divergence of $\mathbf{v}$, can be expressed in terms of the logarithmic derivative of the mean density because

$$\boldsymbol{\nabla}\cdot(\overline{\rho}\mathbf{v}) = 0 \tag{3.2.4}$$

This can be rewritten as

$$\boldsymbol{\nabla}\cdot(\overline{\rho}\mathbf{v}) = \overline{\rho}(\boldsymbol{\nabla}\cdot\mathbf{v}) + (\boldsymbol{\nabla}\overline{\rho})\cdot\mathbf{v} = \overline{\rho}(\boldsymbol{\nabla}\cdot\mathbf{v}) + (\mathbf{v}\cdot\boldsymbol{\nabla})\overline{\rho} \tag{3.2.5}$$

$$\boldsymbol{\nabla}\cdot\mathbf{v} = -\mathbf{v}_r\frac{\partial \ln\overline{\rho}}{\partial r} \tag{3.2.6}$$

The MHD induction equation thus becomes

$$\frac{\partial\mathbf{B}}{\partial t} = \overbrace{(\mathbf{B}\cdot\nabla)\mathbf{v}}^{shearing} - \overbrace{(\mathbf{v}\cdot\nabla)\mathbf{B}}^{advection} + \overbrace{\mathbf{v}_r\mathbf{B}\frac{\partial \ln\overline{\rho}}{\partial r}}^{compression} + \eta\nabla^2\mathbf{B} - (\nabla\eta)\times(\nabla\times\mathbf{B}) \tag{3.2.7}$$

$$\frac{\partial\mathbf{B}}{\partial t} = \lambda\mathbf{B}_p\cdot\boldsymbol{\nabla}\Omega\hat{\boldsymbol{\phi}} + \boldsymbol{\nabla}\times(\mathbf{v}_m\times\mathbf{B}) + \eta\boldsymbol{\nabla}^2\mathbf{B} + \boldsymbol{\nabla}\times\varepsilon \tag{3.2.8}$$

$$\frac{\partial\mathbf{B}}{\partial t} = \underbrace{\lambda\mathbf{B}_p\cdot\boldsymbol{\nabla}\Omega\hat{\boldsymbol{\phi}}}_{\Omega-effect} + \underbrace{\boldsymbol{\nabla}\times(\mathbf{v}_m\times\mathbf{B})}_{meridional\ circulation} + \underbrace{\eta\boldsymbol{\nabla}^2\mathbf{B}}_{molecular\ diffusion} + \underbrace{\boldsymbol{\nabla}\times\varepsilon}_{fluctuating\ emf} \tag{3.2.9}$$

where $\lambda = r\sin\theta$ is the cylindrical radius, Ω is the rotation rate of the plasma, $\boldsymbol{\nabla}\times\varepsilon$ is the fluctuating electromotive force (emf), and the vector fields are broken up in to their toroidal and poloidal components represented by the subscripts t and p respectively such

that, e.g. $\mathbf{B}= B_t + B_p$ and $B_t = \mathbf{B}_\phi\hat{\boldsymbol{\phi}}$ and $B_p = B_r\hat{\mathbf{r}} + B_\theta\hat{\boldsymbol{\theta}}$. Each of the four terms in Equation 3.2.9 describe a portion of the dynamo process in the kinematic mean field regime. The first term, which follows from MHD without any additional approximations, is known as the Ω-effect (see Figure 3.1). This term indicates that the mean toroidal field $\mathbf{B}_\phi$ is generated from the mean poloidal field $\mathbf{B}_p$ and rotational shearing provided by differential rotation. Advection of the magnetic field by meridional circulation is captured in the second term, and the third term of magnetic diffusion remains intact as in Equation 3.2.1.

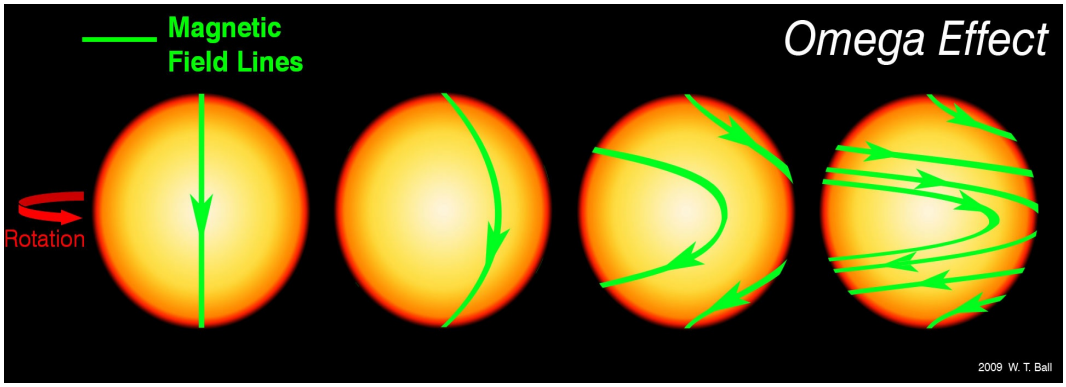

Figure 3.1: Cartoon of the differentional rotation faster at the equator slower at the poles.

3.3 Mean-Field Electrodynamics

The flow field in the solar convection zone is so complex that exact analytical solution of the induction equation (3.2.1) is out of reach, even in the kinematic case. The main concern of solar dynamo theory, however, is not to exactly reproduce the small-scale structure, but to account for the large-scale magnetic field. In order to achieve this, one may take an average, so that the small scales are washed out and knowledge of the flow field is required only through its statistical properties. This has led to mean-field electrodynamics. The outer $\sim 30\%$ of the Sun is in a state of thermally-driven turbulent convection. This turbulence is anisotropic because of the stratification imposed

by gravity, and lacks reflectional symmetry due to the influence of the Coriolis force. Since we are primarily interested in the evolution of the large- scale magnetic field (and perhaps also the large-scale flow) on time scales longer than the turbulent time scale, mean-field electrodynamics offers a tractable alternative to full-blown 3D turbulent MHD. Therefore the kinematic approach should necessarly handle the convective turbulence suitably. The kinematic theory basically has to be of the nature of a mean field theory in which we average over fluctuations around the mean.The fundamental idea on which mean field theory rests is the two scales approach, which consists of a decomposition of the field variables into mean and fluctuating parts. This process naturally implies that an averaging procedure can meaningfully be defined. The derivation of mean field theory can proceed equally from the choice of space averages, time averages or ensemble averages. In the context of axisymmetric dynamo models, longitudinal averages impose themselves rather naturally. For solar and stellar dynamos, the most obvious definition is the azimuthal average, i.e

$$\langle \mathbf{B} \rangle = \frac{1}{2\pi} \int_V \mathbf{B} d\phi \tag{3.3.1}$$

The resulting mean-field dynamo equation does not acquire additional terms, but the mean quantities are subject to fluctuations due to the finite correlation length of convection. These fluctuations may be modeled by allowing the dynamo coefficients to have a random component. By averaging over such fluctuations one obtains a modified dynamo equation that can yield non-decaying solutions for the mean magnetic field for flows with vanishing mean, α. As we are working in the framework of mean field theory, we express both magnetic and velocity fields as the sum of large scale (that corresponds to the mean field) and small scale (associated with hydrodynamic turbulence) contributions.

We assume that the velocity and magnetic field can be decomposed into a mean and fluctuating part so that

$$\mathbf{v} = \langle \mathbf{v} \rangle + \mathbf{v}', \quad and \tag{3.3.2}$$

$$\mathbf{B} = \langle \mathbf{B} \rangle + \mathbf{B}' \quad . \tag{3.3.3}$$

The decomposition of Equation 3.3.2 and 3.3.3 makes sense provided $\langle v' \rangle = \langle v' \rangle = 0$. This is not a linearization, in that it involves no assumption regarding the relative magnitudes of the mean and fluctuating parts. The physical interpretation of Equations 3.3.2 and 3.3.3 is as follows. The velocity and magnetic fields are characterized by a slowly varying component, $\langle \mathbf{v} \rangle$ and $\langle \mathbf{B} \rangle$, which vary on the characteristic large scale L, plus rapidly fluctuating parts, $\mathbf{v}'$ and $\mathbf{B}'$, which vary on the much smaller scale ℓ.

The objective of mean field theory is to produce a closed set of equations for the mean quantities. Substituting Equation 3.3.2 and 3.3.3 into the induction equation, Equation 3.2.1, and averaging, we obtain the following expression for the mean magnetic field

$$\frac{\partial \langle \mathbf{B} \rangle}{\partial t} = \boldsymbol{\nabla} \times \left(\langle \mathbf{v} \rangle \times \langle \mathbf{B} \rangle + \langle \mathbf{v}' \times \mathbf{B}' \rangle - \eta \boldsymbol{\nabla} \times \langle \mathbf{B} \rangle \right) \tag{3.3.4}$$

where $\mathbf{v}$ and $\mathbf{B}$ are longitudinally averaged velocity and magnetic field respectively in the rotating reference frame and $\eta_t(r)$ is a turbulent diffusion. Angular brackets indicate the azimuthal average. The term $\langle \mathbf{v}' \times \mathbf{B}' \rangle$ denotes the correlation of the fluctuating quantities with respect to the azimuthal averages, which gives rise to the α-effect and to enhanced (turbulent) magnetic diffusivit [Cameron and Schüssler(2015)] and actually downward magnetic pumping near the surface. The pumping causes the poloidal field to become predominately radial in the near-surface shear layer, which allows the negative radial shear to effectively act on the radial field to produce a toroidal field [Karak and Cameron(2016)]. Therefore the term $\langle \mathbf{v}' \times \mathbf{B}' \rangle$, which is called the mean electromotive force, or emf for short, plays a central role in this theory. let us rewrite it as

$$\varepsilon = \langle \mathbf{v}' \times \mathbf{B}' \rangle \tag{3.3.5}$$

The term $\langle \mathbf{v}' \times \mathbf{B}' \rangle$, which corresponds to a mean electromotive force ε induced by the fluctuating flow and field components. It appears here because, in general, the cross product $\langle \mathbf{v}' \times \mathbf{B}' \rangle$, usually will not vanish upon averaging, even though $\mathbf{v}$' and $\mathbf{B}$' do

so individually. Evidently, this procedure is meaningful if a separation of spatial and/or temporal scales exists between the (time-dependent) turbulent motions and associated small-scale magnetic fields on the one hand, and the (quasi-steady) large- scale axisymmetric flow and field on the other. In many mean-field solar dynamo, ε is a source term to solve the above MHD induction equation. however instead we use the BL mechanism as a source term. ε must be expressed as some function of $\langle \mathbf{v} \rangle$ and $\langle \mathbf{B} \rangle$. Now ε can be expressed formally by the following series

$$\varepsilon_i = \alpha_{ij} \langle \mathbf{B} \rangle_j + \beta_{ijk} \partial_k \langle \mathbf{B} \rangle_j + \gamma_{ijkl} \partial_j \partial_k \langle \mathbf{B} \rangle_j + ..., \tag{3.3.6}$$

where the tensorial coefficients, α, β, γ, and so forth must depend on $\langle \mathbf{v} \rangle$. Now we have constituted a closed set of equations for the evolution of $\langle \mathbf{B} \rangle$. Here the coefficient α is the crucial parameter for the dynamo generation of magnetic fields, whereas β is the turbulent diffusivity.

We recognize the scalar β as an additional contribution to the effective magnetic diffusivity is sum of the resistive dissipation due to the microscopic magnetic diffusivity, η and turbulent diffusivity, which thus becomes $\eta_t \approx \eta + \beta$. Where we have neglected η compared to β, Equation 3.3.8, which is usually the case within the convection zone. Kinematic mean-field models are based on this dynamo equation, turbulent $\alpha - effect$, plays an amplification role for the dynamo Equation 3.3.7, whereas in STABLE placed by the BL mechanism.

$$\varepsilon = \alpha \mathbf{B} \tag{3.3.7}$$

Turbulent diffusivity; transport

$$\varepsilon = \eta_t \nabla \times \mathbf{B} \tag{3.3.8}$$

magnetic pumping; does transport purpose, this is will give constitute with the advective term on the on MHD inductive equation since it is effective for flux transpot.

$$\varepsilon = \gamma \times \mathbf{B} \tag{3.3.9}$$

$$\varepsilon = \alpha \mathbf{B} - \eta_t \nabla \times \mathbf{B} + \gamma \times \mathbf{B} \tag{3.3.10}$$

This leads to the simplified mean field equation

$$\frac{\partial \mathbf{B}}{\partial t} = \nabla \times (\mathbf{v} \times \mathbf{B} + \varepsilon - \eta \nabla \times \mathbf{B}) \tag{3.3.11}$$

On substituting the above Equations, 3.3.10 in to Equation 3.3.4 we get the dynamo equation

$$\frac{\partial \mathbf{B}}{\partial t} = \nabla \times (\mathbf{v} \times \mathbf{B} - \eta \boldsymbol{\nabla} \times \mathbf{B}) + \nabla \times \varepsilon \tag{3.3.12}$$

$$\frac{\partial \mathbf{B}}{\partial t} = \boldsymbol{\nabla} \times (\mathbf{v} \times \mathbf{B} - \eta \boldsymbol{\nabla} \times \mathbf{B}) + \boldsymbol{\nabla} \times (\alpha \mathbf{B} - \eta_t \boldsymbol{\nabla} \times \mathbf{B} + \gamma \times \mathbf{B}) \tag{3.3.13}$$

$$\frac{\partial \mathbf{B}}{\partial t} = \boldsymbol{\nabla} \times (\mathbf{v} \times \mathbf{B} - (\eta + \eta_t) \boldsymbol{\nabla} \times \mathbf{B}) + \boldsymbol{\nabla} \times (\alpha \mathbf{B} + \gamma \times \mathbf{B}) \tag{3.3.14}$$

$$\frac{\partial \mathbf{B}}{\partial t} = \boldsymbol{\nabla} \times ((\mathbf{v} + \gamma) \times \mathbf{B} - \eta_t \boldsymbol{\nabla} \times \mathbf{B}) + \boldsymbol{\nabla} \times (\alpha \mathbf{B}) \tag{3.3.15}$$

Therefore the component of MHD induction equation can be written as fllow: The radial component of induction equation is given by

$$\begin{aligned} \frac{\partial B_r}{\partial t} &= \frac{1}{r \sin\theta} \left[\frac{\partial (\sin\theta (v_r B_\theta - v_\theta B_r))}{\partial \theta} - \frac{\partial (v_\phi B_r - v_r B_\phi)}{\partial \phi} \right] \\ &- \frac{1}{r^2} \frac{\partial \eta}{\partial \theta} \left(\frac{\partial (r B_\theta)}{\partial r} - \frac{\partial B_r}{\partial \theta} \right) + \frac{1}{r^2 \sin^2\theta} \frac{\partial \eta}{\partial \phi} \left(\frac{\partial B_r}{\partial \phi} - \frac{\partial (r \sin\theta B_\phi)}{\partial r} \right) \\ &+ \eta \left(\nabla^2 B_r - \frac{2 B_r}{r^2} - \frac{2}{r^2 \sin\theta} \frac{\partial (B_\theta \sin\theta)}{\partial \theta} - \frac{1}{r^2 \sin\theta} \frac{\partial B_\phi}{\partial \phi} \right) \quad , \end{aligned} \tag{3.3.16}$$

The latitudial component of induction equation becomes;

$$\begin{aligned} \frac{\partial B_\theta}{\partial t} &= \frac{1}{r \sin\theta} \frac{\partial (v_\theta B_\phi - v_\phi B_\theta)}{\partial \phi} - \frac{1}{r} \frac{\partial (r v_r B\theta - r \mathbf{v}_\theta B_r)}{\partial r} \\ &- \frac{1}{r^2 \sin^2\theta} \frac{\partial \eta}{\partial \phi} \left(\frac{\partial (B_\phi \sin\theta)}{\partial \theta} - \frac{\partial B_\theta}{\partial \phi} \right) + \frac{1}{r} \frac{\partial \eta}{\partial r} \left(\frac{\partial (r B_\theta)}{\partial r} - \frac{\partial B_r}{\partial \theta} \right) \\ &+ \eta \left(\nabla^2 B_\theta + \frac{2}{r^2} \frac{\partial B_r}{\partial \theta} - \frac{B_\theta}{r^2 \sin^2\theta} - \frac{2 \cos\theta}{r^2 \sin^2\theta} \frac{\partial B_\phi}{\partial \phi} \right) \quad , \end{aligned} \tag{3.3.17}$$

And the azimuthal components of induction equation becomes

$$\frac{\partial B_\phi}{\partial t} = \frac{1}{r}\left[\frac{\partial(rv_\phi B_r - rv_r B_\phi)}{\partial r} - \frac{\partial(v_\theta B_\phi - v_\phi B_\theta)}{\partial \theta}\right]$$
$$-\frac{1}{r\sin\theta}\frac{\partial \eta}{\partial r}\left(\frac{\partial B_r}{\partial \phi} - \frac{\partial(r\sin\theta B_\phi)}{\partial r}\right) + \frac{1}{r^2\sin\theta}\frac{\partial \eta}{\partial \theta}\left(\frac{\partial(B_\phi \sin\theta)}{\partial \theta} - \frac{\partial B_\theta}{\partial \phi}\right)$$
$$+\eta\left(\nabla^2 B_\phi + \frac{2}{r^2\sin\theta}\frac{\partial B_r}{\partial \phi} + \frac{2\cos\theta}{r^2\sin^2\theta}\frac{\partial B_\theta}{\partial \phi} - \frac{B_\phi}{r^2\sin^2\theta}\right) \quad . \tag{3.3.18}$$

where $\mathbf{v}$ and $\mathbf{B}$ are the velocity and magnetic field in the rotating reference frame and $\eta_t(r)$ is a turbulent diffusion. These equations are solved by means of the Anelastic Spherical Harmonic (ASH) code, which currently serves as the *dynamical core* for the STABLE model and will be disscused immediately below in §3.3.1.

3.3.1 Anelastic MHD Formulation; ASH

The deep, global, solar convection we are concerned with extends over many density scale heights, and stratification must therefore be incorporated into any realistic model. However, the timescale associated with such large-scale convection is expected to be much longer than acoustic timescales, making a fully compressible treatment undesirable because of the relatively small time steps which would be required in order for any explicit time diferencing scheme to satisfy the Courant-Freidreichs-Lewy (CFL) condition.

Our tool for exploring MHD induction equation (3.2.1) is using Anelastic Spherical Harmonic (ASH) code. ASH is a well-established pseudospectral code which has been used extensively for three-dimensional solar and stellar convection simulations, instabilities, tachocline confinement and many other aspects of solar and stellar internal dynamics [Clune et al.(1999), Brun et al.(2004), Miesch(2005), Miesch and Toomre(2009), Brun(2010)]. The ASH code is able to solve the full set of 3D MHD anelastic equations of motion in a rotating, convective spherical shell with high resolution on massively-parallel computing architectures. Therefore the ASH code has the capability to solve the velocity equation and magnetic induction equation together, but for our kinematic STABLE

model, we have modified ASH to operate in a kinematic regime. We bypass the velocity equation solver and only solve the induction equation by providing observationally motivated velocity fields. Therefore we can use more realistic flows.

In modelling dynamo action over solar cycle timescales, the MHD equations have been solved numerically under the anelastic approximation, nowadays in common usage, retains the possibility that ρ be a function of position and is thus better applicable to stratified environment, but still precludes any temporal variation of density other than associated with thermal dilation. The anelastic approximation filters out sound waves by neglecting the $\partial\rho/\partial t$ term in the mass conservation equation. Thus mass conservation equation is then replaced by

$$\boldsymbol{\nabla}\cdot(\rho\mathbf{v}) = 0. \tag{3.3.19}$$

However still we need to define $\mathbf{B}= \boldsymbol{\nabla}\times\boldsymbol{\nabla}\times(C\hat{r}) + \boldsymbol{\nabla}\times(A\hat{r})$, in Spherical harmonics expansions. Spherical harmonics, $Y_{\ell m}(\theta,\phi)$, are a natural set of functions for this problem because they constitute a complete and orthogonal set of eigenfunctions of the horizontal Laplacian operator in θ and ϕ. That is,

$$\begin{aligned}\boldsymbol{\nabla}_h^2 Y_{\ell m}(\theta,\phi) &= \left[\frac{1}{r^2\sin\theta}\frac{\partial}{\partial\theta}\left(\sin\theta\frac{\partial}{\partial\theta}\right) + \frac{1}{r^2\sin^2\theta}\frac{\partial^2}{\partial\phi^2}\right] Y_{\ell m} \\ &= -\frac{\ell(\ell+1)}{r^2} Y_{\ell m}\end{aligned} \tag{3.3.20}$$

where the eigenvalue is $-\frac{\ell(\ell+1)}{r^2}$. This is convenient because all the diffusion operators involve the Laplacian operator. Each spherical harmonic is a product of a complex Fourier function, $e^{\imath m\phi}$, and an associated Legendre function (of the first kind), $P_\ell^m(\cos\theta)$.

$$Y_{\ell m}(\theta,\phi) = \sqrt{\frac{2\ell+1(\ell-m)!}{4\pi(\ell+m)!}} P_\ell^m(\cos\theta) e^{\imath m\phi}, \tag{3.3.21}$$

For a vector variable that is divergence-free, magnetic field, the $\mathbf{B}$, is represented with a toroidal-poloidal decomposition decomposition

$$\mathbf{B} = \boldsymbol{\nabla}\times\boldsymbol{\nabla}\times(C\hat{r}) + \boldsymbol{\nabla}\times(A\hat{r}), \quad where \tag{3.3.22}$$

$$A(r,\theta_i,\phi_j,t) = \sum_{m=-m_{max}}^{m_{max}} \sum_{\ell=|m|}^{\ell_{max(m)}} A_\ell^m(r,t) Y_{\ell m}(\theta_i,\phi_j) \quad and \tag{3.3.23}$$

$$C(r,\theta_i,\phi_j,t) = \sum_{m=-m_{max}}^{m_{max}} \sum_{\ell=|m|}^{\ell_{max(m)}} C_\ell^m(r,t) Y_{\ell m}(\theta_i,\phi_j) \quad . \tag{3.3.24}$$

The components of the magnetic field becomes

$$B_r = \frac{1}{r^2} \sum_{\ell,m} \ell(\ell+1) C_\ell^m Y_{\ell m} \quad , \tag{3.3.25}$$

$$B_\theta = \frac{1}{r\sin\theta} \sum_{\ell,m} \left(\frac{\partial Y_{\ell m}}{\partial \theta} \sin\theta \frac{\partial (C_\ell^m)}{\partial r} + A_\ell^m \frac{\partial Y_{\ell m}}{\partial \phi} \right) \quad and \tag{3.3.26}$$

$$B_\phi = \frac{1}{r\sin\theta} \sum_{\ell,m} \left(\frac{\partial Y_{\ell m}}{\partial \phi} \frac{\partial (C_\ell^m)}{\partial r} - A_\ell^m \sin\theta \frac{\partial Y_{\ell m}}{\partial \theta} \right) \quad . \tag{3.3.27}$$

3.4 The Imposed Mean Flows and Turbulent Diffusivity

All kinematic solar dynamo models have some basic ingredients in common, most importantly (i) a meridional circulation, (ii) a differential rotation profile, and (iii) a magnetic diffusivity profile (possibly depth-dependent). For the future we will consider 3D and time-dependent flows, here we focus on steady, axisymmetric mean flows, which is summation of the velocity of the meridional flow, $\mathbf{v}_{mc}$ and a velocity as a result of $\Omega(r,\theta)$, that is the angular velocity of the differential rotation.

The evolution of the magnetic field on the solar surface is governed by the simplified induction equation (may be radial component of the induction equation). Some terms of the simplified induction equation represent the advection of magnetic flux by the surface flows, which include differential rotation, meridional flow, and inflows towards active regions (more details on this is given in Chapter 4).

$$\mathbf{v} = \mathbf{v}_{DR}(r,\theta) + \mathbf{v}_{mc}(r,\theta) + \mathbf{v}_{in}(r,\theta,\phi,t) \tag{3.4.1}$$

Now we will look at the flow velocity, $\mathbf{v}$, which consists of the meridional circulation includes the $\mathbf{v}_r$ and $\mathbf{v}_\theta$ components and differential rotation, which contain the $\mathbf{v}_\phi / r\sin\theta$ and can rewrite as:

$$\mathbf{v} = \mathbf{v}(r,\theta)\hat{\boldsymbol{r}} + \mathbf{v}(r,\theta)\hat{\boldsymbol{\theta}} + \mathbf{v}(r,\theta)\hat{\boldsymbol{\phi}} \tag{3.4.2}$$

Here in Equation 3.4.1, $\mathbf{v}_{mc}$ is the velocity of the meridional flow, $\Omega(\theta)$ is the angular velocity of the differential rotation, and $\mathbf{v}_{DR}$ is the velocity due to the differential rotation. This velocity flow collectively given is by the following Equation 3.4.3, where the meridional flow and differentional rotation are consistent with observations.

$$\mathbf{v} = \tilde{\rho}(r)^{-1}\ \boldsymbol{\nabla}\times\left[\psi(r,\theta)\hat{\boldsymbol{\phi}}\right] + \lambda\Omega(r,\theta)\hat{\boldsymbol{\phi}} \tag{3.4.3}$$

where $\psi(r,\theta)$ is the stream function for the meridional mass flux and will discussed in detail in §3.4.1, $\tilde{\rho}(r)$ is the dimensionless density stratification, $\lambda = r\sin\theta$ is the cylindrical radius, and $\Omega(r,\theta)$ is the differential rotation.

3.4.1 Meridional Circulation

Meridional circulation refers to the large-scale axisymmetric flow component confined to meridional (radius-latitude) planes. It is weaker and shows more temporal variability than differential rotation. Directed poleward with speeds of $\sim$ (10 - 20) ms^{-1} at the surface low to midlatitudes, it is also ultimately powered by convection. Observational attempts to detect the expected equatorward return flow, carried out through helioseismology or the tracking of deeply anchored magnetic tracers, have yielded conflicting results, some inferring a return flow located deep in the convective envelope, while others infered a shallow return flow.

Doppler measurements reveal a surface meridional flow with an amplitude of about 20 ms^{-1} from the equator to the poles. This surface meridional flow implies a subsurface return (i.e., equatorward) flow. The structure and strength of the meridional circulation

influence the strength of the Sun's magnetic fields to some extent, but meridional circulation cannot be the most important factor determining the field strength in flux-transport dynamo models. In flux-transport dynamos (and most other dynamos applied to the Sun) the spot-producing toroidal fields are generated by the Sun's differential rotation and the poloidal fields are produced by the action of the so-called α-effect. The α-effect is modeled in different dynamo models in different ways. In Babcock-Leighton type flux-transport dynamo models, such an α-effect arises from the decay of tilted, bipolar active regions that emerge to the surface from below. Thus the two sources of magnetic fields, the differential rotation and a combination of α-effects arising from helical turbulence as well as from the decay of active regions, are primarily responsible for determining the amplitudes of toroidal and poloidal fields, and hence the polar fields. Note that there is no explicit α-effect in the STABLE model; instead the poloidal field generation needed to sustain the dynamo which occurs as a consequence of the spot deposition algorithm described in Section §3.6. The primary role of meridional circulation in flux-transport dynamo models is the advective transport of magnetic fields, and hence the structure and strength of the flow are crucial in the dynamo models for determining the timings, namely the duration of a cycle, its rise and fall pattern and the timing of the reversals of the Sun's polar fields. A transport process like meridional circulation in a flux-transport dynamo redistributes the dynamo-generated magnetic flux, a relatively minor effect in creating an increase or decrease of magnetic flux ([Dikpati and Charbonneau(1999), Dikpati et al.(2010), Gizon et al.(2010)]).

The meridional circulation is introduced as one large single cell directed poleward at the surface, in accordance with solar observations. The inclusion of the meridional circulation in the dynamo theory of the solar cycle turns out to be essential in reproducing the most important features of the 11-yr cycle. The meridional flow is the same as that used by previous studies [Dikpati et al.(2010), Dikpati(2011), Miesch and Teweldebirhan(2016)]

$$\mathbf{v} = \tilde{\rho}(r)^{-1} \, \boldsymbol{\nabla} \times \left[\psi(r, \theta) \hat{\boldsymbol{\phi}} \right] \tag{3.4.4}$$

$$\psi(r,\theta) = -\psi_0 \ \lambda^{-1} \ (\theta - \theta_0) \ f_{mc}(r) \ h_{mc}(r,\theta) \tag{3.4.5}$$

with

$$f_{mc}(r) = \sin\left[\frac{\pi(\tilde{r} - r_b)}{(\tilde{R} - r_b)}\right] \exp\left[-\left(\frac{\tilde{r} - r_0}{\Gamma}\right)^2\right] \tag{3.4.6}$$

and

$$h_{mc}(r,\theta) = (1 - \exp\left[-\beta_1 \tilde{r}\theta^{\epsilon}\right])\,(1 - \exp\left[\beta_2 \tilde{r}(\theta - \pi/2)\right]) \tag{3.4.7}$$

Note that we use meridional circulation a bit different for the benchmark (see details in Chapter 4) and inflow towards active regions (Chapter 5). The r and θ components of the meridional flow are given through the following relations,

$$\mathbf{v} = \tilde{\rho}(r)^{-1} \ \boldsymbol{\nabla} \times \left[\psi(r,\theta)\hat{\boldsymbol{\phi}}\right] \tag{3.4.8}$$

$$\mathbf{v} = \tilde{\rho}(r)^{-1} \ \left[\frac{1}{r\sin\theta}\frac{\partial(\psi\sin\theta)}{\partial\theta}\hat{\boldsymbol{r}} - \frac{1}{r\sin\theta}\frac{\partial(r\psi\sin\theta)}{\partial r}\hat{\boldsymbol{\theta}}\right] \tag{3.4.9}$$

$$v_r(r,\theta) = \tilde{\rho}(r)^{-1} \ \frac{1}{r\sin\theta}\frac{\partial(\psi\sin\theta)}{\partial\theta} \quad . \tag{3.4.10}$$

$$v_\theta(r,\theta) = -\tilde{\rho}(r)^{-1} \ \frac{1}{r\sin\theta}\frac{\partial(r\psi\sin\theta)}{\partial r} \quad . \tag{3.4.11}$$

The parameters within Equations (3.4.5 - 3.4.7) do the following: ψ_0 determines the maximum speed of the flow; θ_0 sets the colatitude where the primary poleward flow cell ends and the secondary equatorward cell begins it ranges from 0 to 45 degrees; R denotes the solar radius and r_b the radius near the bottom of the convection zone down to which the flow penetrates; β_1 and β_2 control how concentrated the flow will be at the pole and equator, respectively; ϵ, taken slightly greater than 2, keeps the flow nonsingular at the pole; and r_0 and Γ are parameters that determine where the streamfunction maximum is and where the streamlines are concentrated. This kind of stream function has been used by many other flux-transport dynamo modellers over the past two decades [Dikpati et al.(2010)], [Dikpati(2011)].

Here $\tilde{r} = r/L$ is a nondimensional radius based on a length scale $L = 1.09 \times 10^{10}$ cm and $\tilde{R} = R/L$. The parameters we use here are as follows: $\psi_0 = 4.32 \times 10^{13}$ cm^2

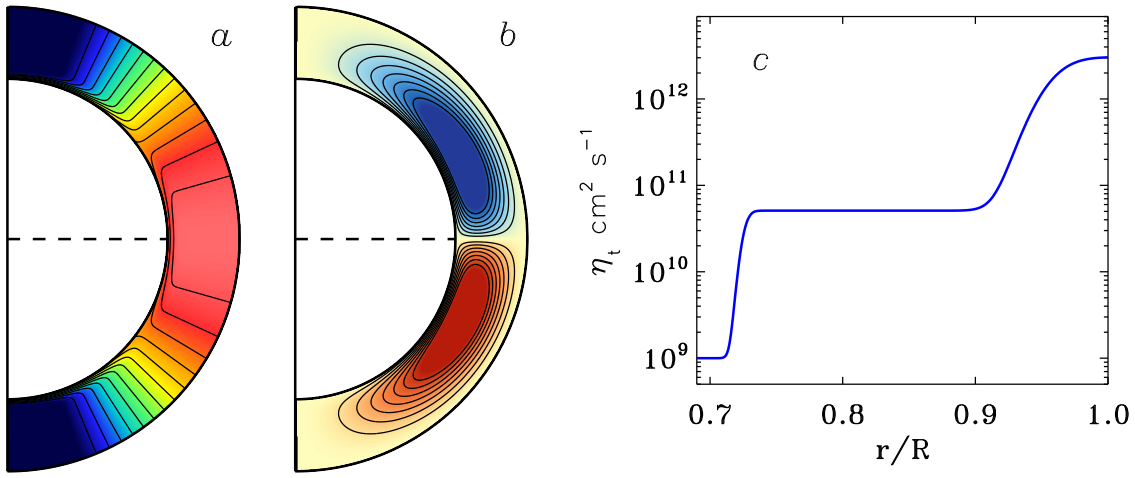

Figure 3.2: Model components;
Mean flows and turbulent diffusion. (a) Angular velocity $\Omega/2\pi$, with color table ranging from 350-480 nHz (blue to red/pink). (b) Meridional circulation, shown as streamlines of the mass flux, with red and blue denoting clockwise and counter-clockwise circulation respectively. Horizontal velocity amplitudes are approximately 14 m s^{-1} and 1.5 m s^{-1} in the upper and lower CZ. (c) turbulent magnetic diffusivity η_t.

s^{-1}, $\theta_0 = 0$, $r_b = 0.69$, $r_0 = (\tilde{R} - r_b)/5$, $\Gamma = 3$, $\beta_1 = 0.1$, $\beta_2 = 0.3$, and $\epsilon = 2 + 10^{-8}$. The resulting profile is illustrated in Fig. 3.2b. The nondimensional density stratification profile in the convection zone given by:

$$\tilde{\rho} = \left(\frac{R}{r} - 0.97\right)^n \tag{3.4.12}$$

with $n = 1.5$.

In both velocity components, $\theta_0 = 0$ ensures that there is a single meridional flow cell that extends all the way to the poles from the equator. In all cases, the change in meridional flow is timed to occur at the epoch of polar reversal.

Note also that the use of an axisymmetric velocity field as given by Equation 3.4.3 implies that the axisymmetric ($m = 0$, where m is the azimuthal wave number) component of Equation 3.2.1 decouples from the non-axisymmetric components ($m \neq 0$). In other words, the mean (longitudinally-averaged) induction equation for the STABLE model is equivalent to a 2D FTD model when $\mathbf{v}$, is axisymmetric and kinematic. This allows us to

make contact with previous 2D FTD models in the literature before moving on to more general 3D, nonlinear flow fields.

This point can be appreciated by averaging Equation 3.2.1 over ϕ, noting that $\mathbf{v}$, η_t, and the curl operator are all independent of ϕ. Though the SpotMaker algorithm (§3.6) is distinct from previous representations of the BL mechanism in the literature, one could in principle devise an axisymmetric source term that is equivalent from the perspective of the mean fields. Thus, in terms of the evolution of the mean fields, the models presented here are similar to the 2D FTD models presented by [Muñoz-Jaramillo et al.(2010)], who used an axisymmetric spot deposition algorithm. However, unlike 2D FTD models, STABLE provides also the corresponding time evolution of the 2D (latitude/longitude) surface field.

3.4.2 Differential Rotation

Differential rotation powered by turbulent Reynolds stresses is a potentially powerful mechanism for spatial organization, as this flow is structured on global scales and, at least in the Sun, remains close to stationary on cycle timescales. Differential rotation is also efficient at dissipating nonaxisymmetric large-scale magnetic fields, thus also favoring the buildup of solar-like axisymmetric large-scale magnetic fields. Rotational influences also lead to a differential rotation pattern characterized by equatorial regions rotating some 30% faster than the poles, with the underlying radiative core rotating at an intermediate rate corresponding to surface midlatitudes [Charbonneau(2014)].

The North-South symmetric component of internal differential rotation has been measured using global helioseismology. The solar rotation rate depends strongly on latitude in the convection zone, with the equator rotating more quickly than the poles. The rotation rate shows only a weak radial shear in the bulk of the convection zone. There is strong radial shear in the very near surface layers (top 35 Mm), and in the tachocline where the differentially rotating convection zone meets the uniformly rotating radiative zone. The

tachocline plays an important role in most dynamo theories of the solar cycle [Gizon et al.(2010)].

The differential rotation, is one very powerful mechanism allowing to build up of a large-scale magnetic field. A situation of great astrophysical interest is the induction of a toroidal magnetic field via the shearing of a pre-existing poloidal magnetic field threading a differentially rotating sphere of electrically conducting fluid.

STABLE uses the SpotMaker spot deposition algorithm to place tilted angles of bipolar magnetic regions (BMRs), when they decay and disperse on the solar surface in response to the dynamo-generated magnetic field. The subsequent evolution of these BMRs due to differential rotation, meridional circulation, and turbulent diffusion naturally generates a mean poloidal field as originally described by [Babcock(1961)] and [Leighton(1964)]. This poloidal field generated in this process largely depends on the amount of flux in BMRs, the frequency of BMR eruptions, and the tilt angles of BMRs and reproduces toroidal field throught the mechanism by differential rotation (velocity shear). This differential rotation in the azimuthal direction varying with depth and latitude. So now we understand how the Babcock-Leighton mechanism can convert a toroidal magnetic field into a poloidal component. Now we need to construct a solar cycle model based on this idea. Production of the toroidal field takes place in the tachocline, as before, but now production of the poloidal field takes place in the surface layers [Miesch and Teweldebirhan(2016)].

In order to build on previous work, we specify $\Omega(r,\theta)$ as in previous STABLE models. In particular, the Ω profile is taken from [Dikpati and Charbonneau(1999)]

$$\Omega(r,\theta) = \Omega_c + \frac{1}{2}\left[1 + \mathrm{erf}\left(2\,\frac{r - r_c}{d}\right)\right](\Omega_s(\theta) - \Omega_c) \tag{3.4.13}$$

where the erf is the error function and Ω_s, is the surface latitudinal differential rotation given by

$$\Omega_s(\theta) = 2\pi\ (\nu_{eq} + a_2\cos^2\theta + a_4\cos^4\theta) \quad . \tag{3.4.14}$$

The other parametric values are set as $\Omega_c = 2\pi\nu_c$ with $\nu_c = 432.8$ nHz, $\nu_{eq} = 460.7$

nHz, a_2 = - 62.9 nHz, a_4 = -67.13 nHz, $r_c = 0.7R$, and $d = 0.05R$, where R is the solar radius. The resulting profile is illustrated in Figure 3.2a. This differential profile closely resembles the best-fit helioseismic solution. This defines a solar-like dierential rotation profile, characterized in the 'envelope' by purely latitudinal dierential rotation (Ω_s) with equatorial acceleration, smoothly matching across a s tachocline of thickness d on a core rotating rigidly at a rate) (see Figure 3.2a). The parameter r_c then corresponds to the central radius of the (spherical) tachocline, where the radial shear is confined. This differential rotation profile resembles rather closely that inferred by fully two-dimensional helioseismic inversions [Dikpati and Charbonneau(1999)]. As obtained by a best-fit to helioseismic frequency splittings. This properly reproduces the primary features of full helioseismic inversions, namely:

A convective envelope (r $\gtrsim$ r_c) where the shear is purely latitudinal, with the equatorial region rotating faster than the poles; a core (r $\lesssim$ r_c) that rotates rigidly, at a rate equal to that of the surface mid- latitudes; a smooth matching of the core and envelope rotation profiles occurring across a thin spherical layer coinciding with the core-envelope interface (r = r_c), known as the tachocline.

The differential rotation profile is quite complex, in that it is characterized by three partially overlapping shear regions: a strong positive radial shear (i.e., $\partial\Omega/\partial r > 0$) in the equatorial regions of the tachocline, an even stronger negative radial shear ($\partial\Omega/\partial r < 0$) in its polar regions, and a significant positive latitudinal shear ($\partial\Omega/\partial\theta > 0$) throughout the convective envelope and extending partway into the tachocline. For a tachocline of half-thickness ω/R = 0.05, the mid-latitude latitudinal shear at r/R = 0.7 is comparable in magnitude to the equatorial radial shear [Charbonneau(2013)].

$$\mathbf{v}_\phi(r,\theta) = r\sin\theta\ [\Omega_c + \frac{1}{2}\left[1 + \mathrm{erf}\left(2\ \frac{r - r_c}{d}\right)\right](\Omega_s(\theta) - \Omega_c)] \tag{3.4.15}$$

The combined effect of circulation, diffusion and differential rotation is to concentrate the magnetic polarity of the trailing spot to high latitude. The polarity of the leading spot

dominates at lower latitudes, but experiences diffusive cancellation with the opposite polarity leading flux from its cousin in the other solar hemisphere. It is this cross-equatorial diffusive cancellation that is ultimately responsible for the buildup of a net hemispheric flux. At mid-latitudes, the effect of differential rotation is to stretch longitudinally the unipolar regions originally associated with each member of the BMR, causing the development of thin banded structures of opposite magnetic polarities [Charbonneau(2013)]. Now the components of the mean velocity that comprised the mean velocity, $\mathbf{v}$, are explicitly defined below:

$$v_r(r,\theta) = \tilde{\rho}(r)^{-1} \frac{1}{r\sin\theta}\frac{\partial(\psi\sin\theta)}{\partial\theta} \quad , \tag{3.4.16}$$

$$v_\theta(r,\theta) = -\tilde{\rho}(r)^{-1} \frac{1}{r\sin\theta}\frac{\partial(r\psi\sin\theta)}{\partial r} \quad , \tag{3.4.17}$$

$$v_\phi(r,\theta) = r\sin\theta[\Omega_c + \frac{1}{2}\left[1+\mathrm{erf}\left(2\,\frac{r-r_c}{d}\right)\right] \quad .(\Omega_s(\theta)-\Omega_c)] \tag{3.4.18}$$

3.4.3 Turbulent Diffusivity

Due to the high value of Reynolds number, $R_e \equiv UL/\nu$, which is hydrodynamic turbulence, the flow in the solar convection zone is turbulent, and the same holds for the magnetic field since it is well frozen into the plasma. This suggests that the problem of the solar dynamo should be approached within the more general framework of MHD turbulence. The complexities of full MHD equations are such that there is no self-consistent, comprehensive turbulence theory. Nevertheless, a number of basic mechanisms and properties are well-established, and they provide a phenomenological view of turbulent dynamo action. Thus, in order to gain insight into the fundamental mechanisms of dynamo action in astrophysical plasmas, simplified MHD turbulence models with controllable and well-defined properties are investigated using various analytical and numerical tools. This is achieved by replacing the gravity force in the Navier-Stokes equation, which drives convection, by a specified external force. Of course, the relevance of such an analysis for the

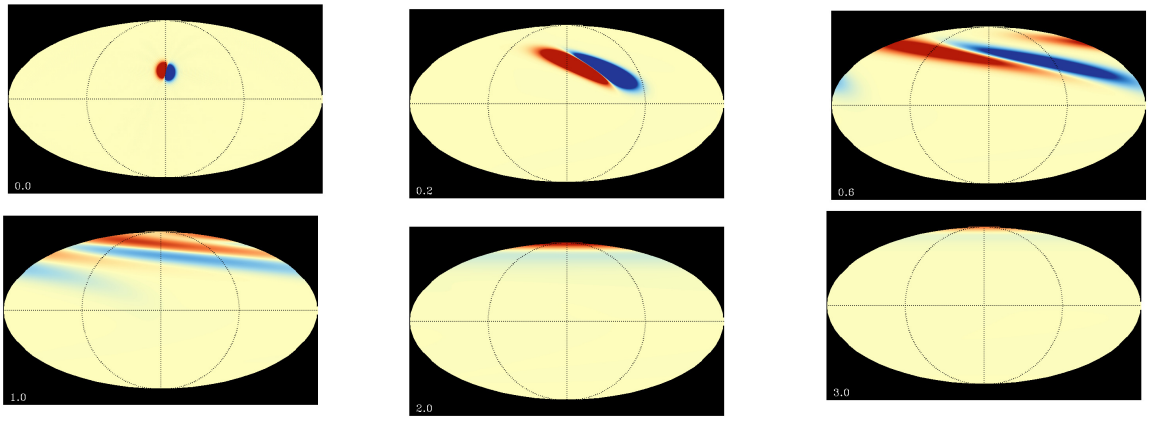

Figure 3.3: Time evolution of surface radial magnetic field:

The time evolution (a-f) of surface radial magnetic field on the surface of the Sun with a single pair (BMRS) in the Northern and initially located at $\pm 25°$, with opposite polarity ordering in each hemisphere, as per Hale's polarity laws. The surface field evolves in response to diffusion and advective transport by differential rotation and a poleward meridional flow, for (upper left panel) 0.0 years, (upper middle panel) 0.2 years, (upper right panel) 0.6 years, (lower left panel) 1.0 years, (lower middle panel) 2.0 years and (lower right panel) 3.0 years. Here red color shows the outwards going radial field and blue color represents inward going radial magnetic field.

Sun must be established, which may not be easy. The turbulent diffusivity is expected to be less within the convection zone and falls drastically at its bottom where convection is less vigorous. We use a two-step diffusivity given by, after [Dikpati and Gilman(2007)]

$$\eta = \eta_c + \frac{\eta_{mid}}{2}\left[1 + \mathrm{erf}\left(2\,\frac{r - r_{da}}{d_a}\right)\right] + \frac{\eta_{top}}{2}\left[1 + \mathrm{erf}\left(2\,\frac{r - r_{db}}{d_b}\right)\right] \quad , \tag{3.4.19}$$

where $\eta_c = 10^9$ cm^2 s^{-1}, below the base of the convection zone down to 0.6R, $\eta_{mid} = 5 \times 10^{10}$ cm^2 s^{-1}, which works in the bulk of the convection zone. The thickness of the three layers with different diffusivities and the transitions between adjacent layers are specified by $r_{da} = 0.725R$, $d_a = 0.0125R$, $r_{db} = 0.956R$, and $d_b = 0.05R$. We consider two values of the turbulent diffusivity in the surface layers: $\eta_{top} = 3 \times 10^{12}$ cm^2 s^{-1}, which works in a thin layer at the surface, as in [Dikpati and Gilman(2007)], as well as a lower value of $\eta_{top} = 10^{12}$ cm^2 s^{-1}. The resulting profile is illustrated in Fig. 3.2*c*.

Note that the relatively low value of η in the mid CZ, 5×10^{10} cm^2 s^{-1} places our simulations in the so-called advection-dominated regime in which the meridional flow dominates over turbulent diffusion for transporting poloidal magnetic flux across the CZ [Yeates et al.(2008), Dikpati and Gilman(2009), Charbonneau(2010)]. Though this serves as a good test case, several recent studies have suggested that the diffusion-dominated regime may be more realistic, based on the correlation of the polar field at solar minimum with the strength of the next cycle ([Jiang, et al.(2017)]), the Waldmeier effect ([Karak and Choudhuri(2011)]), and the efficiency of turbulent transport inferred from helioseismic measurements ([Miesch et al.(2012)]). We will consider the diffusion-dominated regime in chapter 5.

3.4.4 Initial and Boundary Conditions

The numerical solution of the governing equations requires the selection of a spatial discretization strategy appropriate for the spherical coordinate system. Care must be taken to ensure that the terms in the equations remain bounded at the poles, where longitude

becomes multi-valued and as a result vector quantities which are smooth and nonzero in Cartesian representations (e.g. horizontal flow over the poles) yield multi-valued or discontinuous spherical components. This is only one in a series of diffculties which are associated with the coordinate singularities at $\theta = 0$ and π and which are collectively referred to as the pole problem. Another aspect of the pole problem occurs when employing the the most straightforward horizontal discretization, consisting of finite difference derivative approximations on uniform grids in θ and ϕ. In this case, the convergence of meridian lines at the poles leads to small longitudinal grid spacing which can severely limit the maximum allowable timestep according to the Courant-Freidreichs-Lewy (CFL) condition for numerical stability [Miesch(1998)]. This condition requires that the timestep, Δt , satisfy

$$\Delta t \leq |\Delta x/\mathbf{v}|_{min} \tag{3.4.20}$$

where Δx is a measure of the local grid spacing and $\mathbf{v}$, is a measure of the local group velocity of the fastest propagating advective or wave mode admitted by the terms in the equations which are treated by explicit time-stepping methods (for our model, $\mathbf{v}$, can be taken to be the local fluid velocity).

The MHD kinematic induction equations is solved in a segment of the meridional plane with the colatitude $0 \leq \theta \leq \pi$ and the radius $r_b \leq r \leq R_\odot$ where the inner radial extent of the domain (r_b) need not necessarily extend all the way to r = 0, it extend only slightly below the tachocline (e.g. r = 0.7) up to the solar surface, $R_\odot$. Because it is usually assumed that the deep radiative interior can be treated as a perfect conductor, so that r_b is chosen a bit deeper than the lowest extent of the region where dynamo action is taking place. The boundary condition we impose relevant to this depth is which is the lower boundary, r = r_b, we use a perfectly conducting boundary conditions at the bottom ($\partial A/\partial r = C = 0$ at $r = r_b$).

$$A_\phi = 0 \qquad \frac{\partial(r\mathbf{B}_\phi)}{\partial r} = 0 \quad at \quad (r = r_b) \tag{3.4.21}$$

we impose a purely radial magnetic field conditions at the top ($A = \partial C/\partial r = 0$ at $r = R$).

$$\mathbf{B}_\phi = \mathbf{B}_\theta = 0 \qquad\qquad at \quad (r = R_\odot) \tag{3.4.22}$$

It is usually assumed that the Sun is surrounded by a vacuum, $r \geq R_\odot$, in which no electrical currents can flow, i.e., $\boldsymbol{\nabla}\times\mathbf{B} = 0$

$$\mathbf{J}_r = 0 \qquad\qquad for \quad (r \geq R_\odot) \tag{3.4.23}$$

The inner and outer boundaries are both assumed to be impenetrable; impenetrable top and bottom: $v_r = 0|_{r=r_{bot},r_{top}}$, this will be useful in Chapter 5. All simulations are initiated at $t = 0$ with a dipolar seed field that grows and saturates as described in sections §3.6.

3.5 Spot Producing Toroidal Field

Our objective is to construct STABLE solar dynamo model that captures both the solar activity cycle and the observed evolution of large-scale magnetic flux on the solar surface. However, capturing the full complexity of active region formation and dispersal through is currently beyond the capability of a single numerical dynamo model. Here we use an idealized flux emergence algorithm to place spots on the solar surface in response to the dynamo-generated toroidal field near the base of the CZ. As mentioned in sections §3.2 the MHD induction equation, 3.2.1 does not have an explicit α-effect. Instead, we introduce spots as a source to sustain the dynamo with the help of SpotMaker algorithm to treat the BL process and follow their subsequent evolution, which will naturally produce a poloidal emf that will sustain the dynamo. The SpotMaker algorithm is mainly a 3D generalization of the Durney's double ring algorithm [Durney(1997)]. The spot deposition algorithm is described in detailed in [Miesch and Dikpati(2014)], MD14 and we call it SpotMaker.

In SpotMaker, BMRs are placed on the surface based on a spot-producing toroidal field $B^*(\theta, \phi, t)$, which is obtained from $B_\phi(r, \theta, \phi, t)$ by first averaging over the tachocline

thickness radius in the lower CZ (0.70-0.71 R) and then applying a mask that excludes latitudes above 40°.

In achieving this, our first task is to define a measure of the toroidal field that we will use to determine strength flux at the solar surface. Then we want to determine, where to place spots, when to place spots, and how big they will be. Then the first step in the algorithm is to define a spot-producing toroidal flux near the base of the CZ as follow.

$$\hat{\mathbf{B}}_\phi(\theta,\phi,t) = \int_{r_a}^{r_b} h(r)\mathbf{B}_\phi(\theta,\phi,t)dr \quad . \tag{3.5.1}$$

Where

$$\int_{r_a}^{r_b} h(r)dr = 1 \tag{3.5.2}$$

$$h(r) = h_o(r-r_a)(r_b-r) \quad . \tag{3.5.3}$$

$$h_o^{-1} = -\frac{r_b^3 - r_a^3}{3} + (r_a+r_b) - r)\frac{r_b^2 - r_a^2}{2} - r_a r_b(r_b - r_a) \quad . \tag{3.5.4}$$

where $r_a = 0.715$R, $r_b = 0.73$R, and h_0 as a normalization factor. We note that

Another very important thing we should mention here is that, as seen in the observed butterfly diagram, sunspots are found mostly on the lower latitudes and in our model we artificially suppress the sunspot formation at higher latitude using some masking function [Miesch and Dikpati(2014)] given as;

$$g_s(\theta) = \frac{2g_o \sin\theta\cos\theta}{1+exp[-\gamma(\theta-\pi/4)]} \qquad (\theta < \pi/2) \tag{3.5.5}$$

$$g_s(\theta) = \frac{2g_o \sin\theta\cos\theta}{1+exp[-\gamma(3*\pi/4-\theta)]} \qquad (\theta > \pi/2) \tag{3.5.6}$$

The normalization factor is g_o is

$$g_o^{-1} = Max\left\{\frac{2\sin\theta\cos\theta}{1+exp[-\gamma(3*\pi/4-\theta)]}\right\} \tag{3.5.7}$$

where the maximum is to be taken over the range from $0 < \theta < \pi/2$. Note That we will consider another masking mechanism in Chapter 5 and Chapter 6 (see Equation 6.2.2).

The next step is to suppress sunspot formation at high latitudes. Now the spot-producing toroidal field will multiply $\mathbf{B}_\phi$ with a masking function to promote spot formation at low latitudes.

$$\mathbf{B}^*(\theta,\phi,t) = g_s(\theta)|\hat{\mathbf{B}}(\theta,\phi,t)| \quad . \tag{3.5.8}$$

$$\mathbf{B}^*(\theta,\phi,t) = \frac{2g_o|\sin\theta\cos\theta|}{1+exp[-\gamma_s\theta']}|\hat{\mathbf{B}}(\theta,\phi,t)| \quad . \tag{3.5.9}$$

where $\theta' = \theta - \pi/4$ in the Northern hemisphere (NH) and $\theta' = (3 * \pi/4 - \theta$ in the Southern hemisphere (SH). Here we use $\gamma_s = 30$ and choose the normalization g_0 such that the maximum value of the masking function is unity. We refer to the maximum value of $B^*(\theta,\phi,t)$ in the Northern and Southern hemispheres respectively as $B_n^*(t)$ and $B_s^*(t)$. In order for a BMR to be produced in the Northern hemisphere (NH), $B_n^*(t)$ must exceed a threshold value, here taken to be 1 kG. Similarly for the Southern hemisphere (SH) and $B_s^*(t)$. The latitude and longitude of each BMR is chosen randomly from all horizontal grid points where $B^*(\theta,\phi,t)$ exceeds $B_n^*(t)/2$ or $B_s^*(t)/2$, depending on the hemisphere.

The observed flux content in the sunspots and the dynamo-generated strength of the radial field are chosen based on the magnetic flux in each BMR

$$\Phi = 2\Phi_0\frac{|\hat{B}(\theta_s,\phi_s,t_s)|}{B_q}\frac{10^{23}}{1+(\hat{B}(\theta_s,\phi_s.t_s)/B_q)^2}Mx \approx B_s r_s^2 \tag{3.5.10}$$

Here $\hat{B}(\theta_s,\phi_s,t_s)$ is the same as $B^*(\theta_s,\phi_s,t_s)$ but without the mask that suppresses high latitudes (see above). In short, it is the value of $B_\phi(r,\theta,\phi,t)$ taken at the location and time of the BMR (θ_s, ϕ_s, t_s), averaged over a thin radial region near the base of the CZ (0.70-0.71 R). B_q is a quenching field strength that governs the saturation of the dynamo. Here we use $B_q = 10^5$ G. Note that we don't use this in Chapter 5. This is only one of out of the three saturation mechanisms we will consider.

The parameter, Φ_0 is the amplification factor that regulates the flux budget of each BMR; determines whether the dynamo will be sub-critical or super-critical. Our ultimate aim would be to make the dynamo work with $\Phi_0 = 1$, so that the flux in a particular

BMR will have a value of 10^{23} Mx, roughly consistent with solar observetions; the field strength in the strongest active regions equivalent to the quenching field strength. But if the subsurface field at the bottom of the convection zone is not close to the quenching field, then we have to increase the value of Φ_0 in order to get a working dynamo with bigger spots.

While creating sunspot pairs by the SpotMaker algorithm, once the total flux is fixed by Equation (3.5.10), we have the freedom of selecting either the magnetic field strength or the size. We choose the magnetic field strength inside the sunspots to be 3000 G, which fixes the size. This is relation to the magnetic flux eqaution given by:

$$\Phi_S \sim A_s B_s \tag{3.5.11}$$

Typically we specify the spot strength as an input parameter $B_s = 3000\Phi_s$ G and the radius of each spot is determined by its flux content as $r_s = (\Phi_S/B_s)^{1/2}$. However, we often find it practical to set minimum and maximum values for r_s, and then adjust Bs accordingly to give the desired flux. Note that the effective spot area ($\int B_r dA/B_s$). Also, we impose a minimum size of $r_s = 16$ Mm to ensure that all BMRs are well resolved and a maximum size of $r_s = 41$ Mm for the largest spots. If the above calculation for r_s falls outside of these bounds, then r_s is set to its maximum or minimum value and B_s is re-adjusted to give the requisite flux: $B_s = r_s^{-2}\Phi_S$. Now the half distance between spots in radius is given as

$$s_r = s_a r_s \tag{3.5.12}$$

3.6 Flux Emergence and SpotMaker Algorithm

Sunspots appear when deep-seated toroidal flux ropes rise through the convective envelope and emerge at the photosphere. Assuming that they rise radially and are formed where the magnetic field is the strongest, the sunspot butterfly diagram can be interpreted as a

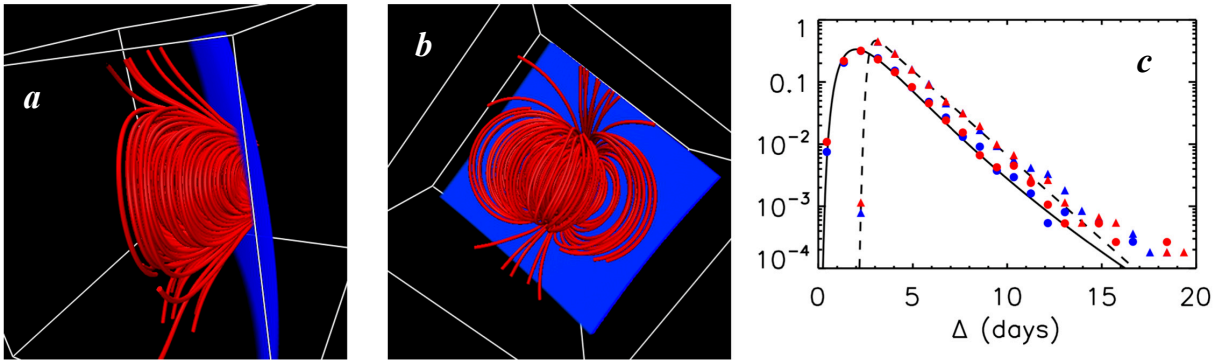

Figure 3.4: Subsurface structure of a BMR produced by SpotMaker: (a,b) Subsurface structure of a BMR produced by SpotMaker and (c) time lag pdf of emergence events. The volume rendering in frames (a) and (b) shows magnetic field lines below the solar surface (red) from two different vantage points, (a) east of the BMR looking west and (b) underneath the BMR, looking up. The blue surface represents the surface of the Sun ($r = R$). The curves in frame (c) represent the log-normal pdf (solid line, $\tau_p = 2$ days, $\tau_s = 3$ days) and the sawtooth pdf (dashed line) as given by eqs. (3.6.4) and (3.6.7). Plot symbols represent normalized histograms of the actual BMR lag times in Cases L1 (circles) and S1 (triangles), for the northern (blue) and southern (red) hemispheres.

spatio-temporal map of the Sun's internal, large-scale toroidal magnetic field component. The poloidal field generation needed to sustain the dynamo occurs as a consequence of the spot deposition algorithm.

In this algorithm, two suitable opposite-polarity spots are placed on the surface of the Sun in response to the dynamo-generated field near the base of the convection zone and then they are allowed to decay in the presence of mean flows (meridional circulation and differential rotation) and diffusivity. The first aim of this algorithm is to find out the suitable position for these spots to be placed on the surface. To do so, we calculate the mean toroidal flux B(θ, ϕ) near the bottom of the convection (see §3.5) zone averaged over the tachocline thickness and find out where this field is crossing the threshold value B_t [Miesch and Dikpati(2014),Miesch and Teweldebirhan(2016),Karak and Miesch(2017)]. A very stable location is the boundary of the convection zone with the stably stratified radiative interior of the Sun. A layer of magnetic field on this boundary becomes unstable

only at a field strength of about 10^5 G. It is believed that if magnetic fields near the bottom of the convection zone are stronger than the threshold value B_t then they become magnetically buoyant and subsequent rise to the surface is what creates the observed bipolar active regions that is the bipolar sunspots on the surface. The action of the Coriolis force on flows in the magnetic field associated with the instability produces the poloidal field of the next cycle, and is observable on surface in the form of the systematic tilt of active region axes with respect to the azimuthal direction. So the latitude and longitude of the spot pair is chosen randomly from all grid points where the mean toroidal flux exceeds B_t , subject to a mask that suppresses spots at high latitudes (see §3.5. When we are able to find the θ_s and ϕ_s where the dynamo-generated toroidal field is more than the threshold value B_t , we put two spots on the surface at that position. Once the position of the bipolar sunspots is decided, the next step is to specify the magnetic field there, by putting some tilt angle between the two sunspots according to Joy's law. For that we use the polynomial profile as given in [Miesch and Dikpati(2014)] and for tilt angle we follow the procedure given in [Stenflo and Kosovichev(2012)]. Based on solar observations we choose the tilt angle to be

$$\delta = 32.1^0 \cos\theta. \tag{3.6.1}$$

As defined above, the purpose of SpotMaker is to place bipolar magnetic regions (BMRs) on the solar surface in response to the dynamo-generated magnetic field. The subsequent evolution of these BMRs due to differential rotation, meridional circulation, and turbulent diffusion naturally generates a mean poloidal field as originally described by [Babcock(1961)] and [Leighton(1964)]. SpotMaker can be regarded as a 3D generalization of the double-ring algorithm developed by [Durney(1997)], [Nandy and Choudhuri(2001)] and [Muñoz-Jaramillo et al.(2010)]. A similar axisymmetric BMR formulation was also used by [Jiang et al.(2013)] when assimilating sunspot data into a 2D FTD model through the subsurface extrapolation of surface fields.

3.6.1 Timing of the Spot Placement

We do not want to put these spots at each time step of our simulation. There are always certain time differences between the appearances of different sunspot groups. So we have used a time delay probability density function (pdf) which allows us to put successive sunspot pairs having a random time delay between their appearances [Miesch and Teweldebirhan(2016)]. In addition to the threshold field strength, the timing of BMR creation is governed by a time delay probability density function (pdf) $P(\Delta)$, where Δ is the time that has elapsed since the last BMR creation in each hemisphere. For example, suppose that a BMR appeared in the NH at time t_0. The timing of the next emergence event (BMR creation) in the Northern Hemisphere (NH) is then given by

$$t_1 = t_0 + \Delta_n \tag{3.6.2}$$

Where Δ_n is chosen randomly based on the time delay pdf $P(\Delta)$. Like all pdf functions, we assumed that it is normalized.

$$\int_0^\infty P(\Delta) d\Delta = 1 \quad . \tag{3.6.3}$$

Similar records are kept independently for the Southern Hemisphere (SH), so the emergence events in each hemisphere are asynchronous. We consider two forms for $P(\Delta)$, illustrated in Figure 3.4*c*. The first is a lognormal pdf given by

$$P_{ln}(\Delta) = \frac{1}{\Delta\sigma\sqrt{2\pi}} \exp\left[-\frac{(\ln\Delta - \mu)^2}{2\sigma^2}\right] \quad . \tag{3.6.4}$$

In practice we specify the parameters mean and mode of the distribution, τ_s and τ_p compute as

$$\sigma^2 = (2/3)\left[\ln(\tau_s) - \ln(\tau_p)\right], \tag{3.6.5}$$

and

$$\mu = \ln\tau_p + \sigma^2 \quad . \tag{3.6.6}$$

This is similar to the time delay pdf used by MD14 but there it was implemented somewhat differently, based on the cumulative pdf.

We also consider a sawtooth pdf that can be approximated as an asymmetric stretched exponential as follows:

$$P_s(\Delta) = P_0 \exp\left[-\frac{|\Delta - \Delta_0|^{n_\pm}}{\sigma_\pm}\right] \quad , \tag{3.6.7}$$

where $n_\pm$ and $\sigma_\pm$ have different values depending on the sign of $\Delta - \Delta_0$. Here we use Δ_0 =3.1 days, $n_+ = 1$, $\sigma_+ = 1.6$ days, $n_- = 4$, $\sigma_- = 0.6$ days. P_0 is a normalization factor ensuring that

$$\int_0^\infty P_s(\Delta) d\Delta = 1 \quad . \tag{3.6.8}$$

Once the timing and location of a BMR is determined, the next step is to specify its spatial structure. This is done by defining a pair of spots on the surface, each specified by a radial magnetic field with circular cross section and a polynomial profile; (see §3.7 Equation 3.7.1). Distances on the solar surface are computed using the haversine formula. The distance between the two spots of a BMR is given by $s_a r_s$, where r_s is the radius of each spot (see Equation 3.5.12), and the trailing spot (in the sense of rotational motion) is displaced poleward relative to the leading spot at an angle that is given by Joy's Law (see Equation 3.6.1).

3.7 Surface Magnetic Field and Spot Profile

Let's decide to put a spot at position latitude θ_s and longitude, ϕ_s, and time t_s, then we to figure out how to go about it.

Start with the surface filed (radial field), which is two-dimensional (latitude, longitude) profile of the spot pair on the solar surface, B_r at the surface r = R because we know what we want this to look like. Call it $B_s(\theta, \phi)$ and write it as follows.

$$B_s = sB_0 \left[g_T(\theta, \phi) - g_L(\theta, \phi)\right] \tag{3.7.1}$$

where s is the sign of B(θ_s, ϕ_s, t_s), at the (co)latitude and longitude of the spot pair, θ_s and ϕ_s and B_0 is the field strength, we will describe it soon below, and g_T and

g_L specify the profile of the leading and trailing spots respectively. Several options have been implemented, including a Gaussian profile, an exponential profile, and a polynomial profile. The latter is the most compact, avoiding the need to loop over all horizontal indices, and is given by

$$g_L(\theta,\phi) = 1 - 3\chi_L^2 + 2\chi_L^3 \qquad (\chi_L \le 1) \tag{3.7.2}$$

$$g_T(\theta,\phi) = 1 - 3\chi_T^2 + 2\chi_T^3 \qquad (\chi_T \le 1) \tag{3.7.3}$$

$$\chi_L = \frac{\sqrt{(\theta-\theta_L)^2 + (\phi-\phi_L)^2}}{r_r} \tag{3.7.4}$$

$$\chi_T = \frac{\sqrt{(\theta-\theta_T)^2 + (\phi-\phi_T)^2}}{r_r} \tag{3.7.5}$$

$$\phi_L = \phi_s + s_r\cos(\delta) \tag{3.7.6}$$

$$\theta_L = \theta_s + s_r\sin(\delta) \tag{3.7.7}$$

$$\phi_T = \phi_s - s_r\cos(\delta) \tag{3.7.8}$$

$$\theta_T = \theta_s - s_r\sin(\delta) \tag{3.7.9}$$

where

$$s^2 r_s^2 = (\theta-\theta_L)^2 + (\phi-\phi_L)^2 \tag{3.7.10}$$

And where r_s is the angular radius of each spot (see below). A similar expression holds for g_T (θ, ϕ).

$$s^2 r_s^2 = (\theta-\theta_T)^2 + (\phi-\phi_T)^2 \tag{3.7.11}$$

3.7.1 Subsurface Structure; Potential Field Extrapolation

In §3.7 we specified the radial field of spot pair at the surface. However, this is a 3D field so we have to also specify the subsurface structure of the field. There are two limits to be considered. The first is that the spot retains connectivity to the tachocline/lower CZ after it emerges. For that we can implement a structure based on the thin flux-tube

equations. For now, let us start with the second limit, namely the case where emerging tube quickly decouples from the tachocline and is confined to the surface layers. This is both easier to implement and it more closely mimicks the Babcock-Leighton α-effect, so, its a good place to start [Miesch and Dikpati(2014)]. The simplest way to extrapolate the surface field downward is then to assume that it is potential:

$$\mathbf{B}_{spot}(r,\theta,\phi) = \boldsymbol{\nabla}\Gamma \tag{3.7.12}$$

which gives us a Laplace equation to solve

$$\boldsymbol{\nabla}^2\Gamma = 0 \tag{3.7.13}$$

It is worth noting that the function is the solution to the Laplace equation.

$$f(r,\theta,\phi) = \left(a_1 r^{\ell} + a_2 r^{-(\ell+1)}\right) Y_{\ell m}(\theta,\phi) \tag{3.7.14}$$

$$\boldsymbol{\nabla}^2 f = 0 \tag{3.7.15}$$

Therefore the solution to this is then given in terms of spherical harmonics with each mode satisfying

$$\Gamma_{\ell m}(r,\theta,\phi) = \sum_{\ell m} \left(a_{\ell m} r^{\ell} + b_{\ell m} r^{-(\ell+1)}\right) Y_{\ell m}(\theta,\phi) \tag{3.7.16}$$

To compute the constants coefficients $a_{\ell m}$ and $b_{\ell m}$ consider the radial field B_r at solar surface r = R.

$$B_r(r=R,\theta,\phi) = \frac{\partial \Gamma_{\ell m}}{\partial r} = \sum_{\ell m} \left(\ell a_{\ell m} r^{\ell-1} - (\ell+1) b_{\ell m} r^{-(\ell+2)}\right) Y_{\ell m}(\theta,\phi) \tag{3.7.17}$$

Now choose $a_{\ell m}$ and $b_{\ell m}$ such that

$$B_r = B_s(\theta,\phi) \qquad\qquad (r = R) \tag{3.7.18}$$

$$B_r = 0 \qquad\qquad (r <= r_p) \tag{3.7.19}$$

This gives

$$a_{\ell m} = \frac{R^2 B^s_{\ell m}}{\ell\left(1 - \hat{r}_s^{2\ell+1}\right)} \tag{3.7.20}$$

$$b_{\ell m} = \frac{\ell}{(\ell+1)} \hat{r}_s^{2\ell+1} a_{\ell m} \tag{3.7.21}$$

Then plug this into Equation 3.7.17 to get $B_r(\theta, \phi, r)$ and compute C as follows:

$$C = \boldsymbol{\nabla}^2 B_r = -\frac{r^2}{\ell(\ell+1)} B_r = -\sum_{\ell m} \left(\frac{a_{\ell m}}{(\ell+1)} r^{\ell+1} + \frac{b_{\ell m}}{\ell} r^{-\ell} \right) Y_{\ell m}(\theta, \phi) \qquad (\ell \neq 0). \tag{3.7.22}$$

Finally, compute $\mathbf{B}$, via equation ($\mathbf{B} = \boldsymbol{\nabla} \times (A\hat{r}) + \boldsymbol{\nabla} \times \boldsymbol{\nabla} \times (C\hat{r})$), where we assume (A =0), thus gives us

$$\mathbf{B} = -\boldsymbol{\nabla} \times \boldsymbol{\nabla} \times \left[\frac{a_{\ell m}}{(\ell+1)} r^{\ell+1} + \frac{b_{\ell m}}{\ell} r^{-\ell} \right] \tag{3.7.23}$$

Note that for simplicity we have defined this as a purely poloidal field, such that A = 0.

The subsurface structure of each spot pair is determined by means of a potential field extrapolation below the surface; (see Equation 3.7.16 Figure 3.4*a*,*b*). We realize that this is a gross approximation to the true subsurface structure of active regions but it serves to localize the BL poloidal field generation to the upper CZ, as in previous 2D FTD models [Dikpati and Gilman(2009), Charbonneau(2010), Muñoz-Jaramillo et al.(2010), Karak et al.(2014)]. The boundary conditions for this subsurface extrapolation ensure that the radial field is equal to the imposed BMR field at the surface ($r = R$) and vanishes below a specified penetration radius, $r = r_s$. The order of the Laplacian precludes further boundary conditions so the horizontal field is not necessarily zero at the surface. This nominally violates the upper boundary condition, Equation 3.4.22 but this violation is quickly corrected within a few time steps with the help of explicit and implicit (numerical) diffusion which quickly make the BMR field radial at the surface.

This initial adjustment is illustrated in Figure 3.5 for the mean (m = 0) component of $\mathbf{B}$, because this is easiest to visualize. This is from a simulation that was initiated with a single BMR at a latitude of 25° and an input parameter representing the initial penetration depth of active regions, $r_s = r_p = 0.90$R. This means that the spot field does not necessarily satisfy the outer boundary condition, often taken to either radial field. Essentially, there is an unresolved current sheet at the surface that dissipates quickly due

to resolved and numerical diffusion. This adjustment mimics the observed tendency for spot fields to become nearly vertical as they fragment and become part of the magnetic network.

The initial magnetic field is identical to that shown in Figure 3.4 a,b but here the simulation is stepped forward in time, following the evolution of the BMR as it is subject to differential rotation, meridional circulation, diffusion, and the boundary conditions. This latitude gives it a tilt angle of 13.6° according to the Joy's law expression given above, so it starts out with a nonzero mean poloidal field component (Figure 3.5*b*). As noted above, the initial field does not satisfy the radial field upper boundary condition (Figure 3.5*a*). However, after one time step (t = 0.07 days), the boundary condition is applied and the horizontal field goes to zero at the surface (Figure 3.5*a*). The turbulent diffusion and the semi-implicit timestepping ensures a smooth transition to the non-zero horizontal field in the interior. By 20 time steps (t = 1.4 days), the adjustment is complete, transitioning to a radial field for r > 0.97R (spanning $\sim$ 30 grid points; Figure3.5a, c). Note that the time step used for this simulation (0.07 days) is the same as that used for all the simulations reported in this paper. The adjustment is similar for the other field components (m > 0).

3.7.2 Flux Depletion

We close this section with a note about flux depletion, which is a more subtle issue than it may first appear. To illustrate the problem, consider the process of flux emergence, beginning with a coherent toroidal field near the base of the CZ. For simplicity we can assume that this initial toroidal field is an axisymmetric flux tube with a flux equal to Φ_s but relaxing this assumption does not change the essential arguments. Now assume that this flux tube rises and emerges, forming a BMR at the surface with an approximately

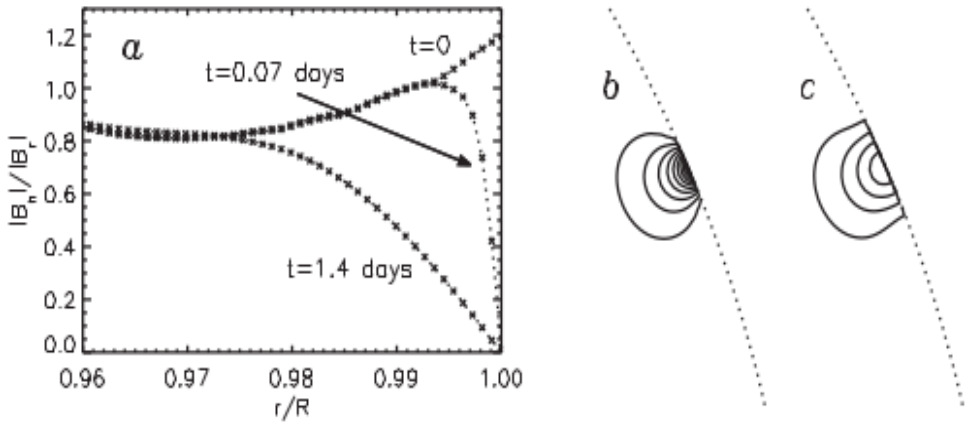

Figure 3.5: Initial BMRs emergence:
Adjustment of the mean (m = 0) field in a simulation that was initiated with a single BMR. (a) Ratio of horizontal to vertical field strength $|B_h|/|B_r|$ as a function of radius near the upper boundary. $|B_h|$ and $||B_r|$ are each averaged over the Northern hemisphere before computing this ratio. The three curves correspond to the initial field (t = 0), the field after one time step (t = 0:07 days) and the field after 20 time steps (t = 1.4 days), as indicated. Crosses represent the radial grid points. Frames (b) and (c) show the structure of the mean poloidal field at t = 0 and after 20 time steps (t = 1.4 days) respectively.

east-west orientation. Now define the toroidal flux through any meridional plane as

$$\Phi_{cut}(\phi, r_o, t) = \int_0^{\pi} \int_0^{r_o} B_\phi(r, \theta, \phi, t)\ r dr d\theta \quad . \tag{3.7.24}$$

where r_o is the outer radius of the domain in question. If we set $r_o = \infty$ and if we neglect magnetic diffusion in the flux emergence process described above, then Φ_{cut} (ϕ, ∞, t) will be independent of ϕ and t. This follows from the topological properties of **B**. Now define the emergence time as t_e and consider a longitude ϕ_b that bisects the BMR, lying between the two polarities. Again, from the topological properties of **B**, we can say that the contribution to Φ_{cut} (ϕ, ∞, t $< t_e$) from the emergent field, r < R, must be equal to Φ_S . In other words, the toroidal flux at longitude ϕ_b in the solar interior r < R is depleted by an amount Φ_S due to the emergence; Φ_{cut} (ϕ, ∞, t $< t_e$ = Φ_{cut} (ϕ, ∞, t $< t_e$ - Φ_S Now consider the mean toroidal magnetic flux threading through the computational

domain of the model

$$\Phi_{mean}(t) = \int_0^{2\pi} \int_0^{\pi} \int_0^{r_o} B_\phi(r,\theta,\phi,t)\ r dr d\theta d\phi \quad . \tag{3.7.25}$$

This will also be depleted by the emergence process. However, the amount it will be depleted will depend on the amount of the tube that has emerged, such that

$$\Phi_{mean}(t\ <\ t_e) - \Phi_S\ <\ \Phi_{mean}(t\ >\ t_e)\ <\ \Phi_{mean}(t\ <\ t_e) \quad . \tag{3.7.26}$$

This is the nature of the flux depletion problem. As stated above, our SpotMaker algorithm can be regarded as a 3D generalization of the axisymmetric double-ring algorithm described by [Nandy and Choudhuri(2001)] and [Muñoz-Jaramillo et al.(2010)]. In those and other papers, the authors take into account flux depletion by subtracting the BMR flux Φ_S from the mean toroidal flux near the base of the CZ. However, it should be noted that this corresponds to the maximum depletion limit given by Equation (3.7.26), $\Phi_{mean}(t\ >\ t_e) = \Phi_{mean}(t\ <\ t_e)\ -\ \phi_S$. This limit would only strictly apply if the entire toroidal flux tube were to pass through the solar surface. Since the presence of a BMR requires some portion of the tube to remain below the solar surface, this limit over-estimates the mean flux loss from an emergence event. So, it should be regarded as a conservative upper limit of flux depletion.

To highlight this point further, we go back to the orginal configuration of an axisymmetric toroidal flux tube with flux Φ_S. Now assume that during flux emergence, only a small segment of this tube, spanning a longitudinal range $Delta\phi$, rises and exits the CZ, leaving the rest of the tube below the surface. Then the mean toroidal flux Φ_{mean} will be depleted by an amount that is approximately equal to $\Phi_S \Delta\phi/2\pi$. Observations indicate that most BMRs have a longitudinal extent of less than 10^o ([Upton and Hathaway(2014)]), implying a mean flux depletion of less than 3% of Φ_S . Though the depletion of mean flux from the tachocline is likely more than this, much of this mean flux would be redistributed throughout the CZ and, given our incomplete understanding

of flux emergence, we currently have no reliable prescription for how best to redistribute this flux.

SpotMaker effectively selects the lower limit of mean flux depletion, $\Phi_{mean}(t > t_e) = \Phi_{mean}(t < t_e)$, which is valid if only a small segment of the tube emerges ($\Delta\phi \ll 2\pi$). Though our imposed BMR field clearly has a subsurface eastwest component ($B_\phi = 0$; see 3.4), the topological nature of the field is poloidal, so it does not change the mean toroidal field B_ϕ . However, at the longitude of emergence, the mean flux is indeed depleted in the sense that $\Phi_{cut}(\phi_b, R,\ t > t_e) = \Phi_{cut}(\phi_b, R,\ t < t_e) - \phi_S$, as described above. Unlike previous 2D FTD models, this flux depletion occurs in the upper CZ rather than the lower CZ/tachocline.

A related question is whether or not the flux emergence process conserves magnetic energy. The current SpotMaker algorithm as laid out here does not; the placement of a BMR increases the magnetic energy. If the progenitor toroidal field is re-established quickly by differential rotation, this approximation may be justified. The lifting and twisting of the field during flux emergence can also increase magnetic energy, as in alternative formulations of the Babcock-Leighton mechanism that are based on a local or non-local α-effect (the kinematic α-effect also does not conserve energy). Still, a more careful treatment of the magnetic flux budget and energetics is certainly warranted and will be pursued in the future. The idealized algorithm presented here should be considered as only a starting point, providing a baseline for comparison as we and others develop more sophisticated flux emergence models.

Chapter 4

STABLE Code Verification and Representative Dynamo Simulation

4.1 STABLE Code Verification

In this section we describe the verfications of the STABLE dynamo with a "A solar mean field dynamo benchmark" [Jouve et al.(2008)]. The ASH code has already been verified by comparing it to three other independent codes on carefully selected hydrodynamic and MHD simulations of global convection [Jones et al.(2011)]. Here we wish to verify the kinematic version of ASH that has been used as a dynamical core for STABLE. As mentioned in Chapter §3, in the special case of kinematic, axisymmetric flow fields, the axisymmetric ($m = 0$) component of the induction equation (3.2.1) decouples from the non-axisymmetric components so it behaves like a 2D FTD model. Thus, though STABLE simulations are explicitly 3D, we can legitimately verify the mean ($m = 0$) field components by comparing them with an equivalent 2D model.

The evolution of the magnetic field, $\mathbf{B}$, in response to the velocity field, $\mathbf{v}$, in kinematic MHD induction equation in a 2D, rotating,spherical shell:

$$\frac{\partial \mathbf{B}}{\partial t} = \nabla \times (\mathbf{v} \times \mathbf{B} - \eta \boldsymbol{\nabla} \times \mathbf{B}) \tag{4.1.1}$$

In mean-field dynamo theory, this is simplified (see §3.3 for further detail) to

$$\frac{\partial \mathbf{B}}{\partial t} = \boldsymbol{\nabla} \times (\mathbf{v} \times \mathbf{B} - \eta_t \boldsymbol{\nabla} \times \mathbf{B}) + \boldsymbol{\nabla} \times (\alpha \mathbf{B}) \tag{4.1.2}$$

For BL models, a surface term $S\hat{e}_\phi$ is used instead of the α-effect term $\alpha\mathbf{B}$ which is involved only in our $\alpha\Omega$ models. Without any significant loss of generality, we can focus on axisymmetric magnetic fields, i.e., fields showing symmetry with respect to an axis, usually rotational. Working in spherical polar coordinates (r, θ, ϕ) with the polar axis coinciding with the field's symmetry axis, the most general axisymmetric (now meaning $\frac{\partial}{\partial\phi} = 0$) magnetic field can be written as:

$$\mathbf{B}(r,\theta,t) = B(r,\theta,t)\hat{\mathbf{e}}_\phi + \boldsymbol{\nabla}\times[A(r,\theta,t)\hat{\mathbf{e}}_\phi] \quad . \tag{4.1.3}$$

where $\mathbf{B}$(r, θ, t)$\mathbf{e}_\phi$, is the toroidal magnetic field and $B_p = \boldsymbol{\nabla}\times[A(r,\theta,t)\mathbf{e}_\phi$, is the poloidal magnetic field. Here the vector potential component $\mathbf{A}$ defines the poloidal component of the magnetic field, $B_p = \boldsymbol{\nabla}\times[A(r,\theta,t)\mathbf{e}_\phi$ i.e., the component contained in meridional (r,θ) planes. The azimuthal component $\mathbf{B}$ is often called the toroidal field, $\mathbf{B}$(r, θ, t)$\mathbf{e}_\phi$. Equation (4.1.3) satisfies the constraint $\boldsymbol{\nabla}\cdot\mathbf{B}$ =0 by construction, and another great advantage of this mixed representation is that the MHD induction equation for the vector $\mathbf{B}$, can be separated in two equations for the scalar components A and B. Therefore, to do so, we write the mean velocity field in the following form:

$$\mathbf{v}(r,\theta,t) = \bar{\omega}\Omega(r,\theta)\hat{\mathbf{e}}_\phi + \mathbf{v}_p(r,\theta) \quad . \tag{4.1.4}$$

where $\varpi = rsin\theta$ and $\mathbf{v}_p(r,\theta) = [v_r(r,\theta)\hat{\mathbf{e}}_r + [v_\theta(r,\theta)\hat{\mathbf{e}}_\theta]$ Now, substitution of Equation 4.1.3 and 4.1.4 into 4.1.2 leads to a series of (vector) terms, some oriented in the (toroidal) $\mathbf{e}_\phi$-direction, others perpendicularly, in the (poloidal) meridional plane. The original, full induction equation can only be satisfied if the to two sub-equations defined by each sets of orthogonal terms are individually satisfied, thus defining two separate evolution equations for A and $\mathbf{B}$. For a magnetic diffusivity η depending merely on r , this poloidal/toroidal separation leads to:

$$\frac{\partial A}{\partial t} = \eta_t\left(\nabla^2 - \frac{1}{\varpi^2}\right)A - \frac{R_m}{\varpi}\mathbf{u}_p\cdot\nabla(\varpi A) + C_\alpha\alpha B + C_s S \tag{4.1.5}$$

$$\frac{\partial B}{\partial t} = \eta_t \left(\nabla^2 - \frac{1}{\varpi^2} \right) B + \frac{1}{\varpi} \frac{\partial \eta}{\partial r} \frac{\partial (\varpi B)}{\partial r} - R_m \varpi \nabla \cdot \left(\frac{B}{\varpi} \mathbf{u}_p \right) + C_\Omega \varpi (\nabla \times A \hat{e}_\phi) \cdot (\nabla \Omega)$$
$$+ C_\alpha \hat{e}_\phi \cdot \nabla \times (\alpha \nabla \times (A \hat{e}_\phi)) \quad . \tag{4.1.6}$$

where the following nondimensional numbers have materialized. The intensity of the α-effect is characterized by

$$C_\alpha = \frac{\alpha_e R}{\eta_t} \tag{4.1.7}$$

The intensity of the rotation Ω is characterized by

$$C_\Omega = \frac{\Omega_e R^2}{\eta_t} \tag{4.1.8}$$

The intensity of the meridional circula tion u_p is characterized by

$$R_m = \frac{u_e R}{\eta_t} \tag{4.1.9}$$

The intensity of the BL source term by

$$C_s = \frac{s_o R}{\eta_t} \tag{4.1.10}$$

In the critical cases, the intensity α_e of the α-effect or s_0 of the BL source term are determined by looking for the threshold for dynamo action whereas in the supercritical cases, α_e and s_0 are fixed to a value about ten times higher than the threshold. Moreover, we note that an α-effect is considered only for the regeneration of the poloidal field and not for the toroidal field so that we choose to study only $\alpha\Omega$ or Babcock-Leighton flux-transport dynamos.

with α_e (dimension m/s), and Ω_e (dimension s^{-1}) as reference values for the α-effect, meridional flow and differential rotation, respectively. Where η_t to depend on r only. Equations 4.1.5 and 4.1.6 respectively describe the evolutions of the poloidal and the toroidal magnetic fields. The terms involving v_p (or equivalently v_r, v_θ) correspond to advection by the meridional circulation, whereas the terms involving η are the diffusive

terms. In order for the fields to be sustained, we need some source terms to compensate for the diffusive terms. It is easily seen from Equation (4.1.6) that the source term for the toroidal field is $C_\Omega \varpi(\nabla \times A\hat{e}_\phi)\cdot(\nabla\Omega)$, which signifies the stretching of the poloidal field by differential rotation to produce the toroidal field. The source term for the poloidal field is the term $C_\alpha \alpha B$ in Equation 4.1.5. The physical interpretation of this term will be discussed in the next paragraph. We may point out that, on substituting Equation 4.1.3 and 4.1.4 into Equation 4.1.2, we get another source term $C_\alpha \hat{e}_\phi \cdot \nabla \times (\alpha \nabla \times (A\hat{e}_\phi))$ in Equation (4.1.6). We have neglected this source term because it is negligible compared to the source term $C_\Omega \varpi(\nabla \times A\hat{e}_\phi)\cdot(\nabla\Omega)$ in Equation (4.1.6). In the situation of strong differential rotation, which is the case for the Sun Equations 4.1.5 and 4.1.6 gives.

$$\frac{\partial A}{\partial t} = \eta\left(\nabla^2 - \frac{1}{\varpi^2}\right)A - \frac{R_m}{\varpi}\mathbf{u}_p\cdot\nabla(\varpi A) + C_\alpha \alpha B + C_s S \tag{4.1.11}$$

$$\begin{aligned}\frac{\partial B}{\partial t} &= \eta\left(\nabla^2 - \frac{1}{\varpi^2}\right)B + \frac{1}{\varpi}\frac{\partial \eta}{\partial r}\frac{\partial(\varpi B)}{\partial r} - R_m \varpi \nabla\cdot\left(\frac{B}{\varpi}\mathbf{u}_p\right) \\ &+ C_\Omega \varpi(\nabla \times A\hat{e}_\phi)\cdot(\nabla\Omega) \quad .\end{aligned} \tag{4.1.12}$$

In order to write these equations in a dimensionless form Equations (4.1.7 - 4.1.10), we used as the length scale the solar radius, R and as time scale the diffusion time, $\frac{R^2}{\eta_t}$ based on the turbulent diffusivity in the envelope $\eta_t = 10^{11}\ cm^2 s^{-1}$. When the additional source term is neglected, ($C_\alpha\alpha$, Equation 4.1.5,) and (Equation 4.1.6) constitute what is called the $\alpha\Omega$ dynamo model. The basic idea of the $\alpha\Omega$ dynamo is that the toroidal and the poloidal fields sustain each other through a feedback loop. The poloidal field can be stretched by the differential rotation to produce the toroidal field, as we see from the source term in Equation 4.1.6. In order to complete the loop, we need a mechanism to generate the poloidal field from the toroidal field. This is formally achieved by the term $C_\alpha\alpha$ in Equation 4.1.5. The term $C_\alpha\alpha$ in Equation 4.1.5 in the present scenario has the significance that the helical turbulence acting on the toroidal field gives rise to the poloidal

field. This is known as the α-effect. The α-effect, however, is possible only if the energy density of the toroidal magnetic field is less than the energy density of turbulence so that the turbulent motions are able to twist the magnetic field. For physical conditions within the solar convection zone, this means that the toroidal magnetic field has to be weaker than 10^4 G. Now we come to the second school of thought due to Babcock-Leighton proces. The bipolar sunspots appear on the solar surface with tilts given by Joy's law. When a tilted bipolar sunspot decays, the two polarities preferentially diffuse around in slightly different latitudes. This gives rise to a dipole moment. Since the bipolar sunspots form from the toroidal field, the net effect of this process is that the toroidal field gets converted into the poloidal field. This process is also phenomenologically described by the term $C_\alpha \alpha$ in Equation 4.1.5 with α concentrated near the solar surface, since the Babcock-Leighton (BL) process takes place near the surface (see Chapter 3 for more details). Although both the α-effect and the BL process are represented in the same way in the kinematic dynamo equations, their physical interpretations are quite different. For example, the coefficient α describing the BL process is given by the tilts and separations of the bipolar sunspots [Jouve et al.(2008), Karak et al.(2014)].

To perform this verification, we consider the 2D FTD benchmark simulations defined by [Jouve et al.(2008)]. Specifically, we seek to reproduce their case SC$'$, which is an FTD model in which the source term for the mean poloidal field is a non-local α-effect intended to mimic the BL mechanism. Thus, for the purpose of verification, we replace the BMR deposition algorithm described in (§3.6) with an explicit poloidal source term as defined in Equation 4.1.13 of [Jouve et al.(2008)], in fact in BL flux-transport dynamo models, the poloidal field owes its origin to the twist of magnetic loops emerging at the solar surface. Thus, the source has to be confined to a thin layer just below the surface and since the process is fundamentally non-local, the source term depends on the variation of toroidal field B_ϕ at the base of the convection zone.

$$S(r,\theta,t,B_\phi) = \frac{1}{2}\left[1+\text{erf}\left(\frac{r-r_{bm}}{d_{bm}}\right)\right]\ \frac{1}{2}\left[\ 1-\text{erf}\left(\frac{r-R}{d_{bm}}\right)\right]$$
$$\left[1+\left(\frac{B_\phi(r_c,\theta,t)}{B_0}\right)^2\right]^{-1}\cos\theta\sin\theta\ B_\phi(r_c,\theta,t) \quad . \tag{4.1.13}$$

where $r_{bm} = 0.95R$, $d_{bm} = 0.01R$ and $r_c = 0.7R$, as above. The resulting plot profile for $S(r,\theta,t,B_\phi)$ is illustrated in Figure 4.1. This is implemented by adding a term to the right-hand-side of eq. (3.2.1) of the form $\boldsymbol{\nabla}\times\left(S\hat{\boldsymbol{\phi}}\right)$, gives the form.

$$\frac{\partial \mathbf{B}}{\partial t} = \boldsymbol{\nabla}\times(\mathbf{v}\times\mathbf{B} - \eta_t\boldsymbol{\nabla}\times\mathbf{B}) + \boldsymbol{\nabla}\times\left(S\hat{\boldsymbol{\phi}}\right) \tag{4.1.14}$$

Note that the presence of the quenching term involving B_0 provides a saturation mechanism for the dynamo, preventing the magnetic energy from growing exponentially without bound. Here we use $B_0 = 2\times10^5$ G. We also replace the velocity field and turbulent diffusion in Equations (3.4.13), (3.4.5), and (3.4.19) with the corresponding expressions Equation (4.1.16), (4.1.18), and (4.1.17) as described in [Jouve et al.(2008)].

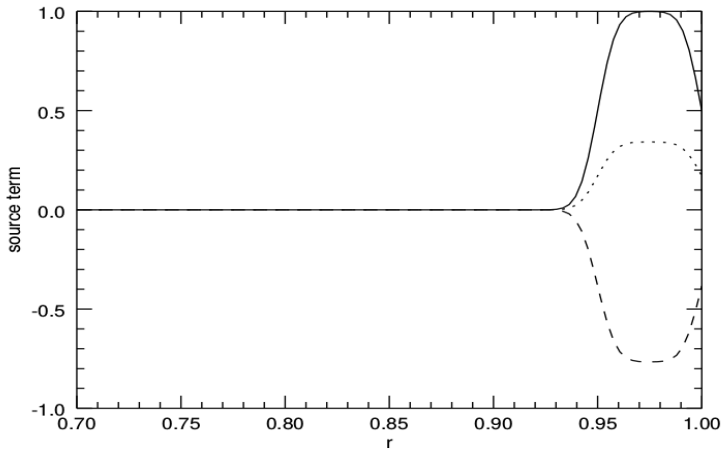

Figure 4.1: Babcock-Leighton source term for the benchmark
Case SC′, replaces the SpotMaker algorithm in STABLE [Jouve et al.(2008)]. The solid curve is with 45 degree, dashed curve is with 25 degree and dotted curve is with 10 degree.

Verification of STABLE dynamo model reproduces most of features produced by solar

dynamo models described in the [Jouve et al.(2008)]. Equation is hydromagnetic induction equation, governing the evolution of the magnetic field **B**, in response to advection by a flow field **v**, and resistive dissipation due to the microscopic magnetic diffusivity η (Equation 4.1.17). This is a kinematic approach, in which the velocity field is given, so we express velocity fields as:

$$\mathbf{v}_p = \tilde{\rho}(r)^{-1}\ \boldsymbol{\nabla}\times\left[\psi(r,\theta)\hat{\boldsymbol{\phi}}\right] + \lambda\Omega(r,\theta)\hat{\boldsymbol{\phi}} \tag{4.1.15}$$

Here $\psi(r,\theta)$, the stream function for the meridional mass flux is represented by Equation 4.1.18, $\tilde{\rho}(r)$ is the dimensionless density stratification which is given Equation 4.1.22 , $\lambda = r\sin\theta$ is the moment arm(cylinderical radius), and the differential rotation, $\Omega(r,\theta)$ is given by Equation 4.1.16. The rotation profile captures some realistic aspects of the Sun's angular velocity, deduced from helioseismic inversions, assuming a solid rotation below 0.65R and a differential rotation above the interface([Jouve et al.(2008)]).

$$\Omega(r,\theta) = \Omega_c + \frac{1}{2}\left[1 + erf(\frac{r-rc}{d})\right](1 - \Omega_c - c_2\cos^2\theta) \tag{4.1.16}$$

Here we use $\Omega_c = .92$ nHz, $c_2 = 0.2$ nHz, $r_c = 0.7R$, and $d = 0.02R$, where R is the solar radius. The resulting profile is illustrated in Figure 3.2a. with this profile the radial shear is maximal at the tachocline.

We assume that the diffusivity in the envelope η is dominated by its turbulent contribution whereas in the stable interior $\eta_c << \eta_t$. We smoothly match the two different constant values with an error function which enables us to quickly and continuously transit from η_c to η_t i.e.

$$\eta(r) = \frac{\eta_c}{\eta_t} + \frac{1}{2}\left(1 - \frac{\eta_c}{\eta_t}\right)\left[1 + erf(\frac{r-rc}{d})\right] \tag{4.1.17}$$

Here we use $\eta_c = 10^9\ \ cm^2s^{-1}$, $\eta_t = = 10^{11}\ cm^2s^{-1}$. The resulting plot profile for η is illustrated in Figure 4.2.

In these BL flux-transport dynamo models, the meridional circulation (MC) is introduced as one large single cell per hemisphere directed poleward at the surface, in

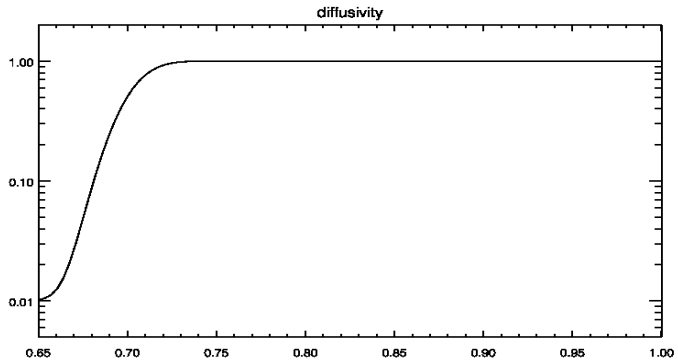

Figure 4.2: Tubulent diffusivity profile for the benchmark
Case SC′ used for the verfication simulation relative to [Jouve et al.(2008)] completed with STABLE. This plot is as a function of η (cm^2/s) versus radius.

accordance with solar observations and is used to link the two sources of the magnetic field namely the base of the CZ and the solar surface. For its profile, we use a large single cell per hemisphere, directed poleward at the surface, vanishing at the bottom boundary r = 0.65R and thus penetrating a little below the tachocline. We take a stream function of the form.

$$\psi(r,\theta) = -\frac{2}{\pi}\frac{(r-r_b)^2}{(1-r_b)}\sin\left(\pi\frac{r-r_b}{1-r_b}\right)\cos\theta\sin\theta \quad . \tag{4.1.18}$$

The comeponents of the meridional flow are then given by relation

$$\mathbf{v}_P = \boldsymbol{\nabla}\times(\psi(r,\theta)\hat{\boldsymbol{\phi}}) \quad . \tag{4.1.19}$$

The resulting expressions are

$$u_r = -\frac{2(1-r_b)}{\pi}\frac{(r-r_b)^2}{(1-r_b)^2}\sin\left(\pi\frac{r-r_b}{1-r_b}\right)(3\cos^2\theta-1) \quad . \tag{4.1.20}$$

$$u_\theta = \left[\frac{3r-r_b}{1-r_b}\sin\left(\pi\frac{r-r_b}{1-r_b}\right) + \frac{r\pi}{(1-r_b)}\frac{(r-r_b)}{(1-r_b)}\cos\left(\pi\frac{r-r_b}{1-r_b}\right)\right]$$
$$\frac{2(1-r_b)}{(r\pi)}\frac{(r-r_b)}{(1-r_b)}\cos\theta\sin\theta \quad . \tag{4.1.21}$$

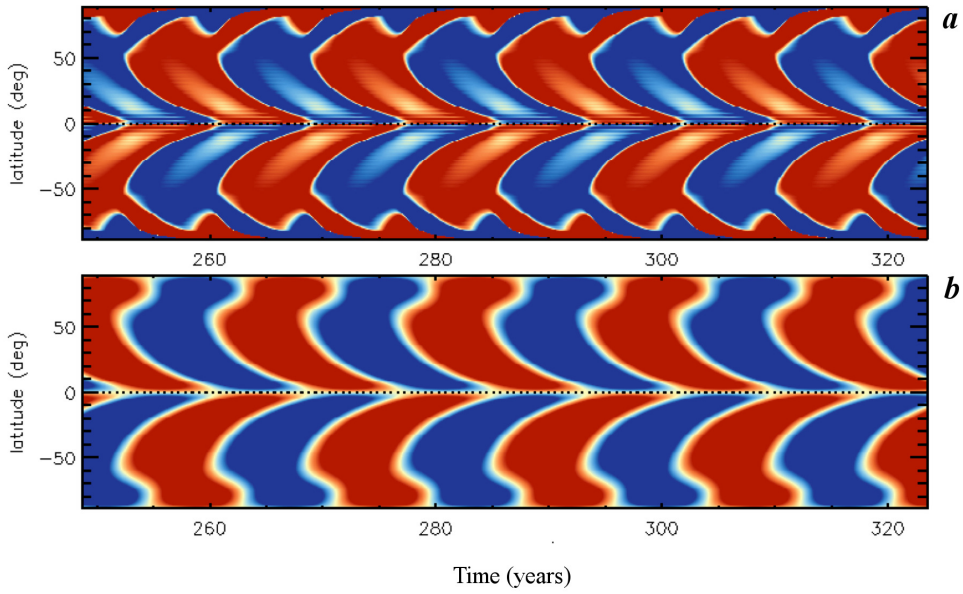

Figure 4.3: Butterfly diagram for the benchmark;

Case SC′ of [Jouve et al.(2008)] complete by STABLE. (a) Mean radial field $\langle B_r \rangle$ at the surface ($r = R$) as a function of latitude and time. Blue and red denote inward and outward polarity respectively. (b) Mean toroidal field $\langle B_\phi \rangle$ near the base of the convection zone ($r = 0.70R$; blue westward, red eastward). Compare with Fig. 14 in [Jouve et al.(2008)].

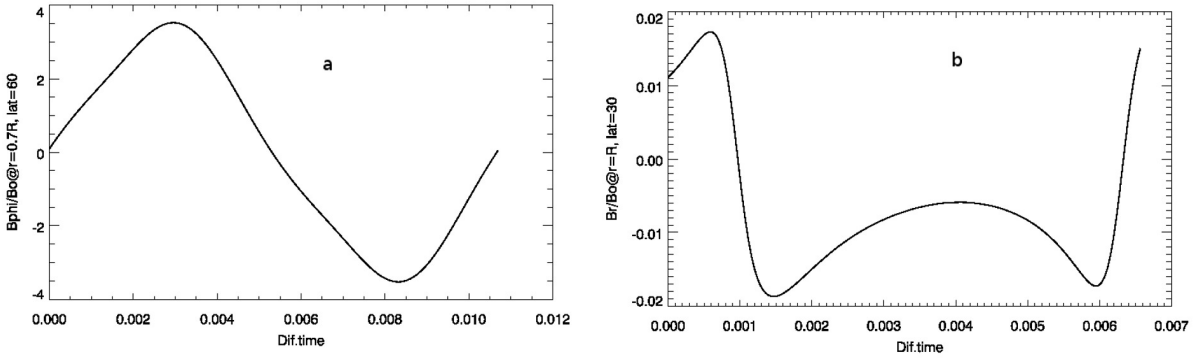

Figure 4.4: Quantitative results for benchmark;
Case SC′ of [Jouve et al.(2008)]. (a) Mean toroidal field $\langle B_\phi \rangle$, normalized by B_0, at $r = 0.7R$ and latitude = 60°. The abscissa is the nondimensional diffusion time $\tau_d = (t - t_0)\eta_0 R^{-2}$, where $\eta_0 = 10^{11}$ cm^2 s^{-1} and t_0 is chosen such that the phase of the cycle corresponds with Fig. 15 in [Jouve et al.(2008)]. (b) Normalized mean radial field $\langle B_r \rangle / B_0$ as a function of τ_d at $r = R$ and latitude = 30°. Compare with Fig. 15 in [Jouve et al.(2008)].

Here we use a nondimensional radius based on a length scale $L = 1.09 \times 10^{10}$ cm. The parameters we use here are as follows: $\psi_0 = 4.32 \times 10^{13}$ cm^2 s^{-1}, $\theta_0 = 0$, $r_b = 0.65$.

The nondimensional density stratification is given by

$$\tilde{\rho}(r) = \left(\frac{R_0}{r} - 0.97 \right)^{3/2} \tag{4.1.22}$$

The resulting contour plot profile for $\psi(r, \theta)$ in Equation 4.1.18, yields a single meridional circulation cell per hemisphere, qualitatively similar to Figure 3.2b, directed poleward at the surface, equatorward near the base of the CZ, and vanishing at the bottom boundary $r_b = 0.65$. Thus, it extends a little below the tachocline, which is centered at $r_c = 0.7R$. The boundary conditions are as described in Chapter 3 §3.4.4; perfectly conducting at the bottom of the shell and radial field at the top. For this benchmark, we use a resolution of $N_\theta, N_\phi, N_r = 128, 256, 100$.

We verified the STABLE model by reproducing a 2D mean-field benchmark and this

model, now reproduces some basic features of the solar cycle including an 11 yr periodicity, equatorward migration of toroidal flux in the deep convection zone, and poleward propagation of poloidal flux at the surface. The poleward-propagating surface flux originates as trailing flux in BMRs, migrates poleward in multiple axisymmetric streams, due to differential rotation and turbulent diffusion, eventually reverses the polar field, thus sustaining the dynamo.

Results are shown in Figures 4.3 and 4.4. These agree well both qualitatively and quantitatively with the results presented in [Jouve et al.(2008)] for eight independent codes. Note that this simulation is performed in 3D but the fields remain axisymmetric due to the nature of the poloidal source; ME_{nax} as defined in §4.2.1 is zero. We consider this a successful verification of the kinematic STABLE model.

4.2 A Representative Dynamo Simulation

Note that the results and discussions presented here in §4.2 and §4.3 are with an explicit sunspots emergence at the solar photosphere using the SpotMaker algorithm in §3.6. These BMRS are not proxy of toroidal flux at the base of the CZ. The Model ingredients for these results such as meridional circulation, differential rotation and turbulent diffusivity are given in Chapter 3 in Equations (3.4.1), (3.4.2) and (3.4.3) respectively. Illustrative results from a typical STABLE dynamo simulation are shown in Figures 4.5–4.8. These are all from Case S1, with parameters summarized in Table 4.1. These and other parameters are defined in Chapter 3 and will be discussed further in §4.3. Here we give a general overview of the self-sustained dynamo solutions achieved with STABLE. Like the other simulations described in §4.3, this case was done with a resolution of $N_\theta, N_\phi, N_r = 512$, 1024, 340.

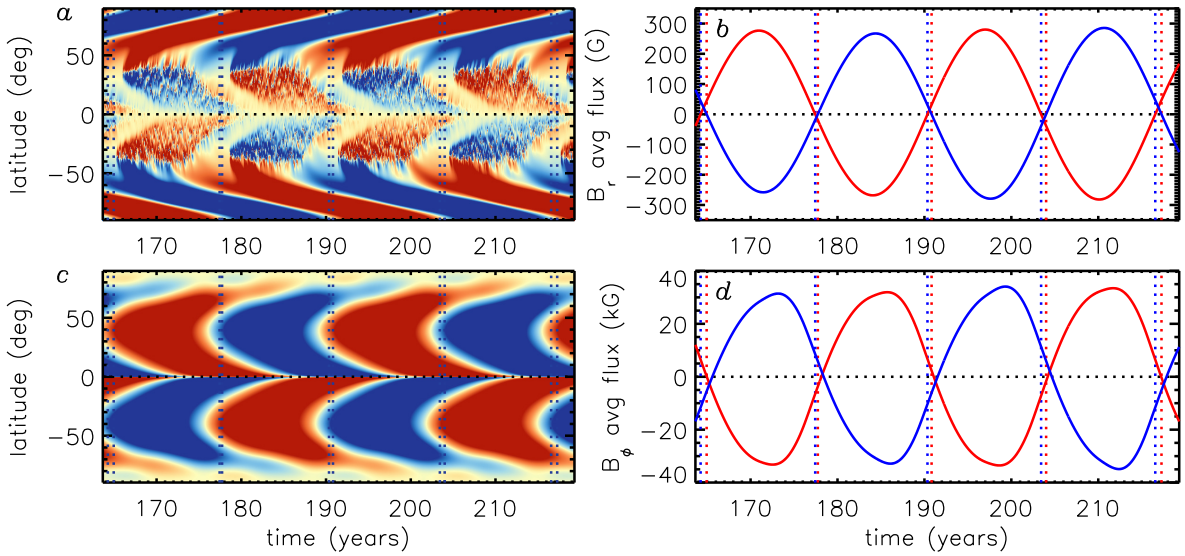

Figure 4.5: Magnetic cycles in Case S1;

(a) $\langle B_r \rangle$ at the surface ($r = R$) as a function of latitude and time, highlighting four magnetic cycles. Red and blue denote outward and inward field respectively. Peak amplitudes can exceed 300 G but the color table saturates at ± 100G. (b) $\langle B_r \rangle$ averaged over the North (blue) and South (red) polar regions, above a latitude of ± 85°. Vertical dotted lines in this and all other frames mark polar field reversals in the NH (blue) and SH (red). Frames (c) and (d) are similar to frames (a) and (b) but for $\langle B_\phi \rangle$ in the lower CZ ($r = 0.71R$). However, the averages in (d) are over the entire NH (blue) and SH (red), as opposed to just the polar regions. Red and blue in (c) denote eastward and westward field respectively, with a saturation level for the color table of 50 kG.

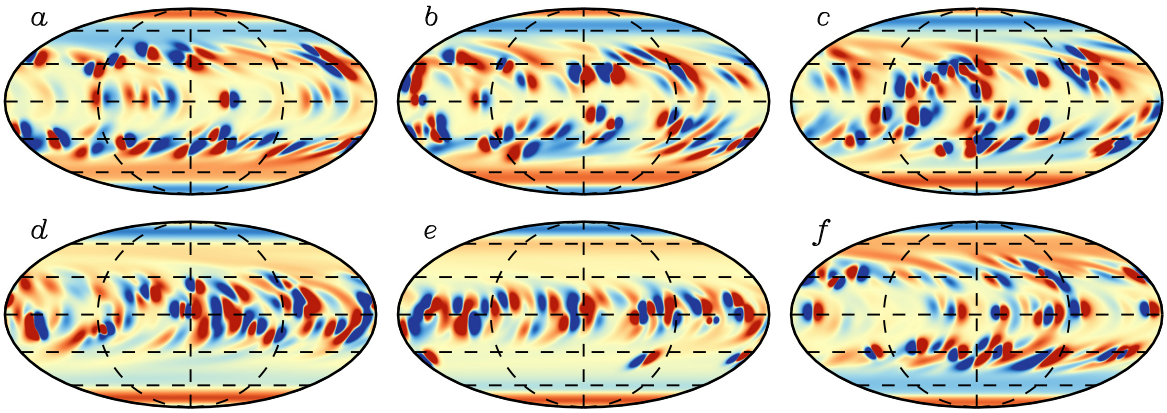

Figure 4.6: Radial magnetic field B_r at the solar surface ($r = R$) in case S1; plotted in Molleweide projection. Dashed lines denote latitudes of 0°, ±30°, and ±60°. Six snapshots are shown, spanning one magnetic cycle: $t =$ (a) 181.0 (b) 183.6, (c) 186.2, (d) 188.9, (e) 191.5, and (f) 194.1 years. Red and blue denote radially outward and inward field respectively, with a saturation level on the color table of ± 500 G.

4.2.1 Overview of Cycle Characteristics

The magnetic cycles are perhaps best demonstrated by the butterfly diagrams in Figs. 4.5a and b. These show the mean (longitudinally-averaged) radial and toroidal field $\langle B_r \rangle$ and $\langle B_\phi \rangle$ at $r = R$ and $r = 0.71R$ respectively for the Northern hemisphere (NH) and Southern hemisphere (SH). Throughout this thesis, angular brackets denote averages over longitude. Also shown in Fig. 4.5 are the time evolution of the (b) polar flux and (d) mean toroidal magnetic flux in each hemisphere, expressed here as an average field strength. Polar field reversals are marked with vertical dotted lines.

As in all advection-dominated FTD models, the equatorward migration of toroidal field at low latitudes in Fig. 4.5c can be attributed to the equatorward meridional circulation near the base of the CZ. This deep-seated toroidal field is often used as a proxy for sunspots but there is no need for such a proxy with STABLE; BMRs appear at the surface explicitly, and migrate equatorward over the course of the cycle (Fig. 4.5a) along with the subsurface $\langle B_\phi \rangle$. The distortion and dispersal of these tilted (Joy's law) BMRs

by differential rotation, meridional circulation, and turbulent diffusion gives rise to a poleward migration of trailing flux that reverses the polar fields (Fig. 4.5*a*), as described by the BL mechanism (Chapter 3).

A conspicuous shortcoming of this model (to trained eyes) is the time it takes for mid-latitude flux to migrate poleward and reverse the polar fields, which we'll refer to as τ_m. In this model, τ_m spans over a decade whereas in the Sun it takes only a few years (e.g. [Hathaway(2010)]). This can be attributed to the imposed meridional flow, which was originally devised to investigate the impact of high-latitude counter-cells, with diverging flows near the poles [Dikpati et al.(2010)]. Thus, the speed of the poleward MC at high latitudes is slower than in some other FTD and SFT models [Dikpati and Gilman(2009), Charbonneau(2010), Karak et al.(2014), Upton and Hathaway(2014)]. We have confirmed that the use of different MC profiles can substantially reduce τ_m and thus eliminate this apparent shortcoming of the model (see Chapters 5 and 6). See results presented in [Karak and Miesch(2017)]. We have also confirmed that τ_m is insensitive to the magnitude of the turbulent diffusion at the surface, η_{top}. Simulations with both higher (not shown here) and lower (see cases L2 and L3 in §4.3) values of η_{top} exhibit similar migration time scales τ_m (see Fig. 4.12). Another apparent shortcoming of the model is the relatively strong polar fields (Fig. 4.5*b*). This can be corrected by reducing the parameter Φ_0; see §4.3.

It is interesting to note that the time evolution of the polar fields (Fig. 4.5*b*) is nearly sinusoidal whereas the toroidal flux is more asymmetric, with a slower rise and faster decay. Note also the slight phase difference between the northern and southern hemispheres. Though this often persists for several cycles, the dynamo sporadically re-synchronizes, maintaining a dipolar parity (see Fig. 4.8*a*). We emphasize again (see Chapter 3) that the spot deposition in each hemisphere is asynchronous and that the build-up of the dipole moment is cumulative, with contributions from multiple active regions. So, the cross-equator cancellation of surface B_r that regulates the polar field strength [Cameron

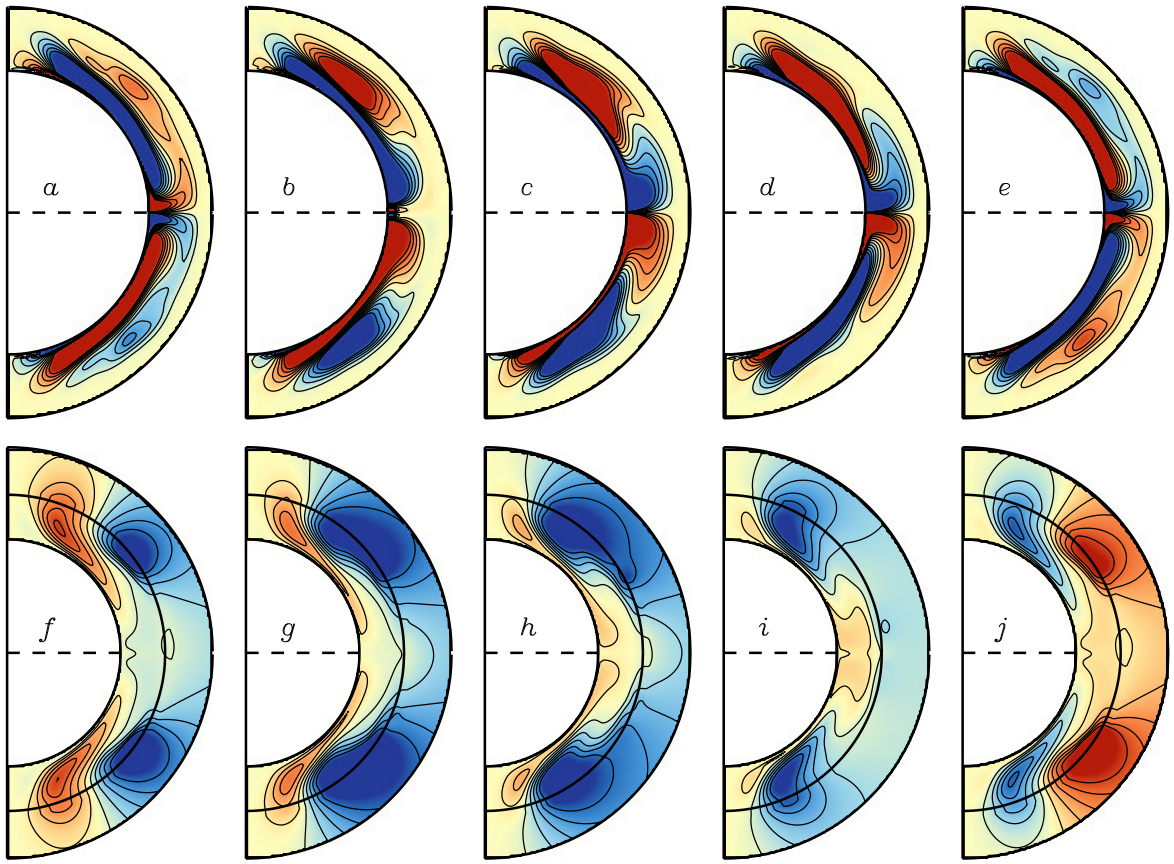

Figure 4.7: Mean toroidal and poloidal magnetic fields:

Mean (a-e) toroidal and (f-j) poloidal magnetic fields in case S1. Five snapshots are shown, spanning the same magnetic cycle as in Fig. 4.6: t = (a,f) 181.0, (b,g) 184.3, (c,h) 187.5, (d,i) 190.8, (e,j) 194.1 years. Frames (a-e) show $\langle B_\phi \rangle$, with red and blue indicating eastward and westward field respectively. Peak field strengths can exceed 100 kG but the color table is clipped at $\pm$ 20 kG. Frames (f-g) show the poloidal magnetic potential with a potential-field extrapolation above $r = R$ (to $r = 1.25R$). Red and blue denote clockwise and counter-clockwise field respectively, with peak values of $\langle B_r \rangle$ on the order of 800 G.

et al.(2013)] occurs only in an integrated sense, involving residual flux from many BMRs as in the Sun. This is the origin of the north-south asymmetry.

Figure 4.6 shows the evolution of the surface fields over the course of a magnetic cycle. A close look at each of these snapshots reveals multiple BMRs, in various stages of evolution. Localized, newly formed BMRs obey Joy's Law (increasing tilt with latitude; see §3.6) by construction and Hale's law (oppose orientation in the NH and SH) by virtue of the dipolar nature of the dynamo mode. Axisymmetric bands of radial field at high latitude arise from the distortion and dispersal of tilted BMRs and they migrate poleward due mainly to the MC. A brief cycle overlap can be discerned in Fig. 4.6*e*, which shows several BMRs with positive (red) leading polarity at a latitude of about -35° coexisting with several other BMRs near the equator with negative (blue) leading polarity. Note also the asymmetry apparent in this same Figure: spots for the new cycle appear at mid-latitudes in the SH slightly before they appear in the NH (see also Fig. 4.5*a*). The evolution of the mean (longitudinally-averaged) fields during this same magnetic cycle is shown in Fig. 4.7.

Most of the magnetic energy (over 99%) is in the mean toroidal field, ME_{tor}, which varies by about 15% over the course of a cycle. This is demonstrated in Fig. 4.8*a* (see also 4.1), which shows the evolution of the total magnetic energy in the mean and non-axisymmetric fields. Interestingly, the minima of the poloidal magnetic energy ME_{pol} do not coincide with the reversals of the polar fields at the surface. Rather, they occur slightly after. Meanwhile, the polar field reversals occur near the maxima of ME_{tor}, though slightly after, by about 0.5 to 1.5 years. This is suggestive of solar observations in which the poloidal field reversals occur near sunspot maximum. However, in the STABLE model, the magnetic energy in BMRs is reflected mainly by the non-axisymmetric field components, ME_{nax}, which reaches a (global) minimum as the polar fields at the surface are reversing. This is also reflected by the butterfly diagram in Fig. 4.5*a*, which suggests that polar fields reverse near a time of minimum sunspot activity. Thus, the phasing of

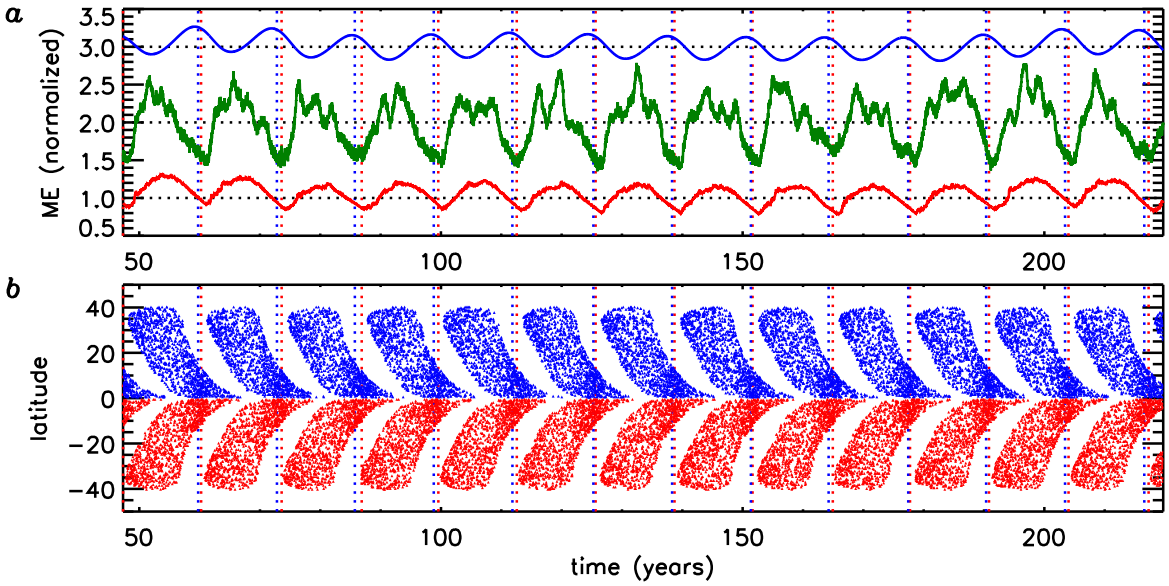

Figure 4.8: Magnetic energy

(a) Total magnetic energy in the mean toroidal field, ME_{tor} (blue), the mean poloidal field ME_{pol} (red), and the non-axisymmetric field components ME_{nax} (green) over a time interval spanning 172 years. All quantities are integrated over the entire computational volume (which spans the entire CZ) and normalized for clarity in plotting. Normalization factors are 1.15×10^{43} erg for ME_{tor}, 1.24×10^{40} erg for ME_{nax}, and 1.49×10^{39} erg for ME_{pol}. After normalization, we added one to the ME_{nax} curve and two to the ME_{tor} curve in order to plot all three curves with minimal overlap. Thus, the mean values for the normalized ME_{tor}, ME_{nax} and ME_{pol} curves are 3, 2, and 1 respectively, as indicated by the black dotted lines. (b) Latitudinal positions of the BMR deposition sites in the NH (blue) and SH (red) over the same time interval. Over this interval, 14,452 BMRs were introduced in the NH and 14,411 BMRs were introduced in the SH. Blue and red vertical dotted lines indicated reversal of the polar fields as in Fig. 4.5.

toroidal and poloidal fields is not in good agreement with solar observations. However, it is likely that this aspect of the simulations will improve as we implement different MC profiles that more faithfully capture the poleward migration time scale of trailing magnetic flux τ_m (see Chapters 5 and 6 for more detail on this). See the discussion above in connection with Fig. 4.5.

It is also interesting to note that the evolution of ME_{nax} over the course of a cycle is asymmetric, with a fast rise and a slow decline. This is similar to the observed evolution of the solar sunspot number [Hathaway(2010)] but it's opposite to the asymmetry noted above with regard to the integrated toroidal flux in Fig. 4.5*d*. Dynamo models often use the subsurface toroidal flux as a proxy for the sunspot number. The differences noted here even for an idealized FTD model such as STABLE suggest that this proxy may not be as reliable as is often assumed. Also, the distribution of the radial field at any instant quickly spreads beyond the emergence sites of BMRs. This can be seen by comparing the butterfly diagram in Fig. 4.5*a* with the actual emergence latitudes in Fig. 4.8*b*. Note that the corresponding longitudinal locations of the emergent BMRs are random.

4.2.2 The Role of Surface Fields in Dynamo Operation

From the perspective of space weather/space climate forecasting, one of the beneficial aspects of FTD models is the disproportionate role that surface magnetism plays in the operation of the dynamo.[1] If the main source of poloidal magnetic flux is indeed the BL mechanism, then we can observe this occurring and we can use this information to help forecast future magnetic activity, and sustain the dynamo. More generally, the generation of the toroidal flux in each hemisphere that is responsible for producing BMRs appears to be linked to the shearing by differential rotation and amplification of the observed

[1]By disproportionate we do not mean to imply that subsurface fields are not important; they are of course essential to sustain the dynamo. We merely mean that surface fields appear to play a greater role in the dynamo than might be expected given their contribution to the total magnetic energy in the CZ and tachocline, which is thought to be relatively small.

poloidal flux that passes through the solar surface. This was demonstrated recently by [Cameron and Schüssler(2015)], hereafter CS15.

$$\frac{\partial \mathbf{B}}{\partial t} = \boldsymbol{\nabla}\times(\mathbf{v}\times\mathbf{B} - \eta\boldsymbol{\nabla}\times\mathbf{B} + \alpha\mathbf{B} - \eta_t\boldsymbol{\nabla}\times\mathbf{B} + \gamma\times\mathbf{B}) \tag{4.2.1}$$

$$\mathbf{v}\times\mathbf{B} = (\mathbf{v}_\theta\mathbf{B}_\phi - \mathbf{v}_\phi\mathbf{B}_\theta)\hat{\boldsymbol{r}} + (\mathbf{v}_\phi\mathbf{B}_r - \mathbf{v}_r\mathbf{B}_\phi)\hat{\boldsymbol{\theta}} + (\mathbf{v}_r\mathbf{B}_\theta - \mathbf{v}_\theta\mathbf{B}_r)\hat{\boldsymbol{\phi}} \tag{4.2.2}$$

$$\frac{\partial \mathbf{B}}{\partial t} = \boldsymbol{\nabla}\times\mathbf{Q} = \boldsymbol{\nabla}\times(\mathbf{Q}_{DR} + \mathbf{Q}_{MC} + \mathbf{Q}_{NA} + \mathbf{Q}_{TD}) \tag{4.2.3}$$

$$\mathbf{Q}_{DR} = (\mathbf{B}_r\hat{\boldsymbol{\theta}} - \mathbf{B}_\theta\hat{\boldsymbol{r}})\mathbf{v}_\phi \tag{4.2.4}$$

$$\mathbf{Q}_{MC} = \mathbf{v}_\theta\mathbf{B}_\phi\hat{\boldsymbol{r}} - \mathbf{v}_r\mathbf{B}_\phi\hat{\boldsymbol{\theta}} + (\mathbf{v}_r\mathbf{B}_\theta - \mathbf{v}_\theta\mathbf{B}_r)\hat{\boldsymbol{\phi}} \tag{4.2.5}$$

$$\mathbf{Q}_{NA} = \alpha\mathbf{B} + \gamma\times\mathbf{B} = \gamma\times\mathbf{B} \tag{4.2.6}$$

$$\mathbf{Q}_{TD} = -(\eta + \eta_t)\boldsymbol{\nabla}\times\mathbf{B} = -\eta_t\boldsymbol{\nabla}\times\mathbf{B} \tag{4.2.7}$$

where $\mathbf{B}(r,\theta,\phi,t)$ and $\mathbf{v}(r,\theta)$, which is axisymmetric are the ϕ-averaged magnetic field and plasma velocity, respectively, and η_t is the magnetic turbulent diffusivity as usual.

We define the contour $d\boldsymbol{\mathcal{S}}$ enclosing the area $\mathcal{S}$ in a meridional plane of the Sun as shown in (Figure 4.9). The direction of the contour is chosen such that the vectorial surface element of $\mathcal{S}$ points into the direction of positive azimuthal field, $\mathbf{B}_\phi$.

The analysis performed by CS15 begins by averaging the longitudinal (ϕ) component of the MHD magnetic induction equation and applying Stokes theorem to the integral of the induction equation over $\mathcal{S}$ yields the time derivative of the net toroidal flux, Φ_{NH}, in the northern hemisphere of the convection zone. If the velocity field is assumed to be axisymmetric, as it is here 3.4.18, this procedure yields the following expression for the evolution of the mean toroidal flux through the NH

$$\begin{aligned}\frac{d}{dt}\int_{\mathcal{S}}\mathbf{B}\cdot d\boldsymbol{\mathcal{S}} &= \frac{d\Phi_{NH}}{dt} = \int_{\mathcal{S}}\boldsymbol{\nabla}\times\left[\mathbf{v}\times\mathbf{B} - \eta_t\boldsymbol{\nabla}\times\mathbf{B}\right]\cdot d\boldsymbol{\mathcal{S}} \\ &= \int_{\delta\mathcal{S}}\left[\mathbf{v}\times\mathbf{B} - \eta_t\boldsymbol{\nabla}\times\mathbf{B}\right]\cdot d\boldsymbol{\ell}\end{aligned} \tag{4.2.8}$$

where

$$\Phi_{NH}(t) = \int_0^{\pi/2}\int_{r_1}^{r_2} B_\phi\, r dr d\theta \equiv \int_{\mathcal{S}}\mathbf{B}\cdot d\boldsymbol{\mathcal{S}} \quad . \tag{4.2.9}$$

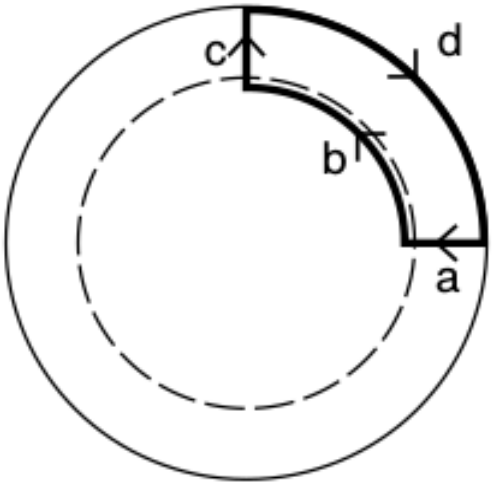

Figure 4.9: Schematic representation of the contour line to calculate torodila flux
Integration contour for the application of Stokes' theorem. The contour (thick solid line) on a meridional plane of the Sun is used to calculate the net toroidal flux in the northern hemisphere generated by the action of differential rotation on the poloidal field. The thin solid curve represents the solar surface, the dashed curve the bottom of the convection zone. The rotation poles are at the top and bottom. The contour consists of a radial segment in the equatorial plane (a), a circular arc slightly below the bottom of the convection zone (b), a part along the axis of rotation (c), and the solar surface (d) [Cameron and Schüssler(2015)].

where $d\boldsymbol{\mathcal{S}}$ is the surface element of $\mathcal{S}$ and $d\boldsymbol{\ell}$ is the line element along $\delta\boldsymbol{\mathcal{S}}$. An analoguous procedure provides the net toroidal flux in the southern hemisphere, Φ_{SH}, is

$$\begin{aligned} \frac{d\Phi_{SH}}{dt} &= \int_{\mathcal{S}} \boldsymbol{\nabla}\times\left[\mathbf{v}\times\mathbf{B} - \eta_t \boldsymbol{\nabla}\times\mathbf{B}\right]\cdot d\boldsymbol{\mathcal{S}} \\ &= \int_{\delta\mathcal{S}} \left[\mathbf{v}\times\mathbf{B} - \eta_t \boldsymbol{\nabla}\times\mathbf{B}\right]\cdot d\boldsymbol{\ell} \end{aligned} \tag{4.2.10}$$

where

$$\Phi_{SH}(t) = \int_0^{\pi/2}\int_{r_1}^{r_2} B_\phi \; r dr d\theta \equiv \int_{\mathcal{S}} \mathbf{B}\cdot d\boldsymbol{\mathcal{S}} \quad . \tag{4.2.11}$$

In eq. (4.2.8), $d\boldsymbol{\ell}$ denotes a differential segment of the closed, clockwise, linear circuit $\delta\mathcal{S}$ that encircles the NH, proceeding radially outward at the north pole, equatorward at the solar surface, inward at the equator, and poleward just below the base of the CZ. This

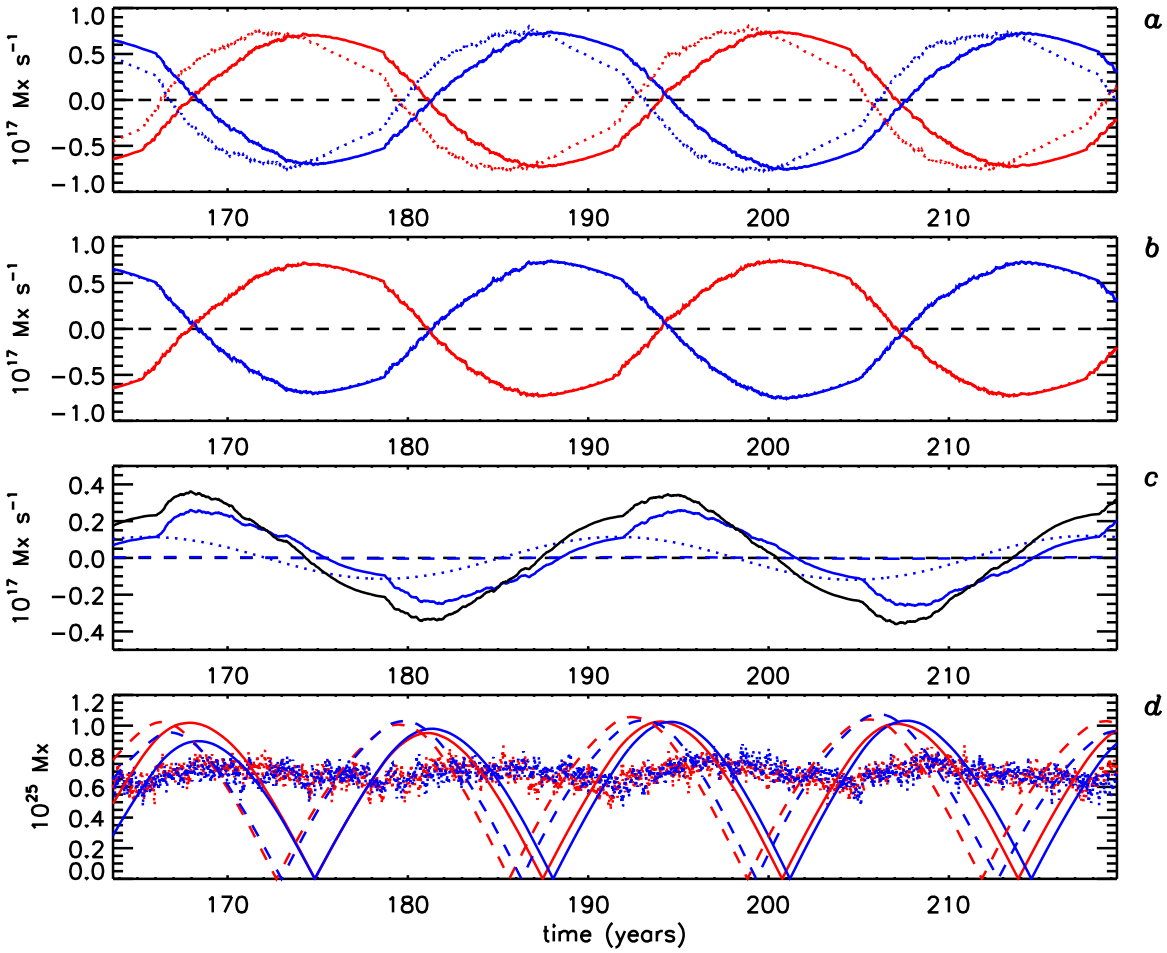

Figure 4.10: Evolution of toroidal flux:

(a) Rate of change of the mean toroidal flux threading the NH $d\Phi_{NH}/dt$ (blue solid line) for a selected time interval in Case S1 spanning four magnetic cycles. Red solid lines indicate its counterpart in the SH, $d\Phi_{SH}/dt$. Dotted lines indicate NH (blue) and SH (red) contributions from the surface DR term in eq. (4.2.12). (b) As in (a) but including contributions from the diffusive terms in eq. (4.2.8). Now the solid and dotted lines coincide. (c) Breakdown of the diffusive contributions to the line integral in eq. (4.2.8), including contributions from the upper (blue solid line), equatorial (blue dotted line), and polar (blue dashed line) branches of the closed circuit. The sum of these contributions is plotted as a black solid line. (d) Time evolution of the absolute value of the net toroidal flux in each hemisphere, $|\Phi_{NH}(t)|$ (blue solid line) and $|\Phi_{SH}(t)|$ (red solid line), together with the predicted evolution obtained by integrating eq. (4.2.12) over the NH (blue dashed line) and SH (red dashed line). Dotted lines show the unsigned vertical flux $|B_r|$ at the surface integrated over the NH (blue) and SH (red). Compare with Fig. 3 in CS15.

astute use of Stokes' theorem links the time evolution of the mean toroidal flux threading through the entire NH to the flows and fields on the boundaries of the CZ. Furthermore, as CS15 demonstrate, the dominant component of this line integral is the shearing of the radial field by the surface DR, which can be written as follows:

$$S^t_{NH}(t) = R^2 \int_0^{\pi/2} \langle B_r \rangle \left(\Omega(R,\theta,t) - \Omega_{eq}\right) \sin\theta d\theta \tag{4.2.12}$$

where $\Omega(r,\theta,t) = \Omega_0 + v_\phi r^{-1} \sin^{-1}\theta$ is the angular velocity. CS15 chose a reference frame rotating with angular velocity Ω_{eq}, which is the value of Ω at $r = R$ and $\theta = \pi/2$ (equatorial surface rate). This choice of reference frame, together with the weak radial dependence of the solar rotation rate at the equator inferred from helioseismology (cf. Fig. 3.2*a*), implies that the contribution from the DR term $(v_\phi \hat{\boldsymbol{\phi}}) \times \langle \mathbf{B} \rangle$ is small for the equatorial portion of the line integral in eq. (4.2.8). Furthermore, the contribution of this DR term to the inner and polar branches of the line integral vanish if there is no mean flux through those boundaries (as here). The impenetrable boundary conditions and the symmetry of the MC ($v_\theta = 0$ at the equator) ensure that the MC contributions to the line integral in eq. (4.2.8) also vanish. Thus, the only terms other than eq. (4.2.12) that contribute significantly to the line integral in eq. (4.2.8) are the diffusive terms. Our perfectly-conducting inner BCs preclude diffusion into the deep interior but diffusion along the polar, upper, and equatorial branches of the line integral is in general non-zero.

The evolution of $S^t_{NH}(t)$ and its counterpart, $S^t_{SH}(t)$, are shown in Fig. 4.10*a* (dotted lines). These are plotted together with the actual time derivative of $\Phi_{NH}(t)$ and $\Phi_{SH}(t)$ (solid lines). CS15 model the diffusive terms as an effective drag, inducing an exponential decay of $\Phi_{NH,SH}$ in the absence of DR. This effectively decreases the amplitude of $d\Phi_{NH,SH}/dt$ during the rising phase of a cycle and leads to a negative phase shift such that reversals and extrema occur earlier than they would without the diffusive terms. However, we find the opposite in our STABLE FTD models. Namely, the presence of the diffusive terms enhances the amplitude of $d\Phi_{NH,SH}/dt$ during the rising phase, inducing

a *positive* phase shift such that reversals and extrema occur *later* than they would otherwise. This is demonstrated by Fig. 4.10*b* where the inclusion of the diffusive terms shifts the dotted curve in Fig. 4.10*a* to the right by about 3 years, until it lies on top of the actual $d\Phi_{NH,SH}/dt$.

To illustrate why this occurs, consider the NH of Fig 4.7, focusing on the toroidal field evolution in the upper row. As the flux from the new cycle is building (red), flux from the previous cycle (blue) is pushed equatorward and upward by the MC (Fig. 4.7*b*-*e*). This causes a decay of the flux from the previous cycle due to diffusion first across the equator and then through the upper boundary (Fig. 4.10*c*). Meanwhile, the diffusion at the poles is negligible. This diffusive expulsion of the flux from the previous cycle causes the net flux $\Phi_{NH}(t)$ to rise, even after the surface DR stops amplifying the flux through $S^t_{NH}(t)$ (Fig. 4.10*a*). For example, by $t = 194.1$, shown in Fig. 4.7*e* and *j*, $S^t_{NH}(t)$ has already reversed sign, as the surface DR generates negative toroidal flux from the new, clockwise poloidal field at low latitudes. Yet, the net toroidal flux is still growing ($d\Phi_{NH}/dt > 0$; see Fig. 4.10*a*) due to the selective removal of opposing flux from the previous cycle by diffusion. This shifts the maximum toward a later time (Fig. 4.10*d*).

Figure 4.10*d* shows the time evolution of the amplitude of $\Phi_{NH,SH}(t)$ (solid lines) together with the predicted evolution based on integrating equation (4.2.12), shown as dashed lines. The integration constant is chosen such that the zeros of the predicted $|\Phi_{NH,SH}(t)|$ curves correspond roughly to the derivative extrema in Fig. 4.10*a* (dotted lines). If we were to include diffusion in the predicted $|\Phi_{NH,SH}(t)|$ curves, then the result would essentially coincide with the actual $|\Phi_{NH,SH}(t)|$ curves (solid lines), as in Fig. 4.10*b*.

We emphasize again that CS15 have no information on the structure of the field or the role of diffusion below the solar surface. Instead, they emphasize the importance of the surface DR term, eq. (4.2.12), which can be computed based on solar observations. They then model the subsurface diffusion as an exponential decay term that shifts the $\Phi_{NH}(t)$ and $\Phi_{SH}(t)$ curves to the left, toward earlier times. We confirm the importance of

the surface DR term in our idealized FTD model but we find that effect of the subsurface diffusion is instead to shift the $\Phi_{NH}(t)$ and $\Phi_{SH}(t)$ curves to the right, toward later times. CS15 verify their argument by demonstrating that the predicted peaks of $|\Phi_{NH}(t)|$ and $|\Phi_{SH}(t)|$ based on $S^t_{NH}(t)$ and $S^t_{SH}(t)$ correlate with observed maxima in the unsigned surface flux, suggesting that the enhanced surface flux arises from the emergence of greater net subsurface flux. If the subsurface diffusion were to shift the predicted flux curves to the right instead of to the left as suggested by our model, then this would improve the CS15 correlation, substantiating the CS15 argument (see their Fig. 3). However, that said, in our model, there is little variation of the unsigned surface flux over the course of the cycle and what little variation there is appears to be anti-correlated with the predicted flux (Fig. 4.10*d*). The positive phase shift due to diffusion improves this correlation slightly but there is still about a four-year delay between the maxima in $|\Phi_{NH,SH}(t)|$ and the peak in the unsigned surface flux.

We close this section by noting that the generation of toroidal flux by the surface DR terms $S^t_{NH,SH}(t)$ generates enough toroidal flux to account for all of the unsigned flux present on the surface. This is even true for Case S1 (Fig. 4.10*d*), in which the flux in BMRs has been artificially enhanced by a factor of five ($\Phi_0 = 5$; see Table 1). CS15 argue that this is also the case for the Sun.

Hale discovered that the magnetic orientations of the eastward and westward parts of bipolar sunspot groups in one solar hemisphere are the same during an 11-year cycle and opposite in the other hemisphere. This implies that the sunspot groups originate from a toroidal field of fixed orientation during a cycle. Toroidal flux of the opposite polarity would lead to sunspot groups violating Hale's law. Since only a small minority of the sunspot groups are actually observed to violate this rule, opposite-polarity toroidal field is largely irrelevant as a source of sunspot groups. In other words, it is the hemispheric net toroidal magnetic flux given by the azimuthal average of the toroidal field that is relevant for the formation of sunspot groups. Here we use a simple method based on

Stokes theorem to show that the emerged surface fields determine the net toroidal flux generated by differential rotation in a solar hemisphere. The time evolution of the net toroidal flux in the convection zone can thus be calculated using only observed quantities (differential rotation and field distribution at the surface). We compare the resulting net toroidal flux with the observed large-scale unsigned surface flux and find that they vary in a similar manner [Cameron and Schüssler(2015)].

4.3 Achieving Self-Sustained Dynamo Action

A shortcoming of the model presented in §4.2 (Case S1) is that the fields are too strong. For example, the average strength of the polar fields is over 200 G (Fig. 4.5*b*). The Sun, by comparison, is about 10 G [Muñoz-Jaramillo et al.(2012)]. This can be attributed in part to the large value of $\Phi_0 = 5$ used to artificially enhance the flux in BMRs as expressed in eq. (3.5.10). We used this large value of Φ_0 in order to ensure that the dynamo is supercritical, meaning that sustained dynamo action can occur despite the inhibiting effects of turbulent diffusion.

Dropping the value of Φ_0 from five to unity causes the dynamo to decay, as shown in Fig. 4.11*a*. This is Case S6, from a series of simulations summarized in Table 1. Case S6 was started from the same initial conditions as Case S1 (Fig. 4.8*a*), provided by a progenitor case with higher Φ_0 (not shown). Though most of the magnetic energy is in the mean toroidal fields, the dynamo cannot operate without the BMRs, which dominate the non-axisymmetric magnetic energy ME_{nax}. As the toroidal field decays due to diffusion, it eventually drops below the threshold field for creating BMRs (see Chapter 3). This causes ME_{nax} to drop rapidly beyond $t \sim 57$ yrs (Fig. 4.11*a*). This is the point of no return; once the dynamo ceases to make BMRs, it will continue to decay indefinitely.

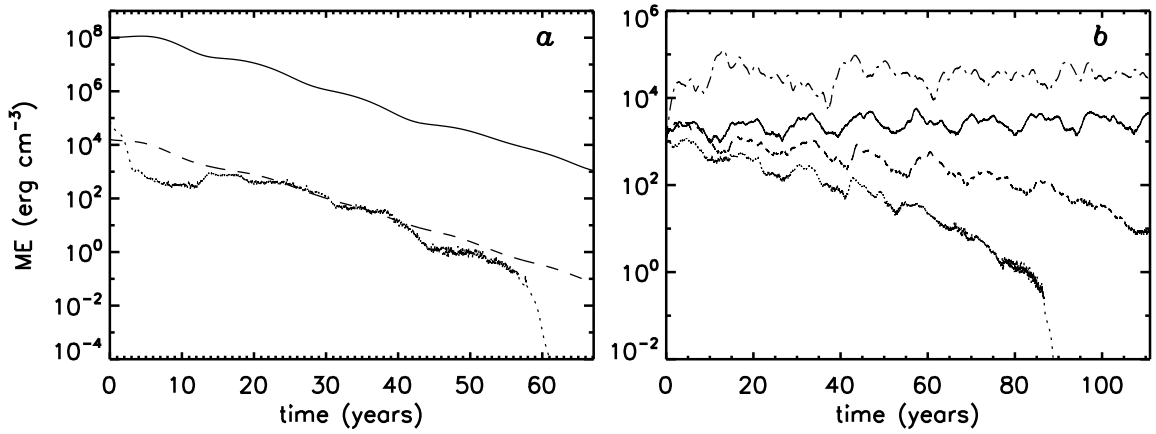

Figure 4.11: Evolution of magnetic energy

(a) Evolution of the magnetic energy, ME, in Case S6, expressed as an average energy density in erg cm^{-3}. Solid, dashed and dotted lines correspond to the mean toroidal (ME$_{tor}$), mean poloidal (ME$_{pol}$), and non-axisymmetric field components (ME$_{nax}$) respectively. (b) ME$_{nax}$ for cases S8 (dashed line), L1 (dotted line), L2 (solid line), and L3 (dot-dashed line).

The most straightforward way to ensure that the dynamo is supercritical is to artificially boost the flux in BMRs by increasing Φ_0. However, other parameters also contribute to the efficiency of the dynamo and it is possible to find supercritical solutions with $\Phi_0 = 1$. One such parameter is the penetration depth of the BMRs, r_s (see Chapter 3). Here, deeper is better. If we take the solution S1 and move the penetration depth up to $0.93R$ instead of $0.9R$ (Case S2 in Table 1), the dynamo dies (becomes subcritical).

Another parameter that affects the efficiency of the dynamo is the spacing between spot pairs, s_a. Recall from 3 that s_a is a nondimensional number that gives the distance between the two opposite polarity components of a BMR relative to the radius of the individual spots. Thus, a large value of s_a implies widely spaced spot pairs, which is beneficial for the dynamo because it maximizes the axisymmetric component of the poloidal flux and it minimizes local cancellation, allowing more trailing flux to reach the poles. A comparison of cases S4 and S5 in 4.1 demonstrates that increasing s_a from 1.5 to 2.5 can make the

Table 4.1: Simulation Summary. The S series of simulations uses the sawtooth pdf of eq. (3.6.7) while the L series uses the lognormal pdf of eq. (3.6.4). Root-mean-square (rms) values listed in columns 8-10 are based on integrals over the entire computational volume and are quoted for the mean toroidal field (B_{tor}), the mean poloidal field (B_{pol}), and the non-axisymmetric field component (B_{nax}), which is mainly composed of BMRs.

Case	Φ_0	r_s	s_a	η_{top} ($\mathrm{cm^2\ s^{-1}}$)	τ_p (days)	τ_s (days)	B_{tor} (rms)	B_{pol} (rms)	B_{nax} (rms)
S1	5	0.9	1.5	3×10^{12}	–	–	22 kG	250 G	720 G
S2	5	0.93	1.5	3×10^{12}	–	–	subcritical	–	–
S3	5	0.93	2.5	3×10^{12}	–	–	subcritical	–	–
S4	2	0.9	2.5	3×10^{12}	–	–	6.8 kG	79 G	200 G
S5	2	0.9	1.5	3×10^{12}	–	–	subcritical	–	–
S6	1	0.9	1.5	3×10^{12}	–	–	subcritical	–	–
S7	1	0.9	2.5	3×10^{12}	–	–	subcritical	–	–
S8	1	0.9	2.5	10^{12}	–	–	subcritical	–	–
L1	1	0.9	2.5	3×10^{12}	2	3	subcritical	–	–
L2	1	0.9	2.5	10^{12}	2	3	11 kG	130 G	300 G
L3	1	0.85	4	10^{12}	1	1.5	72 kG	840 G	960 G

difference between a subcritical and a supercritical dynamo. However, this is not always the case; compare also cases S2 and S3 and cases S6 and S7.

Since the dynamo must overcome diffusion to achieve supercriticality, a reduction in the diffusion can also be beneficial, particularly in the upper CZ where η is largest (Fig. 3.2*c*). This was not enough to revive Case S7; Case S8 is also subcritical even though the value of η_{top} is decreased by a factor of three. However, when combined with more frequent BMR emergence, which we achieved with the lognormal pdf (Fig. 3.4*c*), lower η_{top} did yield supercritical solutions, even for $\Phi_0 = 1$; see Cases L2 and L3 in Table 1. The benefit of lower diffusion is demonstrated unambiguously by comparing cases L1 and L2, which both use the same lognormal emergence pdf. The benefit of more frequent BMR emergence is demonstrated unambiguously by comparing cases S8 and L2.

The difference in dynamo efficiency influences not only the growth or decay rate of the dynamo, but also the nonlinear saturation level. This is demonstrated most dramatically by Case L3 (Table 1). This case has all the features that were shown above to be beneficial,

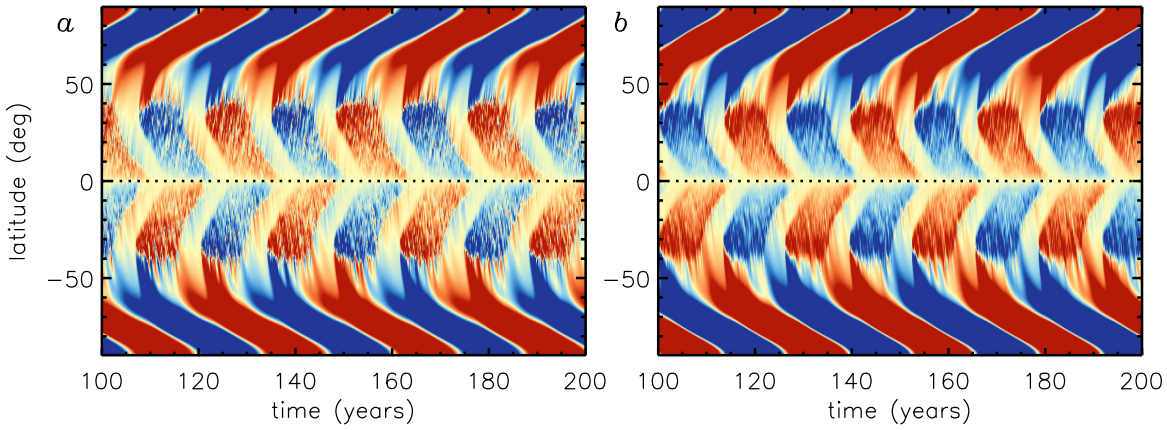

Figure 4.12: Magnetic cycles for Case L2 and L3

As in Fig. 4.5*a* but for Cases (*a*) L2 and (*b*) L3, spanning a century of simulated time. Saturation values for the color table are ± 50 G and ± 200 G respectively.

including deep penetration of BMRs, wide spacing of BMR polarity components, low diffusion, and frequent BMR emergence, with a mean interval between spot appearances of $\tau_s = 1$ day and a mode of $\tau_p = 1.5$ days (Table 1). Even though it has the same quenching field strength as all the other cases, $B_q = 10^5$ G, and a relatively low flux amplification factor of $\Phi_0 = 1$, it achieves stronger fields (more magnetic energy) than all of the other cases. This includes case S1 (discussed in §4.2), which has $\Phi_0 = 5$. Furthermore, though Cases L2 and L3 have the same value of Φ_0, the latter has much stronger fields. It also has a higher ratio of B_{pol}/B_{nax}, approaching unity. This can be attributed to the large value of s_a, which maximizes the mean poloidal field associated with each BMR because the two polarities have minimal overlap in latitude.

Fig. 4.11*b* shows ME_{nax} in cases S8, L1, L2, and L3 for comparison. All were started from the same initial conditions, obtained from the supercritical Case S4 (Table 1). Note that Case L2 in particular has more magnetic energy than its progenitor, S4 (see also Table 1). This demonstrates that lowering the diffusion by a factor of three more than makes up for lowering Φ_0 by a factor of two. Though the two supercritical cases in this

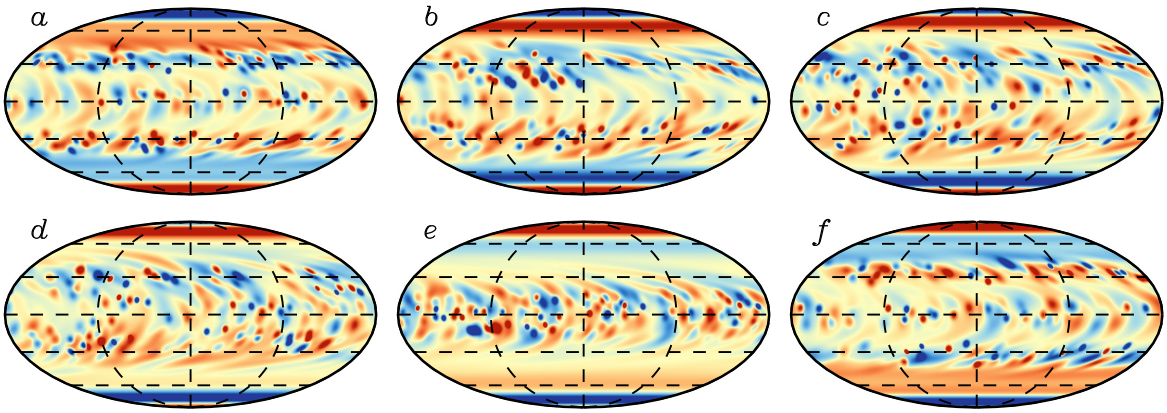

Figure 4.13: Radial magnetic field B_r at the solar surface (r = R) in case L3
As in Fig. 4.6 but for Case L3. The saturation level for the color table is ± 1kG.

plot, L2 and L3, look somewhat irregular at early times, they both settle into a steady magnetic cycle similar to that described in §4.2 for Case S1. This is demonstrated in Fig. 4.12. The most apparent difference between these two cases (Figs. 4.12*a*,*b*) is that case L3 (*b*) has a smoother distribution of low-latitude poloidal flux. This can be attributed to the more frequent BMR emergence rate, which yields more flux patches at any given time. Furthermore, the lower diffusion in both Cases L2 and L3 relative to Case S1 leads to stronger, more compact fields at low latitudes that more closely track the emergence sites; compare Fig. 4.12 with Figs. 4.8*b* and 4.5*a*.

The stronger, more compact fields at low latitudes in Case L3 relative to Case S1 is apparent in Fig. 4.13. Compare this to Fig. 4.6. Each individual spot of a BMR takes longer to disperse so at any given time, there are more spots that are strong and localized. The flux distribution in Case L2 (not shown) is similar. Yet, this change in the flux distribution has little effect on the overall characteristics of the magnetic cycles. The cycle period in all three cases is similar: 13.1 years for S1 and L3, and 13.6 years in L2. The other supercritical solution, Case S4, has a cycle period of 13.0 years.

Though a detailed comparison with observations lies outside the scope of this paper, we note that a cursory comparison of our simulations with solar magnetograms and SFT

models suggests that cases L2 and L3 produce more realistic surface flux distributions. Their lower diffusion and higher frequency of emergence events tends to produce strong flux patches with a wider range of areas that extends below 5 square degrees, reminiscent of observed magnetograms ([Upton and Hathaway(2014)]). As discussed in §3.7.2, the SpotMaker algorithm effectively assumes that only a small portion of a progenitor toroidal loop emerges through the surface so the depletion of mean flux is minimal. In reality, a significant portion of the mean flux in the lower CZ/tachocline would be redistributed throughout the CZ and outside of the domain. Taking this tachocline flux depletion into account would likely inhibit the dynamo; it is unclear whether or not supercritical solutions could still be found for $\Phi_0 = 1$. It would also reduce the ratio of mean toroidal to poloidal field. These issues are indeed important to investigate but they are subtle, and beyond the scope of this work.

Chapter 5

Converging Flows Towards Active Regions: Impacts on Magnetic Cycles

5.1 Surface Dynamics of Emerging Active Regions

The formation of magnetic active regions on the surface of the Sun are one of the central problems of solar physics. It is of the fundamental importance in astrophysics because active regions are one of the primary manifestations of the solar and stellar magnetism. In addition, solar active regions (AR) are the major drivers of the solar variability, geospace and planetary space environments and space weather. Understanding of the emergence and evolution of active regions is a key to developing the knowledge and capability to detect and predict extreme conditions in space. The uninterrupted helioseismic and magnetic data from Solar Dynamics Observatory provide unique opportunities for comprehensive studies that can uncover the basic mechanisms of active region formation, evolution, and their flaring and CME activity [Kosovichev et al.(2016)].

The dominant global-scale flows in the Sun are the differential rotation and the meridional flow (see chapter 3 §3.4.1 and 3.4.2). Helioseismology revealed Large-scale converging flows around active regions, which alter the mean meridional circulation and, thus, the magnetic flux transport affecting the strength and duration of the solar activity cycles.

The solar meridional flow is a large-scale plasma motion which transports material from the equator toward the poles near the surface. These meridional flow variations could possibly play a role in modulating the amplitude and length of the activity cycles. In particular, the cycle period of an advection-dominated Babcock-Leighton type dynamo is sensitive to the strength of the meridional flow [Dikpati and Charbonneau(1999)], because the flow essentially acts like a "conveyor belt" in transporting the field [Dikpati and Gilman(2009)].

Local helioseismology provides a unique opportunity to investigate the subsurface structure and dynamics of active regions and their effect on the large-scale flows and global circulation of the Sun. As the emerging magnetic flux becomes concentrated in sunspots local converging flows are observed beneath the forming sunspots. These flows are most prominent in the depth range 1-3 Mm, (see Figure 5.1) and remain converging after the formation process is completed. On the larger scale converging flows around active region appear as a diversion of the zonal shearing flows towards the active region, accompanied by formation of a large-scale flows diverging in the deeper layers. This process occurs when a substantial amount of the magnetic flux emerged on the surface, and the converging flow pattern remains stable during the following evolution of the active region. In the deeper layers the flows become diverging, and surprisingly strong beneath some active regions [Kosovichev et al.(2016)].

In the photosphere, sunspots are typically surrounded by diverging horizontal outflows, termed moat flows, (see Figure 5.2) with amplitudes of several hundred m s^{-1} . These outflows typically extend to about twice the radius of the penumbra. Moat flows were first detected using direct Doppler measurements and also can be inferred from the motion of small magnetic features. Local helioseismology is a useful tool for studying flows around sunspots. At a depth of 1 Mm, the moat flow has an amplitude of $\sim$ 250 m s^{-1} , which is consistent with the motion of the small magnetic features. This outflow is detected in the

top 4 Mm. Such measurements of the subsurface moat flow have been confirmed by ring-diagram analysis. The moat flow is believed to be driven by a pressure gradient caused by the blockage of heat transport by sunspots. Though much slower, the moat flow appears physically connected with the Evershed flow in the penumbra ([Gizon et al.(2010)] and the cites therein).

The large-scale motion of the magnetic elements is a combination of the large-scale bulk plasma motions advecting the magnetic features and a diffusion type motion caused by the action of the random granular and supergranular flows on large-scale gradients in the distribution of the number density of magnetic field elements. Temporal variations of the meridional flow is connected with a flow pattern that migrates equatorward in parallel with the activity belts as outlined by the butterfly diagram of sunspots. This flow pattern probably reflects the latitudinal inflows toward the activity belts [Cameron and Schüssler,(2010), Gizon and Rempel.(2008)].

Helioseismology helps scientists to improve their knowledge about the interior of the sun. For instance, studying solar rotation and its relation with solar radius and latitude are some of the results of helioseismology. Besides helioseismology has detected spatially extended converging surface flows into solar active regions. These large-scale converging flow play an important role in flux-transport models of the solar dynamo [Gizon et al.(2001)] . This surface inflow is with typical flow velocities of 20 - 30 m/s (velocities up to 50 m/s have been reported) that extend up to 10° from the active region (or which exist as far as 30° from the centers of active regions). These flows arise possibly resulting due to an enhanced radiative cooling rate in the active regions (that is resulting from a temperature deficit due to the excess radiance of small-scale magnetic flux concentrations) [Löptien et al.(2017), Gizon et al.(2010)]. These Large-scale converging flows around active regions, which alter the mean meridional circulation (see Figure 6.1) and, thus, the magnetic flux transport affecting the strength and duration of the solar activity cycles [Hindman et al.(2009)].

In STABLE dynamo model simulations, the inflows to active regions may play an important role in the transport of magnetic flux over the course of the solar cycle. The inflows can affect the dispersal of active regions, since they counterbalance the outward diffusion of magnetic flux by convection. They are also a potential mechanism for modulating the strength of the solar cycle [Cameron and Schüssler,(2012),Belda and Cameron ,(2016),Belda and Cameron ,(2017)]

During the initial emergence of the bipolar structure no specific large-scale flow pattern in the depth range 0-20 Mm is identified. Nevertheless, the region of the flux emergence is characterized by an enhanced horizontal flow divergence that corresponds to the spatial separation of the magnetic polarities. Figure 5.1, in the subsurface layer, 1 - 3 Mm deep, the initial flow pattern corresponds to the two flux concentrations moving away from each other (Figure 5.1a). However, 12 hours later we observe formation of converging flows around the positive polarity, associated with the formation of a sunspot (Figure 5.1b). In later times, a similar converging flow pattern is established beneath the leading negative polarity, and is also associated with the formation of sunspots (Figure 5.1$c-d$) [Kosovichev et al.(2016)].

[Cameron and Schüssler,(2012)] discusses how converging flows into activity belt can limit the amplitude of Babcock-Leighton dynamo models. They give a brief study of the correlation between the amplitude of the solar polar field around activity minimum. The strength of the subsequent cycle and the Sun's axial dipole field as observed around activity minimum reflects the source for the generation of the toroidal magnetic flux of the subsequent cycle. Such a role of the polar field is a key feature of the Babcock-Leighton (BL) dynamo model ([Upton and Hathaway(2014),Charbonneau(2010)]) (see details in 3. In this type of dynamo, the poloidal magnetic field results from the systematic tilt (with respect to the azimuthal/longitudinal direction) of sunspot groups and bipolar magnetic regions in combination with the subsequent redistribution of their magnetic fluxes by near-surface flows. The crucial mechanism for the reversal of the Sun's global dipole field

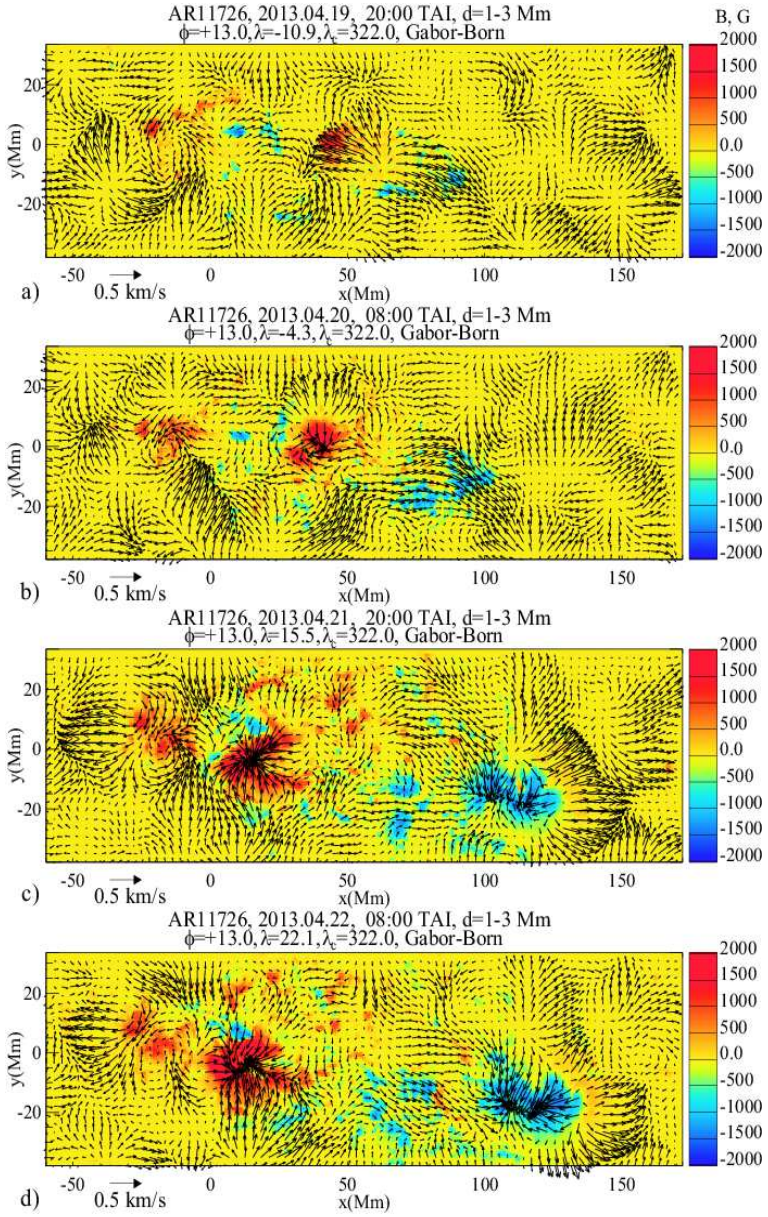

Figure 5.1: Photospheric magnetograms and subsurface flows

Evolution of subsurface flow maps and the photospheric magnetograms during the appearance of emerging bipolar magnetic flux on the solar surface (emergence of active region NOAA 11726) in the depth range 1-3 Mm for four different moments of time: a) 2013.04.19, 20:00 UT; b) 2013.04.20, 08:00 UT, c) 2013.04.21, 20:00 UT, d) 2013.04.22, 08:00 UT. The point x = 0, y = 0 is located at the heliographic coordinates: latitude 13.0, longitude 15.5, and the Carrington longitude 322.0. The travel times were calculated by using the Gabor-wavelet fitting technique, and the inversion for flows was performed by using the Born-approximation kernels. The corresponding surface magnetograms from HMI are shown in the color background. [Kosovichev et al.(2016)].

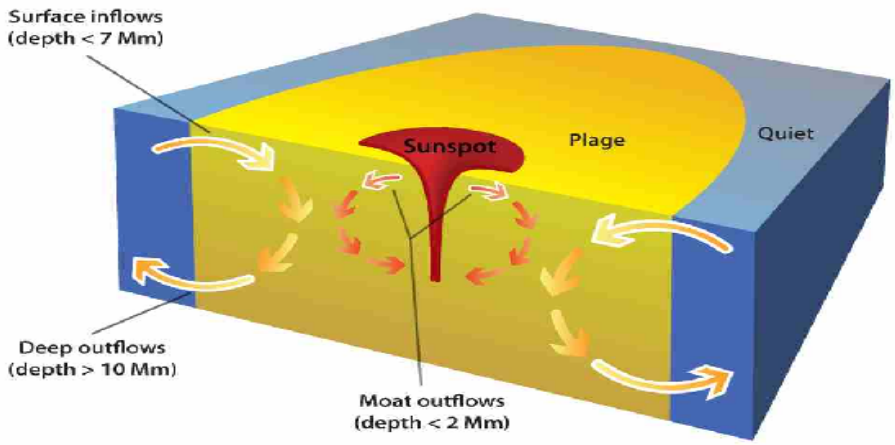

Figure 5.2: Schematic diagram large-scale circulations within active regions

Schematic diagram providing a side view of the large-scale circulations established within active regions. Surface cooling within the plage results in a downdraft which draws fluid in at the surface. Therefore, there is a mean inflow ($\approx$ 20 m s^{-1}) at the active regions periphery. Below a depth of 10 Mm, an outflow manifests that is likely the return flow connected to the surface inflow. The moat flows streaming out from sunspots at the surface impact this inflow somewhere within the plage and presumably join in the down flow. The arrows outlined in white have been observed through a variety of techniques, including local helioseismology and correlation tracking [Hindman et al.(2009)].

is the preferred transport of preceding-polarity flux of bipolar magnetic regions across the equator into the other solar hemisphere, which leads to the reversal of the polar fields and the build-up of an axial dipole field of opposite polarity. Toroidal flux is then generated by the action of differential rotation winding up poloidal field lines threading the Sun.

All the senario could likely leads us to provide a non-linear saturation mechanism for the global dynamo and contribute to the solar cycle variability in the BL dynamo frame work. To address this, we incorporated three non-axisymmetric parametrizations of the inflows in to STABLE model. Then we will produce some of the features of solar activity cycles from the STABLE model with and without (tilt angle saturation mechanism: [Karak and Miesch(2017)]) the inflows to the active regions (sunspots).

The following list items are questions and/or considerations we want to address in this work:

- In this work we aim to investigate how the effect surface converging flows towards active regions affects the surface transport of magnetic flux, as well as their impact on the generation of the Sun's poloidal field and the build-up of the polar fields. Their effects on the global dipole (may affect the build-up of the global magnetic dipole) and subsequent toroidal field to sustain the dynamo. The inflows constitute a potential non-linear mechanism for the saturation of the global dynamo and may contribute to the modulation of the solar cycle in the STABLE (Babcock-Leighton/SFT) framework.

- Does the inclusion of the inflows to the STABLE solar dynamo model leads to the variation of the Solar cycle (in determining the amplitude of solar cycles)? Incorporated such inflows in the STABLE model to study their effect on the evolution of an active region, BMRs and subsequent BL-mechanism to produce surface magnetic filed, the poloidal filed, the emerged BMRs, thus may limit the build-up of magnetic field at the polar caps.

- In general, whether the effects of the inflow towards the active regions, which plays a central role for the saturation of the dynamo?

So far we have described the BL dynamo as a linear process. In addition, at least one nonlinear feedback mechanism is required that limits the amplitude of the generated magnetic field and controls the variation of the cycle amplitude. In the framework of the BL dynamo, potential feedback mechanisms include the back-reaction of the magnetic field on 1) differential rotation, 2) the tilt angles of sunspot groups, and 3) cross-equator transport of magnetic flux. However, Clear evidence for a more global reaction on differential rotation that would affect the generation of the toroidal magnetic field has not been obtained so far. [Cameron and Schüssler,(2012)]. In this BL dynamo model includes three nonlinearities. These are 1) The tilt angle saturation mechanism Equation 6.2.9, 2) time delay distribution obtained from the observed sunspot data is depends on the toroidal flux, B_ϕ at the base of the CZ, Equation 6.2.6. 3) The converging flow towards the active regions depends the surface magnetic field, B_r, (details on this one immediately below).

5.2 Modeling the Inflow into the Active Region

Inflow surrounding active regions are likely to influence the patterns formed by the dispersal of surface flux, including the formation time and field strength of the polar fields. The polar fields plays a large role in determining the heliographic field, and may even determine the amplitudes of the future activity cycles. To investigate the consequences of the active region inflows on the dispersal of surface flux, we have incorporated and additional advective term that approximates the observated inflows [De Rosa and Schrijver (2006)] into STABLE solar dynamo model.

The model of inflow towards the active regions is developed on the frame-work of Surface flux Transport And Babcock-LEighton Dynamo Model. STABLE is a fully 3D hybrid of flux-transport dynamo and surface flux transport model. As briefly describe

in Chapter 3, the STABLE model solves the kinematic magnetohydrodynamic (MHD) induction equation in a 3D, rotating, spherical shell. The induction equation is solved by means of the Anelastic Spherical Harmonic (ASH) code, which currently serves as the dynamical core for the STABLE model. STABLE uses the SpotMaker spot deposition algorithm to place bipolar magnetic regions (BMRs) on the solar surface in response to the dynamo-generated magnetic field. The subsequent evolution of these BMRs due to differential rotation, meridional circulation, and turbulent diffusion naturally generates a mean poloidal field as originally described by Babcock (1961) and Leighton (1964).

We use the STABLE code the version of the code used for 3D kinematic dynamo modeling is STABLE (i.e., Surface Flux Transport And Babcock-LEighton Model) described first by MD14 and later by [Miesch and Teweldebirhan(2016)] (MT16), [Hazra et al.(2017)] (HCM17) and [Karak and Miesch(2017)] (KM17) to simulate the evolution of the magnetic fiel. As we stated above the STABLE uses the SpotMaker spot deposition algorithm to place bipolar magnetic regions (BMRs) on the solar surface in response to the dynamo-generated magnetic field. Nonetheless this time subsequent evolution of these BMRs under the influence of large-scale surface flows (differential rotation, meridional flow and the converging flow towards the sunspots) and turbulent diffusion, which representing the random motion of the magnetic flux elements due to the (numerically unresolved) supergranular flows, naturally generates a mean poloidal field the so called Babcock-Leighton mechanism. The magnetic field at the solar surface is assumed to be radial. The governing equation of the STABLE model is

$$\frac{\partial \mathbf{B}}{\partial t} = \nabla \times (\mathbf{v} \times \mathbf{B} - \eta \nabla \times \mathbf{B}) \tag{5.2.1}$$

where $\mathbf{v}$, is the velocity field, η is the magnetic diffusion. Though this model is fully 3D and no axisymmetric assumption is considered, still this model is kinematic and we provide the velocity field motivated from helioseismology and observations. We solve Equation 5.2.1 using anelastic spherical harmonic (ASH) code, which currently serves as the dynamical core for the STABLE model, as we have see more detail in §3.3.1. The ASH

code has the capability to solve the velocity equation and magnetic induction equation together but for our kinematic model we bypass the velocity equation solver and only solve the induction equation by providing observationally motivated velocity fields. The source term for induction equation 5.2.1 is function which captures the effect of the BL mechanism that is an emergence of magnetic flux at the surface in the form of bipolar magnetic regions appearing at the latitudes and longitudes.

As we have already described in detail in the preceding Chapter §3.3, the MHD induction equation, in Eq. (5.2.1) is simplified to:

$$\frac{\partial \mathbf{B}}{\partial t} = \boldsymbol{\nabla} \times ((\mathbf{v} + \gamma) \times \mathbf{B} - \eta_t \boldsymbol{\nabla} \times \mathbf{B}) \quad . \tag{5.2.2}$$

where η_t is the turbulent diffusion in the solar convection zone and depth dependent only and $\mathbf{v}$, the total flow field is summation of the velocity of the meridional flow, $\mathbf{v}_{mc}$, a velocity as a result of $\Omega(r, \theta)$, that is the angular velocity of the differential rotation and $\mathbf{v}_{in}$ is the inflows velocity includes $v_{in\phi}$, $v_{in\theta}$ and v_{rin} are the longitudinal, latitudinal radial components in spherical coordinates respectively.

$$\mathbf{v} = \mathbf{v}_{DR}(r, \theta) + \mathbf{v}_{MC}(r, \theta) + \mathbf{v}_{in}(r, \theta, \phi, t) \tag{5.2.3}$$

Here our main and first objective to determine the inflow velocity in the Equation (5.2.3) and we will describe the detail in §5.2.1.

5.2.1 Mathematical Formulation of the Inflow towards Active Regions

To implement this we consider the following assumptions. The first assumption is, the inflow velocities are completely poloidal. Second assumption mass flux is completely divergenceless ($\boldsymbol{\nabla} \cdot \overline{\rho} \mathbf{v} = 0$). Now we need to define a flow that converges into each sunspot at the surface. To proceed with that we have to define the mass flux which is decomposed into poloidal(W) and toroidal component (Z) and given by

$$\overline{\rho}\mathbf{v} = \boldsymbol{\nabla}\times\boldsymbol{\nabla}\times(W\hat{\boldsymbol{r}}) + \boldsymbol{\nabla}\times(Z\hat{\boldsymbol{r}}) \quad , \tag{5.2.4}$$

where $\hat{\boldsymbol{r}}$ is a unit vector in the radial direction. This formulation identically satisfies the continuity equation ($\boldsymbol{\nabla}\cdot(\rho\mathbf{v}) = 0$) at all times.

Now using the first assumption neglecting vortical part in Equation 5.2.4; basically this leads to mass flux to be completely poloidal at the surface. This can be done by writing the flow in Equation (5.2.4), in terms of the poloidal mass flux, W only as below.

$$\overline{\rho}\mathbf{v} = \boldsymbol{\nabla}\times\boldsymbol{\nabla}\times(W\hat{\boldsymbol{r}}) \quad . \tag{5.2.5}$$

Now the inflow is non-axisymmetric flow, in spherical polar coordinates the simplifacation of equation (5.2.5). The components of the poloidal mass flux, $\hat{\rho}\mathbf{v}$ will be:

$$\overline{\rho}v_r = -\frac{1}{r^2\sin\theta}\left[\frac{\partial}{\partial\theta}\left(\sin\theta\frac{\partial W}{\partial\theta}\right) + \frac{1}{\sin\theta}\left(\frac{\partial^2 W}{\partial\phi^2}\right)\right] \tag{5.2.6}$$

$$\overline{\rho}v_\theta = \frac{1}{r\sin\theta}\left(\frac{\partial^2(W)}{\partial r\partial\theta}\right) \tag{5.2.7}$$

$$\overline{\rho}v_\phi = \frac{1}{r\sin\theta}\left(\frac{\partial^2 W}{\partial r\partial\phi}\right) \tag{5.2.8}$$

Compare with the Laplacian Equation in Spherical Polar Co-ordinates

$$\boldsymbol{\nabla}^2 = \frac{1}{r^2}\frac{\partial}{\partial r}\left(r^2\frac{\partial}{\partial r}\right) + \frac{1}{r^2\sin^2\theta}\frac{\partial}{\partial\theta}\left(\sin\theta\frac{\partial}{\partial\theta}\right) + \frac{1}{r^2\sin^2\theta}\frac{\partial^2}{\partial\phi^2} \tag{5.2.9}$$

From Equations 5.2.6 and 5.2.9 we have:

$$\overline{\rho}v_r = -\nabla_h^2 W = -\frac{1}{r^2\sin\theta}\left[\frac{\partial}{\partial\theta}\left(\sin\theta\frac{\partial W}{\partial\theta}\right) + \frac{1}{\sin\theta}\left(\frac{\partial^2 W}{\partial\phi^2}\right)\right] \tag{5.2.10}$$

Equation (5.2.6) means that the vertical mass flux is given by the horizontal Laplacian of W: Again when we transform this up into spherical harmonic space (indicated by tildes), then there is a simple relationship between $\mathbf{v}_r$ and W. The Spherical harmonics expansions,

$Y_{\ell m}(\theta, \phi)$, are a natural set of functions for this problem because they constitute a complete and orthogonal set of eigenfunctions of the horizontal Laplacian operator in θ and ϕ. The spectral method is a term that has become associated with the class of pseudospectral numerical methods which involve the expansion of dynamical fields in series of spherical harmonic basis functions, and we adopt that convention here as well. The first step in such a method is to express each of the state variables as a truncated series of the form:

$$W(r, \theta, \phi, t) = \sum_{m=0}^{l_{max}} \sum_{l=m}^{l_{max}} \widetilde{W}_{\ell,m}(r, t) Y_{\ell m}(\theta, \phi) \quad . \tag{5.2.11}$$

where the spherical harmonics are defined as

$$Y_{\ell m}(\theta, \phi) = \sqrt{\frac{2\ell + 1(\ell - m)!}{4\pi(\ell + m)!}} P_\ell^m(\cos\theta) e^{\imath m\phi}, \tag{5.2.12}$$

and the $P_\ell^m(\cos\theta)$ denote the associated Legendre polynomials of degree ℓ and order m.

$$P_\ell^m(\cos\theta) = (-1)^m (\sin\theta)^m \frac{d^m}{d(\cos\theta)^m} (P_\ell(\cos\theta)) \tag{5.2.13}$$

$$P_\ell(\cos\theta) = \frac{1}{2^\ell \ell!} \frac{d^\ell}{d(\cos\theta)^\ell} (\cos^2\theta - 1)^\ell \tag{5.2.14}$$

The inner summation in equation (5.2.11) is generally known as a Legendre transformation and the outer represents a discrete Fourier transformation. The spectral coefcients are then given by

$$\widetilde{W}_{\ell,m}(r, t) = \sum_{m=-m_{max}}^{m_{max}} \sum_{l=|m|}^{l_{max}(m)} W(r, \theta, \phi, t) \frac{\omega_i}{2N_\phi} Y_{\ell m}(\theta, \phi) \quad . \tag{5.2.15}$$

where ω_i are the Gaussian weights for the Legendre polynomials.

The spherical harmonics provide natural basis functions for problems in spherical coordinates because they are eigenfunctions of the of the horizontal Laplacian:

$$\boldsymbol{\nabla}_h^2 Y_{\ell m}(\theta, \phi) = \left[\frac{1}{r^2 \sin\theta} \frac{\partial}{\partial\theta} \left(\sin\theta \frac{\partial}{\partial\theta} \right) + \frac{1}{r^2 \sin^2\theta} \frac{\partial^2}{\partial\phi^2} \right] Y_{\ell m} = -\frac{\ell(\ell + 1)}{r^2} Y_{\ell m} \tag{5.2.16}$$

$$\boldsymbol{\nabla}_h^2 Y_{\ell m}(\theta, \phi) = -\frac{\ell(\ell + 1)}{r^2} Y_{\ell m} \tag{5.2.17}$$

$$\boldsymbol{\nabla}_h^2 = -\frac{\ell(\ell+1)}{r^2} \tag{5.2.18}$$

and as a result, many derivatives appearing in the linear terms can be expressed as simply multiplications in spectral space. This facilitates considerably the application of the semi-implicit time-integration scheme which can then be performed in spectral space.

Upon applying the transformation (5.2.11) to equation (5.2.5), the spectral form of the mass flux is obtained:

$$\overline{\rho} v_r = \frac{1}{r^2} \sum_{\ell,m} \ell(\ell+1) \widetilde{W}_{\ell,m} Y_{\ell m} \tag{5.2.19}$$

$$\overline{\rho} v_\theta = \frac{1}{r \sin\theta} \sum_{\ell,m} \left(\frac{\partial \widetilde{W}_{\ell,m}(r,t)}{\partial r} \sin\theta \frac{\partial Y_{\ell m}}{\partial \theta} \right) \tag{5.2.20}$$

$$\overline{\rho} v_\phi = \frac{1}{r \sin\theta} \sum_{\ell,m} \left(\frac{\partial \widetilde{W}_{\ell,m}(r,t)}{\partial r} \frac{\partial Y_{\ell m}}{\partial \phi} \right) \tag{5.2.21}$$

The summation over ℓ and m is expressed with a shortened notation summations in Equation (5.2.11).

From Equation (5.2.11 and (5.2.10) the relationship looks like this:

$$\overline{\rho} v_r = -\nabla_h^2 W = -\sum_{m=0}^{l_{max}} \sum_{l=m}^{l_{max}} \widetilde{W}_{\ell,m}(r,t) \boldsymbol{\nabla}_h^2 Y_{\ell m} = \sum_{m=0}^{l_{max}} \frac{\ell(\ell+1)}{r^2} \widetilde{W}_{\ell,m}(r,t) Y_{\ell m}(\theta,\phi) \tag{5.2.22}$$

5.2.2 Surface Flux Transport Equation

The region of the flux emergence is characterized by an enhanced horizontal flow divergence that corresponds to the spatial separation of the magnetic polarities. Therefore, to investigate the formation of converging flows around or into the active region let's define the radial field at the surface (r = $R_\odot$) as a function of latitude, longitude, and time:

$$B_S(\theta,\phi,t) \equiv B_r(R,\theta,\phi,t) \tag{5.2.23}$$

Where B_S is the magnetic field at the surface, r = $R_\odot$. At the start of the emergence the zonal flows are diverted towards the active region on the both sides of the emerging magnetic flux, forming a vortex-like structure, B is maximum. The formation of the converging flows appears as a diversion of the zonal shearing flows towards the active region. This process occurs when a substantial amount of the magnetic flux emerges on the surface, and the converging flow pattern remains stable during the evolution of the active region.

We use the STABLE code of to simulate the evolution of the magnetic flux at the solar surface under the influence of large-scale surface flows (differential rotation and meridional flow) and a diffusivity. The evolution magnetic field at the solar surface, $r = R_\odot$ is assumed to be radial. Therefore the explicit simplified radial field component of MHD induction equation in Equation (5.2.2) at r = R, which is surface mangnetic field, B_r, so the governing equation of the STABLE model is

$$\begin{aligned}\frac{\partial B_S}{\partial t} &= -\frac{1}{r\sin\theta}\left[\frac{\partial(\sin\theta v_\theta B_r)}{\partial\theta}+\frac{\partial(v_\phi B_r)}{\partial\phi}\right] \\ &\quad +\frac{\eta}{R^2}\left[\frac{1}{\sin\theta}\frac{\partial}{\partial\theta}\left(\sin\theta\frac{\partial B_r}{\partial\theta}\right)+\frac{1}{\sin^2\theta}\frac{\partial^2 B_r}{\partial\phi^2}\right]-\eta\frac{2B_r}{r^2} \qquad (5.2.24)\end{aligned}$$

where in Equation (5.2.24) $B_S(\theta,\phi)$ denotes the radial component of the magnetic field at the solar surface, r = R, v_ϕ is the velocity in the longitudinal ($\hat{\boldsymbol{\phi}}$) direction, v_θ is the velocity in the latitudinal ($\hat{\boldsymbol{\theta}}$) direction, η is the horizontal diffusivity at the surface (which we have assumed is uniform), ϕ and θ are the solar heliographic longitude and heliographic colatitude respectively and R is the solar radius. The flux concentrations, which representing the radial photospheric magnetic field, depends on the first term on the right hand side represents the advection of magnetic flux by the surface flows, which include differential rotation, meridional flow, and inflows towards active regions, the latter of which we model as a three-dimensional flows.

Studies has been made on this and they noticed that, the inflows toward the active region that connects their activity-related variation with the measured magnetic field at

the solar surface. The inflows are directly related to the surface magnetic field distribution, we have been using in the STABLE model. This is consistent with the theoretical model of flows toward active regions being driven by the cooling associated with the excess brightness of magnetic features in plage and enhanced network regions ([Gizon and Rempel.(2008), Cameron and Schüssler,(2010)], Spruit 2003). The strength of the inflow toward each magnetic feature is taken to be proportional to the radial magnetic field at the surface, $|B_r|$. The flow at any point is the superposition of the effect of all magnetic features. The individual inflows are radially symmetric at the surface, so that the strength of the resulting superposed large-scale flow is proportional to the horizontal gradient of $|B|$.

Since our model is 3D and nonaxisymmetric, so we will consider all components of the inflows; these are latitudinal, longitudunal and radial components. The latitudinal inflow, $v_\theta(r, \theta, \phi, t)$, and the longitudunal inflow, $v_\phi(r, \theta, \phi, t)$, to be proportional to the latitudinal derivative and the longitudinal derivative respectively of the longitudinally averaged magnetic field, $\langle|B|\rangle$ (θ, ϕ, r, t) [Cameron and Schüssler,(2010)], [Cameron and Schüssler,(2012)]. The resulting expression of horizontal velocity at the surface, $\mathbf{v}_S(\theta, \phi, t)$ is given as follow:

$$\mathbf{v}_s(\theta, \phi, t) = c\nabla_h \left(\frac{\sin\theta}{\sin 30^\circ} |B_r|_{sm} \right) \tag{5.2.25}$$

The constant of proportionality, c , is an adjustable constant that we will specify to control the speed of the inflow with those of the helioseismic observed value of the inflow towards the active regions, by requiring that the amplitude of the inflow should be comparable to that reported by ([Gizon et al.(2010)]) and is calibrated as c = 23.77 m $s^{-1}G^{-1}$ deg. The term $\frac{\sin\theta}{\sin 30^\circ}$ In Equation (5.2.25), which suppresses unrealistically strong flow perturbation that would otherwise result at high latitudes from the gradient of the polar fields. Where in Equation 5.2.25, $|B_r|_{sm}$ is the smoothed absolute value of surface magnetic field. We removed small-scale fluctuations from the both latitudinal

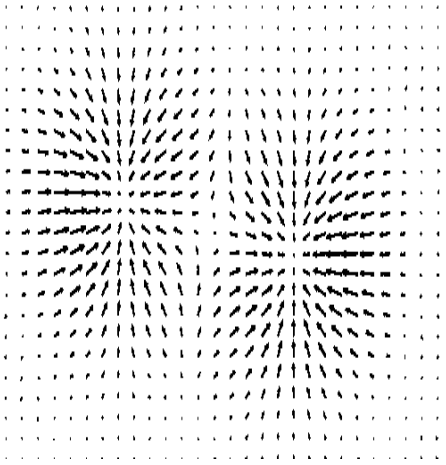

(a) Inflow into individual sunspots before the smoothing sunspot

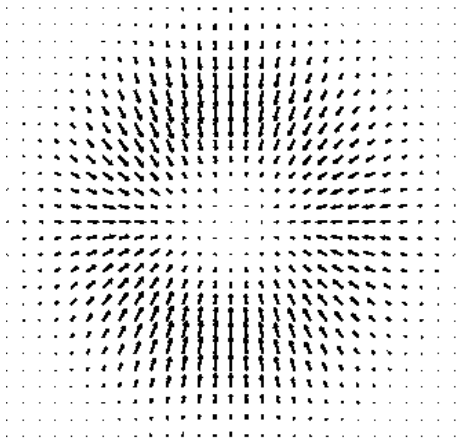

(b) Inflow ino the active region after smoothing the BRMs (sunspot) becomes single polarity

and longitudinal derivatives by smoothing the absolute value of surface magnetic field, B_r with a Boxcar of diameter 15°. In Equation 5.2.25 ∇_h is the horizontal gradient operator given by;

$$\boldsymbol{\nabla}_h = \frac{1}{r}\frac{\partial}{\partial\theta}\hat{e}_\theta + \frac{1}{rsin\theta}\frac{\partial}{\partial\phi}\hat{e}_\phi \quad . \tag{5.2.26}$$

We use the SpotMaker algorithm to put one sunspot pair at latitude 25^o with tilt angle 35^o, Joy's law, at each hemisphere. As a result sunspot appear as pairs of opposite magnetic polarity in both northern ans southern hemispheres 5.4*a*. This satisfies, Hale's polarity laws, the polarity of the leading spots (with respect to the direction of solar rotation) of sunspot pairs is the same in a given solar hemisphere and the polarity of the leading spots of sunspot pairs is opposite in the north and south hemispheres. Then we allow our code to evolve the magnetic field from this sunspot pair leading to the build-up of the polar field.

Figure 5.4*a* shows snapshots of radial magnetic field, B_r on the solar surface, which the inflow velocities produced from. Whereas Figure 5.4*b*, is the absolute value of the magnetic flux density,smoothed with a Boxcar at a radius of 7.5°.

Now define the full 3D horizontal velocity field like this:

$$\mathbf{v}_h(r = R_\odot, \theta, \phi, t) = v_\phi(r, \theta, \phi, t)\hat{\phi} + v_\theta(r, \theta, \phi, t)\hat{\theta} \tag{5.2.27}$$

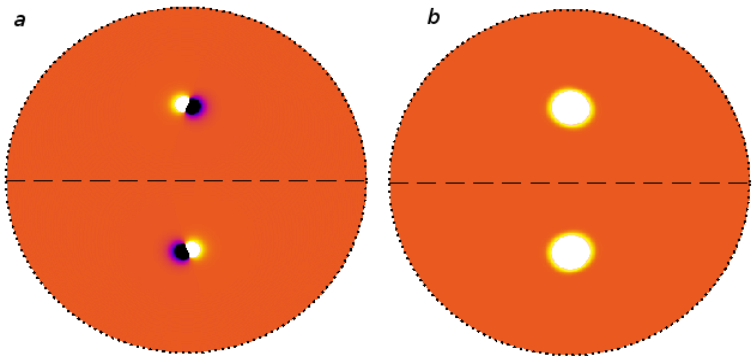

Figure 5.4: Effect of the inflow on the radial magnetic field

(a) Shows Radial magnetic fields, B_r on the surface of the sun with a single BMR in the northern and southern hemispheres, Here red color shows the outwards going radial magnetic field and blue color represents inward going radial field. (b) is the absolute value of the magnetic flux density, $|B_r|$, smoothed with a Boxcar radius of 15°. The color scale is set at ±maximum values of the magnetic fields for each case. For example ± 4.66 G is the color scale for (a) and ±0.10 G is the color scale for Coverging flows towards the active regions from observation.

At the surface r= R (radius of the sun) $\mathbf{v}_h(r = R, \theta, \phi, t) = \mathbf{v}_S(\theta, \phi, t)$.

Now consider the continuity equation, mass is conserved and the mass flux is divergenceless.

Now, from the anelastic mass continuity equation, we know that

$$\boldsymbol{\nabla}\cdot(\overline{\rho}\mathbf{v}) = 0 \tag{5.2.28}$$

$$\boldsymbol{\nabla}\cdot(\overline{\rho}\mathbf{v}) = \frac{1}{r^2}\frac{\partial(r^2\overline{\rho}v_r)}{\partial r} + \nabla_h \cdot (\overline{\rho}\mathbf{v}_h) = 0 \tag{5.2.29}$$

$$\frac{1}{r^2}\frac{\partial(r^2\overline{\rho}v_r)}{\partial r} = -\nabla_h \cdot (\overline{\rho}\mathbf{v}_h) \tag{5.2.30}$$

where ∇_h is the horizontal divergence and $\mathbf{v}_h = v_\theta + v_\phi$ horizontal velocity respectively. Now, just to make the notation easier to read, lets define the horizontal divergence as

$$\Delta = \nabla_h \cdot (\overline{\rho}\mathbf{v}_h) \tag{5.2.31}$$

Next take $\overline{\rho}$ out of the gradient operator because it only depends on r and lets define the horizontal divergence as

$$\frac{1}{r^2}\frac{\partial(r^2\overline{\rho}v_r)}{\partial r} = -\overline{\rho}\nabla_h \cdot \mathbf{v}_h = -\Delta \tag{5.2.32}$$

Let us define $\overline{\rho}v_r(r,\theta,\phi,t)$, using the method of separation of variables, by writing

$$\overline{\rho}v_r(r,\theta,\phi) = H(\theta,\phi)F(r) \quad . \tag{5.2.33}$$

Equation 5.2.32 and 5.2.33, gives as

$$\Delta = -\frac{1}{r^2}\frac{\partial(r^2\overline{\rho}v_r)}{\partial r} = -\frac{1}{r^2}\frac{\partial(r^2H(\theta,\phi)F(r))}{\partial r} = -H\frac{1}{r^2}\frac{\partial(r^2F(r))}{\partial r} \tag{5.2.34}$$

This can be written as:

$$\Delta = -H\frac{1}{r^2}\frac{\partial(r^2F(r))}{\partial r} \tag{5.2.35}$$

Now we need to specify $F(r)$ in (5.2.33). To do this, write $F(r)$ as a polynomial and given as

$$F(r) = a + bx + cx^2 \tag{5.2.36}$$

From this we can define x, as $x = (r - r_p)/(R - r_p)$ where, R is radius at the surface. Here r_p is a penetrartion depth of the inflow, which is equal to the penetrartion radius of the sunspots. It can be the base of the convection zone or it can be higher up, like 0.90R, the latter is value we use in our model.

$F = 0$ at $r = R$ is $x = 1$,

$F = 0$ at $r = r_p$ is $x = 0$ and

$F = 1$ at $r = (R + r_p)/2$ is $x = 1/2$.

These all gives as $a = 0$, $b = 4$ and $c = -4$. Then we have

$$F(r) = x(4 - 4x) \tag{5.2.37}$$

$$F'(r) = 4(1 - 2x)/(R - r_p) \tag{5.2.38}$$

Next we need to determine the $H(\theta,\phi)$. So to determine this consider equation (5.2.32) at the surface r = R

$$\Delta(R,\theta,\phi) = \overline{\rho}\boldsymbol{\nabla}\cdot\mathbf{v}_h = \overline{\rho}(R)\boldsymbol{\nabla}\cdot\mathbf{v}_s \tag{5.2.39}$$

The term, $\boldsymbol{\nabla}\cdot\mathbf{v}_s$ in Equation 5.2.39 is calculated from the divergence of Equation (5.2.25) which gives,

$$\boldsymbol{\nabla}\cdot\mathbf{v}_s = c\nabla_h^2\left(\frac{\sin\theta}{\sin 30^\circ}\langle|B_S|\rangle\right) \tag{5.2.40}$$

Now equation (5.2.35) and (5.2.39) can be give as

$$\Delta = \overline{\rho}(R)\boldsymbol{\nabla}\cdot\mathbf{v}_s = -H\frac{1}{r^2}\frac{\partial(r^2F(r))}{\partial r} \tag{5.2.41}$$

This can be written as:

$$H = -\frac{\overline{\rho}(R)\boldsymbol{\nabla}\cdot\mathbf{v}_s}{\delta} \tag{5.2.42}$$

where $\delta = \frac{1}{r^2}\frac{\partial(r^2F(r))}{\partial r}$, and can be evaluated at r = R, so it is just a single number (not a function of r) and $\overline{\rho}(R)$ is the value of the density at r = R and is calculated as fllows:

$$\delta = \left.\frac{1}{r^2}\frac{\partial(r^2F(r))}{\partial r}\right|_{r=R} = -\frac{4}{R-r_p} \tag{5.2.43}$$

Now take the sherical harmonic transformation of equation (5.2.42)

$$\widetilde{H}_{\ell,m} = -\frac{\overline{\rho}(R)}{\delta}\widetilde{\boldsymbol{\nabla}\cdot\mathbf{v}}_{s\ell,m} \tag{5.2.44}$$

we already have the $\overline{\rho}v_r(r,\theta,\phi) = -\nabla_h^2 W$ and can be written as

$$\overline{\rho}v_r(r,\theta,\phi) = -\nabla_h^2 W = H(\theta,\phi)F(r) \tag{5.2.45}$$

Take the sherical harmonic transformation of equation (5.2.45) we have

$$\frac{\ell(\ell+1)}{r^2}\widetilde{W}_{\ell,m} = \widetilde{H}_{\ell,m}F(r) = -F(r)\frac{\overline{\rho}(R)}{\delta}\widetilde{\boldsymbol{\nabla}\cdot\mathbf{v}}_{s\ell,m} \tag{5.2.46}$$

$$\widetilde{W}_{\ell,m} = -F(r)\frac{r^2}{\ell(\ell+1)}\frac{\overline{\rho}(R)}{\delta}\widetilde{\boldsymbol{\nabla}\cdot\mathbf{v}}_{s\ell,m} \tag{5.2.47}$$

where

$$\widetilde{\boldsymbol{\nabla}\cdot\mathbf{v}}_{s\ell,m} = -c\frac{\ell(\ell+1)}{r^2}\left(\frac{\widetilde{\sin\theta}}{\sin 30^\circ}\langle|B_S|\rangle\right) \tag{5.2.48}$$

Finally from Equation (5.2.11) and 5.2.47 the resulting expansion for poloidal mass flux reads:

$$W(r,\theta,\phi,t) = -F(r)\frac{r^2}{\ell(\ell+1)}\frac{\overline{\rho}(R)}{\delta}\widetilde{\boldsymbol{\nabla}\cdot\mathbf{v}}_{s\ell,m}Y_{\ell m}(\theta,\phi) \quad . \tag{5.2.49}$$

$$\frac{\partial W}{\partial r} = -[2rF(r)+r^2F'(r)]\frac{1}{\ell(\ell+1)}\frac{\overline{\rho}(R)}{\delta}\widetilde{\boldsymbol{\nabla}_h\cdot\mathbf{v}}_{s\ell,m}Y_{\ell m}(\theta,\phi) \quad . \tag{5.2.50}$$

Now substitute Equation (5.2.49) in to poloidal mass flux components Equation (5.2.19 - 5.2.21), and we get the following inflow velocities from the components of mass flux:

$$\mathbf{v}_{inr} = -\frac{1}{\overline{\rho}}\nabla_h^2\ \left(-F(r)\frac{r^2}{\ell(\ell+1)}\frac{\overline{\rho}(R)}{\delta}\widetilde{\boldsymbol{\nabla}\cdot\mathbf{v}}_{s\ell,m}Y_{\ell m}(\theta,\phi)\right) \quad , \tag{5.2.51}$$

$$\mathbf{v}_{in\theta} = \frac{1}{\overline{\rho}r\sin\theta}\frac{\partial}{\partial\theta}\left(-[2rF(r)+r^2F'(r)]\frac{1}{\ell(\ell+1)}\frac{\overline{\rho}(R)}{\delta}\widetilde{\boldsymbol{\nabla}_h\cdot\mathbf{v}}_{s\ell,m}Y_{\ell m}(\theta,\phi)\right) \quad , \tag{5.2.52}$$

$$\mathbf{v}_{in\phi} = \frac{1}{\overline{\rho}r\sin\theta}\frac{\partial}{\partial\phi}\left(-[2rF(r)+r^2F'(r)]\frac{1}{\ell(\ell+1)}\frac{\overline{\rho}(R)}{\delta}\widetilde{\boldsymbol{\nabla}_h\cdot\mathbf{v}}_{s\ell,m}Y_{\ell m}(\theta,\phi)\right) \quad . \tag{5.2.53}$$

Figures (5.6 and 5.7) shows an outflows at greater depths (compare with Figure 5.2).

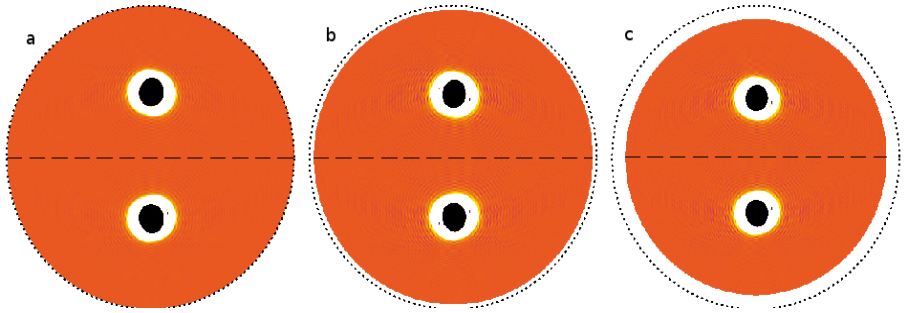

Figure 5.5: Radial inflow

This is from our inflow model; it shows radial inflow, black/white shows downward draft/outward flow of mass flux. Figure *a* is at the surface r=R, *b* at radius of 0.96R and *c*, is at radius of 0.92R.

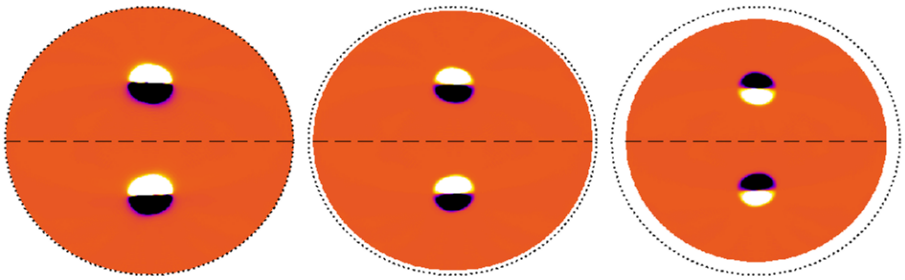

Figure 5.6: Latitudinal inflow

This is latitudinal inflow that shows in the greater depth, outflow manifests that connected to the surface inflow at the surface; Figure, *left panel* is at the surface r=R and *middle panel* at radius of 0.96R and *right panel* is at radius of 0.92R.

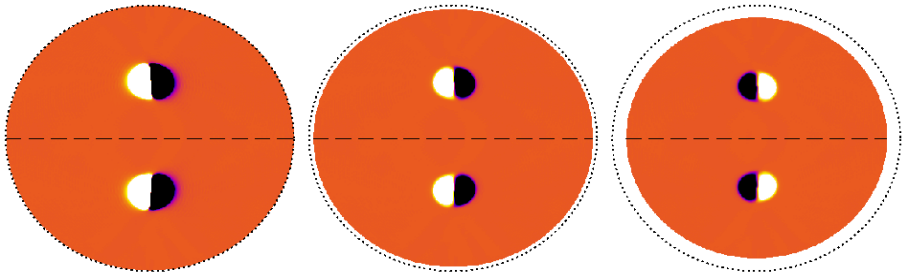

Figure 5.7: Longitudinal inflow

This is longitudinal inflow that shows in the greater depth, outflow manifests that connected to the surface inflow at the surface; Figure, *left panel* is at the surface r=R and *middle panel* at radius of 0.96R and *right panel* is at radius of 0.92R

Chapter 6

Inflows as a Dynamo Saturation Mechanism

We study the effect of the inflows towards the active regions on the evolution of the Sun's large-scale magnetic field by comparing simulations with and without the inflows (that is the reference model: tilt angle saturation mechanism).

6.1 Modifications of Model Ingredients

The evolution of the magnetic field on the solar surface is governed by the simplified induction equation (may be radial component of the induction equation). Some terms of the simplified induction equation represents the advection of magnetic flux by the surface flows, which include differential rotation, meridional flow, and inflows towards active regions

Now we will look at the total flow velocity, $\mathbf{v}$, which consists of the meridional circulation includes the $\langle \mathbf{v}_r \rangle$ and $\langle \mathbf{v}_\theta \rangle$ components, differential rotation, which contain the $\langle \mathbf{v}_\phi \rangle / r \sin\theta$ and inflow, $\mathbf{v}_{in}$, which has three components ($\mathbf{v}_r$, $\mathbf{v}_\theta$, and $\mathbf{v}_\phi$) rewrite as:

$$\mathbf{v} = \tilde{\rho}(r)^{-1} \, \boldsymbol{\nabla} \times \left[\psi(r,\theta) \hat{\boldsymbol{\phi}} \right] + \lambda \Omega(r,\theta) \hat{\boldsymbol{\phi}} + \mathbf{v}_{in} \tag{6.1.1}$$

where $\psi(r,\theta)$ is the stream function for the meridional mass flux and $\tilde{\rho}(r)$ is the dimensionless density stratification, $\lambda = r\sin\theta$ is the cylinderical radius, and $\Omega(r,\theta)$ is the

differential rotation and $\mathbf{v}_{in}$ is the inflow velocity, which is described in Equation (5.2.51-5.2.53).

The meridional circulation is same profile given in many previous publications, particularly in ([Karak and Miesch(2017)]). This MC is bit different from the advection-dominated model presented in (Chapter 3 §3.4.1) to solve the problem discussed in Chapter 4; the poleward migration being too slow (see §4.2.1 for details).

$$\mathbf{v} = \tilde{\rho}(r)^{-1}\ \boldsymbol{\nabla}\times\left[\psi(r,\theta)\hat{\boldsymbol{\phi}}\right] \tag{6.1.2}$$

$$r\sin\theta\ \psi(r,\theta) = -\psi_0\ \ (\tilde{r}-r_b)\ \ f_{mc}(r)\ h_{mc}(r,\theta) \tag{6.1.3}$$

with

$$f_{mc}(r) = \sin\left[\frac{\pi(\tilde{r}-r_b)}{(\tilde{R}-r_b)}\right]\exp\left[-\left(\frac{\tilde{r}-r_0}{\Gamma}\right)^2\right] \tag{6.1.4}$$

and

$$h_{mc}(r,\theta) = \left(1-\exp\left[-\beta_1\theta^{\epsilon}\right]\right)\left(1-\exp\left[\beta_2(\theta-\pi/2)\right]\right) \tag{6.1.5}$$

Here $\tilde{r} = r/L$ is a nondimensional radius based on a length scale $L = 1.09\times10^{10}$ cm and $\tilde{R} = R/L$. The parameters we use here are as follows: $\psi_0 = 4.32\times10^{13}$ cm^2 s^{-1}, $\theta_0 = 0$, $r_b = 0.69$, $r_0 = (\tilde{R}-r_b)/5$, $\Gamma = 3$, $\beta_1 = 0.1$, $\beta_2 = 0.3$, and $\epsilon = 2+10^{-8}$. The resulting profile is similar to the contour plot illustrated in Fig. 3.2(b). The nondimensional density stratification profile in the convection zone given by:

$$\tilde{\rho} = \left(\frac{R}{r}-0.97\right)^n \tag{6.1.6}$$

with $n = 1.5$.

The r and θ components of the meridional flow are given through the relationship, $\mathbf{v} = \tilde{\rho}(r)^{-1}\ \boldsymbol{\nabla}\times\left[\psi(r,\theta)\hat{\boldsymbol{\phi}}\right]$. This meridional circulation profile closely resembles the surface observations, near the surface it is poleward with a maximum speed of 10 m s^{-1}, near the base of the CZ it is equatorward with a speed of about 2 m s^{-1}, and it smoothly goes to zero at the lower boundary (0.69R).

Note that in this study we have considered a single cell circulation per hemisphere. Recent helioseismic inversions suggest that this may not be accurate, but they have not yet converged on a robust determination of what the structure and amplitude may in fact be. In the absence of this information and to make contact with previous BL dynamo models, we have retained the single-celled profile. Others have investigated the role of multicelled circulation profiles in 2D BL/flux transport dynamo models, and they have demonstrated that these models are still viable, provided that the circulation near the base of the convection zone is equatorward and that the convective transport of the poloidal flux (typically parameterized by a turbulent diffusion and a magnetic pumping) is sufficiently efficient [Karak and Miesch(2017)].

Now the heliographic latitudinal component of velocity at the surface are given by

$$v_\theta(R,\theta,\phi,t) = v_{mc}(R,\theta) + v_{in\theta}(R,\theta,\phi,t) \tag{6.1.7}$$

Again we replace v_{mc} by $v_\theta = -\tilde{\rho}(r)^{-1}\ \frac{1}{r\sin\theta}\frac{\partial(r\psi\sin\theta)}{\partial r}\hat{\boldsymbol{\theta}}$ that is meridional circulation along the latitudinal direction and v_θ, from the inflow velocity given in Equation (5.2.52), these also give total flow in the latitudinal direction

$$v_{mc}(r,\theta,\phi,t) = v_{\theta mc}(r,\theta) + v_{\theta in}(r,\theta,\phi,t) \quad . \tag{6.1.8}$$

The solar meridional flow is an important ingredient in Babcock-Leighton type models of the solar dynamo. Global variations of this flow have been suggested to explain the variations in the amplitudes and lengths of the activity cycles [Cameron and Schüssler,(2010)]. The primary effect of the converging large-scale flows around active regions, which alter the mean meridional circulation and thus the magnetic flux transport affecting the strength and duration of the solar ativity cycle (see Figure 6.1).

For differential rotation, we use an analytic function that captures the observed helioseismic data. This profile has been used in many previous publications, particularly in MT16; (for details, see Chapter §3.4.2 Equations (3.4.13 - 3.4.14).

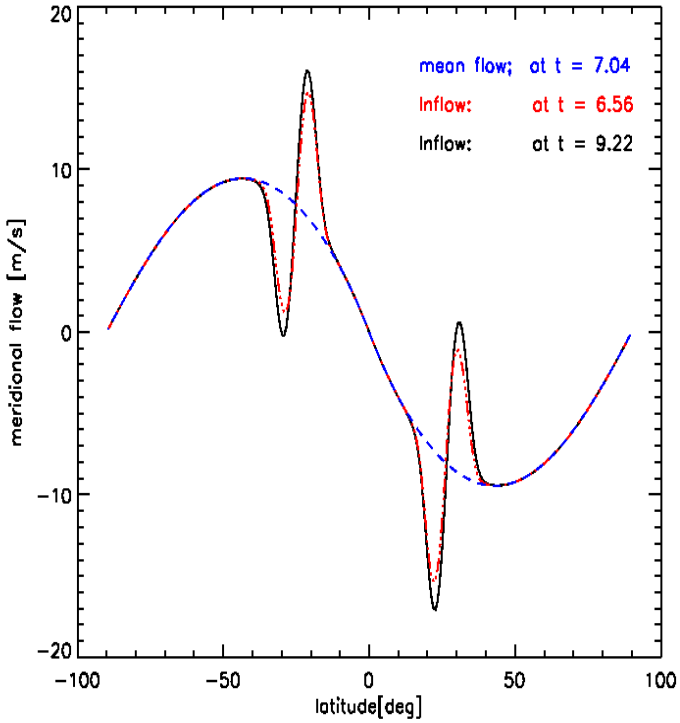

Figure 6.1: Effect of converging flows on the meridional circulation

Effect of converging flows towards the active regions; Variation of latitudinal component of meridional circulation profile for the simulations of a single pairs of sunspot in both hemisphere (see 6.5), v_θ with latitude on the surface. Positive flow velocities are directed northward. The blue curve show the profile without inflow perturbation ($v_{in} = 0$).

Nonetheless the, now the flow along the heliographic longitudinal direction is replaced by the summation of inflow velocity along the heliographic longitude, that is given in Equation (5.2.53) and as a result Ω, is the angular velocity of the differential rotation, the result of this expansion reads;

$$v_\phi(r, \theta, \phi, t) = r \sin\theta \Omega(r, \theta) + v_{in\phi}(r, \theta, \phi, t) \tag{6.1.9}$$

Now the heliographic longitudunal component of velocity at the surface are given by

$$v_\phi(R, \theta, \phi, t) = R_\odot \sin\theta \Omega(R, \theta) + \mathbf{v}_{in\phi}(R, \theta, \phi, t) \tag{6.1.10}$$

In this model; inflow into the active region, we do not consider the small-scale convective flow and thus to capture its mixing effect we consider an effective turbulent diffusivity represented by η_t in Equation 5.2.1. This is actually the sum of the molecular and turbulent diffusivities. We do not have a reliable estimate of η_t in the deep CZ. The mixing length theory and other theoretical studies suggest that the value of η_t in the mid convection zone is of the order of $10^{12}\ cm^2 s^{-1}$ (Parker 1979; [Miesch et al.(2012)]. Near the surface, at least, it is fairly constrained by observations as well as by the surface flux transport model and it is about a few times $10^{12}\ cm^2 s^{-1}$. Hence in our model, we choose the following radial dependent profile for η_t [Karak and Miesch(2017)]:

$$\eta_t = \eta_c + \frac{\eta_{mid}}{2}\left[1 + \mathrm{erf}\left(2\ \frac{r - r_{da}}{d_a}\right)\right] + \frac{\eta_{top}}{2}\left[1 + \mathrm{erf}\left(2\ \frac{r - r_{db}}{d_b}\right)\right] \quad , \tag{6.1.11}$$

where $\eta_c = 1.0 \times 10^9$ cm^2 s^{-1}, $\eta_{mid} = 1.5 \times 10^{12}$ cm^2 s^{-1}, and in the surface layer $\eta_{top} = 3 \times 10^{12}$ cm^2 s^{-1}, while $r_{da} = 0.715R$, $d_a = 0.0125R$, $r_{db} = 0.956R$, and $d_b = 0.025R$.

Note that the relatively higher value of η in the mid CZ, 1.5×10^{12} cm^2 s^{-1} places our simulations in the so-called diffusion-dominated regime where the diffusive flux transport across the CZ dominates over advection by the meridional circulation. In diffusion-dominated dynamos the cycles are faster than that in advection-dominated dynamos, due to enhanced diffusive transport added to the advective transport of magnetic flux. Several recent studies have suggested that the diffusion-dominated regime may be more realistic, based on the correlation of the polar field at solar minimum with the strength of the next cycle ([Jiang, et al.(2017)], [Yeates et al.(2008)]), the Waldmeier effect [Karak and Choudhuri(2011)], and the efficiency of turbulent transport inferred from helioseismic measurements [Miesch et al.(2012)].

6.1.1 Turbulent Pumping

In addition to the large-scale meridional circulation, we include a magnetic pumping in the radial and latitudinal direction, the γ_r effect in our model, it acts only in the large-scale magnetic component, and orginates with the turbulent emf (see §3.3.10). This γ_r appears as an advective term in the mean-field induction equation. Unlike the large-scale circulation, γ is not divergenceless. Theoretical analysis and local magneto-convection simulations predict a downward magnetic pumping in the surface CZ.

Turbulent pumping can also be measured in numerical simulations, which indicate that the predominant effect is a downward pumping driven by the stratification, with magnetic fields being expelled from the high-diffusivity regions to the low diffusivity regions. In the presence of rotation, turbulent pumping also takes place in the latitudinal direction, with a velocity reaching values of the order of a few meters per second at high rotation rates. However we neglect longitudinal pumping in comparison with differential rotation. Although turbulent pumping is seldom explicitly included in the simple mean-field dynamo models to be discussed presently, its impact on dynamo action in the sun and solar-type stars is likely important; this is because it can offset flux loss through magnetic buoyancy, and favors accumulation of magnetic fields in the tachocline, where the large shear and low magnetic diffusivity are conducive to the production of strong toroidal flux rope-like structures, believed to give rise to sunspots following their destabilization, buoyant rise through the convection zone and surface emergence [Charbonneau(2013)].

The γ_r, appearing as an advective term in the dynamo equation 3.3.10, is the magnetic pumping. In most of the simulation, we include a downward magnetic pumping motivated by [Karak and Cameron(2016), Karak and Miesch(2017)].

$$\gamma_r(r) = -\frac{\gamma_{CZ}}{2}\left[1 + erf\left(\frac{(r-0.725R)}{0.01R}\right)\right] - \frac{\gamma_S}{2}\left[1 + erf\left(\frac{(r-0.9R)}{0.02R}\right)\right] \quad . \quad (6.1.12)$$

Due to the lack of knowledge of the exact latitudinal variation of longitudinal pumping, we take it to be only a function of radius. The pumping is efficient near the surface

(mainly caused by the topological asymmetry of the convective flow), while the deeper convection is weaker and less stratified. The pumping helps to boost the efficiency of the dynamo by suppressing the diffusion of toroidal flux through the surface [Karak and Cameron(2016), Karak and Miesch(2017)].

Therefore in Equation 5.2.3, which is the total flow velocity, we replace v_r by contributions from $v_r = \tilde{\rho}(r)^{-1} \frac{1}{r\sin\theta}\frac{\partial(\psi\sin\theta)}{\partial\theta}\hat{\boldsymbol{r}}$, as a result of meridional circulation, γ_r, turbulent pumping, and the contribution of inflow velocity along the radial direction given in Equation 5.2.51 gives

$$v_r(r,\theta,\phi,t) = v_{rmc}(r,\theta) + \gamma_r(r) + v_{rin}(r,\theta,\phi,t) \quad . \tag{6.1.13}$$

6.2 Magnetic Field Dependent BMR Emergence Rate

In the STABLE model we use the SpotMaker algorithm which deposits BMRs on the surface based on the toroidal flux near the base of the convection zone. In Spot-Maker, we do the following steps. First, we compute the strength of the spot-producing toroidal flux near the base of the CZ (see details in section 3.5 and 3.6).

$$\hat{\mathbf{B}}_\phi(\theta,\phi,t) = \int_{r_a}^{r_b} h(r)\mathbf{B}_\phi(\theta,\phi,t)dr \quad . \tag{6.2.1}$$

where, $r_a = 0.70$ R, $r_b = 0.715$R, and $h(r)$ as a normalization factor. We note that to have a prominent equatorward migration of sunspots, the spot-producing toroidal flux is computed above the tachocline where the flow is strongest. A necessary (but not sufficient) condition to produce a BMR that $\hat{\mathbf{B}}_\phi(\theta,\phi,t)$ exceeds a threshold field strength $\mathbf{B}_t(\theta)$. If this condition is satisfied on multiple grid points, then out of those points randomly one point is chosen. Unlike previous publications (MD14, MT16) where a fixed value was taken for this threshold field strength, here we make it latitude dependent such that it increases exponentially towards the higher latitudes. Hence we choose

$$
\begin{aligned}
B_t(\theta) &= B_{t0}\ exp[\kappa_t(\theta - \pi/2)], \qquad for\ \theta\ >\ \pi/2 \\
&= B_{t0}\ exp[\kappa_t(\pi/2 - \theta)], \qquad for\ \theta\ \leq\ \pi/2\ . \qquad (6.2.2)
\end{aligned}
$$

Where $\kappa_t = 5$ and $B_{t0} = 2$ kG. The rapid increase of B_t in latitude is chosen to have sufficient spots near the equator and no spots beyond about $\pm$ 30° latitudes. The advantage of using such latitude-dependent B_t is that now we do not have to choose any arbitrary masking function to suppress spots above a certain latitude (Note that we use different way of masking for the inflow modeling, see 3.5.5 and 3.5.6), which was used in many previous works (e.g.,MD14 and MT16). Another advantage is that now the upper latitudinal bound for BMR emergence is not fixed, and it can vary depending on the toroidal field strength in each cycle and even in each hemisphere. This is consistent with observations that stronger cycles start producing sunspots at slightly higher latitudes. Other than some tachocline instabilities that might be operating in higher latitudes to destabilize the spot-producing toroidal field Equation 6.2.1, we have to confess that, at the moment, we do not have a clear understanding of why BMRs do not appear above a certain latitude, and the arbitrary masking function or the latitude-dependent B_t chosen here may be regarded as a semiempirical model [Karak and Miesch(2017)].

When SpotMaker produces a BMR, we do not reduce the flux locally at the progenitor location, although we do place opposing flux near the surface by virtue of the 3D structure of the BMRs; (see Section §3.7.2 for more details on this issue). Therefore, at every time step of our numerical integration, if the BMR emergence is determined only by the criterion $\hat{\mathbf{B}}_\phi(\theta, \phi)\ >\ B_t$, then we may have BMRs emerging at every time step, and the total number of BMRs will largely be determined by the integration time step and the value of B_{t0}. Thus, to make the emergence rate independent of the numerics and more realistic, we specify a time delay between two successive BMRs based on solar observations. We approximate the time delay distribution obtained from the observed

sunspot data by a log-normal distribution given as;

$$P(\Delta) = \frac{1}{\Delta\sigma\sqrt{2\pi}} \exp\left[-\frac{(\ln\Delta - \mu)^2}{2\sigma^2}\right] \quad . \tag{6.2.3}$$

Where in Equation (6.2.3) we specify the parameters mean and mode of the distribution, τ_s and τ_p and compute as

$$\sigma^2 = (2/3)\left[\ln(\tau_s) - \ln(\tau_p)\right], \tag{6.2.4}$$

and

$$\mu = \ln\tau_p + \sigma^2 \quad . \tag{6.2.5}$$

When $\tau_p = 0.8$ days and $\tau_s = 1.9$ days, the log-normal distribution,6.2.3 reasonably fits the observed data.

The time delay distribution in Equation (6.2.3) is a log-normal distribution given by fixed τ_p and τ_s. Hence as long as the spot-producing toroidal field exceeds the threshold field strength, the eruption can happen almost equally over the whole cycle. We noticed that this contributes to the significant overlap between successive cycles and before the end of a cycle, emergences from the next cycle start, and we do not observe a noticeable cyclic variation in the BMR number. One potential cause of this problem is that we have chosen a fixed time delay distribution over the entire cycle, which is unlikely to be true. In observations, we find more BMRs during solar maxima than during minima. From these observations, we estimate that, during a solar minimum, the mean time delay τ_s (and mode τ_s) of BMR appearance is about 10days (and 1 day). However, as we go toward a solar maximum, the emergence becomes more frequent, and the mean time delay can be as short as a day [Karak and Miesch(2017)].

Motivated by this observed feature, we implement a solar-cycle-dependent time delay distribution by considering τ_p and τ_s as the toroidal field dependent and this the so called cycle dependent BMR emergence rate. We note that the time delay in each hemisphere is always computed separately using Equation (6.2.3) so that no hemispheric symmetry

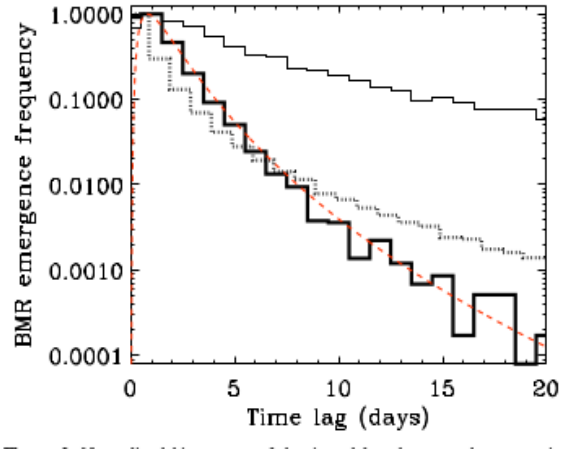

Figure 6.2: Histograms time delay of BMRs

Normalized histograms of the time delays between the successive BMR emergences obtained from the observed data during 1900 - 2002. The thick solid line is obtained by taking data within a three-year window at each cycle maximum, while the thin solid line represents the rest of the data, covering the solar minimum periods. The dashed red line is the fitted log- normal distribution with { τ_p , τ_s } o { 0.8, 1.9 } days, as given by Equation (6.2.3). The dotted line is obtained from our model (Run T1), in which the time delay is related to the magnetic field through Equation (6.2.6) [Karak and Miesch(2017)].

is imposed in this process such that in the northern hemisphere

$$\tau_p = \frac{2.2\ days}{1 + (B_b^N/B_\tau)^2} \quad , \quad \tau_s = \frac{20\ days}{1 + (B_b^N/B_\tau)^2} \quad . \tag{6.2.6}$$

Where B_b^N is the azimuthal-averaged toroidal magnetic field in a thin layer from r = 0.715 R to 0.73 R around 15° latitudes, and the value of B_τ is tuned to 400 G such that we get roughly the same number of BMRs as in observations. For the southern hemisphere, we have the same expressions for τ_s and τ_p , relating to the toroidal field in that hemisphere. In this way, no hemispheric synchronization is made in the waiting time of the BMR appearance, which is physical. We note that Lemerle & Charbonneau (2017) also used a magnetic-field-dependent delay in the BMR emergence through an emergence function, although their number of new BMRs at every numerical time step is extracted from a uniform distribution.

SpotMaker produces the first BMR once the condition $\hat{\mathbf{B}}(\theta, \phi) \ > B_t(\theta)$ is satisfied.

Then after a time Δ since the time of the previous BMR appearance, the SpotMaker produces the next BMR only when both conditions $\hat{\mathbf{B}}(\theta,\phi) \ > B_t(\theta)$ and $dt > \Delta^{N,S}$, where $\Delta^{N,S}$ is the time delay randomly obtained from the long-normal distribution given by Equation (6.2.3) for the northern (or southern) hemisphere. The superscript N,S on Δ is to emphasize that the time delay between BMRs can be different in two hemispheres because the probability is computed separately in two hemispheres. Once SpotMaker decides to produce a BMR on the surface, we need to specify its flux, tilt, separation, and spatial distribution. In comparison to previous publications (MD14; MT16; KM17), here we have some changes in order to make a close connection with observations. In the previous model, the BMR flux was directly related to the toroidal field at the base of the CZ, while in this model, it is obtained from the observed distribution. The observed BMR flux distribution can be approximated using a log-normal distribution:

$$P(\Phi) = \Phi_0 \ \frac{1}{\sigma_\Phi \Phi \sqrt{2\pi}} \ exp\left[-\frac{(ln\Phi - \mu_\Phi)^2}{2\sigma_\Phi^2}\right] \quad . \tag{6.2.7}$$

with μ_Φ= 51.2 and $\sigma_\Phi = 0.77$. Certainly, in the low-flux regime, a log normal is not the best fit of the observed flux as there are many BMRs with fluxes smaller than 5×10^{21} Mx. However, smaller BMRs may not contribute much net poloidal flux because of their smaller flux and large scattered tilts ([Stenflo and Kosovichev(2012)]). Once the flux of the BMR is obtained from the above distribution, the radius is automatically set by specifying a fixed value for the surface field strength of 3 kG. As discussed in MT16, if this radius turns out to be comparable to or smaller than the grid size of the domain, then we set the radius at five times the grid size, and the field strength is reduced accordingly.

The half distance between centers of two spots of a BMR is chosen to be 1.5 times the radius of the spot. As in our earlier model, we have assumed spots to be disconnected from their parent spot-producing fields. The surface fields are extrapolated downward using a potential field approximation as described in MT16, which yields the full 3D structure of a BMR. In our model, BMRs are assumed to be rather shallow by choosing the radial field of the spots to be zero at $r_s = 0.9$ R [Karak and Miesch(2017)].

In our previous publications (MD14, MT16), we have used the standard Joy's law: $\delta = \delta_0 \cos\theta$ for tilt angles of BMRs. Here we make two modifications in it. One is made by adding a random component δ_f around Joy's law. In observations, we notice that Joy's law is a statistical law and there is a considerable scatter around it (Howard 1991; Stenflo & Kosovichev 2012; McClintock et al. 2014; Senthamizh Pavai et al. 2015). Particularly, from the analysis of BMRs measured during 19762008, Wang et al. (2015) reported that the fluctuations of the tilts roughly follow a Gaussian distribution:

$$f(\delta_f) = \frac{1}{\sigma_\delta \sqrt{2\pi}} exp[-\delta_f^2/(2\sigma_\delta^2)] \quad . \tag{6.2.8}$$

with $\sigma_\delta \approx 15^\circ$. We understand that a Gaussian is not the best fit to the observed fluctuations of the data because of its asymmetric shape and considerable outliers near two ends of the distribution. However, to capture the broad picture of the tilt fluctuations in our model, the above Gaussian distribution is sufficient for the observated distribution of BMR tilts within 15 - 20° latitudes. Another modification to Joy's law that implemented by [Karak and Miesch(2017)] here is the tilt-angle saturation; the tilt is suppressed for strong progenitor toroidal fields. Thus the tilt used in our model is given by

$$\delta = \frac{\delta_0 \cos\theta + \delta_f}{1 + (\hat{\mathbf{B}}(\theta, \phi, t)/B_{sat})^2} \quad . \tag{6.2.9}$$

where $\delta_0 = 35^\circ$ and B_{sat} (the saturation field strength) is chosen to 1×10^5 G. In thin flux tube simulations, tilts of the BMRs are produced due to the Coriolis force acting on the toroidal flux tubes during their rise in the CZ. When the spot-producing toroidal field is strong, the field rises fast and the Coriolis force does not get much time to tilt it. Thus, from this theoretical argument, we expect some quenching in the tilt [Karak and Miesch(2017)]. In any case, we shall explore whether the above magnetic field dependent nonlinearity is sufficient to stabilize the growth of the magnetic field in Equation 5.2.2. We note that in our previous model (in Chapters 3 and 4), dynamo saturation was implemented by saturating the flux content of BMRs rather than their

tilt. The tilt angle saturation we use here has more physical justification.

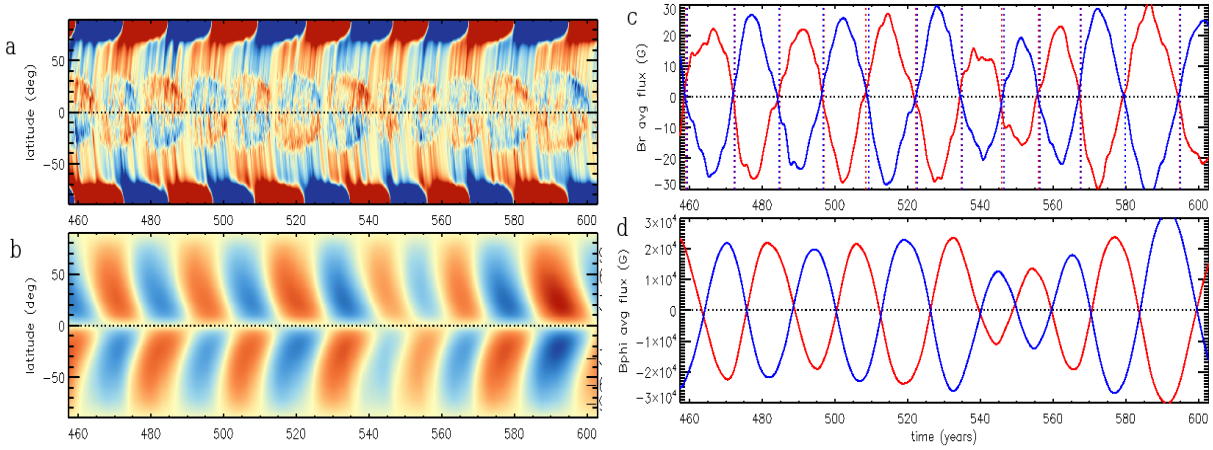

Figure 6.3: Magnetic cycles in Case T3

Butterfly diagram; (a) Mean radial field $\langle B_r \rangle$ at the surface ($r = R$) as a function of latitude and time, highlighting fourteen magnetic cycles. Blue and red denote inward and outward polarity respectively. Peak amplitudes can exceed 300 G but the color table saturates at $\pm$ 100G. (b) Mean toroidal field $\langle B_\phi \rangle$ near the base of the convection zone ($r = 0.71R$; Red and blue denote eastward and westward field respectively blue westward). (c) $\langle B_r \rangle$ averaged over the north (blue) and south (red) polar regions, above a latitude of $\pm$ 70°. Vertical dotted lines in this and all other frames mark polar field reversals in the NH (blue) and SH (red). Frame (d) are similar to frame (c) but for $\langle B_\phi \rangle$ in the lower CZ ($r = 0.71R$). However, the averages in (d) is over the entire NH (blue) and SH (red), as opposed to just the polar regions. with a saturation level for the color table of 90 kG.

The solar magnetic field is predominantly dipolar. One requirement of a theoretical solar dynamo model is that it should have dipolar parity. To make a quantitative measure of the equatorial symmetry of different components of the magnetic field, we compute the symmetric parity (SP) by cross-correlating the fields between two hemispheres in the same way as done in [Karak and Miesch(2017)].

$$SP_j(r,\theta,t) = \frac{\int_{t-T/2}^{t+T/2}(B_j^N - \overline{B_j^N})(B_j^S - \overline{B_j^S})dt'}{\sqrt{\int_{t-T/2}^{t+T/2}(B_j^N - \overline{B_j^N})^2 dt' \int_{t-T/2}^{t+T/2}(B_j^S - \overline{B_j^S})^2 dt'}} \quad . \tag{6.2.10}$$

where j stands for the r, θ, or ϕ component; $B_j^N = \langle B_j \text{ (r, } \theta\text{, } \phi\text{, t')} \rangle_\phi$, $B_j^S = \langle B_j \text{ (r, } \pi - \theta\text{, } \phi\text{, t')} \rangle_\phi$, and overlines denote the average over period T. To identify the short-term

temporal variation of the parity, we take T=3.73 yr. In all the cases, we compute the parity at a fixed radius (at 0.72R for B_ϕ and R for B_r) and average over latitudes ($\pi/2 < \theta \leq \pi$). From the above definition of parity, we expect $SP_j = 1$ for a perfect symmetric field and -1 for an antisymmetric field. We note that for a dipolar field, SP_r = - 1 , SP_θ = 1, and SP_ϕ = - 1 , and the reverse is true for the quadrupolar field.

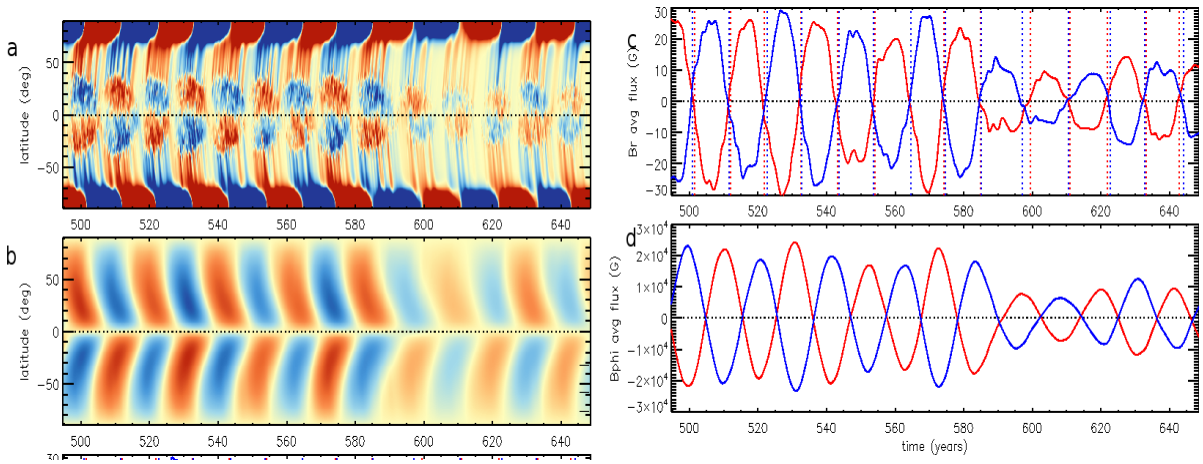

Figure 6.4: Magnetic cycles in Case T2

Butterfly diagram; (a) Mean radial field $\langle B_r \rangle$ at the surface ($r = R$) as a function of latitude and time, highlighting fourteen magnetic cycles. Blue and red denote inward and outward polarity respectively. Peak amplitudes can exceed 300 G but the color table saturates at ± 100G. (b) Mean toroidal field $\langle B_\phi \rangle$ near the base of the convection zone ($r = 0.71R$; Red and blue denote eastward and westward field respectively blue westward). (c) $\langle B_r \rangle$ averaged over the north (blue) and south (red) polar regions, above a latitude of ± 70°. Vertical dotted lines in this and all other frames mark polar field reversals in the NH (blue) and SH (red). Frame (d) are similar to frame (c) but for $\langle B_\phi \rangle$ in the lower CZ ($r = 0.71R$). However, the averages in (d) is over the entire NH (blue) and SH (red), as opposed to just the polar regions. with a saturation level for the color table of 90 kG.

6.3 Effect of the Inflows on the Build-Up of Polar Field

6.3.1 Polar Field Evolution of Two Bipolar Magnetic Regions

We start by questions such as: Do inflows constitute a potential non-linear mechanism for the saturation of the global dynamo? and do contribute to the modulation of the solar cycle in the STABLE framework? After constructing the inflow dynamo model, we now study how individual sunspot pairs contribute to the building up of the polar field and address the question of whether surface converging flows towards active regions would effect on the evolution of a bipolar magnetic regions, BMR. Furthermore, we explore how this affects the surface transport of magnetic flux, as well as their impact on the generation of the Sun's poloidal field and the build-up of the polar fields, and effects on the global dipole (may affect the build-up of the global magnetic dipole) and subsequent toroidal field to sustain the dynamo.

We use the SpotMaker algorithm to place one sunspot pair at latitude 25^o with tilt angle 35^o. Then we allow our code to evolve the magnetic field from two sunspot pairs one at each hemisphere leading to the build-up of the polar field. Snapshots of the surface distribution of the magnetic field, B_r are shown in Figure 6.5, on the solar surface at different times during the evolution process. This figure 6.5 is not a proxy of toroidal flux at the bottom of the convection zone. The consequence on the preceding and following polarities of the BMR; the leading polarity is advected toward the equator while the following polarity make to the pole. We can see this effect from the the corresponding time evolution of the polar fields is shown in Figure 6.6.

We don't provide frames of the surface distribution of the magnetic field of the no-inflow case for comparison, because they turned out to be indistinguishable from Figures 6.5 for two spotpairs in different hemispheres. However there are noticible differece in the polar field evolution. The following sunspot at the higher latitude has the positive polarity and we clearly see that this positive polarity is preferentially transported to the higher latitudes. This positive polarity region gets stretched by the differential rotation into a belt going around the polar axis. When this belt reaches sufficiently high latitude,

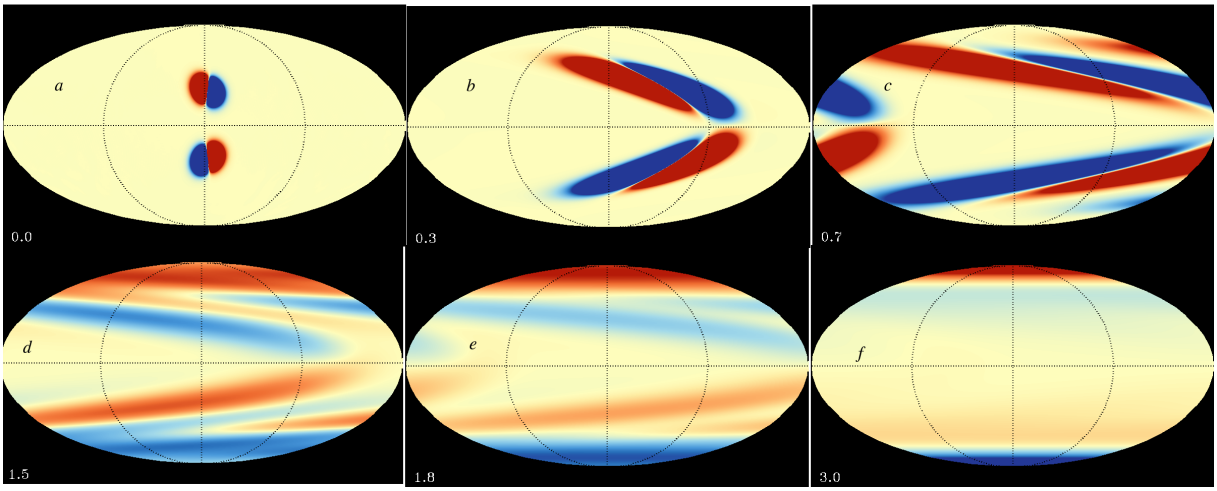

Figure 6.5: Radial field evolution on the surface of the sun form two sunspot pairs (a)Time evolution of radial fields on the surface of the sun with a single sunspot pairs emerged at latitude of $\pm$ 25° in both northern and southern hemispheres for (a) 0.0 years, (b) 0.3 years, (c) 0.7 years, (d) 1.5 years, (e) 1.8 years and (f) 3.0 years. Here red color shows the outwards going radial field and blue color represents inward going radial field.

we see that it is followed by a belt of negative polarity coming from the leading sunspot which was taken at a lower latitude.

The inflows into the active regions may play a significant role in the evolution of active regions and the transport of magnetic flux to the poles. These surface inflows may inhibit the diffusion of magnetic flux out of active regions, thereby prolonging the lifetime of an active region before it breaks up and disperses. See Figure 6.1; the converging large-scale flows around active regions, which alter the mean meridional circulation and thus the magnetic flux transport and the polar field Figure (6.6). Consequently this affecte the strength and duration of the solar ativity cycle (we will see in the immediate §6.4 the details).

In order to illustrate the effect of the converging flow into active regions in the 3D STABLE model flux transport as the source of the polar field, we first study two bipolar magnetic regions (BMRs), that is one pair of sunspots in each hemisphere. The temporal evolution of the corresponding surface flux depends on the coverging flow towards the

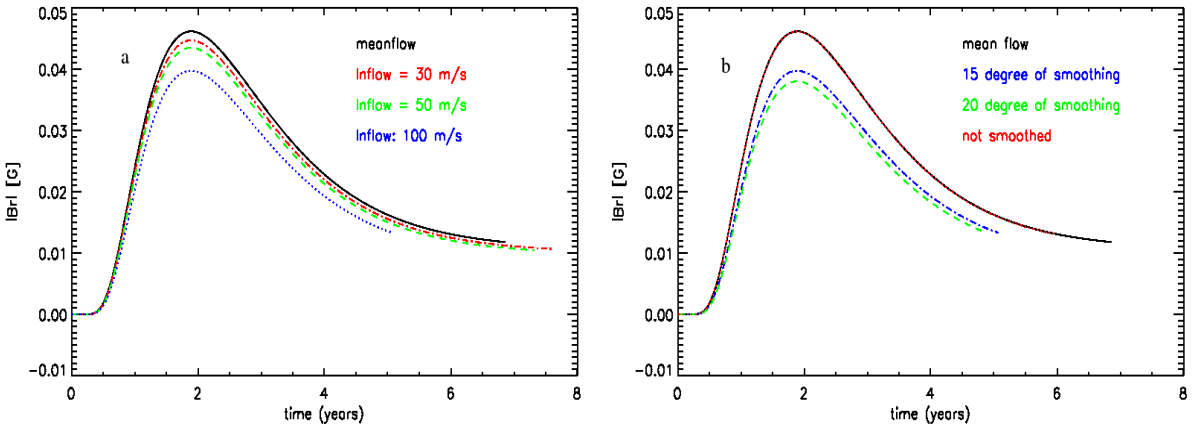

Figure 6.6: Polar field evolution

Time evolution of the polar field strength (average radial field poleward of ±60° latitude) for single sunspot pairs in both hemispheres at emergence angle latitude ±25°, and demonstrates amount of flux build-up at the at different Figure (a), amplitude of inflow velocity: $v_{in} = 0$ or is mean flow (black/solid curve), $v_{in} = 30$ m s^{-1} (red/dotted curve), $v_{in} = 50$ m s^{-1} (green/dashed curve), and $v_{in} = 100$ m s^{-1} (blue/dash dot curve). Figure (b), smoothing radius; black/solid line is mean flow, red/dotted line has no smoothing, blue/dot dushed is with 15○, (green/dashed curve) with smoothing radius of 20○.

active regions, meridional circulation, differential rotation and the emergence latitude; subsequent decaying of the of BMRs gives the poloidal field [Jiang et al.(2010)]. We consider the evolution of a BMR that emerges at t = 0 at a latitude of 25° on the northern and southern hemisphere under the influence of three different flow patterns in STABLE.

We evaluated the effects of the inflows by performing STABLE simulations, for which each emerging BMR associated with with tilt angle (not tilt angle scatter) and with different value of inflow speeds. We start our simulation by putting a single pair of bipolar sunspots in the northern and southern hemisphere at different magnitude of inflow speeds and let it evolve under the axisymmetric mean flows, nonaxisymmetric inflow and diffusion to see the development of the polar field. We have chosen magnetic flux of 1×10^{22} Mx in each spot and its radius is determined by its flux content as $r_s = (\Phi_S/B_s)^{1/2}$ throughout these simulations. In this set of simulations, we shall put two pairs of sunspots

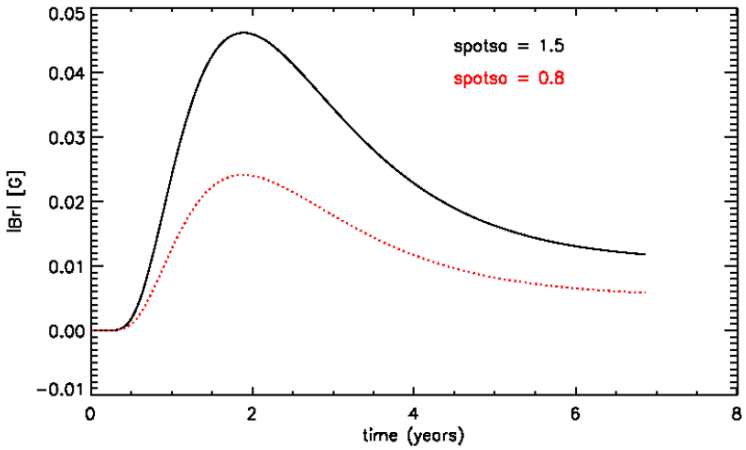

Figure 6.7: Polar field evolution from separation distance between sunspot pairs. Polar field as a function of time for different values of the separation distance between a sunspot pair of sunspot at the northern hemisphere, black/solid line is with separation distatnce between Sunspots ($spotsa = S_a$) = 1.5 and red dotted line is with $S_a = 0.8$

symmetrically in the two hemispheres, to see the effects of cross-equator diffusion of magnetic flux. Consequently Figure 6.6 shows reduction of polar field comparing to the simulation without inflow.

On this work we focus mainly on the general effect of these flows on the evolution of the solar surface field, and particularly on the strength of the polar field. Because the build-up of the magnetic field to the Sun's poles is dominated by the transport of poloidal field produced by the BL process of a BMR. We carry out a parameter study to assess how the strength and extension of the inflow speed affects the build-up of the polar field and global dipole field. The plots for these simulations are shown in Figure 6.6(a) and (b). Inflows faster than 5 m/s markedly affect the evolution of active-region flux. The most important result we find is inflows faster than 30 m/s leads to kill the dynamo (see Figure 6.8). In Figure 6.6(a) we show the stronger (weaker) inflows lead to larger (smaller) reductions of the polar field. In Figure 6.6(b) we show the larger (smaller) smoothing area lead to larger (smaller) reductions of the polar field. We find that inflows decrease the amplitude of the polar field, relative to the reference model (no-inflows scenario). The parameter study

shows that our inflow model is sensitive to parameters such as the separation distance between Sunspots (see Figure 6.7). Again Figure 6.6*b* show the build-up of the polar filed depends on the smoothing area of the active regions.

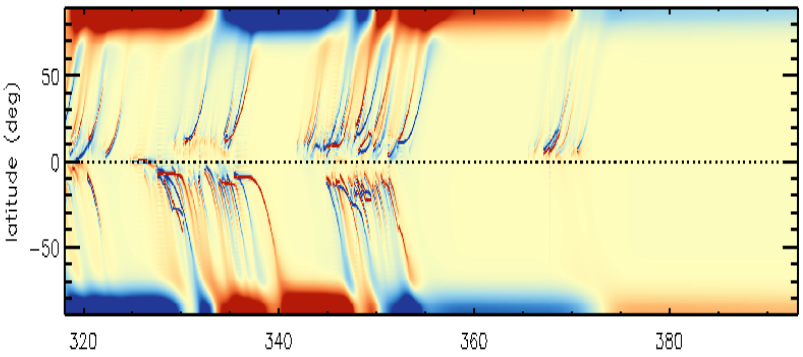

Figure 6.8: Maximum inflow amplitude (30 m/s) that kills the dynamo.

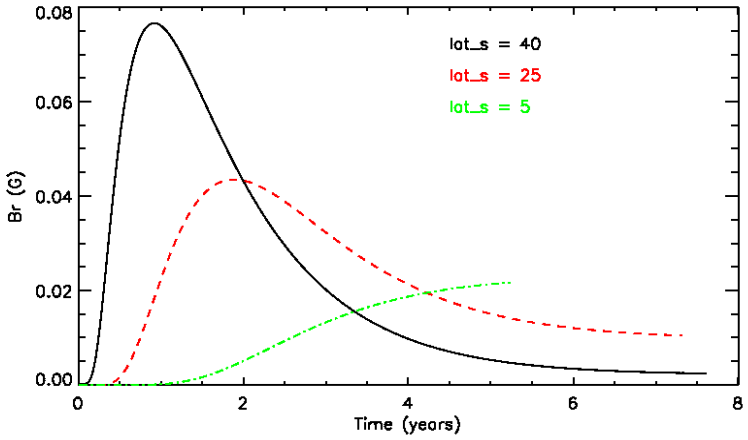

Figure 6.9: Polar field at emergence latitude

Polar field evolution with time for different emergence angle of sunspot pairs in both hemispheres with an inflow speed 50 m/s. Black solid, red dashed, and green dash dotted lines represent the polar field for the sunspot emergence at 40°, 25°, and 5°, respectively. Magnetic field is in Gauss and time is given in years.

We have also evaluated the effects of the inflows by performing STABLE simulation of the polar magnetic flux for two sunspot pairs emerging at different latitudes on the two

hemispheres Figure 6.9, to find out how much flux from the sunspots reaches the poles Figure 6.10. We calculate the polar flux by integrating B_r over only those regions of the surface between 60° latitude and the pole where B_r has one sign (positive in the north pole). While positioning the sunspot pairs by hand using the SpotMaker algorithm, we injected 1 $\times 10^{22}$ Mx flux in each spot. A normalized polar flux is computed by dividing the signed flux by the input flux (1×10^{22} Mx). In Figure 6.10*b*, we have shown the percentage of normalized polar flux with time for the spot pairs emerging at different latitudes. It is evident from this figure that around 1.7% of the input flux can reach the pole when the spot pair emerges at a high latitude like 40°, whereas 0.6% of the input flux can reach the pole when the spot pair is at a low latitude like 5°. Keeping in mind that we have used an unrealistically high tilt of 35°, we point out that the flux reaching the poles will be less for more realistic tilts [Hazra et al.(2017)]. Interestingly, we notice that the inflow develops more axial flux when sunspots emergence at low latitude, like 5°. we can clearly see this differece from Figure 14 of [Hazra et al.(2017)], which is 0.2% for sunspots placed at 5°. This is because the inflows affecting the cross-equator transport of leading-polarity magnetic flux.

6.4 Simulations of Magnetic Cycles

The BL mechanism represents the poloidal field source in Babcock-Leighton-type models of the solar dynamo and is crucial for the build-up and reversals of the polar fields in (STABLE) simulations. The evolution of the polar field is a consequence of Hale's polarity rules, together with the tilt angle distribution which has a systematic component of a tilt-angle (Joy's law). We determine the inflow from the surface magnetic field, B_r, and the flux content in the sunspots is consistent with observation and study the effects of this inflow on the evolution of the solar surface field using STABLE simulations. By performing simulations with a number of different realizations of parameters we study

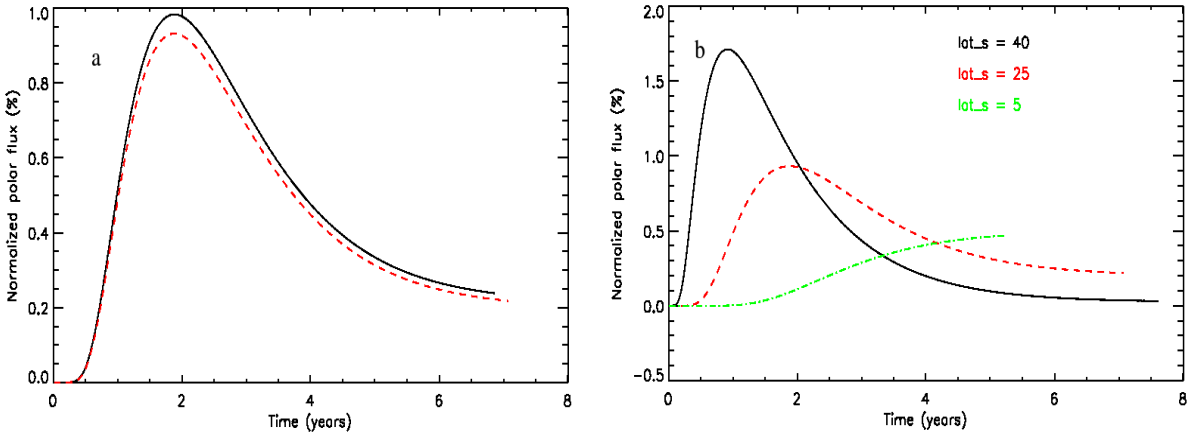

Figure 6.10: Polar field evolution in %

Polar flux evolution with time for different emergence angle of sunspot pairs in both hemispheres. (a) Black/solid curve, is without inflow, red/dashed curve is with inflow of amplitude 50 m/s; represent the percentage of normalized polar flux able to reach the pole for the sunspot emergence at 25°. (b) Black/solid, red/dashed and green/dotted lines represent the percentage of normalized polar flux able to reach the pole for the sunspot emergence at 40°, 25°, and 5°, respectively and with an inflow of amplitude 50 m/s.

the effect of the inflow on the global magnetic field, especially on the evolution of the build-up of polar field. In the framework of Babcock-Leighton dynamo models, the inflow into the active regions therefore constitutes a significant inhibit on the evolution STABLE solar dynamo model.

Results from Run 6.1 T1 with $\eta_{mid} = 1.5 \times 10^{12} cms^{-1}$ and with no fluctuations around Joy's law are shown in Figure 6.15. We note that in addition to changes in η_{mid}, γ_{CZ} and γ_S, two more changes have been made in this Table 6.1 (diffusion-dominated model) series of simulations form the previous advection-dominated model. First, the meridional circulation profile has also been changed (see Equation 6.1.2). To enhance the efficiency of the toroidal flux advection in this diffusion-dominated model, we made the meridional flow speed near the base of the CZ faster than in the previous advection-dominated model (Mt16).

Table 6.1: Simulation Summary. The T series of simulations are without converging flow in to the active regions while the C series are simulations with converging flow in to the active regions. Root-mean-square (rms) values listed in column 6 are based on integrals over the entire computational volume and are quoted for the mean toroidal field, (B_{tor}) and the mean poloidal field (B_{pol}).

Case	Φ_0	σ_δ	η_{CZ} ($\mathrm{cm^2\ s^{-1}}$)	γ_{CZ}, γ_S ($\mathrm{cm\ s^{-1}}$)	B_{tor} (kG)	B_{pol} (G)	Period (yr)	# of (reversals)	$\mathbf{v}_{in}$ (m/s)
T1	2.4	0	1.5×10^{12}	2, 20	44	2160	10.6	14	–
T2	2.4	15°	1.5×10^{12}	2, 20	65	3123	10.94	14	–
T3	3.4	15°	1.5×10^{12}	2, 20	91	3503	12.3	12	–
C1	2.4	0	1.5×10^{12}	2, 20	19	686	12.3	11	10
C2	2.4	0	1.5×10^{12}	2, 20	–		–	–	30

We recall that in the previous models ([Miesch and Teweldebirhan(2016)] in the so-called advection-dominated regime), the bulk diffusivity η_{mid} was taken to be $\eta_{mid} = 5 \times 10^{10}$ $\mathrm{cm^2\ s^{-1}}$, which is much smaller than the surface diffusivity $\eta_{top} = 3 \times 10^{12}$ $\mathrm{cm^2\ s^{-1}}$ (see §3.4.3). Previous studies from 2D BL models have demonstrated that a weaker diffusion promotes quadrupolar parity [Karak and Miesch(2017)]. Thus, we increase η_{mid} to a much larger value of $\sim 10^{12}$ $\mathrm{cm^2\ s^{-1}}$ (this is the so called diffusion-dominated regime). Unfortunately, at this higher value of η_{mid}, we do get a decaying solution (subcritical solution). One way to get a stable solution is to shift the observed flux distribution toward larger values (i.e., $\Phi_0 > 1$).

Another effective way to counteract the decaying; by [Karak and Cameron(2016)] have shown that a downward pumping near the surface reduces the diffusion of the flux across the surface and helps to achieve a dynamo at a higher value of turbulent diffusivity, η_t than hitherto. Thus, the turbulent pumping (§6.1.1) makes the dynamo efficient and thus allows us to use a smaller value of Φ_0. However when the pumping in the whole CZ is increased, the downward transport of the poloidal field becomes more efficient, which, in turn, reduces the cycle length (that is the time lag between poloidal and toroidal field conversion) [Karak and Miesch(2017)].

In Figure 6.11 the shortcoming of the model presented in [Miesch and Teweldebirhan(2016)] (example see Figure 4.5) is solved (see §4.3 for the details). The longitude-averaged, B_r butterfly diagram superficially resembles to the results presented in Chapter 4, although the inflow model is for the diffusion-dominated and inflow case in contrast to the solution of [Miesch and Teweldebirhan(2016)] obtained for the case dominated by advection due to the meridional circulation. The differences between the two cases become clear on looking at the distribution of the magnetic field.

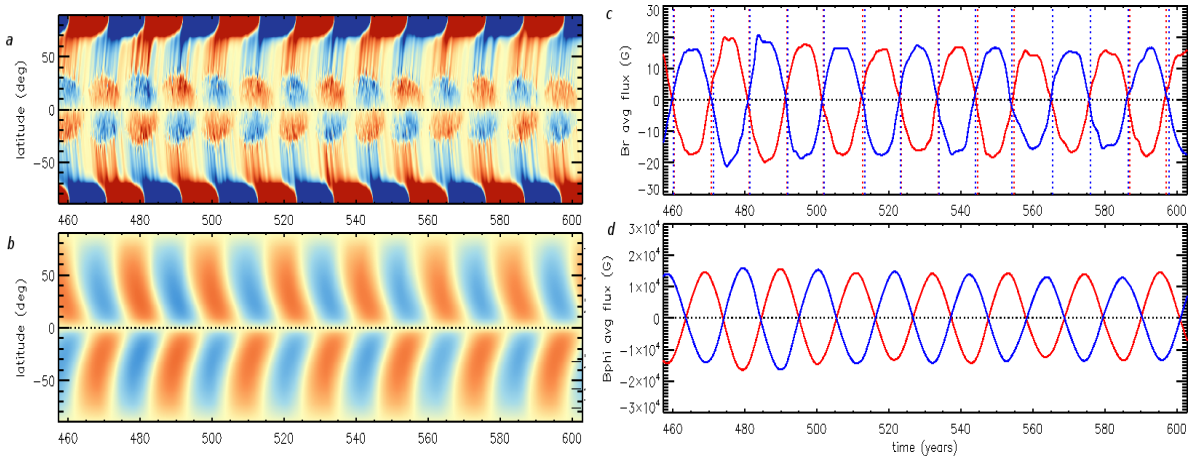

Figure 6.11: Magnetic cycles in Case T1

Butterfly diagram; (a) Mean radial field $\langle B_r \rangle$ at the surface ($r = R$) as a function of latitude and time, highlighting fourteen magnetic cycles. Blue and red denote inward and outward polarity respectively. Peak amplitudes can exceed 300 G but the color table saturates at ± 100G. (b) Mean toroidal field $\langle B_\phi \rangle$ near the base of the convection zone ($r = 0.71R$; Red and blue denote eastward and westward field respectively blue westward). (c) $\langle B_r \rangle$ averaged over the north (blue) and south (red) polar regions, above a latitude of ± 70°. Vertical dotted lines in this and all other frames mark polar field reversals in the NH (blue) and SH (red). Frame (d) is similar to frame (c) but for $\langle B_\phi \rangle$ in the lower CZ ($r = 0.71R$). However, the averages in (d) is over the entire NH (blue) and SH (red), as opposed to just the polar regions. with a saturation level for the color table of 90 kG.

In Table 6.1 series of simulations, the delay distribution of BMR eruptions is dependent on the magnetic field through Equation 6.2.6. The quenching, B_q in Run T2 $Bsat$ is four times smaller and $\Phi_0 = 3.4$. All the inflow model runs have spatial resolutions of 200 × 256 × 512 in r, θ, and ϕ, respectively.

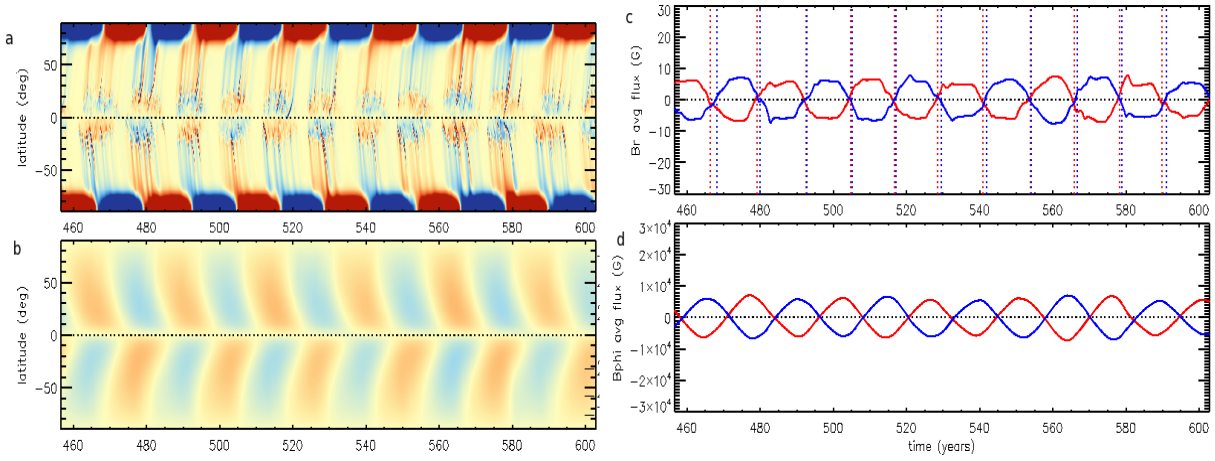

Figure 6.12: Magnetic cycles in Case C1

As Figure 6.11 but for case C1

In Figure 6.11 The morphology of our radial field resembles observations more closely than our previous model with advection-dominated regime (see Chapter 4; Figure (4.5) and (4.12)). We mention that fluctuations of BMR tilts in our model were approximated by a Gaussian distribution with $\sigma_\delta = 15°$. We have demonstrated that in the present model, the cumulative effect of the short term variations of the tilt angle is capable of producing a variation in the magnetic cycle as seen in Figure 6.4,*c*. Thus we can conclude that a potential cause of solar cycle variability is the observed scatter of the tilt angle [Karak and Miesch(2017)]..

In Equation 6.2.6 once the toroidal field at the base of CZ is stronger, it reduces τ_s and τ_p to make the BMR eruption more frequent. This frequent eruption makes the poloidal field production faster, which ulimately causes the stronger fields and faster polarity reversals and the cycle period is shorter than the previous case of a fixed delay distribution (see plots in Chapter 4; Figure (4.5) and (4.12)).

In Figure 6.11 we show such a plot for our reference model, which is produced from tilt angle saturation simulation to saturate the dynamo growth. Where as result in Figure 6.12 use inflow mechanism to halt the dynamo growth. We use 10 m/s inflow velocity

into active regions (see Figure 6.13) and with smoothing radius 7.5° for this simulations, while keeping all other parameters exactly the same as in our reference model. Figure 6.11(a) shows a butterfly diagram obtained by putting the longitude-averaged B_r in a time-latitude plot. One clearly sees the butterfly diagram of sunspots at lower latitudes and the poleward advection of the magnetic field by the meridional circulation at higher latitudes, but in these Figures the differece is clear the sunspot appearance becomes very weak in Figure 6.12 compared to Figure 6.11(a). We find that the inflows enhance flux cancellation, this is how they affect the polar field build-up (see Figure 6.12,c).

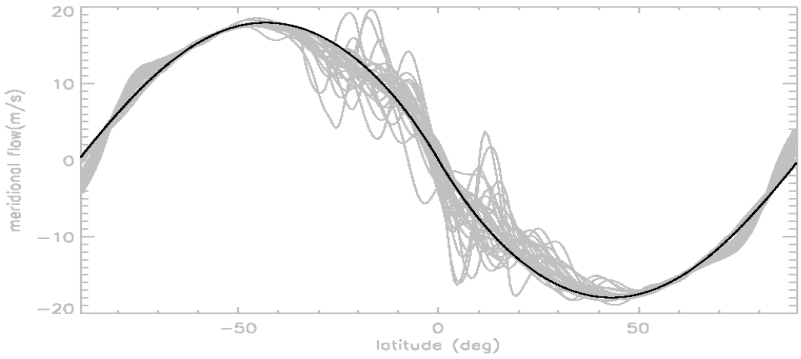

Figure 6.13: Meridional flow plus inflow. The Brown curve is with in flow and the black curve is without inflow.

The distortion and dispersal of these tilted (Joy's law) BMRs by differential rotation, meridional circulation, inflow into the acive regions (sunspots), and turbulent diffusion gives rise to a poleward migration of trailing flux that reverses the polar fields Figure 6.11 (a), as described by the BL mechanism. Thus, according to our results, this leads to a stronger reduction of the polar field built up during cycles of higher activity in Figure 6.12c. Since, in the framework of a Babcock-Leighton dynamo, the polar field is a measure of the poloidal field providing the basis for the toroidal field in the subsequent cycle, the meridional flow perturbation is important for the nonlinear modulation and limitation of the cycle amplitude.

Another important point to note in Figure 6.12 is the stronger reduction of the polar

field built up leads to the stronger reduction of toroidal filed, $\mathbf{B}_\phi$ at the base of the CZ; Figure 6.12 *b* and *d*. Thus, the average cycle period is longer (12.3 years) compare to the reference model (10.5 years) (see Table 6.1). The reason is not difficult to understand. Once the toroidal field at the base of CZ is stronger, it reduces τ_s and τ_s (Equation 6.2.6) to make the BMR eruption more frequent (in Figure 6.11). This frequent eruption makes the poloidal field production faster, which ultimately causes the stronger fields and faster polarity reversals. The reverse is true when the toroidal field at the base of CZ is weaker, it increases τ_s and τ_s (Equation 6.2.6) this delays the BMR eruption (in Figure 6.12). This BMRs eruption delay makes the poloidal field production slower, which ultimately causes the weaker fields and long polarity reversals (see Table 6.1 for the detail of average period of the scolar cycles). See 14 number of reversals in Figure 6.11, while in Figure 6.12 only 11 number of reversals in 140 years.

The correlation between the amplitude of the solar polar field around activity minimum and the strength of the subsequent cycle suggests that the Sun's axial dipole field as observed around activity minimum reflects the source for the generation of the toroidal magnetic flux of the subsequent cycle, as opposed to being a mere epiphenomenon of an otherwise fully hidden subsurface dynamo process. Such a role of the polar field is a key feature of the Babcock-Leighton (BL) dynamo model. In this type of dynamo, the poloidal magnetic field results from the systematic tilt (with respect to the azimuthal/longitudinal direction) of sunspot groups and bipolar magnetic regions in combination with the subsequent redistribution of their magnetic fluxes by near-surface flows. The crucial mechanism for the reversal of the Sun's global dipole field is the preferred transport of preceding-polarity flux of bipolar magnetic regions across the equator into the other solar hemisphere, which leads to the reversal of the polar fields and the build-up of an axial dipole field of opposite polarity. Toroidal flux is then generated by the action of differential rotation winding up poloidal field lines threading the Sun [Cameron and Schüssler,(2012)].

In Figure 6.14 is illustrated the amount of daily flux produced by the simulation Table

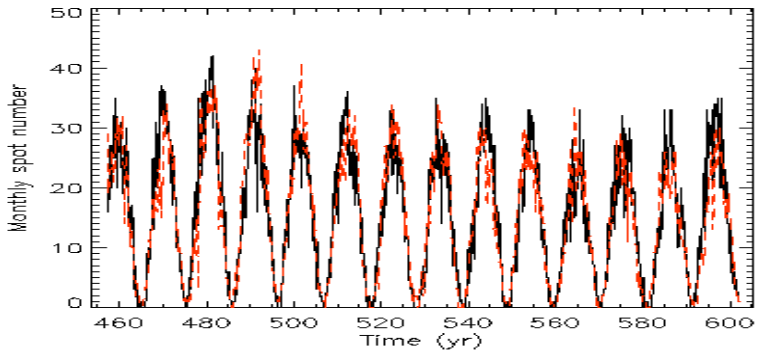

Figure 6.14: Case T1 (without inflow) of Table 6.1: Monthly smoothed sunspot number black/red: north/south respectively.

6.1 case T1 comparable to the observed BMR flux budget by [Karak and Miesch(2017)]. We recall that the frequency of BMR emergences is governed by a delay distribution of the type given in Equation (6.2.6). This produces a much more realistic variation of the surface BMR flux as shown in Figure 6.14 and 6.15. Also the sunspot number (SSN) goes up and down with time in a similar fashion as the real sunspot cycle. We remember that this is the first and actual SSN produced by the model and it is not a proxy. The inflow model produces an observable variation in the amplitude of the cycle; the monthly SSN Figure 6.15.

In the BL process, decay and dispersal of tilted BMRs on the solar surface produce poloidal field at the end of the cycle (see Figure 6.12(c)). Thus we expect the polar flux of a cycle to depend on the amount of flux that has emerged in BMRs during that cycle (see Figure 6.15) and we expect these two quantities to be highly correlated. In Figure 6.15 we show magnetic cycle variation, we realize that the causes of the magnetic cycle variation in this model are the nonlinearities in inflow and in the delay distribution in the BMR emergence process.

Our simulation also produces most of the other features of the solar cycle. However, there are some differences seen in this simulation compared to the previous advection-dominated model. The tilt quenching (6.14), which produces the stable solution, is much

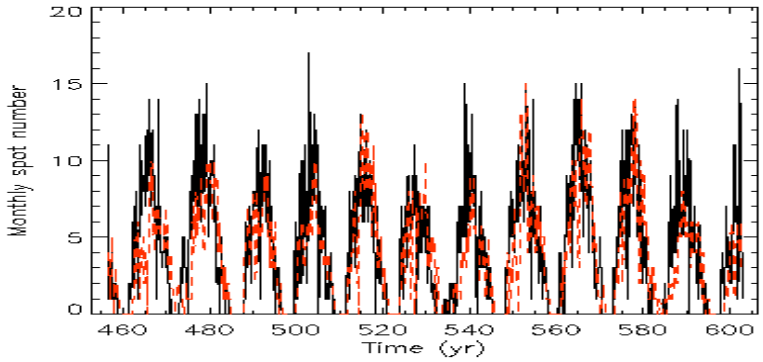

Figure 6.15: Case C1 (with inflow)of Table 6.1: Monthly smoothed sunspot number black/red: north/south respectively.

weaker than in the previous model, the shortcoming coming of the previous more is solved. This small amount of quenching is sufficient to halt the dynamo growth [Karak and Miesch(2017)]. Comparing Figure 6.14, which is produced from tile angle saturation simulation with Figure 6.15, which is produced from inflow into active regions saturation simulation, we notice a greater variation in the Sunspot number. This also leads to the strong variation in the magnetic field demonstrated in the butterfly diagram.

This happens because converging flows squeeze the field together and makes the different polarities reconnect. In other words, it prevents the trailing flux from going to the poles and the leading flux from going to the equator, thus, the magnetic flux transport affecting the strength and duration of the solar activity cycles.

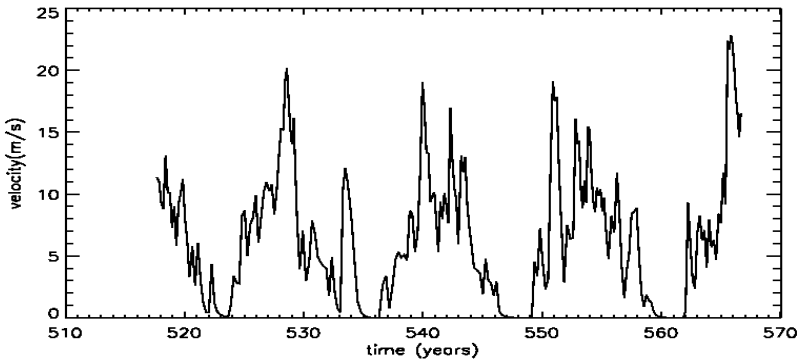

Figure 6.16: The average inflow obtained from the inflow simulation of case C1 of Table 6.1.

Chapter 7

Conclusions

The Sun is an active star and manifests its magnetic field through its solar activities, which is observed on its surface. Understanding the activity and magnetic cycle of the Sun is crucial since its variability has a direct impact on our technological society by disturbing high frequency radio signals, impairing satellites and damaging power grids. For decades the scientific community has developed observational, theoretical and numerical tools in order to be able to understand the inner working of the Sun, while at the same time aiming to be able to predict solar activity.

Our knowledge of the solar magnetic field is largely derived from observations of the photosphere and the regions above it. The current accepted scenario states that this surface magnetism is linked to an internal dynamo. 3D Babcock-Leighton/Flux Transport solar dynamo model have studied to be very useful tools to test and validate ideas and distinguish among scenarios of the solar dynamo such as BL-dynamo mechanism and to progress in our effort to understand the Sun. The meridional circulation in the dynamo theory turns out to be essential in reproducing the most important features of the 11-years cycle.

We present STABLE (Surface flux Transport And BabcockLEighton) solar dynamo model. STABLE is a 3D BabcockLeighton/Flux Transport dynamo model in which the source of poloidal field is the explicit emergence, and dispersal of bipolar magnetic regions (BMRs). The initial results of 3D STABLE dynamo model presented in MD14

and MT16 has been serving as a baselinefor subsequent studies that incorporate 3D Babcock-Leighton/Flux Transport solar dynamo model. Such as the paper by [Hazra et al.(2017), Karak and Miesch(2017)], the latter tilt angle saturation mechanism and inflow into the active regions. The inflow model is non-linear feedbacks mechanism to saturate the Babcock-Leighton dynamo mechanism.

The use of kinematic, axisymmetric flow fields implies that the evolution of mean fields reduces to an equivalent 2D FTD model, though there is no explicit α-effect, instead, poloidal field is generated by the BL mechanism in response to the spontaneous appearance of BMRs, as in the 2D FTD model of [Muñoz-Jaramillo et al.(2010)]. BMRs are placed on the surface based on a spot-producing toroidal field, near the base of the CZ. The BMR deposition approach may be regarded as the limit in which emergent toroidal flux structures decouple quickly from their roots in the deep CZ. In order to verify the STABLE model (Chapter 4), we provisionally replaced this BMR deposition algorithm with an axisymmetric BL source term and we were able to reproduce the 2D FTD benchmark CS$'$ defined by [Jouve et al.(2008)].

The STABLE model exhibits many promising features that are in good agreement with solar observations. Like other FTD models, it sustains regular magnetic cycles with equatorward propagation of toroidal flux at low to mid latitudes near the base of the CZ. However, unlike many other mean-field and convective dynamo models, there is no need to use this subsurface toroidal flux as a proxy for sunspot number. Instead, sunspots/BMRs appear at the surface of the Sun for STABLE explicitly and, can be tracked by means of the non-axisymmetric component of the magnetic energy (Figure 4.8). The evolution of the radial magnetic field at the surface is similar to SFT models, with the distortion and dispersal of low-latitude, tilted BMRs by differential rotation, meridional circulation, and turbulent diffusion producing high-latitude, axisymmetric bands of poloidal flux that migrate poleward and eventually reverse the polar fields. This process is essential for the operation of the dynamo.

The most prominent feature of solar magnetism is the 11 year sunspot cycle (if one considers field reversals the real period is 22 years), which is reflected in the changing number of sunspots appearing on the surface of the Sun. At the beginning of a cycle spots appear at latitudes of about $\lesssim 30°$, while close to the end they appear almost at the equator. This property is commonly summarized in the so-called solar butterfly diagram Figure 6.11.

As in other FTD models, the period and amplitude of the magnetic cycles are largely determined by the meridional flow speed and the three types of saturation mechanism, first the quenching of the poloidal source (through the B_q factor in Equations (3.5.10), second the tilt-angle saturation mechanism (6.2.9), and third the inflow saturation mechanism (5.2.51 -5.2.53). However, other parameters do play a significant role. For fixed BMR delay distribution presented in Chapter 3 and 4, though the MC and B_q are the same in all simulations presented (with the exception of the benchmark in §4.1), the total magnetic energy produced by the dynamo can vary by more than two orders of magnitude (see Table 4.1). The cycle period is less sensitive to the BMR structure, emergence rate, and diffusion, but it can still vary significantly, from 10.6 years in Case T1 (see Table 6.1) to 13.6 years in Case L2 (see Table 4.1).

Factors that influence the dynamo efficiency include the emergence rate and penetration depth of BMRs, the spacing between the two polarity components of a BMR, the tilt angle between the polarity components of a BMR (see Figure 6.7, the inflow speed into the active regions (see Figure 6.8), and the smoothing areas we considered to remove small scale perturbation (see Figure 6.6,*b*). Poloidal field generation is more efficient if each BMR is wider and deeper, and if the number of BMRs is increased by increasing the frequency of emergence (see Figure 3.4*c*). Lower diffusion also enhances the dynamo efficiency and makes the distribution of radial flux at the surface more intermittent (Figure 4.13). Any of these factors can make the difference between a subcritical and supercritical solution (§4.3).

One deficiency of the advection-dominated regimes model is long time it takes for residual flux from mid-latitude BMRs to migrate poleward and reverse the polar fields (Figures 4.5 and 4.12). This does not agree well with solar observations, both in terms of the migration speed and the phasing between low-latitude toroidal flux as traced by sunspots and high-latitude polar field reversals. As discussed in §4.2.1, this was due to a relatively low speed for the high-latitude meridional flow and now we correctly addressed in the current versions of STABLE, diffusion-dominated reimes. See respective results of the current versions of STABLE in Figures (6.4), (6.11) and (6.12).

Boundary conditions appear to be important for the solar dynamo. In particular, it is clear from solar observations that substantial magnetic flux passes through the surface of the sun and that the shearing of this poloidal flux by the surface DR generates toroidal flux in each hemisphere by means of the Ω-effect. CS15 argue that this is the dominant source of mean toroidal flux in the Sun and can account for all the flux that emerges in BMRs. We find that this is indeed the case for our FTD models. However, we find that the role of turbulent diffusion is somewhat different than that envisioned by CS15 (§4.2.2). They modeled turbulent diffusion as an effective drag term that inhibited the generation of net toroidal flux in each hemisphere $\Phi_{NH,SH}(t)$. We find instead that it promotes the generation of net flux by selectively dissipating residual oppositely-signed flux from the previous cycle. Thus, instead of inducing a negative phase shift in $\Phi_{NH,SH}(t)$ as argued by CS15, we find that diffusion induces a positive phase shift, causing the maxima and reversals in $\Phi_{NH,SH}(t)$ to occur later than they would without diffusion.

The BL mechanism represents the poloidal field source in Babcock-Leighton-type models of the solar dynamo and is crucial for the build-up and reversals of the polar fields in STABLE simulations. The evolution of the polar field is a consequence of Hale's polarity rules, together with the tilt angle distribution which has a systematic component of a tilt-angle (Joy's law). We determine the inflow from the surface magnetic filed, B_r, and the flux content in the sunspots is consistent with observation and study the effects

of this inflow on the evolution of the solar surface field using STABLE simulations. By performing simulations with a number of different realizations of parameters we study the effect of the inflow on the global magnetic field, especially on the evolution of the build-up of polar field. In the framework of Babcock-Leighton dynamo models, the inflow into the active regions therefore constitutes a significant inhibition of the operationof STABLE solar dynamo model.

We studied the effect of the converging flow in to the active regions in STABLE framework. we determine the inflow velocity from the surface magnetic flux. We carried out simulations of solar cycles with a STABLE model, which follows the cyclic evolution of the surface field determined by explicit flux emergence and advective transport by surface flows. The results presented here show that the converging flow to the active regions in 3D Babcock-Leighton decrease the strength of the polar fields resulting from the surface flux transport. According to our results, this leads to a stronger reduction of the polar field built up during the solar activity cycles. Its relation to the strength of a cycle means that the flow perturbation could be an important factor in determining the amplitude of Babcock-Leighton-type solar dynamo model. Since, in the framework of a Babcock-Leighton dynamo, the polar field is a measure of the poloidal field providing the basis for the toroidal field in the subsequent cycle. Eventually this supports the inflows towards the active regions provide a non-linear mechanism capable of saturating the global dynamo of the solar cycle within the Babcock-Leighton paradigm.

We present a self-excited 3D solar dynamo model solution that is totally sustained by the observed distribution of tilted BMRs with converging flows towards the active regions. The dynamo action is responsible for the evolution of the magnetic field in the Sun. To the best of our knowledge, this is the first self-excited 3D kinematic dynamo solution that includes converging flows towards the active regions for the saturation dynamo in the framework of Babcock-Leighton solar dynamo. We believe this class of 3D BL/FTD models shows great promise as a “Solar Dynamo Frontier”.

Appendices

Appendix A: Usefule Mathematical Identities and Theorems Fom vector Calculus

Vector Identities

$$\mathbf{A}\cdot(\mathbf{B}\times\mathbf{C}) = \mathbf{C}\cdot(\mathbf{A}\times\mathbf{B}) = \mathbf{B}\cdot(\mathbf{C}\times\mathbf{A}) \tag{7.0.1}$$

$$\mathbf{A}\times(\mathbf{B}\times\mathbf{C}) = \mathbf{B}(\mathbf{A}\cdot\mathbf{C}) - \mathbf{C}(\mathbf{A}\cdot\mathbf{B}) \tag{7.0.2}$$

$$(\mathbf{A}\times\mathbf{B})\times\mathbf{C} = \mathbf{B}(\mathbf{A}\cdot\mathbf{C}) - \mathbf{A}(\mathbf{B}\cdot\mathbf{C}) \tag{7.0.3}$$

$$\nabla\times\nabla f = 0 \tag{7.0.4}$$

$$\nabla\cdot(\nabla\times\mathbf{A}) = 0 \tag{7.0.5}$$

$$\nabla\cdot(f\mathbf{A}) = (\nabla f)\cdot\mathbf{A} + f(\nabla\cdot\mathbf{A}) \tag{7.0.6}$$

$$\nabla\times(f\mathbf{A}) = (\nabla f)\times\mathbf{A} + f(\nabla\times\mathbf{A}) \tag{7.0.7}$$

$$\nabla\cdot(\mathbf{A}\times\mathbf{B}) = \mathbf{B}\cdot(\nabla\times\mathbf{A}) - \mathbf{A}\cdot(\nabla\times\mathbf{B}) \tag{7.0.8}$$

$$\nabla(\mathbf{A}\cdot\mathbf{B}) = (\mathbf{B}\cdot\nabla)\mathbf{A} + (\mathbf{A}\cdot\nabla)\mathbf{B} + \mathbf{B}\times(\nabla\times\mathbf{A}) + \mathbf{A}\times(\nabla\times\mathbf{B}) \tag{7.0.9}$$

$$\nabla\cdot(\mathbf{AB}) = (\mathbf{A}\cdot\nabla)\mathbf{B} + \mathbf{B}(\nabla\cdot\mathbf{A}) \tag{7.0.10}$$

$$\nabla\times(\mathbf{A}\times\mathbf{B}) = (\mathbf{B}\cdot\nabla)\mathbf{A} - (\mathbf{A}\cdot\nabla)\mathbf{B} - \mathbf{B}(\nabla\cdot\mathbf{A}) + \mathbf{A}(\nabla\cdot\mathbf{B}) \tag{7.0.11}$$

$$\nabla\times(\nabla\times\mathbf{A}) = \nabla(\nabla\cdot\mathbf{A}) + \nabla^2\mathbf{A} \tag{7.0.12}$$

Vector Operators

$$\frac{D}{Dt} = \frac{\partial}{\partial t} + u_r \frac{\partial}{\partial r} + \frac{u_\theta}{r}\frac{\partial}{\partial \theta} + \frac{u_\phi}{r sin\theta}\frac{\partial}{\partial \phi} \tag{7.0.13}$$

$$\boldsymbol{\nabla} f = \frac{\partial f}{\partial r}\hat{e}_r + \frac{1}{r}\frac{\partial f}{\partial \theta}\hat{e}_\theta + \frac{1}{r sin\theta}\frac{\partial f}{\partial \phi}\hat{e}_\phi \tag{7.0.14}$$

$$\begin{aligned}(\mathbf{u}\cdot\nabla)\mathbf{A} = &\left(\mathbf{u}\cdot\nabla A_r - \frac{u_\theta A_\theta}{r} - \frac{u_\phi A_\phi}{r}\right)\hat{e}_r + \\ &\left(\mathbf{u}\cdot\nabla A_\theta - \frac{u_\phi A_\phi}{r}cot\theta + \frac{u_\theta A_r}{r}\right)\hat{e}_\theta + \left(\mathbf{u}\cdot\nabla A_\phi + \frac{u_\phi A_r}{r} + \frac{u_\phi A_\theta}{r}cot\theta\right)\hat{e}_\phi\end{aligned} \tag{7.0.15}$$

$$(\boldsymbol{\nabla}\cdot\mathbf{A}) = \frac{1}{r^2}\frac{\partial(r^2 A_r)}{\partial r} + \frac{1}{r\sin\theta}\frac{\partial(A_\theta \sin\theta)}{\partial \theta} + \frac{1}{r\sin\theta}\frac{\partial A_\phi}{\partial \phi} \tag{7.0.16}$$

$$\begin{aligned}\nabla\times\mathbf{A} = &\frac{1}{r\sin\theta}\left(\frac{\partial(A_\phi\sin\theta)}{\partial\theta} - \frac{\partial(A_\theta)}{\partial\phi}\right)\hat{e}_r \\ &+\frac{1}{r\sin\theta}\left(\frac{\partial A_r}{\partial\phi} - \frac{\partial(r\sin\theta A_\phi)}{\partial r}\right)\hat{e}_\theta + \frac{1}{r}\left(\frac{\partial(rA_\theta)}{\partial r} - \frac{\partial(A_r)}{\partial\theta}\right)\hat{e}_\phi\end{aligned} \tag{7.0.17}$$

$$\boldsymbol{\nabla}^2 = \frac{1}{r^2}\frac{\partial\left(r^2\frac{\partial}{\partial r}\right)}{\partial r} + \frac{1}{r^2\sin\theta}\frac{\partial\left(\sin\theta\frac{\partial}{\partial\theta}\right)}{\partial\theta} + \frac{1}{r^2\sin^2\theta}\frac{\partial^2}{\partial^2\phi} \tag{7.0.18}$$

$$\begin{aligned}\boldsymbol{\nabla}^2\mathbf{A} = &\left(\nabla^2 A_r - \frac{2A_r}{r^2} - \frac{2}{r^2\sin\theta}\frac{\partial(A_\theta\sin\theta)}{\partial\theta} - \frac{1}{r^2\sin\theta}\frac{\partial A_\phi}{\partial\phi}\right)\hat{e}_r + \\ &\left(\nabla^2 A_\theta + \frac{2}{r^2}\frac{\partial A_r}{\partial\theta} - \frac{A_\theta}{r^2\sin^2\theta} - \frac{2\cos\theta}{r^2\sin^2\theta}\frac{\partial A_\phi}{\partial\phi}\right)\hat{e}_\theta + \\ &\left(\nabla^2 A_\phi + \frac{2}{r^2\sin\theta}\frac{\partial A_r}{\partial\phi} + \frac{2\cos\theta}{r^2\sin^2\theta}\frac{\partial A_\theta}{\partial\phi} - \frac{A_\phi}{r^2\sin^2\theta}\right)\hat{e}_\phi\end{aligned} \tag{7.0.19}$$

Appendix B

The Fundamental Magnetohydrodynamic Equations

The equation of motion

$$\frac{Du}{Dt} = -\frac{1}{\rho}\nabla p - 2\Omega \times \mathbf{u} + \mathbf{g} + \frac{1}{\rho}\nabla\cdot\tau + \frac{1}{\mu_0\rho}(\nabla \times \mathbf{B}) \times \mathbf{B} \tag{7.0.20}$$

$$\begin{aligned}\rho\left(\frac{Du_r}{Dt} - \frac{u_\theta^2 + u_\phi}{r}\right) &= -\rho\frac{\partial\Phi}{\partial r} - \frac{\partial P}{\partial r} + \frac{B_\phi}{\mu_0 r\sin\theta}\left(\frac{\partial B_r}{\partial\phi} - \frac{\partial\left(B_\phi r\sin\theta\right)}{\partial r}\right)\\ &-\frac{B_\theta}{\mu_0 r}\left(\frac{\partial r B_\theta}{\partial r} - \frac{\partial B_r}{\partial\theta}\right) + \frac{1}{r\sin\theta}\left[\frac{\sin\theta}{r}\frac{\partial\left(r^2\tau_{rr}\right)}{\partial r} + \frac{\partial\left(\tau_{r\theta}\sin\theta\right)}{\partial\theta} + \frac{\partial\tau_{r\phi}}{\partial\phi}\right]\\ &-\frac{\tau_{\theta\theta} + \tau_{\phi\phi}}{r}\end{aligned} \tag{7.0.21}$$

$$\begin{aligned}\rho\left(\frac{Du_r}{Dt} + \frac{u_r u_\theta}{r} - \frac{u_\phi\cot\theta}{r}\right) &= -\frac{\rho}{r}\frac{\partial\Phi}{\partial\theta} - \frac{1}{r}\frac{\partial P}{\partial\theta} +\\ \frac{B_r}{\mu_0 r}\left(\frac{\partial(rB_\theta)}{\partial r} - \frac{\partial\left(B_r\right)}{\partial\theta}\right) &- \frac{B_\phi}{\mu_0 r\sin\theta}\left(\frac{\partial\left(B_\phi\sin\theta\right)}{\partial\theta} - \frac{\partial B_\theta}{\partial\phi}\right) +\\ \frac{1}{r\sin\theta}\left[\frac{\sin\theta}{r}\frac{\partial\left(r^2\tau_{\theta r}\right)}{\partial r} + \frac{\partial\left(\tau_{\theta\theta}\sin\theta\right)}{\partial\theta} + \frac{\partial\tau_{\theta\phi}}{\partial\phi}\right] &+ \frac{\tau_{\theta r}}{r} - \frac{\tau_{\phi\phi}\cot\theta}{r}\end{aligned} \tag{7.0.22}$$

$$\begin{aligned}\rho\left(\frac{Du_\phi}{Dt} + \frac{u_r u_\phi}{r} + \frac{u_\theta u_\phi\cot\theta}{r}\right) &= -\frac{\rho}{r\sin\theta}\frac{\partial\Phi}{\partial\phi} - \frac{\rho}{r\sin\theta}\frac{\partial P}{\partial\phi} +\\ \frac{B_\theta}{\mu_0 r\sin\theta}\left(\frac{\partial\left(B_\phi\sin\theta\right)}{\partial\theta} - \frac{\partial B_\theta}{\partial\phi}\right) &- \frac{B_r}{\mu_0 r\sin\theta}\left(\frac{\partial B_r}{\partial\phi} - \frac{\partial\left(B_\phi r\sin\theta\right)}{\partial r}\right) +\\ \frac{1}{r\sin\theta}\left[\frac{\sin\theta}{r}\frac{\partial\left(r^2\tau_{\phi r}\right)}{\partial r} + \frac{\partial\left(\tau_{\phi\theta}\sin\theta\right)}{\partial\theta} + \frac{\partial\tau_{\phi\phi}}{\partial\phi}\right] &+ \frac{\tau_{\phi r}}{r} + \frac{\tau_{\phi\theta}\cot\theta}{r}\end{aligned} \tag{7.0.23}$$

The Energy Equation

$$\frac{De}{Dt} + (\gamma - 1)e\nabla\cdot\mathbf{u} = \frac{1}{\rho}\left[\nabla\cdot\left[(\chi + \chi_r)\nabla T\right] + \phi_\nu + \phi_B\right] \tag{7.0.24}$$

$$\rho T\frac{DS}{Dt} = \nabla\cdot\left[(\chi + \chi_r)\nabla T\right] + \phi_\nu + \phi_B \tag{7.0.25}$$

$$\phi_\nu = \frac{\mu}{2}(\frac{\partial u_i}{\partial r_j} + \frac{\partial u_j}{\partial r_i} - \frac{2}{3}\delta_{ij}\nabla\cdot\mathbf{u})^2 + \zeta(\nabla\cdot\mathbf{u})^2 \tag{7.0.26}$$

$$\Phi_\nu = 2\mu(D_{rr}^2 + D_{\theta\theta}^2 + D_{\phi\phi}^2 + 2D_{r\theta}^2 + 2D_{\theta\phi}^2 + 2D_{\phi r}^2) + \left(\zeta - \frac{2}{3}\mu\right)(\nabla\cdot\mathbf{u})^2 \tag{7.0.27}$$

$$\Phi_\eta = \frac{\eta}{\mu_0}(\nabla\times\mathbf{B})^2 \tag{7.0.28}$$

$$\Phi_\eta = \frac{\eta}{\mu_0 r^2\sin^2\theta}\left[\left(\frac{\partial(B_\phi\sin\theta)}{\partial\theta} - \frac{\partial B_\theta}{\partial\phi}\right)^2 + \left(\frac{\partial B_r}{\partial\phi} - \frac{\partial(r\sin\theta B_\phi)}{\partial r}\right)^2\right] + \frac{\eta}{\mu_0 r^2\sin^2\theta}\left[\sin^2\theta\left(\frac{\partial(rB_\theta)}{\partial r} - \frac{\partial B_r}{\partial\theta}\right)^2\right] \tag{7.0.29}$$

$$\rho T\frac{DS}{Dt} = \Phi_\nu + \Phi_\eta + \frac{1}{r^2}\frac{\partial\left(\chi r^2\frac{\partial T}{\partial r}\right)}{\partial r} + \frac{1}{r^2\sin\theta}\frac{\partial\left(\chi\sin\theta r^2\frac{\partial T}{\partial\theta}\right)}{\partial\theta} + \frac{1}{r^2\sin^2\theta}\frac{\partial\left(\chi r^2\frac{\partial T}{\partial\phi}\right)}{\partial\phi} \tag{7.0.30}$$

The MHD Eduction Equation

The radial component

$$\frac{\partial B_r}{\partial t} = \frac{1}{r\sin\theta}\left[\frac{\partial(\sin\theta(u_rB_\theta - u_\theta B_r))}{\partial\theta} - \frac{\partial(u_\phi B_r - u_r B_\phi)}{\partial\phi}\right] - \frac{1}{r^2}\frac{\partial\eta}{\partial\theta}\left(\frac{\partial(rB_\theta)}{\partial r} - \frac{\partial B_r}{\partial\theta}\right) + \frac{1}{r^2\sin^2\theta}\frac{\partial\eta}{\partial\phi}\left(\frac{\partial B_r}{\partial\phi} - \frac{\partial(r\sin\theta B_\phi)}{\partial r}\right) + \eta\left(\nabla^2 B_r - \frac{2B_r}{r^2} - \frac{2}{r^2\sin\theta}\frac{\partial(B_\theta\sin\theta)}{\partial\theta} - \frac{1}{r^2\sin\theta}\frac{\partial B_\phi}{\partial\phi}\right) \tag{7.0.31}$$

The latitudial component

$$\frac{\partial B_\theta}{\partial t} = \frac{1}{r\sin\theta}\frac{\partial(u_\theta B_\phi - u_\phi B_\theta)}{\partial\phi} - \frac{1}{r}\frac{\partial(ru_r B\theta - ru_\theta B_r)}{\partial r} - \frac{1}{r^2\sin^2\theta}\frac{\partial\eta}{\partial\phi}\left(\frac{\partial(B_\phi\sin\theta)}{\partial\theta} - \frac{\partial B_\theta}{\partial\phi}\right)$$
$$+\frac{1}{r}\frac{\partial\eta}{\partial r}\left(\frac{\partial(rB_\theta)}{\partial r} - \frac{\partial B_r}{\partial\theta}\right)$$
$$+\eta\left(\nabla^2 B_\theta + \frac{2}{r^2}\frac{\partial B_r}{\partial\theta} - \frac{B_\theta}{r^2\sin^2\theta} - \frac{2\cos\theta}{r^2\sin^2\theta}\frac{\partial B_\phi}{\partial\phi}\right) \tag{7.0.32}$$

The Azimuthal components

$$\frac{\partial B_\phi}{\partial t} = \frac{1}{r}\left[\frac{\partial(ru_\phi B_r - ru_r B_\phi)}{\partial r} - \frac{\partial(u_\theta B_\phi - u_\phi B_\theta)}{\partial\theta}\right] - \frac{1}{r\sin\theta}\frac{\partial\eta}{\partial r}\left(\frac{\partial B_r}{\partial\phi} - \frac{\partial(r\sin\theta B_\phi)}{\partial r}\right)$$
$$+\frac{1}{r^2\sin\theta}\frac{\partial\eta}{\partial\theta}\left(\frac{\partial(B_\phi\sin\theta)}{\partial\theta} - \frac{\partial B_\theta}{\partial\phi}\right)$$
$$+\eta\left(\nabla^2 B_\phi + \frac{2}{r^2\sin\theta}\frac{\partial B_r}{\partial\phi} + \frac{2\cos\theta}{r^2\sin^2\theta}\frac{\partial B_\theta}{\partial\phi} - \frac{B_\phi}{r^2\sin^2\theta}\right) \tag{7.0.33}$$

Appendix C

Parameter Summary Used In The STABLE Code

Item	Description	default value	Eq.	input
Φ_0	determines how much flux in a spot	1.0	3.5.10	spot_alpha
r_a	lower radius for averaging B_ϕ	0.7	3.5.1	spot_ra
r_b	upper radius for averaging B_ϕ	0.715	3.5.1	spot_rb
B_q	quenching field strength	1×10^5	3.5.10	spot_Bq
τ_s	mean time between spot formation (in days)	1.5	3.6.5	spot_taus
τ_p	mode of spot interval pdf (in days)	2.5	3.6.6	spot_taup
B_t	threshold field strength for launching a spot	2×10^3	6.2.2	spot_Bt
r_s	penetration radius of spot	0.9	5.2.38	spot_rs
B_s	Field strength in spot	3×10^3	3.7.1	spot_Bs
δ_0	Joy's Law	32.1°	3.6.1	spot_delta0
s_a	sets the distance between spots	1.5	–	spot_sa
B_a	threshold used for axisymmetry	0.5	–	spot_Ba
n_s	minimum number of grid points across a spot	5.0	–	spot_ns
m_s	maximum number of grid points across a spot	4000	–	spot_ms
r_d	central radius of depletion loop	–	–	spot_ra
σ_θ	latitudinal width of depletion loop	–	–	spot_ra
σ_ϕ	longitudinal width of depletion loop	–	–	spot_ra

Item	Description	Default value	Eq.	input
Ψ_0	Nondimensional amplitude of ψ	30	(3.4.5)	kindy_mc
θ_0	positive to put in a polar counter-cell	0-40°	(3.4.5)	kindy_theta
r_b	(nondimensional) Radius where MC closes	0.69R	(3.4.6)	kindy_rb
ν_c	core rotation rate	432.8 nHz	(3.4.13)	kindy_omega1
ν_{eq}	surface equatorial rotation rate	460.7 nHz	(3.4.14)	kindy_omega2
a_2	used for Ω	-62.9 nHz	(3.4.14)	kindy_omega3
a_4	used for Ω	-67.13 nHz	(3.4.14)	kindy_omega4
r_c	tachocline location	0.7	(3.4.13)	kindy_r2
d	tachocline width	0.05	(3.4.13)	kindy_d2
η_{top}	diffusivity at top	3×10^{12}	(3.4.19)	eta_top
η_{mid}	diffusivity at mic CZ	1.5×10^{12}	(3.4.19)	eta_mid
η_c	diffusivity at core	1×10^{10}	(3.4.19)	eta_floor
r_{da}	location of first η transition	0.715	(3.4.19)	eta_r0
r_{db}	location of second η transition	0.956	(3.4.19)	eta_r1
d_a	width of first η transition	0.0125	(3.4.19)	eta_d0
d_b	width of second η transition	0.025	(3.4.19)	eta_d1

Bibliography

[Babcock(1961)] Babcock, H.W., 1961. The topology of the sun's magnetic field and the 22-year cycle. ApJ 133, 572–587.

[Baumann et al.(2004)] Baumann, I., Schmitt, D., Schüssler, M., Solanki, S.K., 2004. Evolution of the large-scale magnetic field on the solar surface: A parameter study. A&A 426, 1075–1091.

[Belda and Cameron ,(2016)] Belda, M., Cameron, R., 2016. Surface flux transport simulations: Effect of inflows toward active regions and random velocities on the evolution of the Suns large-scale magnetic field(not finished the details) A&A 586, A73.

[Belda and Cameron ,(2017)] Belda, M., Cameron, R., 2017. Inflows towards active regions and the modulation of the solar cycle: a parameter study(not finished the details) A&A 597, A21.

[Boyd and Sanderson(2003)] Boyd T.J.M., Sanderson J.J., 2003. The Physics of Plasmas. Cambridge University Press .

[Brown(2009)] Brown B. P., 2009. Convection and Dynamo Action in Rapidly Rotating Suns. PhD thesis, University of Colorado, Boulder.

[Brun(2010)] Brun, A.S., 2010. Modeling the sun and stars in 3d. EAS Pub. Ser. 44, 81–95.

[Brun et al.(2004)] Brun, A.S., Miesch, M.S., Toomre, J., 2004. Global-scale turbulent convection and magnetic dynamo action in the solar envelope. ApJ 614, 1073–1098.

[Cameron et al.(2010)] Cameron, R., Jiang, J., Schmitt, D., Schüssler, M., 2010. Surface flux transport modeling for solar cycles 15-21: Effects of cycle-dependent tilt angles of sunspot groups. ApJ 719, 264–270.

[Cameron and Schüssler,(2010)] Cameron, R., Schüssler, M., 2010. Changes of the solar meridional velocity profile during cycle 23 explained flows toward the activity belts ApJ 720, 1030–1032.

[Cameron and Schüssler,(2012)] Cameron, R., Schüssler, M., 2012. Are the strengths of solar cycles determined by converging flows towards the activity belts? A&A 548, A57.

[Cameron and Schüssler(2015)] Cameron, R., Schüssler, M., 2015. The crucial role of surface magnetic fields for the solar dynamo. Science 347, 1333–1335.

[Cameron et al.(2013)] Cameron, R.H., Dasi-Espuig, M., Jiang, J., Isik, E., Schmitt, D., Schüssler, M., 2013. Limits to solar cycle predictability: Cross-equatorial flux plumes. A&A 557, A141 (6 pp.).

[Chan et al.(2004)] Chan, K.H., Liao, X., Zhang, K., Jones, C.A., 2004. Non-axisymmetric spherical interface dynamos. A&A 423, L37-L40.

[Charbonneau(2010)] Charbonneau, P., 2010. Dynamo models of the solar cycle. Living Reviews in Solar Physics 7. Http://www.livingreviews.org/lrsp-2010-3.

[Charbonneau(2013)] Charbonneau, P., 2013. Solar and Stellar Dynamos. Swiss Society for Astrophysics and Astronomy Edited by O. Steiner Springer.

[Charbonneau(2014)] Charbonneau, P., 2014. Solar dynamo theory. ARA&A 52, 251–290.

[Charbonneau(2016)] Charbonneau P., 2016. Dynamo Models of the Solar Cycle. Living Reviews in Solar Physics 13. Http://www.livingreviews.org/lrsp-lrsp-2016-1.

[Clune et al.(1999)] Clune, T.C., Elliott, J.R., Miesch, M.S., Toomre, J., Glatzmaier, G.A., 1999. Computational aspects of a code to study rotating turbulent convection in spherical shells. Parallel Computing 25, 361–380.

[De Rosa and Schrijver (2006)] De Rosa, M. L., Schrijver, C. J., 2006. Consequences of large-scale flows around active regions om the dispersal of magnetic filed across the solar surface. in Proceedings of SOHO 18/GONG 2006/HELAS I, Beyond the spherical Sun, ed. K. Fletcher & M. Thompson ESA Special Publication 624, 12.

[Dasi-Espuig et al.(2010)] Dasi-Espuig, M., Solanki, S.K., Krivova, N.A., Cameron, R., Peñuela, T., 2010. Sunspot group tilt angles and the strength of the solar cycle. A&A 518, A7 (10pp).

[DeVore et al.(1984)] DeVore, C.R., Boris, J.P., Sheeley, N.R., 1984. The concentration of the large-scale solar magnetic field by a meridional surface flow. Solar Phys. 92, 1–14. doi:10.1007/BF00157230.

[Dikpati(2011)] Dikpati, M., 2011. Polar field puzzle: Solutions from flux-transport dynamo and surface-transport models. ApJ 733, 90 (7 pp).

[Dikpati and Charbonneau(1999)] Dikpati, M., Charbonneau, P., 1999. A babcock-leighton flux transport dynamo with solar-like differential rotation. ApJ 518, 508–520.

[Dikpati(2002)] Dikpati, M., Corbard, T., Thompson, M.J., Gilman, P.A., 2002. Flux-transport dynamo with near-surface radial shear. ApJL 575, L41-L45.

[Dikpati and Gilman (1999)] Dikpati, M., Gilman, P.A., 1999. Joint instability of latitudinal differential rotation and concentrated toroidal fields below the solar convection zone. ApJ 512, 417-441.

[Dikpati and Gilman (2001)] Dikpati, M., Gilman, P.A., 2001. Flux-transport dynamos with a-effect from global instability of tachocline differential rotation: a solution for magnetic parity selection in the sun. ApJ 559, 428-442.

[Dikpati and Gilman(2007)] Dikpati, M., Gilman, P.A., 2007. Steps for building a calibrated flux-transport dynamo for the sun. Solar Phys. 241, 1–5.

[Dikpati and Gilman(2009)] Dikpati, M., Gilman, P.A., 2009. Flux-transport solar dynamos. Space Sci. Rev. 144, 67–75.

[Dikpati et al.(2010)] Dikpati, M., Gilman, P.A., de Toma, G., Ulrich, R.K., 2010. Impact of changes in the sun's conveyor-belt on recent solar cycles. Geophys. Res. Let. L14107, (6 pp).

[Durney(1997)] Durney, B.R., 1997. On a babcock-leighton solar dynamo model with a deep-seated generating layer for the toroidal magnetic field. iv. ApJ 486, 1065–1077.

[Gizon et al.(2001)] Gizon, L., Duvall Jr, T.L., Larsen, R.M.,2001. Probing surface flows and magnetic activity with time-distance helioseismology. IAU Symposium 203, 189.

[Gizon et al.(2010)] Gizon, L., Birch A. C., Spruit H. C. ,2010. Local Helioseismology: Three Dimensional Imaging of the Solar Interior. ARA&A 48, 289.

[Gizon and Rempel.(2008)] Gizon, L., Rempel M., 2008. Observation and Modeling of the Solar-Cycle Variation of the Meridional Flow. Sol.Phys. 251, 241–250.

[Glatzmaier(2012)] Glatzmaier G. A., 2012. Introduction to Modeling Convection in Planets and Stars. PRINCETON SERIES IN ASTROPHYSICS

[Goldston and Rutherford(1995)] Goldston, R. B., Rutherford, A., 1995. Introduction To Plasmas Physics. IOP .

[Moffatt(1978)] MofiFatt, H. K., 1978. Magnetic field generation in electrically conducting fluids.. Cambridge University Press.

[Hale et al.,(1919)] Hale, G. E., Ellerman, F.,Nicholson, S. B., Joy, A. H.,1919. THE MAGNETIC POLARITY OF SUNSPOTS. ApJ 153.

[Hathaway(2010)] Hathaway, D.H., 2010. The solar cycle. Living Reviews in Solar Physics 7. Http://www.livingreviews.org/lrsp-2010-1.

[Hathaway(2012)] Hathaway, D.H., 2012. Supergranules as probes of the sun's meridional circulation. ApJ 760, 84 (6pp).

[Hathaway and Upton(2016)] Hathaway, D., Upton, L., 2016. Predicting the Amplitude and Hemispheric Asymmetry of Solar Cycle 25 with Surface Flux Transport. JGRA 121, A10 (10pp)..

[Hazra et al.(2017)] Hazra, S., Choudhuri, A.R., Miesch, M., 2017. A Theoretical Study of the Build-up of the Sun's Polar Magnetic Field by using a 3D Kinematic Dynamo Model. ApJ 835, 39, (16pp).

[Hazra et al.(2014)] Hazra, S., Passos, D., Nandy, D., 2014. A stochastically-forced time-delay solar dynamo model: Self-consistent recovery from a maunder-like grand minimum necessitates a mean-field alpha-effect. ApJ 789, 5 (7pp).

[Hickmann et al.(2015)] Hickmann, K.S., Godinez, H.C., Henney, C.J., Arge, C.N., 2015. Data assimilation in the adapt photospheric flux transport model. Solar Phys. 290, 1105–1118.

[Hindman et al.(2009)] Hindman, B. W., Haber, D. A., Toomre, J., 2009. SUBSURFACE CIRCULATIONS WITHIN ACTIVE REGIONS. APJ 698, 1749–1760.

[Jiang et al.(2013)] Jiang, J., Cameron, R.H., Schmitt, D., Isik, E., 2013. Modeling solar cycles 15 to 21 using a flux transport dynamo. A&A 553, A128 (6pp).

[Jiang, et al.(2017)] Jiang, J., Chatterjee, P., Choudhuri, A.R., 2007. Solar activity forecast with a dynamo model. MNRAS 381, 1527–1542.

[Jiang et al.(2010)] Jiang, J., Işik, E., Cameron, R.H., Schmitt, D., Schüssler, M., 2010. The effect of activity-related meridional flow modulation on the strength of the solar polar magnetic field. ApJ 717, 597–602.

[Jiang et al.(2014a)] Jiang, J., Cameron, R.H., Schüssler, M., 2014a. Effects of the scatter in sunspot group tilt angles on the large-scale magnetic field at the solar surface. ApJ 791, 5 (10pp).

[Jiang et al.(2014b)] Jiang, J., Hathaway, D.H., Cameron, R., Solanki, S.K., Gizon, L., Upton, L., 2014b. Magnetic flux transport at the solar surface. Space Sci. Rev. 186, 491–523.

[Jiang and Cao(2017)] Jiang, J., Cao, J., 2017. Predicting solar surface large-scale magnetic field of Cycle 24. Accepted for publication in JASTP (arXiv:1707.00268).

[Jones et al.(2011)] Jones, C.A., Boronski, P., Brun, A.S., Glatzmaier, G.A., Gastine, T., Miesch, M.S., Wicht, J., 2011. Anelastic convection-driven dynamo benchmarks. Icarus 216, 120–135.

[Jouve et al.(2008)] Jouve, L., Brun, A., Arlt, R., Brandenburg, A., Dikpati, M., Bonanno, A., Käpylä, P.J., Moss, D., Rempel, M., Gilman, P., Korpi, M.J., Kosovichev, A.G., 2008. A solar mean field dynamo benchmark. A&A 483, 949–960.

[Karak and Miesch(2017)] Karak, B., Miesch, M., 2017. Solar Cycle Variability Induced by Tilt Angle Scatter in a Babcock-Leighton Solar Dynamo Model. APJ 847, 69, 17 pp.

[Karak and Cameron(2016)] Karak, B., Cameron R., 2016. BABCOCK-LEIGHTON SOLAR DYNAMO: THE ROLE OF DOWNWARD PUMPING AND THE EQUATORWARD PROPAGATION OF ACTIVITY. APJ 832, 94, 12 pp.

[Karak et al.(2014)] Karak, B., Jiang, J., Miesch, M., Choudhuri, A., Charbonneau, P., 2014. Flux transport dynamos: From kinematics to dynamics. Space Sci. Rev. 186, 561–602.

[Karak and Choudhuri(2011)] Karak, B.B., Choudhuri, A.R., 2011. The waldmeier effect and the flux transport solar dynamo. MNRAS 410, 1501–1512.

[Kosovichev et al.(2016)] Kosovichev, A. G., Zhao, J., Ilonidis, S., 2016. The waldmeier effect and the flux transport solar dynamo. ArXiv e-prints arXiv:1607.04987v1.

[Leighton(1964)] Leighton, R.B., 1964. Transport of magnetic fields on the sun. ApJ 140, 1547–1562.

[Lemerle et al.(2015)] Lemerle, A., Charbonneau, P., Carignan-Dugas, A., 2015. A coupled 2 × 2 babcock-leighton solar dynamo model. i. surface magnetic flux evolution. ApJ 810, 78 (18 pp).

[Löptien et al.(2017)] Löptien, B., Birch, A. C., Duvall Jr. T. L., Gizon, L., Proxauf, B., Schou, J., 2017. Measuring solar active region inflows with local correlation tracking of granulation. A&A 606, A28 (10 pp).

[McClintock and Norton(2013)] McClintock, B.H., Norton, A.A., 2013. Recovering joy's law as a function of solar cycle, hemisphere, and longitude. Solar Phys. 287, 215–227.

[Miesch(1998)] Miesch, M.S., 1998. Turbulence and Convection in Stellar and Interstellar Enviroments. Ph.D. thesis, University of Colorado, Boulder.

[Miesch(2005)] Miesch, M.S., 2005. Large-scale dynamics of the convection zone and tachocline. Living Reviews in Solar Physics 2. Http://www.livingreviews.org/lrsp-2005-1.

[Miesch and Dikpati(2014)] Miesch, M.S., Dikpati, M., 2014. A three-dimensional babcock-leighton solar dynamo model. ApJL 785, L8 (5pp).

[Miesch et al.(2012)] Miesch, M.S., Featherstone, N.A., Rempel, M., Trampedach, R., 2012. On the amplitude of convective velocities in the deep solar interior. ApJ 757, 128 (14pp).

[Miesch and Teweldebirhan(2016)] Miesch, M.S., Teweldebirhan, K., 2016. A three-dimensional Babcock-Leighton solar dynamo model: Initial results with axisymmetric flows. Advanced in space Research 58, 1571-1588.

[Miesch and Toomre(2009)] Miesch, M.S., Toomre, J., 2009. Turbulence, magnetism, and shear in stellar interiors. Ann. Rev. Fluid Mech. 41, 317–345.

[Muñoz-Jaramillo et al.(2012)] Muñoz-Jaramillo, A., Sheeley, N.R., Zhang, J., DeLuca, E.E., 2012. Calibrating 100 years of polar faculae measurements: Implications for the evolution of the heliospheric magnetic field. ApJ 753, 146 (14pp). doi:10.1088/0004-637X/753/2/146.

[Muñoz-Jaramillo et al.(2010)] Muñoz-Jaramillo, A., Nandy, D., P.C.H.Martens, Yeates, A.R., 2010. A double-ring algorithm for modeling solar active regions: Unifying kinematic dynamo models and surface flux-transport simulations. ApJL 720, L20–L25.

[Muñoz-Jaramillo et al.(2015)] Muñoz-Jaramillo, A., Senkpeil, R. R., Windmueller, J. C., Amouzou, E. C. , 2015. Small-Scale and Global Dynamos and the Area and Flux Distributions of Active Regions, Sunspot Groups, and Sunspots: A Multi-Database Study. ApJL 800, 48(19pp).

[Nandy and Choudhuri(2001)] Nandy, D., Choudhuri, A.R., 2001. Toward a mean field formulation of the babcock-leighton type solar dynamo. i. α-coefficient versus durneys double-ring approach. ApJ 551, 576–585.

[Ossendrijver(2003)] Ossendrijver, M., 2003. The solar dynamo. A&A 11, 287–367.

[Passos et al.(2015)] Passos, D., Miesch, M.S., Charbonneau, P., 2015. Meridional circulation dynamics from 3d magnetohydrodynamic global simulations of solar convection. ApJ 800, L18 (5pp).

[Schatten et al.(1978)] Schatten, K.H., Scherrer, P.H., Svalgaard, L., Wilcox, J.M., 1978. Using dynamo theory to predict the sunspot number during solar cycle 21. Geophys. Res. Lett. 5, 411–414. doi:10.1029/GL005i005p00411.

[Schrijver and DeRosa(2003)] Schrijver, C.J., DeRosa, M.L., 2003. Photospheric and heliospheric magnetic fields. Solar Physics 212, 165–200.

[Schrijver and Siscoe(2009)] Schrijver, C. J., Siscoe, G. L., 2009. HELIOPHYSICS: Plasma Physics of the Local Cosmos. Cambridge University Press .

[Schrijver and Siscoe(2010)] Schrijver, C. J., Siscoe, G. L., 2010. HELIOPHYSICS: Space Storms and Radiation: Causes and Effects. Cambridge University Press .

[Schrijver and Siscoe(2010)] Schrijver, C. J., Siscoe, G. L., 2010. HELIOPHYSICS: Evolving Solar Activity and the Climates of Space and Earth. Cambridge University Press .

[Schrijver et al.(2016)] Schrijver, C. J., Bagenal, F., Sojka, J. J. 2016. HELIOPHYSICS: Active stars, their astrospheres, and impacts on planetary environments. Cambridge University Press .

[Stenflo and Kosovichev(2012)] Stenflo, J.O., Kosovichev, A.G., 2012. Bipolar magnetic regions on the sun: Global analysis of the soho/mdi data set. ApJ 745, 129 (12pp).

[Svalgaard et al.(2005)] Svalgaard, L., Cliver, E.W., Kamide, Y., 2005. Sunspot cycle 24: Smallest cycle in 100 years? Geophys. Res. Lett. 32, 1104. doi:10.1029/2004GL021664.

[Upton and Hathaway(2014)] Upton, L., Hathaway, D., 2014. Predicting the sun's polar magnetic fields with a surface flux transport model. ApJ 780, 5 (8p.).

[Wang et al.(1991)] Wang, Y.M., Sheeley, N.R., Nash, A.G., 1991. A new solar cycle model including meridional circulation. ApJ 383, 431–442.

[Weber.(2014)] Weber, M. A. , 2014. THE DYNAMIC EVOLUTION OF ACTIVE-REGION-SCALE MAGNETIC FLUX TUBES IN THE TURBULENT SOLAR CONVECTIVE ENVELOPE. Ph.D. thesis, Colorado State Univ.

[Weiss and Thompson(2009)] N.O. Weiss, M.J. Thompson, 2009. The Solar Dynamo. Space Sci Rev 144, 53–66.

[Yeates and Munoz-Jaramillo(2013)] Yeates, A.R., Munoz-Jaramillo, A., 2013. Kinematic active region formation in a three-dimensional solar dynamo model. MNRAS 436, 3366–3379.

[Yeates et al.(2008)] Yeates, A.R., Nandy, D., Mackay, D.H., 2008. Exploring the physical basis of solar cycle predictions: Flux transport dynamics and the persistence of memory in advection- versus diffusion-dominated solar convection zones. ApJ 673, 544–556.

[Zhao et al.(2013)] Zhao, J., Bogart, R.S., Kosovichev, A.G., Duvall, Jr., T.L., Hartlep, T., 2013. Detection of equatorward meridional flow and evidence of double-cell meridional circulation inside the sun. ApJL 774, L29 (6pp).

Declaration

This dissertation is my original work, has not been presented before in any other University and that all the sources of material used for the thesis have been dully acknowledged.

Name: Kinfe Teweldebirhan Gebreegzabihar

Signature:

Place and time of submission: Addis Ababa University, June 2018

This thesis has been submitted for examination with my approval as Supervisor.

Name: Prof. Mark S. Miesch

Signature:

Name: Dr. Abraham Amaha

Signature: